Biophysical characterization of the VHP35 protein by NMR spectroscopy

Dissertation

zur Erlangung des Doktorgrades der Naturwissenschaften
(Dr. rer. nat.)

der

Naturwissenschaftlichen Fakultät II
Chemie, Physik und Mathematik

der Martin-Luther-Universität
Halle-Wittenberg

vorgelegt von

Paul Becker
geboren am 04.09.1984 in Schwerin

Date of defense: 14.10.2022

Reviewer:

1. Prof. Dr. rer. nat. Jochen Balbach
2. Prof. Dr. rer. nat. Dariush Hinderberger
3. Prof. Dr. rer. nat. Werner Kremer

For *Christine*, *Frank*,
Kerstin and *Luise*

Abstract

The path of folding/unfolding to the functional state is characterized on the native side by a multitude of conformational substates, which are characterized by different structural and energetic properties. In this respect, the pressure-sensitive model protein VHP35 [1] and the variant VHP35_L69A are suitable proteins for a comprehensive biophysical analysis of the folding intermediates under changing physical conditions, in particular pressure, by solution NMR. Within the experimentally accessible temperature (278 - 368 K) and pressure (0.1 - 240 MPa) range, VHP35 reveals a hyperbolic phase boundary in the temperature-pressure phase space, which is the result of pressure-induced stabilizing volumetric rearrangements, including a smaller hydration shell leading to higher compressibility in the native state compared to the unfolded state. The latter difference in compressibility disappears by the L69A substitution resulting in an elliptic phase boundary and entropic pressure-induced destabilization. Supported by control structure calculations, distinct conformational differences for the pressure-dependent conformers are revealed between the wild type and the variant at 278 K, essentially within the backbone and particularly in the C-terminal helix. In the case of VHP35, this corresponds to heterogeneously distributed structural and dynamic changes mainly within the helix $\alpha 2$ to helix $\alpha 3$ and in particular R55 and the hydrophobic core residues F47, F51, L61, K65. In contrast, the structural changes of VHP35_L69A occur mainly within the C-terminal helix $\alpha 3$, especially within the KKEK motif and R55, L63, and K73, accompanied by increased variation in flexibility within the helix $\alpha 1$, especially in D46, and helix $\alpha 3$. For both systems, R55 in particular plays an important role with regard to pressure-dependent stability.

Zusammenfassung

Der Weg der Faltung/Entfaltung zum funktionellen Zustand ist auf der nativen Seite durch eine Vielzahl von konformationellen Unterzuständen gekennzeichnet, die durch unterschiedliche strukturelle und energetische Eigenschaften gekennzeichnet sind. In dieser Hinsicht sind das druckempfindliche Modellprotein VHP35 [1] und die Variante VHP35_L69A geeignete Proteine für eine umfassende biophysikalische Analyse der Faltungsintermediate unter wechselnden physikalischen Bedingungen, insbesondere Druck, mittels Lösungs-NMR. Innerhalb des experimentell zugänglichen Temperatur- (278 - 368 K) und Druckbereichs (0,1 - 240 MPa) zeigt VHP35 eine hyperbolische Phasengrenze im Temperatur-Druck-Phasenraum, die das Ergebnis von druckbedingten stabilisierenden volumetrischen Umlagerungen ist, einschließlich einer kleineren Hydrathülle, die zu einer höheren Kompressibilität im nativen Zustand im Vergleich zum entfalteten Zustand führt. Der letztgenannte Unterschied in der Kompressibilität verschwindet durch die L69A-Substitution, was zu einer elliptischen Phasengrenze und einer entropischen, druckinduzierten Destabilisierung führt. Unterstützt durch Kontrollstrukturberechnungen zeigen sich deutliche Konformationsunterschiede für die druckabhängigen Konformere zwischen dem Wildtyp und der Variante bei 278 K, im Wesentlichen innerhalb des Rückgrats und insbesondere in der C-terminalen Helix. Im Fall von VHP35 entspricht dies heterogen verteilten strukturellen und dynamischen Veränderungen hauptsächlich innerhalb der Helix α2 bis Helix α3 und insbesondere R55 und den hydrophoben Kernresten F47, F51, L61, K65. Im Gegensatz dazu treten die strukturellen Veränderungen von VHP35_L69A hauptsächlich innerhalb der C-terminalen Helix α3 auf, vor allem innerhalb des KKEK-Motivs und R55, L63 und K73, begleitet von einer erhöhten Variation der Flexibilität innerhalb der Helix α1, vor allem in D46, und Helix α3. Für beide Systeme spielt vor allem R55 eine wichtige Rolle im Hinblick auf die druckabhängige Stabilität.

Contents

Abbreviations

AA	*amino acid*
CPMG	*Carr-Purcell-Meiboom-Gill*
ct	*constant time*
HPLC	*high performance liquid chromatography*
HSQC	*heteronuclear single quantum correlation*
INEPT	*insensitive nuclei enhancement by polarization transfer*
NMR	*nuclear magnetic resonance*
NOE	*nuclear Overhauser effect*
NOESY	*nuclear Overhauser enhancement spectroscopy*
PDB	*Protein Data Bank*
r.f.	*radio-frequency*
RMSD	*root-mean-square deviation*
TOCSY	*total correlation spectroscopy*
VHP	*villin headpiece*
WATERGATE	*water suppression by gradient-tailored excitation*

1. Introduction

1.1. Proteins and the folding mechanism

Proteins are the most important functional biological molecules in life. In cells, they perform a variety of tasks, e.g. catalyzing metabolic reactions, signal transduction, transport or DNA replication. The unbranched polymers consist of L-α-amino acids linked by amide bonds. In most organisms, the primary sequence of the polymer is composed of a combination of 20 proteinogenic amino acids. The tertiary and quatenary structure of proteins is determined by non-bonding intra- and intermolecular interactions. These include the conformation of the dihedral angles of the peptide bond, hydrogen bonds, van der Waals forces, electrostatic and hydrophobic interactions, which depend on the sequence of the polypeptide chain and its local environment, such as the solvent [2, 3]. Thus, under physiological conditions the amino acid composition determines the native conformation (n) of the protein and thus its function [4, 5]. The tertiary structure is characterized by the spatial arrangement of the local secondary structure elements, like α-helices, β-sheets and turns. From a thermodynamic point of view, the conformational space of a protein is defined by an energy landscape in which the native state corresponds to the state with the lowest free energy [6]. The *de novo* prediction of the three dimensional structure of a protein from its amino acid sequence is still a challenging task and is referred to as the protein folding problem [7]. Nevertheless, recent developments in computational biology achieved by deep-learning algorithms show interesting progress [8, 9].

Despite these advances, protein folding is a complex dynamic process in which, even at thermodynamic equilibrium, a multitude of conformational substates might coexist within the ensemble of conformations of the native state [10–13]. This has been studied experimentally using a variety of methods including solution NMR spectroscopy, fluorescence spectroscopy, circular dichroism and small angle X-ray scattering [14–16]. The function of proteins is linked to these structural fluctuations, and the perturbation of the native conformation therefore leads to a shift in equilibrium in favor of the less populated, higher-energy substates (n^*) [17–19]. The stability of the different folding intermediates can be described by a funnel-shaped energy landscape with respect to a reaction coordinate [20, 21]. In general, protein stability is defined by the Gibbs free energy, which is an expression of internal energy, entropy and volume. The energetically different conformations of a system thus correspond to different values of these parameters [22, 23].

There are several ways to induce these conformations with their different thermodynamical properties, e.g. by varying the chemical (pH, denaturant), the biochemical (inser-

tion of point mutations) or the physical (temperature, pressure) environment. Despite the limitations of each of the strategies, changes in temperature, for example, provide thermal insights or chemical perturbations provide information under stable physical conditions. In contrast, varying pressure redistributes populations between the folded and the unfolded states via volume differences [24–28]. In general, when hydrostatic pressure is used, a change from 0.1 MPa to about 300 MPa leads to dissociation of oligomeric proteins or to conformational fluctuations in the case of monomeric proteins, and a change of up to 1 GPa leads to the unfolding of monomeric proteins [29, 30]. The physical basis of this process is the shift toward conformations with a smaller overall volume (Le Chatelier's principle) due to the elimination of the solvent-excluded voids by imperfect protein packing [31–33]. This is accompanied by a weakening of hydrophobic interactions caused by the solvent water through increased solvent density on exposed surfaces in the unfolded state and electrostriction of polar and charged groups [34–36]. In general, hydrogen bonds are strengthened under pressure, while hydrophobic interactions are weakened by water molecules penetrating the inner cavities of the protein core [37–41].
On this basis, the pressure cells commonly used in NMR spectroscopy (limit 300 MPa) [42–46] can be used to reversibly shift the equilibrium of a globular, monomeric system, which is sensitive to changes in partial molar volume, to less populated, higher energy substates or partially unfolded states and, in rare cases, to complete unfolding [47–50]. NMR spectroscopy methods allows one to obtain the structure, thermodynamic properties and conformational dynamics of these conformations with atomic resolution. The pressure-dependent thermodynamic properties determined by quantitative analysis of population shifts underpin the changes of partial molar volumes and internal cavities revealed by high-resolution NMR structures [50, 51]. Information about changes in the dynamics and the nonlinear shift dependence of the backbone complement the thermodynamic and structural picture on a residue-specific level [52–60]. In this context, the biophysical characterization of the pressure-dependent folding reaction is another promoting contribution to the elucidation of the protein folding mechanism.

1.2. The thermostable 35-residue subdomain within villin headpiece

The approach to understanding protein folding also depends on the complexity of the system under consideration. Compared to full-length proteins, *in vitro* or *de novo* derived, independently folding, small polypeptide chains or subdomains of proteins with a well-defined tertiary structure are more feasible models to study. An example of this property is the monomeric, 35 residues subdomain (VHP35) of the villin headpiece domain from chicken villin and the derived, physically similar, recombinant VHP36 (retains an additional N-terminal initiator methionine residue) [61]. Both have been extensively studied and have been shown to be useful tools in bridging the gap between experimental and computational approaches to protein folding.

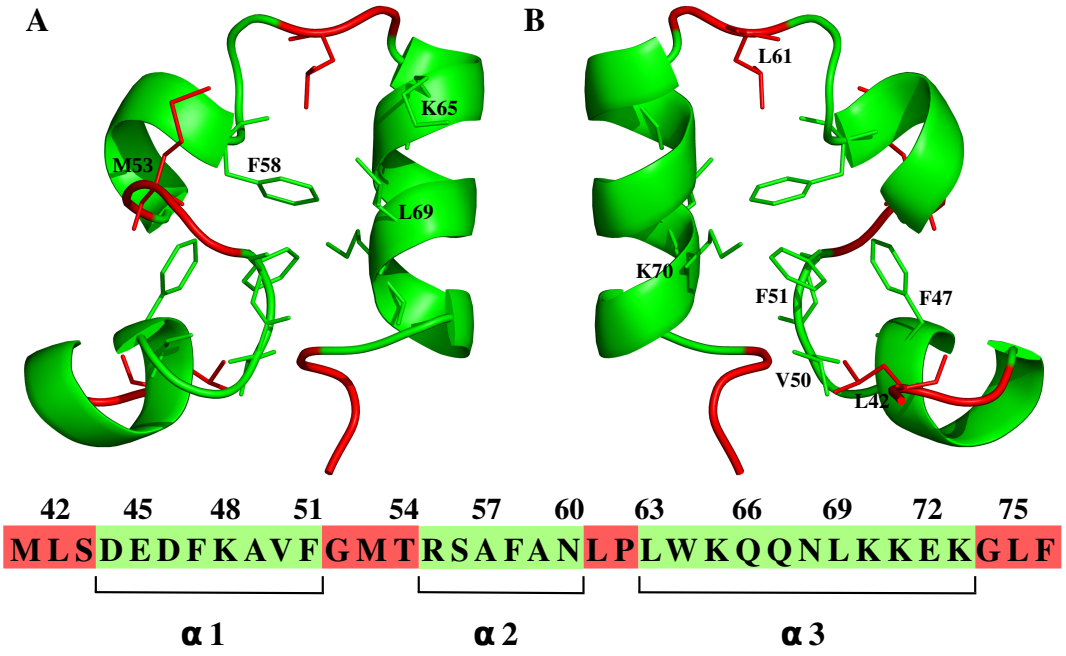

Figure 1.1.: **NMR structure and sequence of VHP36 (PDB: 1VII):** (A) shows the energy minimized average structure of VHP36 with the three α-helices (*green*), α1 to α3, and the turns, N- and C-terminus (*red*). The residues of the hydrophobic core (L42, F47, V50, F51, M53, F58, L61, K65, L69, K70) are shown without hydrogens [62–65]. (B) shows the rotation by 180° about the y-axis. Below the amino acid sequence with background color corresponding to the secondary structure. The residues are numbered according to their position in the 76 amino acid headpiece domain.

The sequence of VHP35 is part of the 92.5 kDa F-actin-binding protein villin, which is involved in the maintenance of the microvilli in the absorptive epithelial cells [66–68]. It consists of six repeating gelsolin-like domains of 150 residues each forming the core domain and a headpiece domain of 76 residues at the C-terminus [69]. Within the 8 kDa headpiece, VHP35 spans residues 42 - 76 (residues 791 - 825 of the intact chicken villin), including a KKEK motif essential for binding of villin to actin [70]. The subdomain is one of the smallest known naturally occurring sequences whose tertiary structure corresponds to that in the intact headpiece domain [62, 63, 65, 71]. With a midpoint of the temperature transition (T_m) in the range of 337 - 343 K of VHP35 or a T_m of about 340 - 346 K of VHP36, the proteins show similar thermal stability as also the intact headpiece domain with a T_m of about 347 - 349 K [61, 65, 72–76]. This is accompanied by a free energy of unfolding ($\Delta G^\circ_\mathrm{u}$) of about 7 - 13 kJ/mol of VHP35 or a $\Delta G^\circ_\mathrm{u}$ of about 11.8 - 13.8 kJ/mol of VHP36, which is a significant amount compared to to the overall thermodynamic stability of the headpiece with a $\Delta G^\circ_\mathrm{u}$ of about 18 kJ/mol.
Both the biologically isolated VHP35 as well as the recombinant protein fold autonomously and cooperatively into a globular structure without disulfide bonds and binding of ligands or metals. The structure is a motif of three α-helices surrounding a closed-packed

hydrophobic core (Fig. 1.1). The nine key residues comprising the hydrophobic core are all more than 70 % solvent inaccessible. A cluster of the three conserved phenylalanine residues F47, F51, and F58 forms the bulk of the hydrophobic core and contributes significantly to thermal stability [64]. Since the three residues are incorporated into the first two helices, the third helix is less stable [77]. Nevertheless, underpinned by studies of several mutation sites, including within the hydrophobic core, the information specifying the three dimensional structure and the thermodynamic stability is distributed throughout the sequence [64, 65, 78–82]. Following a two state model, VHP35 or VHP36 folds within 3.23 - 4.3 μs [72, 83–86].
Investigations of the molecular dynamics revealed a transient population of an unfolding higher energy intermediate (n^*) on the native side [75, 86–88]. At equilibrium, n^* is populated at ambient pressure up to 57 % and changes to the native state with a time constant of of about 600 ns [1]. The substate is a precursor to a partially unfolded state. Changing the pressure up to 390 MPa shifts the population of n^* to 64 %. The higher energy conformer shows a volume difference of ΔV° = -1.6 ml/mol compared to the native state. The slightly more solvent-exposed conformation of n^* is accompanied by weakened interactions and increased structural flexibility within the C-terminal helix [1, 89]. This is consistent with the dominant of the three unfolding pathways of VHP35 studied, in which helix α3 is segmentally destabilized before the others unfold [90–92]. Another option is the reverse way, in which helix α1 and helix α2 unfold first [82, 93]. The third option is characterized by the initial destabilization of the least thermodynamically stable helix α2 compared to the other helices, resulting in a cooperative unfolding pathway [94, 95]. In light of this, the pressure sensitve conformer n^* and the conformational heterogeneity of the folding/unfolding pathways of VHP35 are an interesting starting point for further biophysical studies.

1.3. Motivation

The function of proteins is linked to their structure. The pathway of folding/unfolding to the functional state is characterized by partially folded intermediates and a multitude of conformational substates on the native side. Investigation of the structural, molecular dynamics and thermodynamic properties of folding intermediates and substates provides a more comprehensive molecular understanding of protein folding. In this regard, based on the pressure-sensitive conformer n^* of the model protein VHP35 described by Neumaier *et al.* [1], the motivation of this research is a comprehensive biophysical analysis of the folding intermediates of VHP35 and the variant VHP35_L69A under changing physical conditions, in particular pressure, using solution NMR. Specifically, the characterization of the pressure-dependent, up to 240 MPa, structures of the proteins by NMR spectroscopy. Furthermore, the residue-specific analysis of the pressure-dependent chemical shifts and the pressure-dependent dynamics on a picosecond to nanosecond time scale. This picture is complemented by the measurement of the temperature-pressure Gibbs free energy landscape of VHP35 and VHP35_L69A obtained by 1D ^{1}H spectra. The alanine mutation of VHP35 at the hydrophobic core residue leucine 69 within the

helix $\alpha 3$ was created in order to generate an artificial void and to increase flexibility and decrease stability within the C-terminal helix. Comparison of the wild type and the variant will provide further insights into understanding pressure-induced unfolding.

2. Materials and Methods

2.1. Preparation of mixed labeled VHP35 and VHP35_L69A samples

The preparation of the protein samples was carried out by Uwe Fandrich from the group of Prof. Dr. Thomas Kiefhaber.

Protein expression and purification

VHP35 or VHP35_L69A was cloned into the Champion pET vector with His_6-SUMO at the N-terminus. The plasmid was transformed into *Escherichia coli* Rosetta pLysS cells. Labeled proteins were generated by growing the bacteria in M9 minimal medium containing ^{15}N ammonium chloride and $^{13}C_6$-glucose. In general, the protein expression (wild type or mutant) was carried out in 1 l cultures of *E. coli* Rosetta pLysS grown at 37 °C until the $OD_{600} = 0.8$ was reached. Protein expression was induced with 1 mM Isopropyl-β-D-thiogalactopyranosid (IPTG), and cells were harvested by centrifugation after 4 hours.
Cells were resuspended in 40 ml 50 mM Tris/HCl buffer, 350 mM NaCl, pH 7.5 at 4 °C and disrupted with French pressure cell press at 70 MPa. The cell extract was separated by centrifugation at 25000 rpm for 30 minutes at 4 °C and filtrated through 0.45 μm membranes. Protein was purified from the soluble fraction using Ni-affinity chromatography with a gradient of 500 mM Imidazol in 50 mM Tris/HCl buffer, 350 mM NaCl, pH 7.5. The eluate was concentrated and dialyzed with 4 l 50 mM Tris/HCl buffer, 350 mM NaCl, pH 7.5 in a 6 - 8 kDa tube. Proteolytic cleavage was performed with SUMO-protease. Further purification by HPLC was carried out on a Kinetex C18 column. Fractions containing protein were lyophilized and stored at -20 °C. Protein purity was analyzed by 16,5 % Tris/Tricin Gel and mass spectrometry.

2.2. NMR spectroscopy

NMR measurements were recorded using a Bruker Avance III 600 (TXI triple resonance probe) spectrometer. The $^{15}N/^{13}C$-labeled proteins were studied at 278 K in 10 mM K_2HPO_4/KH_2PO_4 buffer (pH 7.0), 30 or 60 μM 3-(Trimethylsilyl)-1-propanesulfonic acid-d_6 sodium salt (DSS-d_6), 10 % D2O, and with a concentration of 1.3 mM of VHP35 or 1.5 mM of VHP35_L69A. All spectra were directly or indirectly referenced to DSS. High-pressure NMR measurements were performed in a commercial 3 mm ceramic cell

(Daedalus Innovations LLC) connected to a home-built pressure generation up to 250 MPa [96]. The NMR resonance assignment of wild-type VHP35 has been reported previously [61,62]. Backbone assignment of the wild type or the variant was achieved by 2D ^{1}H,^{15}N-*f*HSQC [97], triple-resonance experiments *tr*HNCACB [98,99], HNCO [100], 3D NOESY-HSQC [101] supplemented by side-chain assignments from a ^{1}H,^{13}C-*ct*HSQC [102], ^{1}H,^{13}C-*ct*HSQC-TOCSY and 3D HCCH-TOCSY [103] experiments. R_1, R_2 and ^{1}H,^{15}N heteronuclear NOE (*h*NOE) [104] data for backbone ^{15}N nuclei were measured by 2D HSQC. Experimental time-points for R_1 were 0, 0.05, 0.1, 0.2, 0.3, 0.5, 0.7, 1, 1.2, 1.5 s. R_2 measurements used a CPMG pulse train [105] with time points of 0, 0.008, 0.016, 0.032, 0.048, 0.064, 0.096, 0.128, 0.16, 0.192 s. The *h*NOE experiment was recorded with proton saturation period of 3 s. Data were collected at ambient pressure and 240 MPa.
The pressure dependence of ^{15}N chemical shifts was determined using ^{1}H,^{15}N-*f*HSQC at ambient pressure up to 240 MPa in steps of 20 MPa. One-dimensional (1D) ^{1}H spectra under presaturation solvent suppression were measured at 0.1 MPa to 240 MPa in steps of 50 MPa and at a temperature range from 278 K to 368 K in steps of 5 K.
The NMR pulse sequences used here are listed in Appendix B. All NMR data were processed by Bruker TopSpin 3.6.2 and analyzed by CARA 1.9.1.7 [106] and PINT [107].

2.2.1. Heteronuclear single quantum coherence

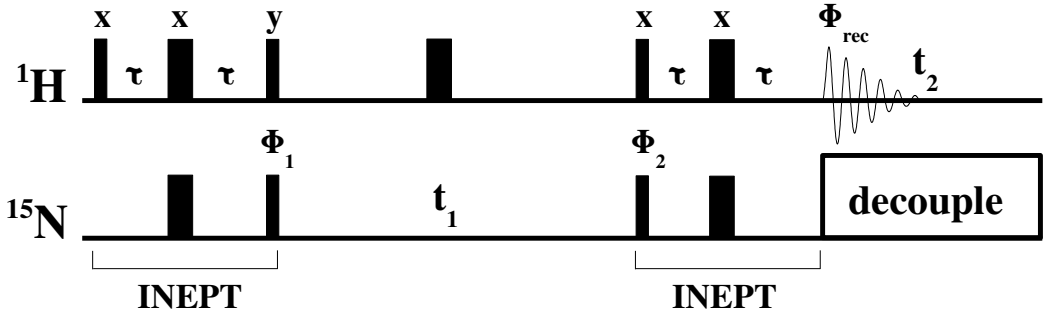

Figure 2.1.: **Basic ^{1}H,^{15}N-HSQC pulse sequence:** Inverse detection of the heteronuclear chemical shift correlation between ^{1}H and ^{15}N via $^{1}J_{\mathrm{NH}}$-coupling. The initial INEPT sequence transfers the polarization from ^{1}H into the anti-phase heteronuclear single-quantum coherence. The anti-phase ^{15}N magnetization evolves during the subsequent t_1 evolution period. The reverse INEPT sequence converts the frequency-labeled ^{15}N magnetization back to an in-phase ^{1}H magnetization. Heteronuclear decoupling is applied during the detection period t_2. Narrow bars correspond to $\pi/2$-pulses and wider bars represent π-pulses. The nominal value for $\tau = 1/(4J_{\mathrm{NH}})$. Phase cycling is for Φ_1 = x,-x, Φ_2 = x,x,-x,-x and for the receiver Φ_{rec} = x,-x,-x,x.

NMR spectroscopy is a powerful technique for studying the structure, dynamics, and chemical kinetics of a molecule at the atomic level. The selection of the appropriate NMR experiments to assign the resonance signals of a molecule is essentially determined by the length and the structure of the system. As molecular weight increases, high-resolution multidimensional NMR spectroscopy provides the basis for resolving signal overlap and enhancing the resolution. The experiments are based on the correlation of the polarization transfer between different spins via scalar coupling through chemical bonds or via dipolar coupling through space [108].
The 2D heteronuclear single-quantum coherence (HSQC) experiment allows one to obtain a 2D heteronuclear correlation map of the chemical shifts between directly-bonded ^{1}H and X-heteronuclei (commonly, ^{13}C and ^{15}N). The ^{1}H,^{15}N-HSQC of a protein shows the amide groups of the backbone and the side chain group of tryptophane (Nϵ-Hϵ), asparagine (Nδ-Hδ2), glutamine (Nϵ-Hϵ2), arginine (Nη2-Hη2) and histidine (Nϵ-Hϵ). Due to the absence of an amide proton, prolins are not shown in the spectrum.
The experiment is characterized by the coherence transfer from spin I (^{1}H) to a heteronuclear spin S (^{15}N) via J-coupling. The transfer is realized by INEPT (Insensitive Nuclei Enhancement by Polarization Transfer) blocks (Fig. 2.1). The concept is explained below using the product operator formalism. The first INEPT sequence cause the conversion of in-phase proton magnetization (-I_{y}) into anti-phase magnetization (-$2I_{\mathrm{x}}S_{\mathrm{z}}$)

$$\begin{aligned} I_{\mathrm{z}} &\xrightarrow{\frac{\pi}{2}I_{\mathrm{x}}-\tau-\pi(I_{\mathrm{x}}+S_{\mathrm{x}})-\tau} -2I_{\mathrm{x}}S_{\mathrm{z}} \xrightarrow{\frac{\pi}{2}(I_{\mathrm{y}}+S_{\mathrm{x}})} -2I_{\mathrm{z}}S_{\mathrm{y}} \\ &\xrightarrow{\Omega_S t_1 S_{\mathrm{z}}} 2I_{\mathrm{z}}S_{\mathrm{y}}\cos(\Omega_S t_1) - 2I_{\mathrm{z}}S_{\mathrm{x}}\sin(\Omega_S t_1) \\ &\xrightarrow{\frac{\pi}{2}(I_{\mathrm{x}}+S_{\mathrm{x}})-\tau-\pi(I_{\mathrm{x}}+S_{\mathrm{x}})-\tau} I_{\mathrm{x}}\cos(\Omega_S t_1) - 2I_{\mathrm{y}}S_{\mathrm{x}}\sin(\Omega_S t_1). \end{aligned} \tag{2.1}$$

At the end of the INEPT block, a $\pi/2$ y-pulse on spin I and x-pulse on spin S transfers the anti-phase magnetization to the heteronuclear spin (-$2I_{\mathrm{z}}S_{\mathrm{x}}$). The spin S evolves the chemical shift Ω_S during the variable evolution time t_1. The π-pulse on the proton in the middle of this period refocuses the heteronuclear scalar coupling (J_{IS}). A reverse-INEPT block converts the frequency-labeled ^{15}N magnetization back to in-phase ^{1}H magnetization. The result is an unobservable double quantum magnetization (-$2I_{\mathrm{y}}S_{\mathrm{x}}$) and in-phase ^{1}H magnetization (I_{x}). During the acquisition time t_2, heteronuclear decoupling is applied. During t_2, the spin I evolves the chemical shift Ω_I in the following way

$$I_{\mathrm{x}}\cos(\Omega_S t_1) \xrightarrow{\Omega_I t_2 I_{\mathrm{z}}} I_{\mathrm{x}}\cos(\Omega_S t_1)\cos(\Omega_I t_2) + I_{\mathrm{y}}\cos(\Omega_S t_1)\sin(\Omega_I t_2). \tag{2.2}$$

Phase-sensitive quadrature detection is used to detect a single resonance line for each I-S spin pair, yielding the following signal

$$S(t_1, t_2) = \cos(\Omega_S t_1)e^{\mathrm{i}\Omega_I t_2}. \tag{2.3}$$

In combination with ^{15}N, ^{13}C isotope labeling, the HSQC experiment forms the template to realize sequence specific assignment of proteins. Fot double-labeled protein molecules, a broadband selective π-pulse was applied on the third channel to decouple the ^{15}N or ^{13}C spins. Water suppression was achieved by presaturation, pulsed-field gradients,

and the 3-9-19 WATERGATE sequence [109]. Phase-sensitive quadrature detection was acquired using TPPI-States [110] or echo-antiecho. The two-dimensional heteronuclear correlation experiments are integral components of all heteronuclear three- and four-dimensional NMR experiments.

2.2.2. Residue-specific assignment

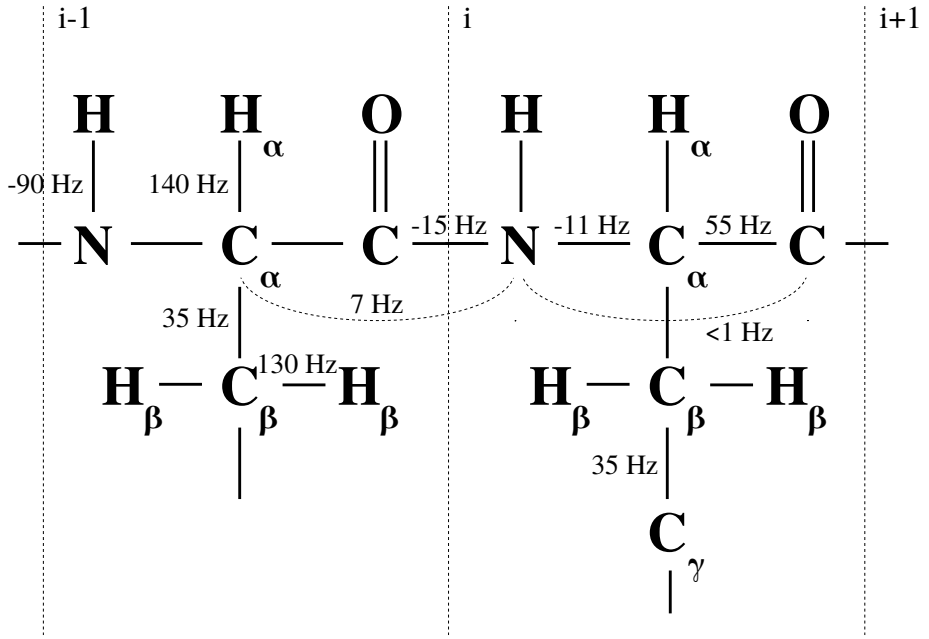

Figure 2.2.: **Heteronuclear coupling constants in proteins:** Spin system (i) with characteristic J-coupling constants that used for magnetization transfer in ^{13}C, ^{15}N labeled proteins [111].

Sequential assignment of backbone and side chain signals from VHP35 and VHP35_L69A was enabled with 2D ^{1}H,^{15}N/^{13}C-HSQC experiments in combination with several 3D triple resonance experiments. The backbone assignment was realized by combining of TROSY-HNCACB and HNCO experiments, previous resonance assignment [61,62], and the specific chemical shifts of amino acids in disordered polypeptid chains [112]. In the case of the HNCACB, coherence transfer is realized within a spin system from $^{1}H_N$ via ^{15}N to $^{13}C_\alpha$ and $^{13}C_\beta$. The transfer reveals sequential information due to similar coupling constants. Specifically, this means that the magnetization is transfered from the ^{15}N to the $^{13}C_\alpha^{i}$ (11 Hz) as well as to the $^{13}C_\alpha^{i-1}$ (7 Hz) precursor (Fig. 2.2). In this way, the chemical shifts of the C_α and C_β of the spin system and their precursors are obtained. This provides the link to the resonances of the ^{1}H,^{13}C-HSQC.
In combination with the HNCO experiment, which connects the resonances of the amid proton to the precursor carbonyl group, a sequential assignment can be implemented. Based on ^{1}H,^{13}C-*ct*HSQC experiments, the side-chain assignments of the aliphatic and

aromatic groups were determined by 3D HCCH-TOCSY and ^{1}H,^{13}C-*ct*HSQC-TOCSY measurements. The TOCSY correlates all carbons or carbon-coupled protons within a spin system, respectively (Fig. 2.2). The combination resolves the chemical shift information of the carbons and their covalently bonded protons.

2.2.3. Dynamic parameters

Spin relaxation experiments are used to study the global and local dynamics of proteins. NMR spin relaxation depends on stochastic thermal motions (Brownian motion) that modulate nuclear magnetic spin Hamiltonians to regain thermal equilibrium. The process is characterized by longitudinal relaxation for the return of spin populations to their Boltzmann distribution values and by transverse relaxation for the decay of coherences. The mechanism is caused by time-dependent fluctuating magnetic fields at the sites of the nuclear spins. For nuclei with spin 1/2, the main sources of the field fluctuations are dipolar coupling and chemical shift anisotropy (CSA).
Different types of protein dynamics can be observed, such as molecular vibrations, side chain rotations, chemical exchange processes and protein folding. Their time scales range from picoseconds to tens of seconds [113, 114]. In this work, longitudinal (R_1) and transverse (R_2) relaxation rates and heteronuclear Overhauser effects (hNOE) were measured to study backbone dynamics in the range of the picosecond to nanosecond time scale.
The relaxation rates are functions of the spectral density function ($J(\omega)$) [115]. It gives the intensity of the time- and frequency-dependent spin orientations caused by local magnetic field fluctuations. The function is described by correlation functions of time-dependent random rate processes. For spherical molecules, the Fourier-transformed equation is

$$J(\omega) = \frac{\tau_c}{(1+\omega^2\tau_c^2)}, \tag{2.4}$$

where ω is the frequency of the relaxation-inducing random rate process and τ_c is the rotational correlation time of the molecule. For the backbone amide ^{15}N spins of proteins in solution, the relaxation parameter are given by

$$R_1 = \frac{1}{T_1} = \frac{d^2}{4}\Big[J(\omega_H-\omega_N) + 3J(\omega_N) + 6J(\omega_H+J\omega_N)\Big] + \frac{\omega_N^2\Delta\sigma^2}{3}J(\omega_N), \tag{2.5}$$

$$\begin{aligned} R_2 = \frac{1}{T_2} =& \frac{d^2}{8}\Big[4J(0) + J(\omega_H-\omega_N) + 3J(\omega_N) + 6J(\omega_H) + 6J(\omega_H+\omega_N)\Big] \\ &+ \frac{\omega_N^2\Delta\sigma^2}{18}\Big[4J(0) + 3J(\omega_N\Big] + R_{ex}, \end{aligned} \tag{2.6}$$

$$hNOE = 1 + \frac{d^2}{4R_1}\frac{\gamma_H}{\gamma_N}\Big[6J(\omega_H+\omega_N) - J(\omega_H-\omega_N)\Big], \tag{2.7}$$

where γ_H and γ_N are the gyromagnetic ratios, and ω_H and ω_N are the Larmor frequencies of the proton and the nitrogen, respectively. R_{ex} represents the slow conformational exchange rate in the range from μs to ms. $\Delta\sigma$ describes the difference of axial and

parallel elements of the CSA of ^{15}N with an average value of 165 ppm [116]. And the dipolar coupling d is given by

$$d = \frac{\mu_0 \hbar \gamma_N \gamma_H}{4\pi \langle r_{NH} \rangle^3}, \tag{2.8}$$

where μ_0 is the magnetic constant, $\hbar$ is the reduced Planck constant, and $\langle r_{NH} \rangle$ is the average internuclear distance of the ^{1}H-^{15}N pair.

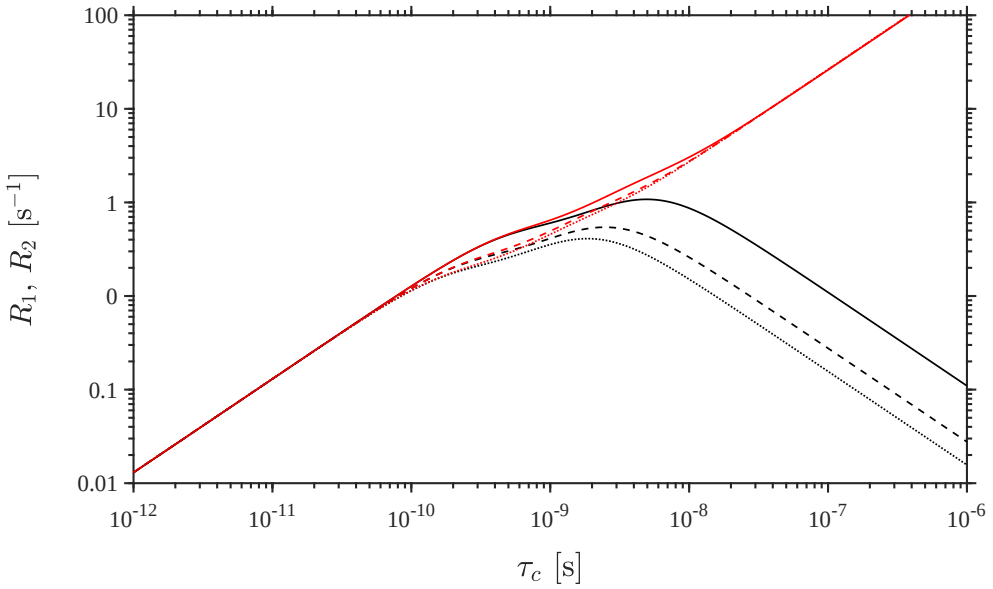

Figure 2.3.: **Double-logarithmic plot of ^{15}N relaxation rates as a function of the rotational correlation time τ_c:** The longitudinal R_1 (*black*) and the transverse R_2 (*red*) relaxation rates *versus* the correlation time, depending on different magnetic fields B_0 (*solid*: B_0 = 7,04 T, *dashed*: B_0 = 14,1 T, *dotted*: B_0 = 18,8 T). Calculated curves of R_1, R_2 based on the equations 2.5 and 2.6 with an average internuclear distance $\langle r_{NH} \rangle$ = 1.02 $\AA$ and an average CSA $\Delta\sigma_N$ = 165 ppm.

Figure 2.3 shows the longitudinal and transverse relaxation rates of ^{15}N as a function of the rotational correlation time. For spherical molecules in non-viscous solutions, τ_c is proportional to the molecular weight. As the size of the molecule increases, R_2 increases linearly with τ_c. R_2 is essentially field independent, being dominated by $J(0)$. The term represents the dephasing of the transverse magnetization by an inhomogeneous local magnetic field. The relaxation rate R_1 is mainly influenced by $J(\omega_N)$, which represents the contribution of single quantum transitions of the ^{15}N nucleus. Therefore, at higher higher magnetic fields, the value decreases at different rates after the maximum ($\omega_N \tau_c \approx 1$). The measurement of R_1 and R_2 rates was accomplished by pseudo-3D ^{1}H,^{15}N-HSQC experiments [117]. Where the pseudo third dimension defines the relaxation delay t.

R_1 rates were obtained by inversion recovery experiments (π - t - $\pi/2$). Here the longitudinal magnetization is prepared by a π-pulse which generates an inverted population

distribution. A second $\pi/2$-pulse converts the population difference into observable coherences after the delay t.
The CPMG sequence ($(\pi/2)_x$ - τ_{cp} - π_y - τ_{cp}) was used to measure the transverse relaxation rate. The $(\pi/2)_x$-pulse induces a transverse magnetization. The decay of the M_{xy} magnetization is obtained after the spin-echo period $t = [\tau_{cp}$ - π_y - $\tau_{cp}]_n$. The variation of this time delay gives $t = 2n\tau_{cp}$, where 2n is the number of spin-echo periods and τ_{cp} is the length of a single spin-echo period. Refocusing by the π_y-pulse eliminates magnetic field inhomogeneities and chemical shift evolution.
Heteronuclear rates were realized via reverse INEPT sequences, including the inversion-recovery or CPMG sequence (Fig. 2.1). The rates were determined by nonlinear least-squares fitting of the experimental data points ($I(t)$) to two-parameter mono-exponential equation

$$I(t) = I_0 \exp(-R_{1,2}t). \tag{2.9}$$

The errors in the fitted relaxation rate constants were estimated using the jackknife method.

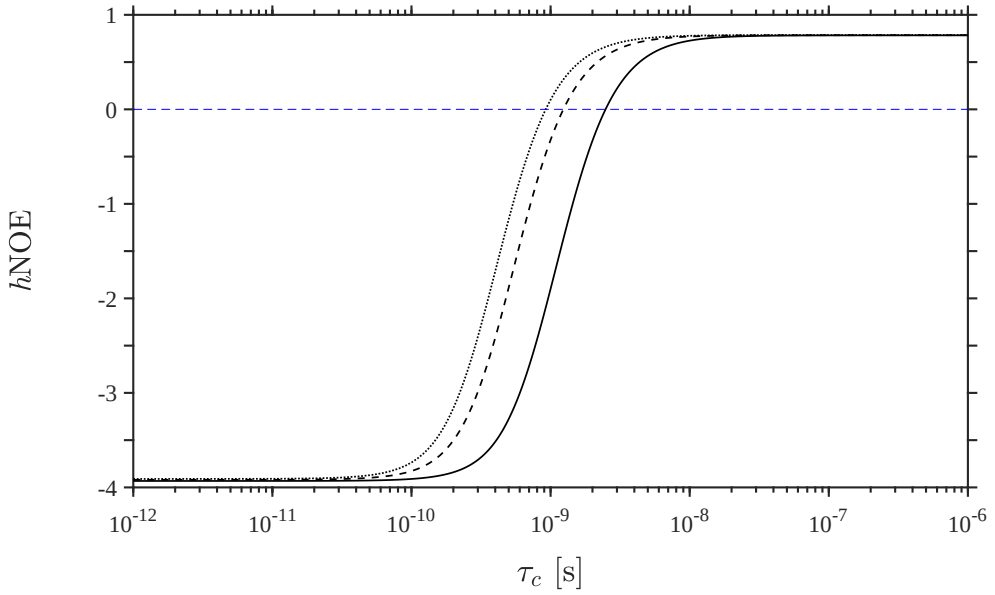

Figure 2.4.: **Logarithmic plot of heteronuclear ^{15}N{^{1}H}-NOE as a function of the rotational correlation time τ_c:** The hNOE *versus* the correlation time depending on different magnetic fields B_0 (B_0 = 7,04 T *solid*, B_0 = 14,1 T *dashed*, B_0 = 18,8 T *dotted*). Calculated curves of hNOE based on the equation 2.7 with an average internuclear distance $\langle r_{NH} \rangle = 1.02$ Å and an average CSA $\Delta\sigma_N = 165$ ppm.

The ^{15}N{^{1}H} heteronuclear NOE provides information about the motion of individual N-H bond vectors. The NOE is based on the distance-dependent dipolar cross-relaxation between spins (§ 2.2.4). This can be observed in the time-dependent changes in the intensities of the dipolar-coupled spins (Eq. 2.10). Applying a weak r.f. field at the

proton induces the saturation of the spins, resulting in an equalized population. The saturation affects the steady-state equilibrium of the heteronuclear spin (^{15}N), which is described by the NOE enhancement factor (η_{HN}). hNOE is the ratio of the longitudinal magnetization of the heteronuclear spin at equilibrium when the proton is saturated (I_{sat}) and at thermal equilibrium (I_{ref}). The ratio of the intensities gives

$$h\mathrm{NOE} = \frac{I_{\mathrm{sat}}}{I_{\mathrm{ref}}} = 1 + \eta_{HN} = 1 + \frac{\sigma_{HN}}{\rho_N}\frac{\gamma_H}{\gamma_N}, \tag{2.10}$$

where η_{HN} is defined by the longitudinal cross-relaxation rate σ_{HN}, the longitudinal relaxation rate of the amide ρ_N and the gyromagnetic ratios γ_H and γ_N. The relaxation rates are expressions of the spectral density functions as described in equation 2.7. The NOE enhancement factor depends on the correlation time and thus on the motion of the molecule (Fig. 2.4). As τ_{c} increases, the change of hNOE is associated with larger molecular weight. Variations in individual values indicate differences in the internal motions within the molecule. The hNOE of the N-H bond vector ranges from -3.93 and 0.9 due to the negative value of γ_N. The field dependence results from the contribution of the longitudinal relaxation rate.
Like the relaxation rates, the heteronclear NOE was measured using pseudo-3D ^{1}H,^{15}N correlation experiments alternating with and without proton saturation prior to the $\pi/2$-pulse for ^{15}N. The cycle is defined in the third dimension. Coherence transfer back to the amide proton was realized via a single reverse INEPT sequence (Fig. 2.1).

2.2.4. NOEs

As described above, the nuclear Overhauser effect is based on distance-dependent dipolar cross-relaxation between spins that are subject to Brownian molecular motion [118]. The random isotropic tumbling of the molecule generates time-dependent magnetic fluctuations at the spins. These field fluctuations induce frequency-dependent relaxation mechanisms. For two dipolar coupled spins, the time-dependent return of the longitudinal magnetization of a spin (I_{z}) to thermal equilibrium (I^0_{z}) is given by the following Solomon equation

$$\frac{dI_{\mathrm{z}}}{dt} = -\rho_I^{\mathrm{auto}}(I_{\mathrm{z}} - I^0_{\mathrm{z}}) - \sigma_{IS}^{\mathrm{cross}}(S_z - S^0_{\mathrm{z}}). \tag{2.11}$$

S_{z} is the time-dependent and S^0_{z} the equilibrium longitudinal magnetization of the diploar coupled spin. The Solomon equation describes the longitudinal relaxation of a spin as the sum of auto-relaxation (ρ^{auto}) and cross-relaxation (σ^{cross}) processes. The relaxation rates are expressions of spectral density functions (Eq. 2.4)

$$\rho^{\mathrm{auto}} = \frac{d^2}{10}\Big[J(0) + 3J(\omega) + 6J(2\omega)\Big], \tag{2.12}$$

$$\sigma^{\mathrm{cross}} = \frac{d^2}{10}\Big[J(0) - 6J(2\omega)\Big], \tag{2.13}$$

with the dipolar coupling d (Eq. 2.8). Hence, the longitudinal relaxation depends on the relative orientation and distance ($\propto 1/\mathrm{r}^6$) of the coupled spins. The distant-dependent

exchange of longitudinal magnetization of the dipolar coupled spins through space leads to a perturbation of the population at the considered spins. The observable change of the signal intensities is referred to as the NOE.
The NOE can be used to provide information about inter-proton distances for structure determination or about the motion of a molecule. The latter is obtained via the steady-state NOE or *h*NOE (Eq. 2.10, § 2.2.3).

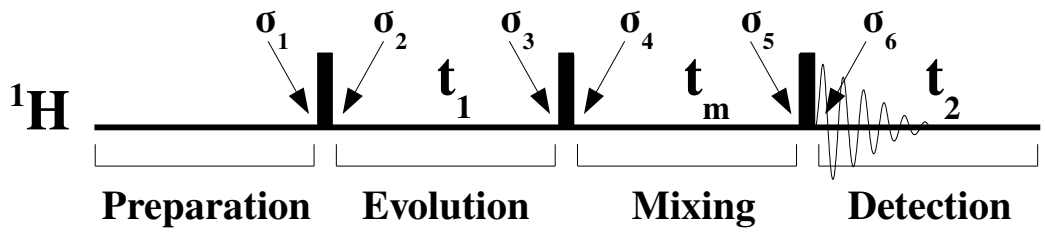

Figure 2.5.: **Basic NOESY pulse sequence [119]:** After excitation by the first $\pi/2$-pulse and the free variable evolution period t_1, transverse magnetization evolves. The second $\pi/2$-pulse generates longitudinal magnetization. During the NOE mixing time (t_m), an exchange of magnetization between spins via cross-relaxation or chemical exchange occurs. The final pulse generates observable in-phase transverse magnetization of the spins under consideration. Narrow bars represent $\pi/2$-pulses. Density matrices at different time points in the sequence (σ_1 - σ_6) are discussed in the text.

The inter-proton distances are obtained by measuring the transient NOE (NOEs) with the NOESY (nuclear Overhauser effect spectroscopy) experiment. Since the NOEs are based on cross-relaxations, the experiment is sensitive to spin distance ranges of 5 $\AA$ or less. Figure 2.5 shows the product operator formalism of a basic NOESY experiment for a homonuclear, not scalar coupled two-spin system (I and S). The initial density matrix (σ_1) of the longitudinal magnetization of the dipolar coupled spins in thermal equilibrium is given by

$$\sigma_1 = I_\mathrm{z} + S_\mathrm{z}. \tag{2.14}$$

After the excitation by the first $\pi/2$-pulse and the subsequent t_1 period, the system evolves under the chemical shifts (ω_I, ω_S)

$$\begin{aligned}\sigma_3 = &\Big[- I_\mathrm{y}\cos(\omega_I t_1) + I_\mathrm{x}\sin(\omega_I t_1)\Big]\exp(-R_2 t_1) + \\ &\Big[- S_\mathrm{y}\cos(\omega_S t_1) + S_\mathrm{x}\sin(\omega_S t_1)\Big]\exp(-R_2 t_1).\end{aligned} \tag{2.15}$$

The second $\pi/2$-pulse generates a non-equilibrium population difference within the spin levels. Through phase cycling the transverse components of the magnetization are suppressed and the density matrix is given by

$$\sigma_4 = \Big[I_\mathrm{z}\cos(\omega_I t_1) + S_\mathrm{z}\cos(\omega_S t_1)\Big]\exp(-R_2 t_1). \tag{2.16}$$

The result of the phase cycle-edited density matrix during the mixing time t_m is the evolving longitudinal cross relaxation between dipolar coupled spins

$$\begin{aligned}\sigma_5 =&\Big[I_\mathrm{z}a_{11}(t_\mathrm{m})\cos(\omega_I t_1))\Big]\exp(-R_2 t_1) + \Big[I_\mathrm{z}a_{21}(t_\mathrm{m})\cos(\omega_I t_1))\Big]\exp(-R_2 t_1) + \\ &\Big[S_\mathrm{z}a_{22}(t_\mathrm{m})\cos(\omega_S t_1))\Big]\exp(-R_2 t_1) \; + \Big[S_\mathrm{z}a_{12}(t_\mathrm{m})\cos(\omega_S t_1))\Big]\exp(-R_2 t_1).\end{aligned} \tag{2.17}$$

Here the amplitudes a_ij are solutions of the time-dependent Solomon equations of the longitudinal magnetization

$$a_\mathrm{diag} = a_{11} = a_{22} = \cosh(\sigma^\mathrm{cross} t_\mathrm{m})\exp(\rho^\mathrm{auto} t_\mathrm{m}), \tag{2.18}$$

$$a_\mathrm{cross} = a_{21} = a_{12} = \sinh(\sigma^\mathrm{cross} t_\mathrm{m})\exp(\rho^\mathrm{auto} t_\mathrm{m}), \tag{2.19}$$

with the the auto- and cross-relaxation rates described in equation 2.12 and 2.13. The final $\pi/2$-pulse generates observable transverse in-phase magnetization of the spins under consideration. The following signal is measured during the detection time t_2

$$\begin{aligned}S(t_1, t_2) \propto &\Big[a_{11}(t_\mathrm{m})\cos(\omega_I t_1)) + a_{21}(t_\mathrm{m})\cos(\omega_I t_1))\Big]\exp(-R_2 t_1)\exp(-i\omega_I t_2) + \\ &\Big[a_{22}(t_\mathrm{m})\cos(\omega_S t_1)) + a_{12}(t_\mathrm{m})\cos(\omega_S t_1))\Big]\exp(-R_2 t_1)\exp(-i\omega_S t_2).\end{aligned} \tag{2.20}$$

The spectrum contains two diagonal peaks whose amplitudes are given by a_diag and two cross-peaks whose amplitudes given by a_cross. For short mixing times t_m the amplitudes of cross-peaks corresponds to

$$a_\mathrm{cross}(t_\mathrm{m}) \cong \sigma^\mathrm{cross} t_\mathrm{m} \propto r^{-6}. \tag{2.21}$$

Apart from the correlation time (τ_c), σ^cross depends only on the distance (r) between the spins. Therefore, the integral of the transient NOE is directly proportional to the distance r. In the case of a multiple spin system, the longitudinal magnetization could be mediated via the neighboring nuclear spins. This phenomenon is called spin diffusion [120]. As the mixing time increases, auto-relaxation and spin diffusion processes increasingly contribute to the NOE signal. Therefore, a compromise between the suppression of spin diffusion and a sufficient NOE signal intensity must be chosen in the experiment. Suitable mixing times for proteins range from 60 to 120 ms.
NOEs were obtained using 3D NOESY-HSQC experiment. The experiment consists of a homonuclear 2D NOESY pulse sequence (Fig. 2.5) followed by a ^{1}H,^{15}N/^{13}C-HSQC pulse sequence (Fig. 2.1). ^{1}H,^{15}N/^{13}C correlations were realized by double INEPT transfer.

2.3. Molecular structure determination

The structures of VHP35 and VHP35_L69A were calculated with ARIA 2.3.1 [121] and CNS [122], using ambiguous NOEs, the protein sequence and by TALOS+ [123] derived

dihedral information as structural restraints. Structure calculations were performed using the following simulated annealing protocol: High-temperature sampling at 10,000 K (10,000 steps), the first annealing stage from 10,000 to 1,000 K (5,000 steps), and the second annealing stage from 1,000 to 50 K (4,000 steps). With the ARIA protocol, 60 conformers were calculated in the first iteration and 400 conformers in the final iteration. An ensemble of the 10 structures with the lowest energy was used for further structural analysis. Ramachandran analysis was performed by using PROCHECK-NMR [124]. Structural visualization, alignment, atomic distances, solvent-accessible cavity detection, and calculation of the solvent-accessible surface area (SASA) were realized with PyMOL 1.7.2.1 (DeLano Scientific LLC). Theoretical molecular surface volume (V_{MS}), van der Waals volume (V_{VDW}) and void volume (V_{VOID}) were calculated with ProteinVolume 1.3 (Fig. 2.6) [125].

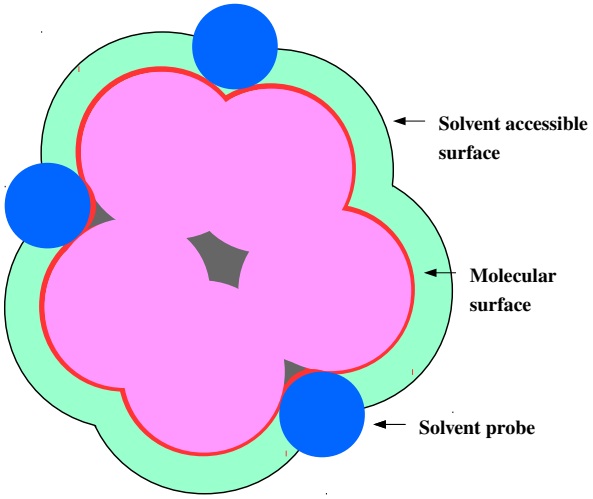

Figure 2.6.: **Schematic diagram depicting of the surface and volume definitions according to Chen *et al.* [125]:** The solvent-accessible surface (*black* line) is defined by the radius of the solvent probes (*blue* circles) around the protein surface. The volume enclosed by this surface is called the solvent-accessible volume. The molecular surface volume (*red* line) is the sum of the intrinsic volume of the protein atoms, termed van der Waals volume (*magenta*), and the void volumes or solvent-excluded volumes (*gray*). The envelope volume (*turquoise*), which reflects the solute-solvent interactions, is then the difference between the solvent-accessible volume and the molecular surface volume.

2.3.1. Concept of structure calculation

The parameters obtained by the NMR experiments described above contain spatial and structural information. The resulting software-based restraints form the basis for calculating a three-dimensional structure of a biomolecule in solution. In this work, structure determination was performed using the software packages ARIA 2.3.1 (ambiguous re-

straints for iterative assignment) and CNS (crystallography and NMR system). This is intended to serve as a basis for explaining some general concepts in the following.

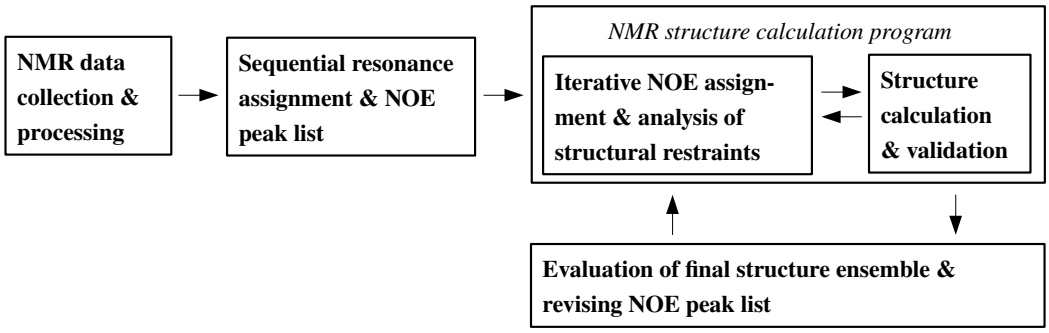

Figure 2.7.: **General procedure of protein structure determination based on NMR data:** NOE assignment and structure calculations are performed iteratively and verified by software-based structure validation (e.g. RMSD, lowest energy conformers, restraint analysis, etc.). Violated restraints, RMSD and calculated energies of the final structure ensemble determine the revision of the input data.

The general procedure of structure determination by NMR consists of several steps, which are shown in Figure 2.7. ARIA converts the experimentally derived NOE intensities into calibrated ambiguous distance restraints and performs automated NOE assignment for the structure generation with CNS. The software requires a list of assigned chemical shifts, the protein sequence, and uninterpreted or partly assigned multidimensional homo- or heteronuclear resolved NOE cross-peak lists to derive a basic dataset of restraints. In addition, other data can be added to derive further constraints, such as amide hydrogen exchange protection data for hydrogen bond restraints, residual dipolar couplings for orientational restraints and chemical shifts, scalar couplings and the protein sequence for the determination of dihedral angle restraints. In this work, the program TALOS+ (torsion angle likelihood obtained from shifts and sequence similarity) was used for automatic determination of the dihedral angles. The software uses a neural network algorithm and a database of tripeptide backbone secondary chemical shifts of high resolution structures. The local geometry of the backbone of a protein is described by the two dihedral angles ϕ and ψ [126]. The combinations of ϕ and ψ can be visualized in the Ramachandran plot. The plot illustrates the permissible conformational regions of an amino-acid residue within the secondary structure of a protein. The chemical shifts of the backbone atoms are sensitive to the local backbone geometry and can therefore be used to derive the dihedral information [127]. When combined with the protein sequence, TALOS+ predicts the secondary structure on the basis of the chemical shifts.
In order to generate structural distance restraints, ARIA performs automated, iterative assignment, calibration, violation analysis, and merging of the experimental derived NOE intensities. The initial assignment is based on the chemical shifts. The calibration method of the volumes or amplitudes of the NOESY cross-peaks includes the isolated

spin pair approximation (ISPA) or the relaxation matrix analysis. The relaxation matrix takes into account the spin diffusion. The theoretical volume $V_{ij}^{th}(t_m)$ of two contributing spins (i, j) gives the following relaxation matrix

$$V_{ij}^{th} = V_{ij}^{th}(0)(\exp[t_m R])_{ij}, \tag{2.22}$$

where t_m is the mixing time, $V_{ij}^{th}(0)$ at $t_m = 0$, and R is the cross-relaxation rate (Eq. 2.13). The theoretical volumes are used for distance calibration. The interproton distance d_{ij} for each spin pair (i, j) is given by

$$d_{ij} = (\alpha^{-1} V_{ij}^{exp})^{-\frac{1}{6}} = \left(\left[\frac{\Sigma_i V_i^{exp}}{\Sigma_i V_i^{th}} \right]^{-1} V_{ij}^{exp} \right)^{-\frac{1}{6}}, \tag{2.23}$$

with the experimental volume V_{ij}^{exp} and the calibration constant α. The calibration constant is the fraction of the ensemble averaged experimental and theoretical volumes. The constant is calculated with a cutoff of V, which corresponds to a cutoff distance of 6 $\mathring{A}$. In the case of ambiguous assignment possibilities due to similar chemical shifts of the NOEs, ARIA generates ambiguous distance restraints (ADR)

$$\bar{d} = \left(\sum_{k=1}^{n} d_k^{-6} \right)^{-\frac{1}{6}}. \tag{2.24}$$

Here, n is the total number of contributing spins pairs within a defined chemical shift range $\pm\Delta$. The distance d_k corresponds to a possible assignment of a spin pair i and j (Eq. 2.23). To eliminate improbable assignment possibilities, the relative contribution C_k (sum of the normalized partial distances) of each assignment possibility of an ADR is given by

$$\sum_{k=1}^{n} C_k = \sum_{k=1}^{n} \left(\frac{d_k^{-6}}{\sum_{k=1}^{n} d_k^{-6}} \right) = 1. \tag{2.25}$$

The final partial assignment is then achieved by ordering the contributions by decreasing size (n_p) and discarding the smallest contributions by an user-defined ambiguity cutoff (p) such that

$$\sum_{k=1}^{n_p} C_k \geq p. \tag{2.26}$$

The threshold p decreases from 1.0 to 0.8 in each iteration . The calibration and weighting of the signals does not generate any error limits. Therefore, lower (L) and upper (U) bounds are derived by estimating the error by a second-order polynomial. The margin of error is given by

$$[L, D] = d_{ij} \pm 0.125 d_{ij}^2. \tag{2.27}$$

The derived unambiguous and ambiguous distance restraints with the given errors must satisfy structural consistency. Therefore, the erroneous distance restraints are usually

incorrect relative to the entire data set. The violations are checked by a self-correcting distance-geometry algorithm

$$f_{\mathrm{i}} = S^{-1} \sum_{\mathrm{j}=1}^{\mathrm{S}} \Big[\Theta(L_{\mathrm{i}} - d_{\mathrm{i}}^{(\mathrm{j})} + t) + (U_{\mathrm{i}} - d_{\mathrm{i}}^{(\mathrm{j})} - t) \Big]. \tag{2.28}$$

Here, a given distance restraint (i) is systematically violated with respect to the number of converged structures (S) if it is outside the error bounds (Eq. 2.27) by more than the user-defined threshold $f_{\mathrm{i}} = 0.5$. Θ is the Heaviside function, j the specific structure number, and t is the user-defined violation tolerance. The structure ensemble is then calculate based on the merged distance restraint set and other restraints.
The structural restraints that enter the structure calculation with CNS represent potential energy contributions. The restraints are integrated into objective functions. This means that the total potential energy of the protein is given as a sum of potential energy terms (E_{i}). These are contributions from van der Waals interactions, bond angles, NOEs, etc. For example, the objective function of the distance restraint ($\bar{d}_{\mathrm{i}}$) with the bounds (L_{i}, U_{i}) is given by

$$E_{\mathrm{NOE}} = \sum_{\mathrm{i}} \begin{cases} (L_{\mathrm{i}} - \bar{d}_{\mathrm{i}})^2 & \text{if } \bar{d}_{\mathrm{i}} < L_{\mathrm{i}} \\ 0 & \text{if } L_{\mathrm{i}} < \bar{d}_{\mathrm{i}} < U_{\mathrm{i}} \\ (\bar{d}_{\mathrm{i}} - U_{\mathrm{i}})^2 & \text{if } U_{\mathrm{i}} < \bar{d}_{\mathrm{i}} < S \\ A(\bar{d}_{\mathrm{i}} - S)^{-1} + B(\bar{d}_{\mathrm{i}} - S) + C & \text{if } \bar{d}_{\mathrm{i}} > S. \end{cases} \tag{2.29}$$

It is a soft flat-bottom harmonic-wall potential with linear asymptotes for large violations, which limit the maximal force exerted by a violated distance restraint. S is the violation at which the potential changes between the harmonic and asymptotic shape. C is the slope of the asymptote. And the variables A and B keep the potential continuous and differentiable.
The structure calculation is performed using a molecular dynamics-based simulated annealing protocol (MDSA). The goal is to minimize the total potential energy function (E_{total}) while taking into account the derived structural restraints. The calculation of the dynamics of the protein is provided by numerical solution of Newton's equation of motions. In Cartesian coordinates, the motion for all N atoms i with mass m_{i} is given by

$$\begin{aligned} m_{\mathrm{i}} \frac{d^2 \vec{r}_{\mathrm{i}}(t)}{dt^2} &= -\nabla E_{\mathrm{total}}(\vec{r}_{\mathrm{i}}) \\ \vec{v}_{\mathrm{i}}(t + \Delta t) &\simeq \vec{v}_{\mathrm{i}}(t) + \frac{d^2 \vec{r}_{\mathrm{i}}(t)}{dt^2} \Delta t \\ \vec{r}_{\mathrm{i}}(t + \Delta t) &\simeq \vec{r}_{\mathrm{i}}(t) + \vec{v}_{\mathrm{i}}(t) \Delta t + \frac{d^2 \vec{r}_{\mathrm{i}}(t)}{dt^2} \Delta t^2. \end{aligned} \tag{2.30}$$

Using this approach, the velocities $\vec{v}_{\mathrm{i}}$ and the position $\vec{r}_{\mathrm{i}}$ of all atoms can be calculated for each time interval Δt.
In an iterative procedure, an ensemble of conformers with the lowest energies (typically 20) is generated in several runs (0 - 8). In general, an internally generated elongated

starting structure is used in the first cycle (0). In each iteration, the initially heated structures are gradually cooled (simulated annealing) to reach the global energy minimum and a small *RMSD* value between the conformers with the lowest energies from the previous cycle. The temperature is directly correlated with the kinetic energy and thus with the velocity of the N atoms (Eq. 2.30). The refinement of the final ensemble is performed in explicit solvent. The quality of the ensembles is checked by detecting inconsistent cross-peaks, geometric (WHAT IF, PROCHECK, PROSA II) and structural consistency (*lowest energy*) with respected to the given restraints. The quality of the calculation is documented in various output files (*report file*, *noe_violation.list*, etc.). Evaluation of the derived structural parameters and the number and size of NOE violations determines the refinement of the structural restraints (Fig. 2.7). Unsatisfactory results require reassessment.

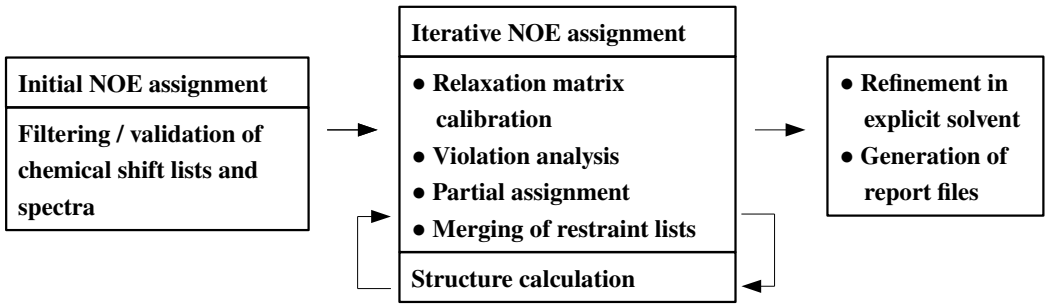

Figure 2.8.: **Overview of the structure determination with ARIA:** The arrows in the middle box reflect the gradual cooling (simulated annealing) during the structural calculation.

2.4. Thermodynamics

The thermodynamic equilibrium configuration of a system is described by a thermodynamic potential. This is a state function with a set of thermodynamic parameters that define the macroscopic state space of the system. The configuration of the system depends on the number of particles. Size-dependent or extensive parameters (Z_e) reflect the variation of intrinsic physical properties of the system. For example the amount of substance (N), the volume (V), the entropy (S), etc. Size-independent or intensive (Z_i) parameters reflect the environmental conditions of the system, such as temperature (T), pressure (p), chemical potential (μ), etc. The variation of the intensive parameter $Z_\mathrm{i}\{T, \mu, p\}$ changes the size-independent equilibrium configuration of the system.
The equilibrium state of a protein at constant temperature and pressure is described by the Gibbs free energy (dG). It is given by Gibbs's fundamental equation of thermodynamics

$$dG(N, T, p) = \mu dN - SdT + V dp. \tag{2.31}$$

The thermodynamic stability of a protein is determined by the difference in Gibbs free energy (ΔG) between the native (n) and the unfolded (u) states. For constant solution

conditions (N = const.), the difference between the two states from equation 2.31 gives the standard Gibbs free energy

$$d\Delta G_{\mathrm{u}}^{\circ} = -\Delta S_{\mathrm{u}}^{\circ} dT + \Delta V_{\mathrm{u}}^{\circ} dp. \tag{2.32}$$

Here, $\Delta S_{\mathrm{u}}^{\circ}$ is the difference in entropy and $\Delta V_{\mathrm{u}}^{\circ}$ the difference in volume between the two states. The stability of the native state of a proteins is determined by the change in Gibbs free energy ΔG_{u} during an unfolding reaction

$$\Delta G_{\mathrm{u}} = \Delta G_{\mathrm{u}}^{\circ} + RT \ln K_{\mathrm{u}}, \tag{2.33}$$

with the universal gas constant R and the equilibrium constant K. At equilibrium, the Gibbs free energy $\Delta G_{\mathrm{u}} = 0$. Thus, for measurements under equilibrium conditions the standard Gibbs free energy applies

$$\Delta G_{\mathrm{u}}^{\circ} = G_{\mathrm{u}}^{\circ} - G_{\mathrm{n}}^{\circ} = -RT \ln K_{\mathrm{u}}. \tag{2.34}$$

By varying an intensive parameter Z_{i}, the Gibbs free energy and other thermodynamic parameters of a protein can be determined.

2.4.1. Thermodynamic parameter

The thermodynamic stability of a protein is obtained by determining the equilibrium constant K. By varying an intensive variable Z_{i}, the equilibrium between the folded and the unfolded state is shifted, and so is K. First, we consider the dependence of the protein stability as a function of temperature T. The fractions of the native ($f_{\mathrm{n}}(T)$) and unfolded ($f_{\mathrm{u}}(T)$) protein can be quantified from one-dimensional ^{1}H NMR spectra [51]. This is achieved by integrating separate frequency intervals within the high-field region of the spectrum. The frequency intervals define the regions of the two states in which the integrals $I_{\mathrm{n}}(T)$, containing only native signals (well-separated methylene or methyl groups), and $I_{\mathrm{u+n}}(T)$, containing a mixture of resonances of the two states and in which most of the unfolded aliphatic signals occur. The sum of $I_{\mathrm{n}}(T)$ and $I_{\mathrm{u+n}}(T)$ gives the total intensity $I_{\mathrm{tot}}^{\mathrm{ali}}(T)$ and is used to normalize $I_{\mathrm{n}}(T)$. The fraction $f_{\mathrm{n}}(T)$ is then given by

$$f_{\mathrm{n}}(T) = \frac{\left(\dfrac{I_{\mathrm{n}}(T)}{I_{\mathrm{tot}}^{\mathrm{ali}}(T)}\right) f_{\mathrm{n}}(T_{\mathrm{max}})}{\left(\dfrac{I_{\mathrm{n}}(T_{\mathrm{max}})}{I_{\mathrm{tot}}^{\mathrm{ali}}(T_{\mathrm{max}})}\right)}, \tag{2.35}$$

with the scaling factors $f_{\mathrm{n}}(T_{\mathrm{max}})$ representing the fraction at maximal stability and the normalized integral $I_{\mathrm{n}}(T_{\mathrm{max}})$ at the corresponding temperature T_{max}. The value of T_{max} is obtained from the maximum of the temperature transition $I_{\mathrm{n}}/I_{\mathrm{tot}}^{\mathrm{ali}}$ *versus* T. The state of maximum stability $f_{\mathrm{n}}(T_{\mathrm{max}})$ is obtained by a grid search for minimum χ^2 by fitting the

equation 2.35 to the temperature transition [96] or is known from other measurements. The equilibrium constant $K_\mathrm{u}(T)$ of the unfolding is then defined as

$$K_\mathrm{u}(T) = \frac{f_\mathrm{u}(T)}{f_\mathrm{n}(T)} \quad \text{and} \quad f_\mathrm{u}(T) = 1 - f_\mathrm{n}(T). \tag{2.36}$$

As described above, for a two-state model of protein folding at equilibrium, the standard Gibbs free energy of unfolding $\Delta G^\circ_\mathrm{u}(T)$ is given by

$$\Delta G^\circ_\mathrm{u}(T) = -RT \ln K_\mathrm{u}(T) = -RT \ln \left(\frac{f_\mathrm{u}(T)}{1 - f_\mathrm{u}(T)} \right). \tag{2.37}$$

Rewritten, the unfolded fraction is then

$$f_\mathrm{u}(T) = \frac{\exp\left[- \dfrac{\Delta G^\circ_\mathrm{u}(T)}{RT} \right]}{1 + \exp\left[- \dfrac{\Delta G^\circ_\mathrm{u}(T)}{RT} \right]}. \tag{2.38}$$

The change in the standard Gibbs free energy as a function of temperature is an expression of the enthalpy $\Delta H^\circ_\mathrm{u}(T)$ and the entropy $\Delta S^\circ_\mathrm{u}(T)$ (Gibbs–Helmholtz equation)

$$\Delta G^\circ_\mathrm{u}(T) = \Delta H^\circ_\mathrm{u}(T) - T\Delta S^\circ_\mathrm{u}(T). \tag{2.39}$$

With the relations $\Delta c_\mathrm{p} = (\partial(\Delta H^\circ_\mathrm{u})/\partial T)\big|_p$ and $\Delta c_\mathrm{p}/T = (\partial(\Delta S^\circ_\mathrm{u})/\partial T)\big|_p$ and provided that the difference in molar heat capacity (Δc_p) between the native and the denatured states is temperature independent [3], the derived Gibbs free energy difference is then

$$\Delta G^\circ_\mathrm{u}(T) = \Delta H^\circ_\mathrm{u}(T_\mathrm{m}) \left(\frac{T_\mathrm{m} - T}{T_\mathrm{m}} \right) - \Delta c_\mathrm{p} \left(T_\mathrm{m} - T + T \cdot \ln\left(\frac{T}{T_\mathrm{m}} \right) \right). \tag{2.40}$$

The change in enthalpy $\Delta H^\circ_\mathrm{u}(T_\mathrm{m})$ at the midpoint of the temperature transition T_m corresponds to $f_\mathrm{n} = f_\mathrm{u}$ or $\Delta G^\circ_\mathrm{u}(T_\mathrm{m}) = 0$. Substituting the equation 2.40 into the equation 2.38, we obtain for the fraction of unfolded protein

$$f_\mathrm{u}(T) = \frac{\exp\left[- \dfrac{\Delta H^\circ_\mathrm{u}(T_\mathrm{m}) \left(\frac{T_\mathrm{m} - T}{T_\mathrm{m}} \right) - \Delta c_\mathrm{p} \left(T_\mathrm{m} - T + T \cdot \ln\left(\frac{T}{T_\mathrm{m}} \right) \right)}{RT} \right]}{1 + \exp\left[- \dfrac{\Delta H^\circ_\mathrm{u}(T_\mathrm{m}) \left(\frac{T_\mathrm{m} - T}{T_\mathrm{m}} \right) - \Delta c_\mathrm{p} \left(T_\mathrm{m} - T + T \cdot \ln\left(\frac{T}{T_\mathrm{m}} \right) \right)}{RT} \right]}. \tag{2.41}$$

A least-squares fit of the experimentally derived f_u-values allows us to determine $\Delta H_\mathrm{u}(T_\mathrm{m})$, Δc_p and T_m. The change in entropy at T_m is given by

$$\Delta S^\circ_\mathrm{u}(T_\mathrm{m}) = \frac{\Delta H^\circ_\mathrm{u}(T_\mathrm{m})}{T_\mathrm{m}}. \tag{2.42}$$

The temperature of maximum stability $T_{\max}$ corresponds to the stationary point at which

$$\frac{\partial \Delta G_{\mathrm{u}}^{\circ}(T)}{\partial T} = -\Delta S_{\mathrm{u}}^{\circ}(T) \approx \frac{\Delta H_{\mathrm{u}}^{\circ}(T)}{T_{\mathrm{m}}} + \Delta c_{\mathrm{p}} \cdot \ln\left(\frac{T}{T_{\mathrm{m}}}\right) \stackrel{!}{=} 0. \tag{2.43}$$

The value of maximum stability $\Delta G_{\mathrm{u}}^{\circ}(T_{\max})$ is then calculated to be

$$T_{\max} = T_{\mathrm{m}} \cdot \exp\left[- \frac{\Delta H_{\mathrm{u}}^{\circ}(T_{\mathrm{m}})}{\Delta c_{\mathrm{p}} \cdot T_{\mathrm{m}}} \right]. \tag{2.44}$$

So far, the thermodynamic stability has been considered as a function of temperature and at constant pressure. The variation of the pressure p at constant temperature is given by

$$\Delta G_{\mathrm{u}}^{\circ}(p) = \Delta G_0 + \Delta V_0 (p - p_0) + \frac{\Delta \hat{\beta}}{2} (p - p_0)^2, \tag{2.45}$$

where $\Delta \hat{\beta}$ is the change in compressibility, ΔV_0 is the volume difference between the native and the unfolded states, and p_0 is an arbitrary reference pressure (generally ambient pressure). The ratio of f_{n} and f_{u} at the arbitrary reference pressure also depends on the other intensive state configurations and *vice versa*. Thus, measurements of unfolding transitions as a function of pressure with additional variation of one of these quantities lead to a set of functions $f_{\mathrm{u}}(p) \mid_{Z_{\mathrm{i}}}$. Where at the reference pressure the transition midpoint of Z_{i} ($f_{\mathrm{n}}(Z_{\mathrm{i}}) = f_{\mathrm{u}}(Z_{\mathrm{i}})$) sets the limit for determining thermodynamic parameters. For example, if we consider temperature, the determination of thermodynamic parameters by varying the pressure is thus limited by T_{m}. The fraction of the unfolded state $f_{\mathrm{u}}(p)$ due to pressure transition at constant temperature is determined by

$$f_{\mathrm{u}}(p) = \frac{\exp\left[- \dfrac{\Delta G_{\mathrm{u}}^{\circ}(p)}{RT} \right]}{1 + \exp\left[- \dfrac{\Delta G_{\mathrm{u}}^{\circ}(p)}{RT} \right]}. \tag{2.46}$$

With equation 2.45 this yields

$$f_{\mathrm{u}}(p) = \frac{\exp\left[- \dfrac{\frac{\Delta \hat{\beta}}{2}(p - p_0)^2 + \Delta V_0 (p - p_0) + \Delta G_0}{RT} \right]}{1 + \exp\left[- \dfrac{\frac{\Delta \hat{\beta}}{2}(p - p_0)^2 + \Delta V_0 (p - p_0) + \Delta G_0}{RT} \right]}. \tag{2.47}$$

Setting $\Delta G_{\mathrm{u}}^{\circ}(p) = 0$ (Eq. 2.45), the pressure transition midpoint p_{m} is then obtained by

$$p_{\mathrm{m}} = p_0 - \frac{\Delta V_0}{\Delta \hat{\beta}} + \sqrt{\left(\frac{\Delta V_0}{\Delta \beta}\right)^2 - 2\frac{\Delta G_0}{\Delta \hat{\beta}}}. \tag{2.48}$$

2.4.2. Temperature–pressure phase space

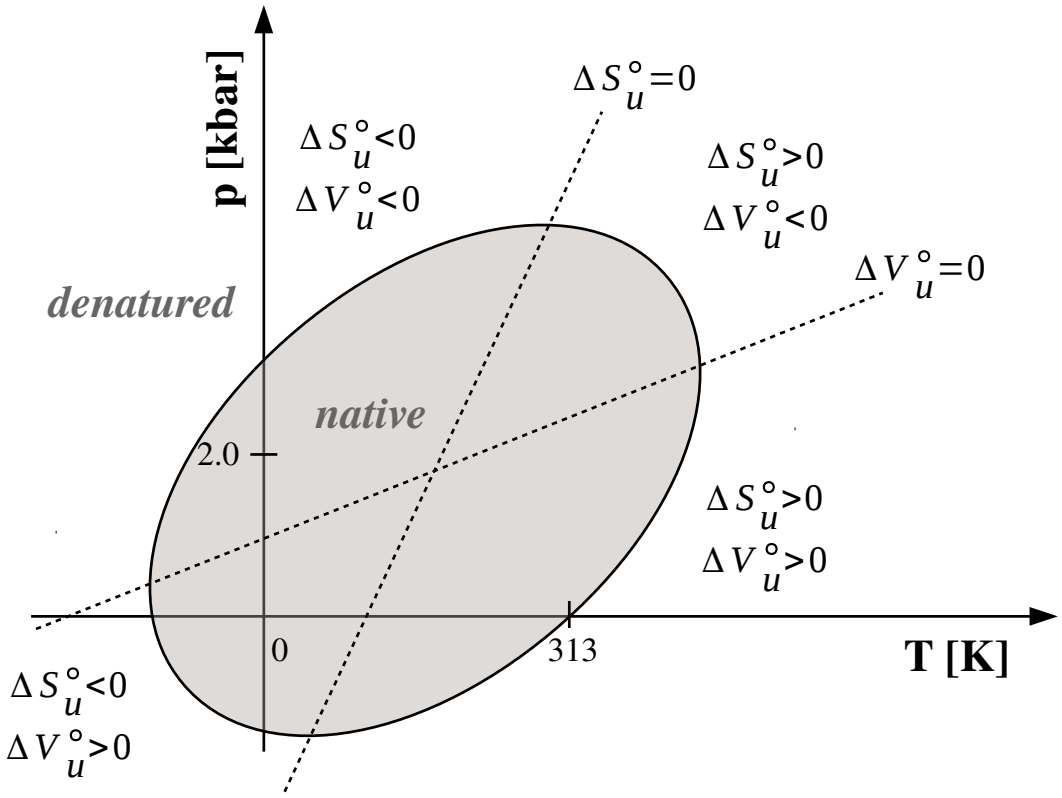

Figure 2.9.: **Theoretical temperature–pressure stability phase diagram of a globular protein (two-state model):** Transition from the native (*gray*) to the unfolded state induced by pressure and temperature (heat or cold), with the phase boundary curve defined by $\Delta G^\circ_\mathrm{u} = 0$ ($f_\mathrm{n} = f_\mathrm{u}$). The relative position of the slope at p_max, where $\Delta S^\circ_\mathrm{u} = 0$ and at T_max, where $\Delta V^\circ_\mathrm{u} = 0$.

A global description of the thermodynamic stability of a protein is achieved by considering a multidimensional approach in terms of the intensive parameters $Z_\mathrm{i}\{T, \mu, p\}$. At constant solution conditions, the difference in Gibbs free energy of the denatured and the native states is given as a function of temperature and pressure [22, 128]. Assuming a two-state folding reaction, the function of unfolding is defined as $\Delta G^\circ_\mathrm{u} = G^\circ_\mathrm{u}$ - G°_n (Eq. 2.34), which is obtained by integration with respect to some arbitrary reference points T_0 and p_0

$$\begin{aligned}\Delta G^\circ_\mathrm{u}(p,T) =& \frac{\Delta\hat{\beta}}{2}(p-p_0)^2 + \Delta\hat{\alpha}(p-p_0)(T-T_0) - \Delta c_\mathrm{p}\left[T\cdot\ln\left(\frac{T}{T_0}-1\right)+T_0\right] \\ &+ \Delta V_0(p-p_0) - \Delta S_0(p-p_0) + \Delta G_0,\end{aligned} \tag{2.49}$$

where Δ denotes the change of the corresponding parameter during denaturation. $\hat{\alpha}$ corresponds to the thermal expansion factor, $\hat{\beta}$ to the isothermal compressibility factor,

and c_p to the heat capacity. The volume V_0, the entropy S_0 and the free Gibbs energy G_0 refer to the state at $Z_\mathrm{i}\{T_0, p_0\}$. In the vicinity of the reference point T_0, the equation 2.49 simplifies by a second-order approximation to

$$\begin{aligned}\Delta G^\circ_\mathrm{u}(p,T) =& \frac{\Delta\hat{\beta}}{2}(p-p_0)^2 + \Delta\hat{\alpha}(p-p_0)(T-T_0) - \frac{\Delta c_\mathrm{p}}{2T_0}(T-T_0)^2 \\ &+ \Delta V_0(p-p_0) - \Delta S_0(p-p_0) + \Delta G_0.\end{aligned} \tag{2.50}$$

The equation 2.50 maps the difference in Gibbs free energy between the denatured and the native states in a three-dimensional phase space. The solutions for $\Delta G^\circ_\mathrm{u} = 0$ are given by a general equation for a conic section in the T-p plane, which can be a line, an ellipse, a parabola, or a hyperbola. The constraint ensuring the elliptic-like shape of the transition line for a protein is $\Delta\hat{\alpha}^2 > \Delta c_\mathrm{p} \cdot \Delta\hat{\beta}/T_0$ (Fig. 2.9). The T-p phase diagram shows the temperature and pressure range in which a protein exists in its native globular structure ($\Delta G^\circ_\mathrm{u} > 0$) or in the unfolded state ($\Delta G^\circ_\mathrm{u} < 0$). The exact elliptic shape of the transition line depends on the secondary structural composition of the protein, which corresponds to the different specific values of the thermodynamic parameters of the protein. The parameters of the conic phase boundary are described by a set of single partial derivatives of the second-order Taylor series

$$\begin{aligned}
&\left.\frac{\partial\Delta G^\circ_\mathrm{u}}{\partial p}\right|_{T_\mathrm{i}} = \Delta V_0(p, T_\mathrm{i}), && \left.\frac{\partial^2\Delta G^\circ_\mathrm{u}}{\partial p^2}\right|_{T} = \left.\frac{\partial\Delta V^\circ_\mathrm{u}}{\partial p}\right|_{T} = \Delta\hat{\beta}, \\
&\left.\frac{\partial\Delta G^\circ_\mathrm{u}}{\partial T}\right|_{p_\mathrm{i}} = -\Delta S_0(p_\mathrm{i}, T), && \left.\frac{\partial^2\Delta G^\circ_\mathrm{u}}{\partial T^2}\right|_{p} = -\left.\frac{\partial\Delta S^\circ_\mathrm{u}}{\partial T}\right|_{p} = -\frac{\Delta c_\mathrm{p}}{T}, \\
&\frac{\partial^2\Delta G^\circ_\mathrm{u}}{\partial p\partial T} = -\left.\frac{\partial\Delta S^\circ_\mathrm{u}}{\partial p}\right|_{T} = \left.\frac{\partial\Delta V^\circ_\mathrm{u}}{\partial T}\right|_{p} = \Delta\hat{\alpha}.
\end{aligned} \tag{2.51}$$

The partial derivatives for the factors $\Delta\hat{\beta}$ or $\Delta\hat{\alpha}$ represent the slope of the change in isothermal compressibility ($\Delta\beta$) or in thermal expansion ($\Delta\alpha$). The values of $\Delta\beta$ and $\Delta\alpha$ reflect on the relative volume change of a protein by pressure or temperature and are defined as follows

$$\Delta\alpha = \left(\frac{1}{V}\right)\left(\frac{\partial\Delta V}{\partial T}\right)\bigg|_{p}, \quad \Delta\beta = -\left(\frac{1}{V}\right)\left(\frac{\partial\Delta V}{\partial p}\right)\bigg|_{T}, \tag{2.52}$$

where V represents the volume of the atoms, the enclosed cavities and the surrounding hydration shell [129]. The change results from difference in volume between the folded and unfolded protein. Here, the unfolded state is characterized by small or no cavity volumes and a varying hydration shell compared to the native protein. The change in thermal expansion $\Delta\alpha$ and the change in compressibility $\Delta\beta$ are associated with $\Delta\hat{\alpha}$ and $\Delta\hat{\beta}$ as follows

$$\Delta\hat{\alpha} = V\Delta\alpha, \quad \Delta\hat{\beta} = V\Delta\beta. \tag{2.53}$$

The stationary points of the ellipse in the pressure-temperature phase space (Fig. 2.9) are determined by the slope of the tangent to the phase boundary

$$\frac{\partial T}{\partial p} = -\frac{\frac{\partial \Delta G_{\mathrm{u}}^{\circ}}{\partial p}}{\frac{\partial \Delta G_{\mathrm{u}}^{\circ}}{\partial T}} = \frac{\Delta V_0 + \Delta\hat{\beta}(p-p_0) + \Delta\hat{\alpha}(T-T_0)}{\Delta S_0 - \Delta\hat{\alpha}(p-p_0) + \Delta c_{\mathrm{p}}\dfrac{T-T_0}{T_0}}. \tag{2.54}$$

The function is a modified version of the Clausius-Clapeyron equation. At the maximum with respect to temperature ($T_{\max}$) or pressure ($p_{\max}$), the native state is most stable. At $p_{\max}$, the slope of the ellipse is zero and $\Delta S_{\mathrm{u}}^{\circ} = 0$. At $T_{\max}$ the derivative becomes infinite and $\Delta V_{\mathrm{u}}^{\circ} = 0$. This results in the following two straight lines for $\Delta V_{\mathrm{u}}^{\circ} = 0$ and $\Delta S_{\mathrm{u}}^{\circ} = 0$, which intersect in the center of the ellipse

$$p(T)\Big|_{\Delta S_{\mathrm{u}}^{\circ}} = \frac{\Delta c_{\mathrm{p}}}{\Delta\alpha}\frac{T-T_0}{T} + \frac{\Delta S_0}{\Delta\alpha} + p_0, \tag{2.55}$$

$$p(T)\Big|_{\Delta V_{\mathrm{u}}^{\circ}} = -\frac{\Delta\alpha}{\Delta\beta}\frac{T-T_0}{T} - \frac{\Delta V_0}{\Delta\beta} + p_0. \tag{2.56}$$

Further points on the ellipse to be considered are the transition points of the system. As described above, they are given at $\Delta G_{\mathrm{u}}^{\circ} = 0$ (Eq. 2.50) with respect to some reference point. The transition point induced by temperature (heat (+) or cold (-)) $T_{\mathrm{m}}\Big|_{p_0}$ (generally at atmospheric pressure) is given by

$$T_{\mathrm{m}}\Big|_{p_0} = T_0 - \frac{\Delta S_0 T_0}{\Delta c_{\mathrm{p}}} \pm \sqrt{\left(-\frac{\Delta S_0 T_0}{\Delta c_{\mathrm{p}}}\right)^2 + 2\frac{\Delta G_0 T_0}{\Delta c_{\mathrm{p}}}}. \tag{2.57}$$

And with increasing pressure the midpoint $p_{\mathrm{m}}\Big|_{T_0}$ is then obtained by

$$p_{\mathrm{m}}\Big|_{T_0} = p_0 - \frac{\Delta V_0}{\Delta\hat{\beta}} + \sqrt{\left(\frac{\Delta V_0}{\Delta\beta}\right)^2 - 2\frac{\Delta G_0}{\Delta\hat{\beta}}}. \tag{2.58}$$

2.4.3. Pressure-induced chemical shift analysis

In general, the observed chemical shift $<\delta_{\mathrm{i}}>$ of a spin i in an ensemble with N molecules is a frequency-weighted average of the individual chemical shifts δ_{i}. At thermal equilibrium, $<\delta_{\mathrm{i}}>$ correspond to M states s_{j}. For fast exchange on the NMR time scale, the observed chemical shift of spin i is given by

$$<\delta_{\mathrm{i}}> = \sum_{\mathrm{j}=1}^{\mathrm{M}} p(s_{\mathrm{j}})\delta_{\mathrm{i}}(s_{\mathrm{j}}) = \frac{1}{Z}\sum_{\mathrm{j}=1}^{\mathrm{M}} \delta_{\mathrm{i}}(s_{\mathrm{j}}) \exp\left[-\frac{G(s_{\mathrm{j}})}{RT}\right], \tag{2.59}$$

with $p(s_{\mathrm{j}})$ the probability of the state s_{j}, $G(s_{\mathrm{j}})$ the corresponding Gibbs free energy, and Z the partition function of all M states [130].

In a two-state model of a given nucleus i in fast exchange ($|\Delta\omega\tau_e| << 1$; $\Delta\omega \mathrel{\widehat{=}}$ difference of the resonance frequencies ω_1 and ω_2; τ_e, exchange correlation time), one observes a population-weighted, time-averaged chemical shift. With the chemical shifts δ_1 and δ_2 representing the two states, the Gibbs free energy with the equilibrium constant K is given as follows

$$\Delta G^\circ = -RT\ \ln K = -RT\ \ln\left(\frac{\delta_2 - \delta}{\delta - \delta_1}\right). \tag{2.60}$$

The observed δ is then written as

$$\delta = \frac{\delta_2 + \delta_1 \cdot \exp\left[-\dfrac{\Delta G^\circ(p)}{RT}\right]}{1 + \exp\left[-\dfrac{\Delta G^\circ(p)}{RT}\right]}. \tag{2.61}$$

The pressure dependence of the chemical shift $\delta(p)$ at constant temperature is obtained by using equation 2.45

$$\delta(p) = \frac{\delta_2 + \delta_1 \cdot \exp\left[-\dfrac{\dfrac{\Delta\hat{\beta}}{2}(p-p_0)^2 + \Delta V_0(p-p_0) + \Delta G_{12}}{RT}\right]}{1 + \exp\left[-\dfrac{\dfrac{\Delta\hat{\beta}}{2}(p-p_0)^2 + \Delta V_0(p-p_0) + \Delta G_{12}}{RT}\right]}, \tag{2.62}$$

with ΔG_{12} corresponds to the difference between the two states at p_0, T_0. The pressure-induced shift from state 1 to state 2 results from volume differences. The system shifts to a state with smaller overall volume by favoring the state with smaller partial molar volume (principal of least action). At the molecular level, hydrogen bonds are strengthened under pressure, while hydrophobic interactions are weakened under compression. These structural changes simultaneously cause a change in the chemical environment of the nuclear spins, and thus a change in the chemical shift $\delta(p)$.
Based on the equation 2.45, the experimentally determined pressure dependence of the chemical shift $\delta(p)$ at constant temperature can be fitted to a second-order Taylor expansion at p_0

$$\delta(p) = b_0 + b_1(p - p_0) + b_2(p - p_0)^2, \tag{2.63}$$

where b_1 represents the linear and b_2 represents the quadratic pressure coefficient [58]. The value b_0 represents the chemical shift at p_0. The linear coefficient reflects a linear change in volume of the system with unchanged compressibility, which is associated with the compression of hydrogen bonds [57,131]. The nonlinear quadratic dependence of the chemical shift is attributed to the transition to a different conformational state with a different compressibility [55]. The pressure coefficients correlate with the differences in the compressibility factor, partial molar volume and Gibbs free energy [59]. Assuming

a two-state model and considering the equation 2.62, the ratio of b_2 and b_1 defines a partition function as follows

$$\frac{b_2}{b_1} = -\frac{\Delta\hat{\beta}(p_0)}{\Delta V(p_0)} - \frac{\Delta V(p_0)}{RT_0}\tanh\left(\frac{\Delta G^\circ}{2RT_0}\right). \tag{2.64}$$

Under consideration of a fast exchange

$$\left|\frac{\Delta G^\circ_{\mathrm{u}}}{2RT}\right| << 1, \tag{2.65}$$

the ratio of the coefficients is simplified to

$$\frac{b_2}{b_1} = -\frac{\Delta\hat{\beta}(p_0)}{\Delta V(p_0)}. \tag{2.66}$$

The relation can only usefully be achieved with a complete pressure-induced chemical shift transition. Otherwise, the second-order polynomial fit (Eq. 2.63) and the derived pressure coefficients are generally used for a phenomenological description.

3. Results

In the following chapter, the results of the biophysical characterization of the 35-residue monomeric wild-type villin headpiece subdomain VHP35 and the variant VHP35_L69A from *gallus gallus* are presented. This involves the investigation of the structural, molecular dynamics and thermodynamic properties under changing physical conditions of the proteins under consideration.

3.1. Referencing and calibration

All spectra recorded for this work are referenced to the proton signals of the deuterated (CH_3 groups excluded) 3-(Trimethylsilyl)-1-propanesulfonic acid-d_6 sodium salt (DSS-d_6). Indirect referencing of the ^{15}N and ^{13}C nuclei for the ^{1}H,^{15}N and ^{1}H,^{13}C-HSQC spectra was determined by the ratio of the gyromagnetic ratios ($\gamma_{^{15}\mathrm{N}}/\gamma_{^{1}\mathrm{H}} = 0.101$; $\gamma_{^{13}\mathrm{C}}/\gamma_{^{1}\mathrm{H}} = 0.251$). DSS-$d_6$ is largely stable and chemically inert over the pressure and temperature range used in this work. The concentrations used ranged from 30 to 60 μM.
Temperature calibration for the 3 mm ceramic cell (Daedalus Innovations LLC) was perfomed using 80 % ethylene glycol in 20 % DMSO-d_6. The calibration curve was obtained by plotting the difference in chemical shifts $\Delta\delta$ between the OH and CH_2 singlets of ethylene glycol as a function of temperature set at the spectrometer probe head. The thermometric solution is valid for a temperature range from 273 K to 416 K. The actual temperature is calculated by the following correction formula:

$$T[K] = \frac{(4.218 - \Delta\delta)}{0.009132}. \tag{3.1}$$

Calibration was measured on a TXI probe head with an air flow of 535 l/h for temperatures from 278 K to 373 K.

3.2. Thermodynamic stability of VHP35 and VHP35_L69A

The thermodynamic stability of VHP35 and VHP35_L69A was recorded in a series of 1D ^{1}H NMR spectra by varying the temperature at fixed pressures from 0.1 to 240 MPa in steps of 50 MPa. The temperature transition of VHP35 was measured from 278K to 368 K and of VHP35_L69A from 278 K to 348 K in steps of 5 K. The reversibility of the

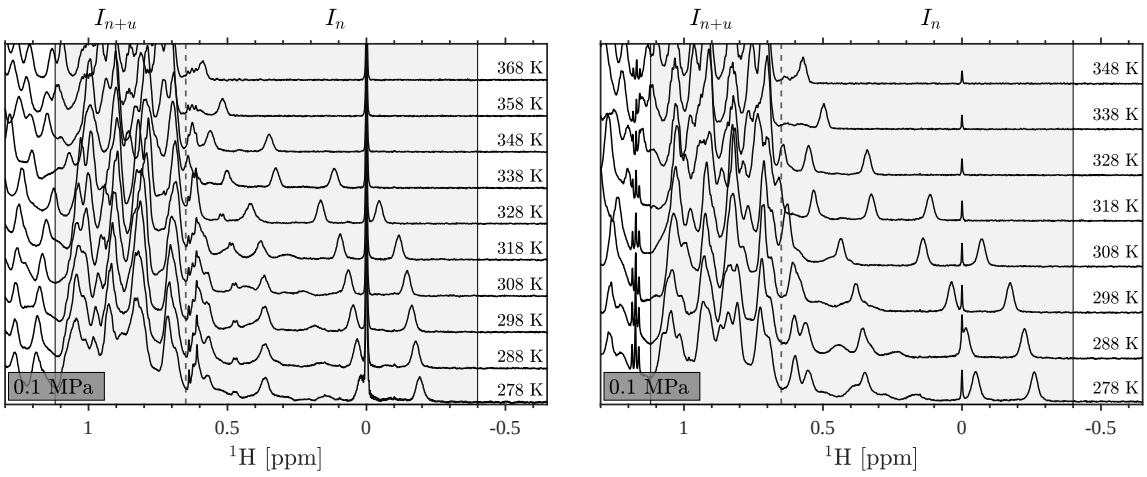

Figure 3.1.: **High-field region of the 1D ^{1}H NMR spectra of VHP35 (*left*) and VHP35_L69A (*right*) at various temperatures and at 0.1 MPa:** The *grey* area (VHP35: -0.4 to 1.105 ppm; VHP35_L69A: -0.4 to 1.12 ppm) shows the intervals of $I_{\mathrm{n+u}}$ and the solely native region I_{n} (Eq. 2.35) subdivided by the *dashed* line (at 0.65 ppm). The native region contains the proton resonances of L61(Hδ_1) and V50(Hγ_2). The spectra are referenced to DSS-d_6 set at 0 ppm.

measurements was tested by comparing spectra under ambient conditions before and after each temperature transition. As an example, Figure 3.1 shows a temperature series of 1D ^{1}H NMR spectra at 0.1 MPa for each protein. The complete data set is shown in Figure A.2 and A.3 in Appendix A. Assuming a two-state model (u↔n), the fraction of unfolded ($f_{\mathrm{u}}(T)$) and folded ($f_{\mathrm{n}}(T)$) protein is determined by integrating the spectrum in the corresponding sections and normalized by the total integral (Sec. 2.4.1). For this purpose, the resonances in the high-field region (aliphatic signals) and, in particular, for the solely folded fraction, the separated methyl and methylene groups in the range from about -0.5 ppm to about 0.6 ppm are of interest. The boundaries of the total integral ($I_{\mathrm{tot}}^{\mathrm{ali}}$) were set from -0.4 to 1.105 ppm for VHP35 and from -0.4 to 1.12 ppm for VHP35_L69A. To ensure that all resonances containing only folded protein (I_{n}) were monitored over the entire temperature and pressure range, the interval was defined from -0.4 to 0.65 ppm in each case. Interference of the DSS-d_6 signal was handled by subtracting the corresponding resonance interval (VHP35: -0.01 to 0.01 ppm; VHP35_L69A: -0.004 to 0.004 ppm) from I_{n}. The native region of VHP35 contains the proton resonances of L61(Hδ_1) and V50(Hγ_2), which can be assigned to the three prominent signals at around -0.19, 0.02, and 0.38 ppm at 278 K (Fig. 3.1) [73]. This also applies to the variant. The assignment of these signals was verified using ^{1}H,^{13}C-*ct*HSQC in combination with a 3D HCCH-TOCSY experiment. The decrease and the shift of the observed methylene and methyl resonances of I_{n} indicates a heat-induced shift of the equilibrium from the native to the unfolded state.

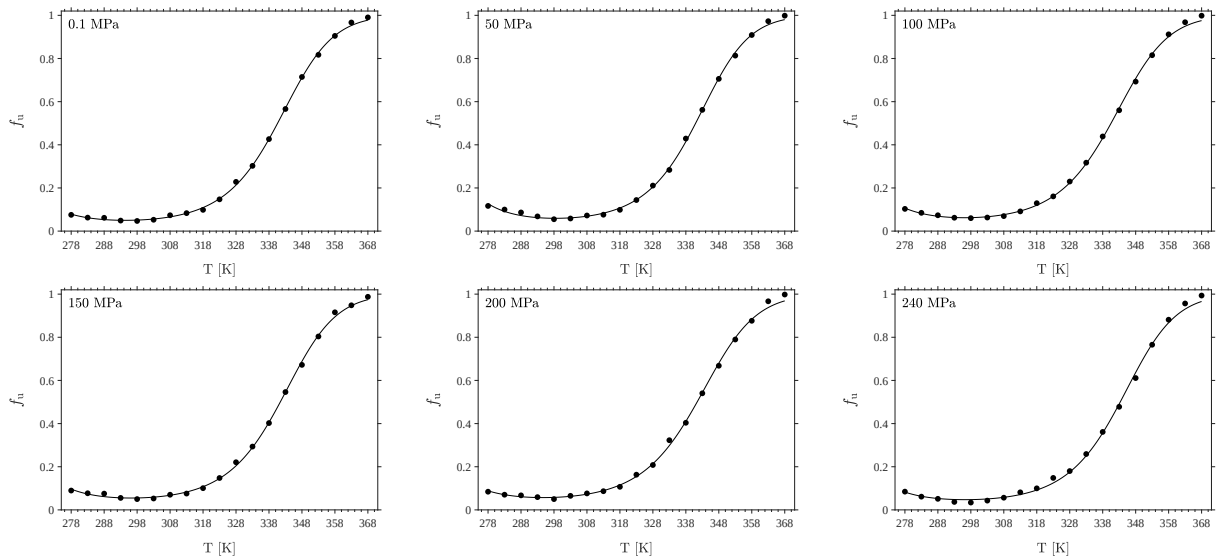

Figure 3.2.: **Fractions of unfolded VHP35 as a function of temperature at different pressures:** The unfolded fractions (f_u) obtained from the 1D ^{1}H NMR spectra (Eq. 2.35) were fitted (*solid* line) with the equation 2.41, resulting in the thermodynamic parameters listed in Table 3.1.

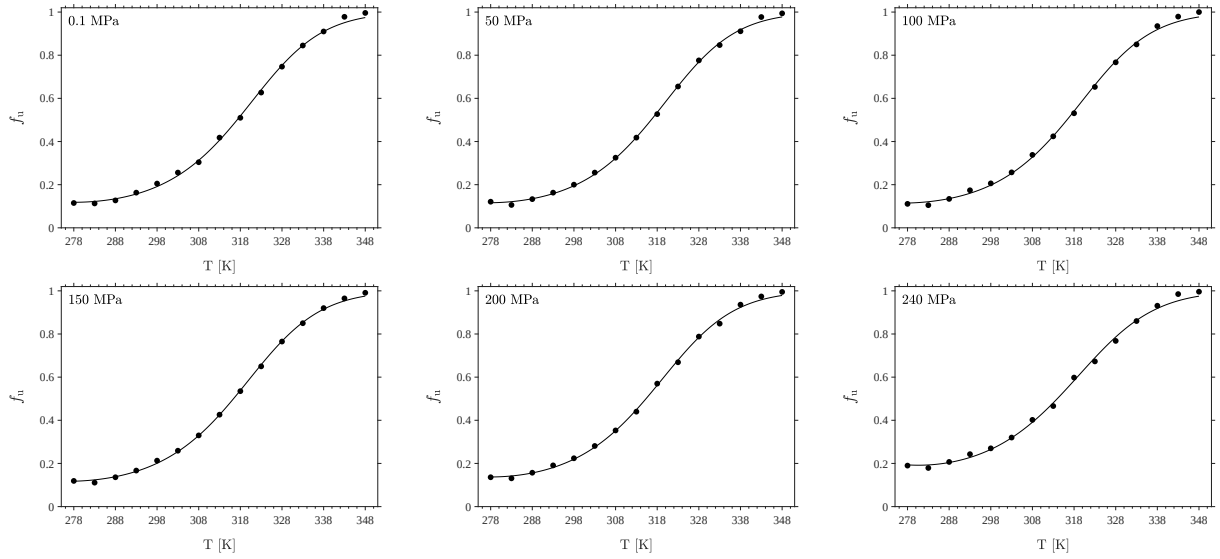

Figure 3.3.: **Fractions of unfolded VHP35_L69A as a function of temperature at different pressures:** The unfolded fractions (f_u) obtained from the 1D ^{1}H NMR spectra (Eq. 2.35) were fitted (*solid* line) with the equation 2.41, resulting in the thermodynamic parameters listed in Table 3.2.

Quantification in terms of fraction of unfolded VHP35 and VHP35_L69A was determined by equation 2.35 with $f_u = 1 - f_n$. The fraction depends on the temperature at constant pressure. The fractions of unfolded VHP35 and VHP35_L69A are shown in Figure 3.2 and 3.3 for the measured temperature and pressure combinations. The fraction of maximum protein stability ($f_n(T_{max})$) in equation 2.35 was first estimated from the experimental temperature transition curve at the respective pressure. The optimal value of $f_n(T_{max})$ is yielded by a grid search for minimal χ^2. For example, fitting the experimental $f_n(T)$-values at 0.1 MPa gives $f_n(T_{max}) = 0.953$ for VHP35 at $T_{max} = 297.3$ K and $f_n(T_{max}) = 0.887$ for VHP35_L69 at $T_{max} = 280.4$ K. A comparison of all generated fits of both proteins is shown in Figure 3.4. For VHP35, it can be seen that with increasing pressure the transition curves are shifted to higher transition temperatures, indicating stabilization of the system.

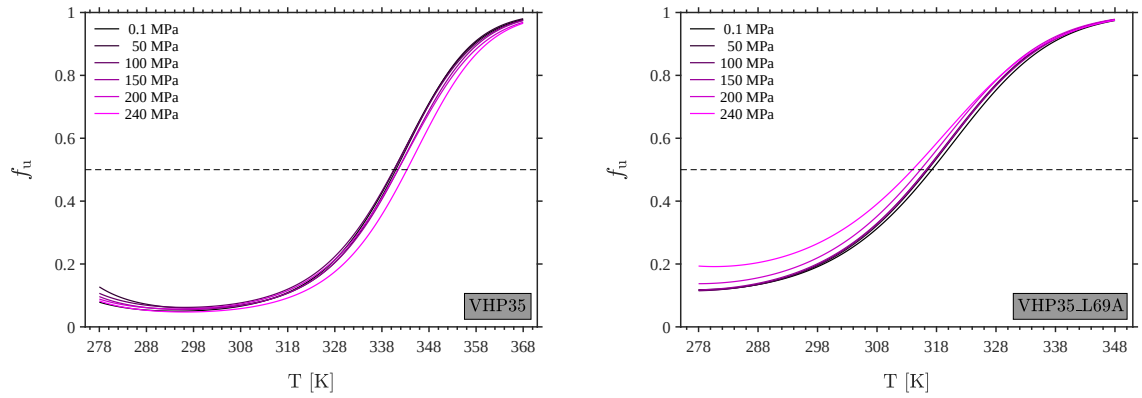

Figure 3.4.: **Superposition of the fits of unfolding (f_u) VHP35 and VHP35_L69A at different pressures:** The *dashed* line corresponds to $f_u = f_n = 0.5$.

In contrast, the transition curves of VHP35_L69 shift in the opposite direction with increasing pressure, indicating destabilization of the system. In addition, comparison of the two proteins implies that the variant is less stable than the wild type due to the lower fraction of $f_n(T)$ at T_{max} and lower unfolding temperatures.
The quantitative analysis of the thermodynamic stability is performed by fitting equation 2.41 to the experimentally determined data points $f_u(T)$. This yields the thermodynamic parameters of the change in enthalpy at the transition point $\Delta H_u^\circ(T_m)$, the change in molar heat capacity (Δc_p), and the transition temperature T_m of denaturation. The change in entropy $\Delta S_u^\circ(T_m)$ at T_m and the temperature of maximum stability T_{max} are then given by equation 2.42 and 2.44. Using the equation 2.40, one can then calculate $\Delta G_u^\circ(T_{max})$. The thermodynamic parameters obtained are given in Tables 3.1 and 3.2. In the case of VHP35, the resulting thermodynamic quantities show a relatively small variation for a pressure change up to 240 MPa. $\Delta G_u^\circ(T_{max})$ and T_m increase slightly over the measured pressure range, implying increasing protein stability. In contrast, the pressure-induced decrease in $\Delta G_u^\circ(T_{max})$ and T_m of VHP35_L69A, especially in the last step at 240 MPa, shows a shift toward the unfolded state. Nevertheless, the Δc_p and T_{max}

values of the variant remain stable within the the errors up to 240 MPa. Comparison of $\Delta G_{\mathrm{u}}^{\circ}(T_{\mathrm{max}})$ and T_{m} of the proteins shows that VHP35 is the thermodynamically more stable system in the observed pressure range. To better illustrate the parameters listed in Tables 3.1 and 3.2, the plots of $\Delta G_{\mathrm{u}}^{\circ}(T_{\mathrm{max}})$, T_{max}, T_{m}, $\Delta H_{\mathrm{u}}^{\circ}(T_{\mathrm{m}})$, $\Delta S_{\mathrm{u}}^{\circ}(T_{\mathrm{m}})$ and Δc_{p} are shown in Figure A.1 as a function of pressure.

Table 3.1.: **Thermodynamic parameters derived from fitting the fractions of the unfolded VHP35 by equation 2.41 as a function of temperature at different pressures.**

p [MPa]	T_{m} [K]	T_{max} [K]	$\Delta G_{\mathrm{u}}^{\circ}(T_{\mathrm{max}})$ [J/mol]	Δc_{p} [J/(mol·K)]	$\Delta H_{\mathrm{u}}^{\circ}(T_{\mathrm{m}})$ [J/mol]	$\Delta S_{\mathrm{u}}^{\circ}(T_{\mathrm{m}})$ [J/(mol·K)]
0.1	340.6 ±0.12	297.3 ±0.57	7242 ±323	2411 ±58	111533 ±1482	327.4 ±4.22
50	340.9 ±0.16	300.9 ±0.49	6885 ±564	2703 ±69	115001 ±1972	337.2 ±5.61
100	340.5 ±0.16	298.8 ±0.59	6718 ±462	2418 ±66	107494 ±1776	315.6 ±5.06
150	341.4 ±0.16	299.1 ±0.61	7039 ±464	2454 ±69	111025 ±1862	325.1 ±5.29
200	341.4 ±0.22	297.7 ±0.95	6910 ±537	2262 ±90	105688 ±2352	309.5 ±6.68
240	343.3 ±0.24	299.2 ±1.01	7431 ±654	2405 ±105	113316 ±2855	330.1 ±8.07

Table 3.2.: **Thermodynamic parameters derived from fitting the fractions of the unfolded VHP35_L69A by equation 2.41 as a function of temperature at different pressures.**

p [MPa]	T_{m} [K]	T_{max} [K]	$\Delta G_{\mathrm{u}}^{\circ}(T_{\mathrm{max}})$ [J/mol]	Δc_{p} [J/(mol·K)]	$\Delta H_{\mathrm{u}}^{\circ}(T_{\mathrm{m}})$ [J/mol]	$\Delta S_{\mathrm{u}}^{\circ}(T_{\mathrm{m}})$ [J/(mol·K)]
0.1	317.2 ±0.27	280.3 ±1.78	4662 ±235	2008 ±139	78668 ±2006	247.9 ±6.11
50	316.5 ±0.21	279.6 ±1.42	4699 ±167	2016 ±110	79049 ±1550	249.7 ±4.73
100	316.2 ±0.27	278.9 ±1.92	4724 ±175	1973 ±143	78402 ±1986	247.8 ±6.06
150	316.3 ±0.17	278.8 ±1.17	4660 ±115	1932 ±85	77063 ±1188	243.5 ±3.62
200	315.3 ±0.23	280.1 ±1.4	4263 ±235	2006 ±113	74896 ±1578	237.5 ±4.82
240	313.9 ±0.36	282.3 ±1.61	3366 ±512	1971 ±143	65704 ±2047	209.2 ±6.27

The change in Gibbs free energy $\Delta G_{\mathrm{u}}^{\circ}(T)$ for each point $f_{\mathrm{u}}(T)$ of the system is given by the equation 2.37. Equation 2.40 is used to calculate the Gibbs free energy graph for each set of temperatures at a fixed pressure. Combined with equation 2.39, one can determine the enthalpy $\Delta H_{\mathrm{u}}^{\circ}$ and the entropy $\Delta S_{\mathrm{u}}^{\circ}$ as a function of temperature. For both proteins, Figure 3.5 shows the derived fits at 0.1 MPa. A complete data set is illustrated in Figure A.4 and A.5, respectively, in Appendix A. In both systems, $\Delta H_{\mathrm{u}}^{\circ} > \Delta S_{\mathrm{u}}^{\circ}$ remains at all measured pressures up to the transition temperature. Comparison of the $\Delta G_{\mathrm{u}}^{\circ}(T)$

transition curves (Fig. 3.6) of VHP35 and VHP35_L69A confirms the thermodynamic stabilities already observed in the unfolding transitions (Fig. 3.4). Up to a pressure of 240 MPa, the Gibbs free energy of VHP35 increases, while that of VHP35_L69A decreases in this range.

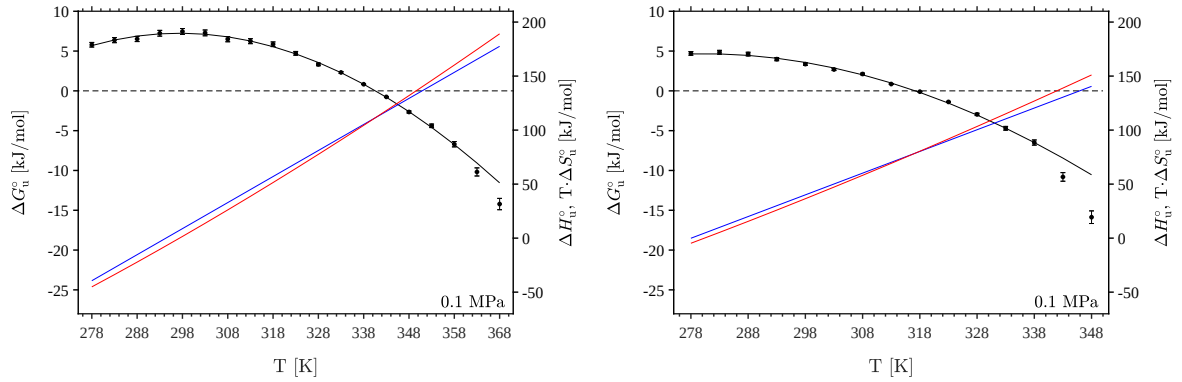

Figure 3.5.: **The Gibbs free energy (ΔG°_u), enthalpy (ΔH°_u) and entropy (ΔS°_u) of VHP35 (*left*) and VHP35_L69A (*right*) as a function of temperature at 0.1 MPa:** The change in ΔG°_u is determined by the equation 2.37 and the error was assumed to be 5 %. The fits of ΔG°_u (*black*), ΔH°_u (*blue*) and ΔS°_u (*red*) are given by equation 2.40 and 2.39.

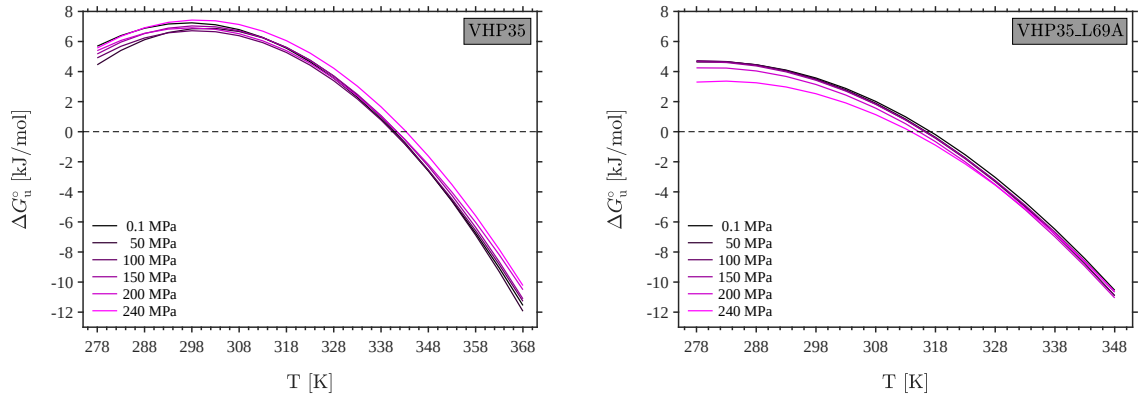

Figure 3.6.: **Superposition of the fits of Gibbs free energy (ΔG°_u) of VHP35 and VHP35_L69A at various pressures:** The fits of ΔG°_u are given by equation 2.40. At $\Delta G^\circ_u = 0$ (*dashed* line) $f_u = f_n = 0.5$.

The thermodynamic stability as a function of pressure $\Delta G^\circ_u(p)$ is obtained by plotting the data set of $\Delta G^\circ_u(T)$ against pressure and using the quadratic equation 2.45. With respect to a reference pressure p_0 (0.1 MPa), this yields the pressure-dependent parameters of the change in Gibbs energy ΔG_0, the change in volume ΔV, and the change in compressibility $\Delta\hat{\beta}$, which are listed in Tables 3.3 and 3.4. The values of ΔG_0 reflect on the temperature transition at 0.1 MPa. Therefore, the systems are most stable at the

Table 3.3.: **Thermodynamic parameters derived from fitting the Gibbs free energy of VHP35 by the equation 2.45 as a function of pressure at different temperatures.**

T [K]	ΔG_0 [kJ/mol]	ΔV [ml/mol]	$\Delta\hat{\beta}$ [ml/(mol·MPa)]
278 K	5.52 ±0.36	-8.99 ±7.06	0.08 ±0.06
283 K	6.12 ±0.33	-11.84 ±6.49	0.11 ±0.05
288 K	6.40 ±0.23	-11.57 ±4.55	0.12 ±0.04
293 K	7.15 ±0.32	-13.60 ±6.23	0.14 ±0.05
298 K	7.47 ±0.20	-11.99 ±3.89	0.12 ±0.03
303 K	7.31 ±0.34	-8.65 ±6.76	0.08 ±0.05
308 K	6.57 ±0.26	-2.67 ±5.03	0.04 ±0.04
313 K	6.30 ±0.25	-0.33 ±4.84	0.00 ±0.04
318 K	5.89 ±0.31	-6.95 ±6.07	0.06 ±0.05
323 K	4.77 ±0.17	-2.86 ±3.34	0.02 ±0.03
328 K	3.45 ±0.17	-3.36 ±3.38	0.05 ±0.03
333 K	2.47 ±0.31	-4.75 ±6.16	0.05 ±0.05
338 K	0.85 ±0.13	-2.95 ±2.53	0.05 ±0.02
343 K	-0.69 ±0.15	-3.19 ±2.97	0.05 ±0.02
348 K	-2.62 ±0.15	0.14 ±2.94	0.04 ±0.02
353 K	-4.35 ±0.06	-2.11 ±1.14	0.05 ±0.01
358 K	-6.68 ±0.33	-7.61 ±6.51	0.09 ±0.05
363 K	-10.50 ±0.73	4.92 ±14.25	0.00 ±0.11
368 K	-15.71 ±3.26	-43.78 ±64.11	0.37 ±0.51

temperature in the vicinity to $T_{\max}$ (Tab. 3.1, 3.2). For VHP35, this corresponds to 298 K. An increase in pressure at this temperature results in compression of the protein with values of $\Delta V = -11.99 \pm 3.89$ ml/mol and $\Delta\hat{\beta} = 0.12 \pm 0.03$ ml/(mol·MPa). In the case of VHP35_L69A, the protein expands at 283 K with incresing pressure, as reflected in the values of $\Delta V = 8.86 \pm 2.18$ ml/mol and $\Delta\hat{\beta} = -0.11 \pm 0.02$ ml/(mol·MPa). Overall, the fits of $\Delta G^{\circ}_{\mathrm{u}}(p)$ (Fig. 3.7) at different fixed temperatures show only a small quadratic dependence that correlates with a small change in compressibility. The compelete dataset is shown in Figures A.6a, A.6b and A.7 in Appendix A. Despite the errors, the values of $\Delta\hat{\beta}$ for VHP35 show a tendency to decrease at higher fixed temperatures, while ΔV tends to increases. Accordingly, the volume of the system increases with the pressure at higher temperatures. In contrast, the values of VHP35_L69A tend to shift in the opposite direction at higher fixed temperatures. Thus, the system is more compressed by pressure in this temperature range. This is illustrated in Figure A.8 in Appendix A. Comparison of the $\Delta G^{\circ}_{\mathrm{u}}(p)$ fits (Fig. 3.8) reveals that neither systems is destabilized by

pressure at the different temperatures. Therefore, it was not possible to determine the pressure transition points (p_m) for any of the proteins.

Table 3.4.: **Thermodynamic parameters derived from fitting the Gibbs free energy of VHP35_L69A by the equation 2.45 as a function of pressure at different temperatures.**

T [K]	ΔG_0 [kJ/mol]	ΔV [ml/mol]	$\Delta\hat{\beta}$ [ml/(mol·MPa)]
278 K	4.57 ±0.20	7.31 ± 3.85	-0.10 ±0.03
283 K	4.79 ±0.11	8.86 ± 2.18	-0.11 ±0.02
288 K	4.51 ±0.17	4.63 ± 3.42	-0.08 ±0.03
293 K	3.91 ±0.18	4.46 ± 3.53	-0.07 ±0.03
298 K	3.33 ±0.11	3.74 ± 2.11	-0.06 ±0.02
303 K	2.63 ±0.09	3.79 ± 1.68	-0.05 ±0.01
308 K	2.03 ±0.16	-0.18 ± 3.22	-0.03 ±0.03
313 K	0.83 ±0.05	1.48 ± 0.94	-0.03 ±0.01
318 K	-0.16 ±0.09	0.32 ± 1.71	-0.03 ±0.01
323 K	-1.46 ±0.10	-2.54 ± 2.05	0.01 ±0.02
328 K	-3.02 ±0.18	-4.29 ± 3.47	0.02 ±0.03
333 K	-4.72 ±0.08	0.31 ± 1.52	-0.01 ±0.01
338 K	-6.43 ±0.35	-7.87 ± 6.87	0.03 ±0.05
343 K	-11.13 ±0.73	17.25 ± 14.34	-0.15 ±0.11
348 K	-15.75 ±3.51	-26.15 ± 69.03	0.25 ±0.55

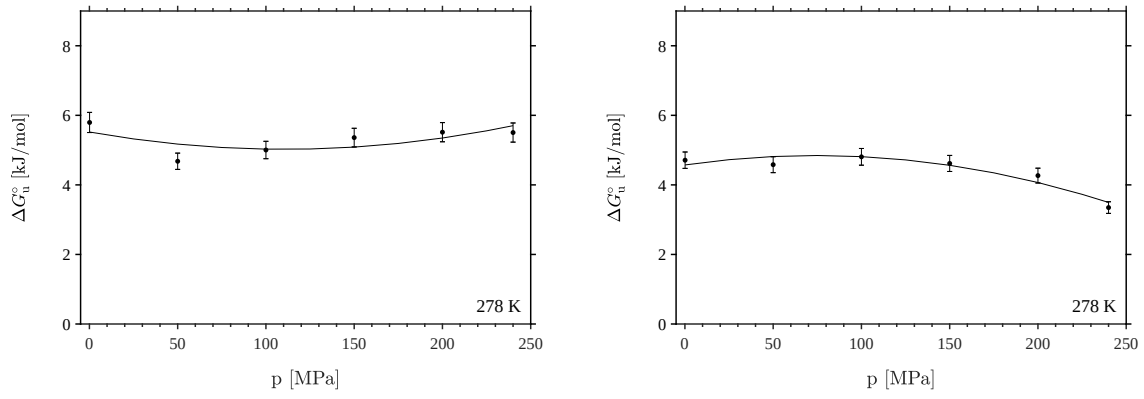

Figure 3.7.: **The Gibbs free energy (ΔG_u°) of VHP35 (*left*) and VHP35_L69A (*right*) as a function of pressure at 278 K:** The change in ΔG_u° is determined by the equation 2.37 and the error was assumed to be 5 %. The fits of ΔG_u° (*solid* line) are given by the equation 2.45.

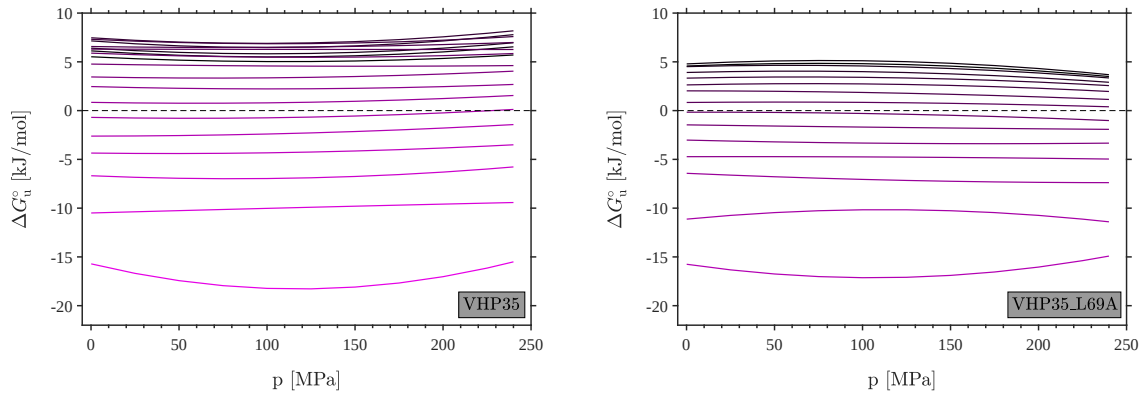

Figure 3.8.: **Superposition of the fits (Eq. 2.45) of Gibbs free energy (ΔG_u°) of VHP35 and VHP35_L69A at various temperatures:** The color of the fits changes in steps of 5 K from 278 K (*black*) up to 368 K (*light purple*) for VHP35 and up to 348 K (*light purple*) for VHP35_L69A. At $\Delta G_u^\circ = 0$ (*dashed* line) $f_u = f_n = 0.5$.

A general description of the thermodynamic stability of proteins is given by a stability phase diagram with respect to all intensive parameters studied. $\Delta G_u^\circ(T, p)$ as a function of temperature and pressure gives a three-dimensional surface on the temperature-pressure plane (T,p-plane). The transition line between the unfolded and native state is defined by $\Delta G_u^\circ(T, p) = 0$. The solution on the T,p-plane is a conic section given by the equation 2.50 with respect to the arbitrary reference points T_0 and p_0. The resulting second-order curve in the T-p plane can be a line or a circle of elliptical, parabolic or hyperbolic shape. Since the conic section is calculated using an equation for a three-dimensional structure, one parameter of the equation can be freely chosen. The most accurately determined parameter experimentally was the Gibbs free energy ΔG_0.

Table 3.5.: **Thermodynamic parameters derived from fitting the Gibbs free energy of VHP35 and VHP35_L69A by the equation 2.50 as a function of temperature and pressure with respect to T_0 and p_0.**

		VHP35	VHP35_L69A
T_0	[K]	298	283
p_0	[MPa]	0.1	0.1
ΔG_0	[kJ/mol]	7.47 ±0.20	4.79 ±0.11
ΔS_0	[J/(mol·K)]	6.74 ±1.45	16.47 ±1.75
Δc_p	[kJ/(mol·K)]	2.31 ±0.02	1.99 ±0.03
$\Delta\hat{\alpha}$	[ml/(mol·K)]	0.11 ±0.005	0.05 ±0.007
ΔV_0	[ml/mol]	-10.05 ±0.41	-3.43 ±0.29
$\Delta\hat{\beta}$	[ml/(mol·MPa)]	0.07 ±0.003	-0.01 ±0.002

The fit of VHP35 was obtained with the $\Delta G_0 = 7.47$ kJ/mol at reference points $p_0 = 0.1$ MPa and $T_0 = 298$ K (Tab. 3.3) and of VHP35_L69A with the $\Delta G_0 = 4.79$ kJ/mol at $p_0 = 0.1$ MPa and $T_0 = 283$ K (3.4). The selected values correspond to those closest to the maximum stability. A global fit of the equation 2.50 to the $\Delta G^{\circ}_{\mathrm{u}}(T, p)$ values result in the thermodynamic parameters listed in Table 3.5. Except for the change in the compressibility factor $\Delta\hat{\beta}$, the derived parameters of VHP35 correspond within the errors to the values of the temperature (Tab. 3.1) and pressure transitions (Tab. 3.3). $\Delta\hat{\beta}$ differs by about 0.05 ml/(mol·MPa), but is still positive. In the case of VHP35_L69A, the heat capacity Δc_{p} is in range of the values of the considered transition curve (Tab. 3.2). The obtained change in the compressibility factor $\Delta\hat{\beta}$ is about a factor 10 smaller and the change in volume ΔV_0 is negative and about 11 ml/mol smaller than the derived value of the pressure transition at 283 K (Tab. 3.4).
One explanation for this is the small pressure effect within the measured range and the resulting low quality of the fit of the pressure transition. In comparison, the systems show similar values of change in heat capacity and relatively small changes in the compressibility factor and thermal expansion factor with respect to their reference points. In the observed temperature-pressure range, the change in volume ΔV_0 of VHP35 is larger than the ΔV_0 of the variant. For the entropy ΔS_0, it is exactly the opposite. Nevertheless, the derived values are quite small.

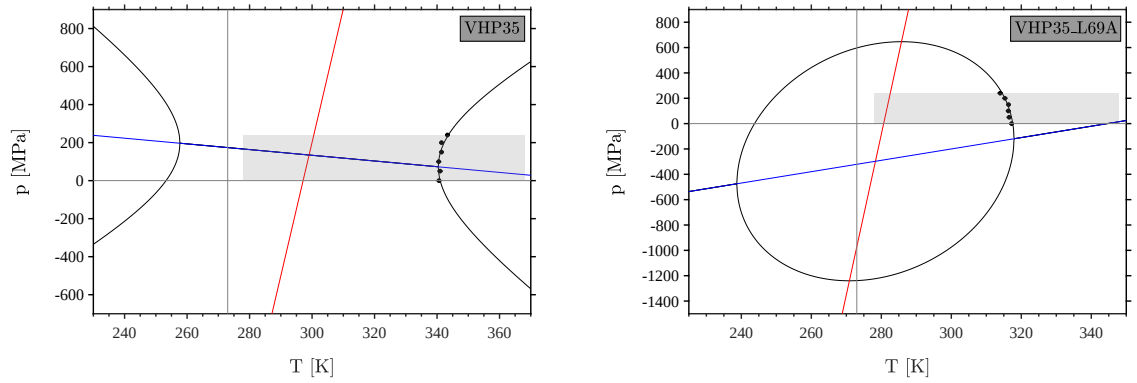

Figure 3.9.: **Temperature–pressure stability phase diagram of VHP35 and VHP35_L69A:** The transition line (*black*) illustrates $\Delta G^{\circ}_{\mathrm{u}}(T, p) = 0$ according to equation 2.50 derived from global fit of all NMR-derived populations (*gray* section). The *black* circles represent the experimental derived temperature transition points at the respective pressures, with error bars partially within the symbol size. The lines (Eqs. 2.55, 2.56) correspond to $\Delta S = 0$ (*red*) and to $\Delta V = 0$ (*blue*).

The phase boundaries in the pressure-temperature phase diagrams of the proteins agree with the determined temperature transition points T_{m} (Fig. 3.9). The plot of the transition line of VHP35 shows a hyperbolic shape and of VHP35_L69A an elliptic shape. Figure 3.9 shows the fully calculated phase boundaries, where the region of negative pressures has no physical meaning. The mathematical boundary conditions of

the conic section are given by the relation $\Delta\hat{\alpha}^2 > \Delta c_\mathrm{p} \cdot \Delta\hat{\beta}/T_0$ for an elliptical shape, $\Delta\hat{\alpha}^2 = \Delta c_\mathrm{p} \cdot \Delta\hat{\beta}/T_0$ for a parabolic shape, and $\Delta\hat{\alpha}^2 < \Delta c_\mathrm{p} \cdot \Delta\hat{\beta}/T_0$ for a hyperbolic shape. From Table 3.5 this is confirmed by a $\Delta\hat{\alpha}^2 = 0.012$ and a $\Delta c_\mathrm{p} \cdot \Delta\hat{\beta}/T_0 = 0.54$ for VHP35 and by a $\Delta\hat{\alpha}^2 = 0.0025$ and a $\Delta c_\mathrm{p} \cdot \Delta\hat{\beta}/T_0 = -0.07$ for VHP35_L69A. The hyperbolic curve of the wild type is defined by the positive value of $\Delta\hat{\beta}$. This corresponds with the observation that the system is stabilized within the measured pressure range (Fig. 3.4) and yields the derived phase boundary. In contradiction, the derived line of $\Delta V = 0$ shows that the system shifts from $\Delta V > 0$ toward the section of $\Delta V < 0$ with increasing pressure (see Fig. 2.9), corresponding to a smaller volume of VHP35 at high pressure. The line of $\Delta V = 0$ or of $\Delta S = 0$ correspond to the stationary points of the system at the considered values (Eq. 2.55, 2.56). The elliptical shape of VHP35_L69A is defined by the negative value of $\Delta\hat{\beta}$. The derived two lines of $\Delta V = 0$ and of $\Delta S = 0$ show that the experimental data points are located in the section of $\Delta V < 0$ and of $\Delta S > 0$. Nevertheless, the derived phase space diagrams are extrapolations, which depend essentially on the temperature transitions, since the pressure midpoints p_m could not be determined in the measured pressure range.

3.3. High pressure conformers

To gain insights into the pressure-dependent conformational changes, the following methods in this chapter were performed at ambient pressure and at 240 MPa. NMR resonance assignments of the backbone of VHP35 and of VHP35_L69A were obtained by 2D ^{1}H,^{15}N-*f*HSQC, 3D *tr*HNCACB, 3D HNCO, 3D NOESY-HSQC experiments and by a previously reported resonance assignment of the wild-type VHP35 [61, 62]. Side-chain assignments were determined by 2D ^{1}H,^{13}C-*ct*HSQC, 3D ^{1}H,^{13}C-*ct*HSQC-TOCSY, and 3D HCCH-TOCSY experiments (Sec. 2.2). The spectra of the protein backbone, the aliphatic region, and the aromatic region of VHP35 and of VHP35_L69A are shown in the Figures A.9, A.10, A.11 and A.18, A.19, A.20. Chemical shifts for each protein are listed in Tables A.1,A.2,A.3 and A.5, A.6, A.7.
The high-resolution three-dimensional structures were calculated with ARIA 2.3.1 using ambiguous NOE cross-peak lists, a list of assigned chemical shifts, the protein sequence, and TALOS+ derived dihedral angle information as structural restraints (Sec. 2.3). Experimentally derived NOE intensities were obtained by ^{13}C-edited (aliphatic and aromatic region) and ^{15}N-edited (backbone) 3D NOESY-HSQC experiments. The calculated final ensembles of the 10 lowest energy structures and the minimized average structure for 0.1 and 240 MPa, respectively, were verified by *control* ensembles for each pressure. Thus, the *control* NOE list for the structure calculation at 0.1 MPa contained those NOEs that were also found in the NOE list at 240 MPa and *vice versa* (Tab. A.4, A.8).

Table 3.6.: **Structural calculation statistics of the 10 lowest-energy final and the corresponding *control* conformers of VHP35 at 0.1 MPa and 240 MPa.**

	Final	*Control*	Final	*Control*
Pressure [Mpa]	0.1	0.1	240	240
NOEs	1511	1479	1567	1479
NMR distance restraints [$\AA$]				
Intra-residue ($\|i-j\|=0$)	301	304	327	308
Sequential ($\|i-j\|=1$)	96	96	100	96
Medium range ($1<\|i-j\|<5$)	58	57	70	63
Long range ($\|i-j\|\geq 5$)	22	23	26	25
Ambiguous	212	187	200	193
Total	689	667	723	685
Noe violations [$\AA$]				
> 0.5	-	-	-	-
> 0.3	-	-	-	0.1 $\pm$0.3
> 0.1	18.4 $\pm$1.8	19.8 $\pm$2.4	23.8 $\pm$1.5	16.3 $\pm$1.9
NOE RMSD [$\AA$]	0.02 $\pm$0.001	0.03 $\pm$ 0.001	0.03 $\pm$0.0006	0.03 $\pm$0.0008
Energies [kcal/mol]				
E_{bond}	4.8 $\pm$0.3	5.4 $\pm$0.5	6.3 $\pm$0.4	5.3 $\pm$0.4
E_{angle}	35.7 $\pm$2.3	36.1 $\pm$1.9	38.3 $\pm$3.5	37.5 $\pm$2.2
E_{improper}	67.2 $\pm$14.5	61.7 $\pm$12.8	71.5 $\pm$11.1	63.3 $\pm$12.6
E_{NOE}	25.7 $\pm$1.8	25.9 $\pm$2.5	30.5 $\pm$1.3	23.6 $\pm$1.3
E_{dihed}	169.5 $\pm$2.9	169.4 $\pm$1.3	181.1 $\pm$3.1	178.4 $\pm$2.2
E_{total}	302.9 $\pm$21.8	298.5 $\pm$19	327.7 $\pm$19.4	308.1 $\pm$18.7
RMSD of Cartesian coordinates [$\AA$]				
Backbone atoms	0.6 $\pm$0.1	0.6 $\pm$0.1	0.6 $\pm$0.1	0.6 $\pm$0.1
All heavy atoms	0.9 $\pm$0.2	1 $\pm$0.1	1 $\pm$0.1	0.9 $\pm$0.1
Ramachandran statistics [%]				
Most favored	96.3 $\pm$2.48	96.3 $\pm$3.33	99.7$\pm$ 1	97.3 $\pm$2.11
Allowed	3.66 $\pm$2.48	3.34 $\pm$3.16	0.33$\pm$ 1	2.65 $\pm$2.11

Table 3.7.: **Structural calculation statistics of the 10 lowest-energy final and the corresponding *control* conformers of VHP35_L69A at 0.1 MPa and 240 MPa.**

	Final	*Control*	Final	*Control*
Pressure [MPa]	0.1	0.1	240	240
NOEs	2018	1874	1961	1874
NMR distance restraints [$\AA$]				
Intra-residue ($\|i-j\|=0$)	371	356	379	372
Sequential ($\|i-j\|=1$)	144	142	145	140
Medium range ($1<\|i-j\|<5$)	154	138	151	138
Long range ($\|i-j\|\geq 5$)	37	28	49	36
Ambiguous	260	231	232	233
Total	966	895	956	919
Noe violations [$\AA$]				
> 0.5	-	-	0.1 $\pm$0.3	-
> 0.3	0.1 $\pm$0.3	0.2 $\pm$0.4	0.9 $\pm$0.7	0.1 $\pm$0.3
> 0.1	28.4 $\pm$2.4	32.6 $\pm$1.6	26.7 $\pm$1.9	14.9 $\pm$2.9
NOE RMSD [$\AA$]	0.03 $\pm$0.001	0.03 $\pm$0.001	0.03 $\pm$0.002	0.02 $\pm$0.002
Energies [kcal/mol]				
E_{bond}	6.1 $\pm$0.3	8.2 $\pm$0.4	6.9 $\pm$0.5	5.1 $\pm$0.4
E_{angle}	37.4 $\pm$2.1	46.2 $\pm$1.9	40.2 $\pm$2.2	37.9 $\pm$3.3
E_{improper}	59.3 $\pm$9.9	64.2 $\pm$8.4	82.1 $\pm$10.2	66.4 $\pm$10.2
E_{NOE}	36.3 $\pm$1.8	47.5 $\pm$2.8	47.9 $\pm$7.2	26.1 $\pm$4.2
E_{dihed}	177.8 $\pm$2.2	169.6 $\pm$1.7	166.1 $\pm$1.9	163.5 $\pm$3.3
E_{total}	316.9 $\pm$16,3	335.7 $\pm$15.2	343.2 $\pm$22	299 $\pm$21.4
RMSD of Cartesian coordinates [$\AA$]				
Backbone atoms	0.3 $\pm$0.1	0.3 $\pm$0.1	0.4 $\pm$0.1	0.4 $\pm$0.1
All heavy atoms	0.7 $\pm$0.1	0.9 $\pm$0.1	1 $\pm$0.2	1 $\pm$0.1
Ramachandran statistics [%]				
Most favored	97 $\pm$1.89	98.7 $\pm$2.33	95.3 $\pm$2.36	96.7 $\pm$2.74
Allowed	2.98 $\pm$1.89	1.33 $\pm$2.33	4.67 $\pm$2.36	3.33 $\pm$2.74

The *control* NOE cross-peak lists contained the same number and assignments of NOEs for each pressure. Subsequent comparison with these *control* data sets should reveal pressure-induced conformational rearrangements. Table 3.6 and 3.7 summarize the statistics of the structure calculation and the number of NOEs of the final and *control* ensembles of VHP35 and of VHP35_L69A at 0.1 and 240 MPa, respectively. Superpositions of the 10 lowest-energy confomers of the respective protein and pressure are shown in Figures A.12, A.13, A.14, A.15, A.21, A.22, A.23, and A.24. Atomic distances, solvent-accessible surface area, and solvent-accessible cavities with a solvent probe radius of 1.4 $\mathring{A}$ were determined using PyMOL. Theoretical molecular surface volume, van der Waals volume, and void volume were calculated with a minimum probe radius of 0.02 $\mathring{A}$ and a minimum surface probe distance of 0.1 $\mathring{A}$ using ProteinVolume (Fig. 2.6) [125].

Table 3.8.: **Solvent-accessible surface area (SASA) and the molecular surface volume (V_{MS}) with the corresponding van der Waals volume (V_{VDW}) and void volume (V_{VOID}) of VHP35 and VHP35_L69A at 0.1 MPa and 240 MPa (Fig. 2.6) [125]. The difference ($\Delta^{[240,0.1]}$) is obtained from the values between 240 MPa and 0.1 MPa.**

		VHP35			VHP35_L69A		
Pressure	[MPa]	0.1	240	$\Delta^{[240,0.1]}$	0.1	240	$\Delta^{[240,0.1]}$
SASA	[$\mathring{A}^2$]	2944	2882	-62	2973	2952	-21
V_{VDW}	[$\mathring{A}^3$]	3649	3645	-4	3596	3598	2
V_{VOID}	[$\mathring{A}^3$]	870	965	95	886	901	15
V_{MS} (= $V_{\mathrm{VDW}} + V_{\mathrm{VOID}}$)	[$\mathring{A}^3$]	4519	4610	91	4482	4499	17

3.3.1. NMR structures of VHP35

With an overall RMSD of 0.6 $\mathring{A}$ for the heavy atoms of the backbone, each of the 10 final lowest-energy conformers of VHP35 at 0.1 MPa folds into three α-helical segments (Fig. A.12), as described in Section 1.2 (Fig. 1.1). Considering the different measurement conditions (T, pH, N), the corresponding minimized average NMR structure is structurally consistent with the previously published NMR structure of VHP36 (PDB: 1VII) [62] and the x-ray crystal structure of VHP35_N68H (PDB: 1YRF) [65] (Fig. 3.10). The main-chain RMSD between 1VII and 1YRF is 2.04 $\mathring{A}$. In comparison, the derived NMR structure of VHP35 shows an RMSD of 2.12 $\mathring{A}$ to 1VII and an RMSD of 1.22 $\mathring{A}$ to 1YRF [77, 132]. Moreover, the superposition of α1 shows that VHP35 adopts a similar orientation to 1YRF, reflecting congruences in the packing of the core and in the helix–helix interactions [65] (Fig. 3.10).

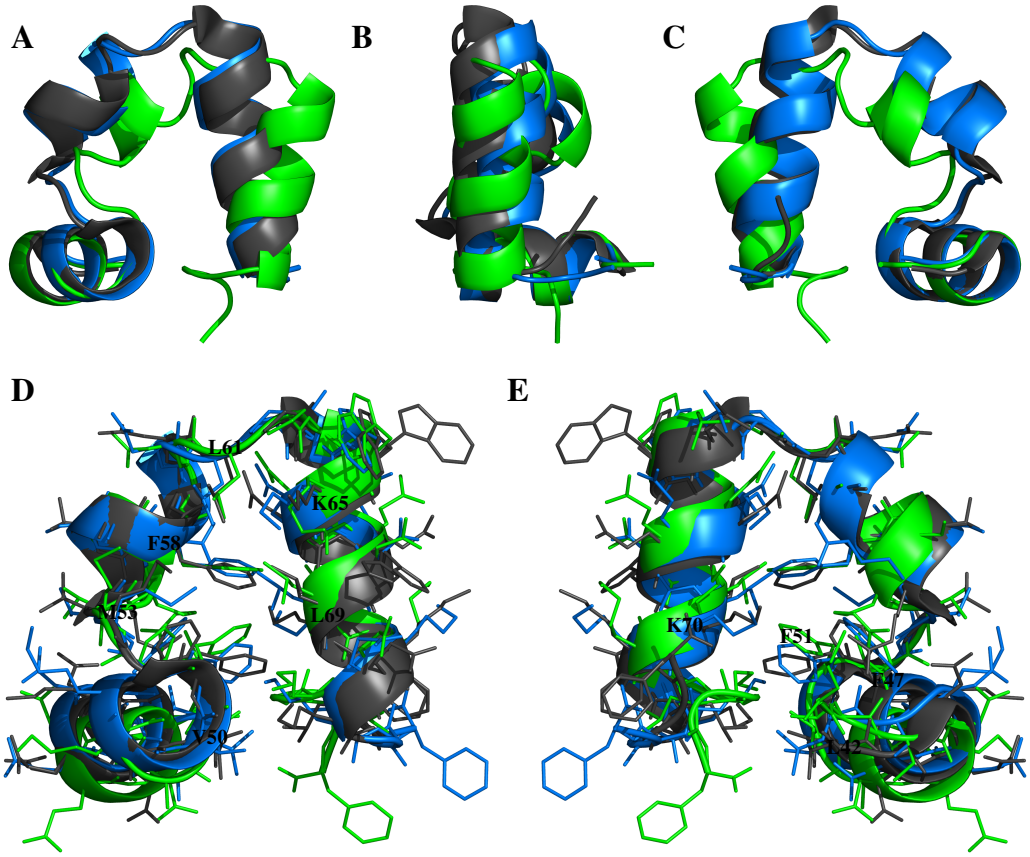

Figure 3.10.: **Superposition of the backbone heavy atoms of the final minimized average NMR structure of VHP35 at 0.1 MPa, the minimized average NMR structure of VHP36 (PDB: 1VII), and the x-ray crystal structure of VHP35_N68H (PDB: 1YRF):** (A) shows the superposition of α1 (residues 44 - 51) and (D) for all backbone residues of the *blue* colored VHP35 at 0.1 MPa (278 K, pH 7.0), *green* colored 1VII (303 K, pH 3.7) an *grey* colored 1YRF (293 K, pH 6.7). The main-chain RMSD between VHP35 and 1VII is 2.12 $\AA$ and for 1YRF is 1.22 $\AA$. (B) and (C) show the rotation by 90° and (E) shows the rotation by 180° about the y-axis. Side chains are shown as sticks without hydrogens, and hydrophobic core residues are labeled.

The 10 final or *control* conformers with lowest-energy of VHP35 at 0.1 MPa and 240 MPa, respectively, describe in atomic detail the three α-helical segments with the hydrophobic core residues (Fig. A.12, A.13, A.14, A.15). The calculated ensembles show similar structural calculation statistics with respective overall main-chain RMSDs of about 0.6 $\AA$ (Tab. 3.6). The RMSD of the backbone heavy atoms between the final and the *control* minimized average NMR structure is 0.96 $\AA$ at 0.1 MPa and 1.65 $\AA$ at 240 MPa (Fig. 3.11). The RMSD between the respective *control* structures is 0.91 $\AA$. Nevertheless, the respective *control* structures for each pressure reflect the same pressure-dependent

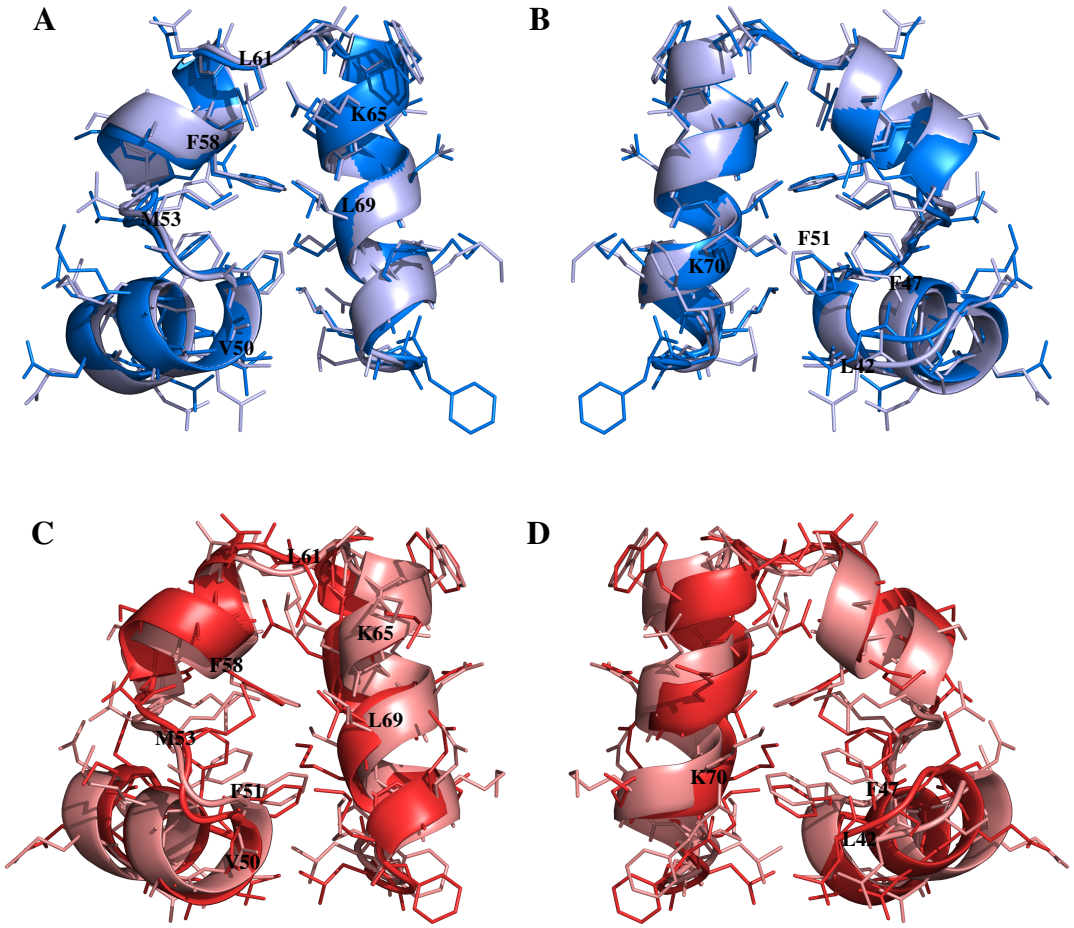

Figure 3.11.: **Superposition of the backbone heavy atoms of the final and the *control* minimized average NMR structure of VHP35 at 0.1 MPa and 240 MPa (Tab. 3.6):** (A) shows VHP35 at 0.1 MPa (*blue*) and the corresponding *control* structure (*light blue*) with an RMSD of 0.96 *Å*. (C) shows the structure of VHP35 at 240 MPa (*red*) and the corresponding *control* structure (*light red*) with an RMSD of 1.65 *Å*. (B) and (D) show the rotation by 180° about the y-axis. Side chains are shown as sticks without hydrogens, and hydrophobic core residues are labeled.

orientation of the three α-helical segments and the hydrophobic core residues as the final structures. This indicates that not only pressure-induced new or lost NOE contacts show structural differences between 0.1 MPa and 240 MPa, but also all individual distance constraints. The latter are much less obvious from the experimental NOESY experiments, because only small changes of many cross-peak intensities cause these rearrangements. Structural differences are mainly found within the N-terminal helix (α1). Nevertheless, the uniquely assigned NOEs of the final ensembles at 0.1 MPa or at 240 MPa are structurally consistent with the calculations and none of them violates distance restraints (Tab. A.4).

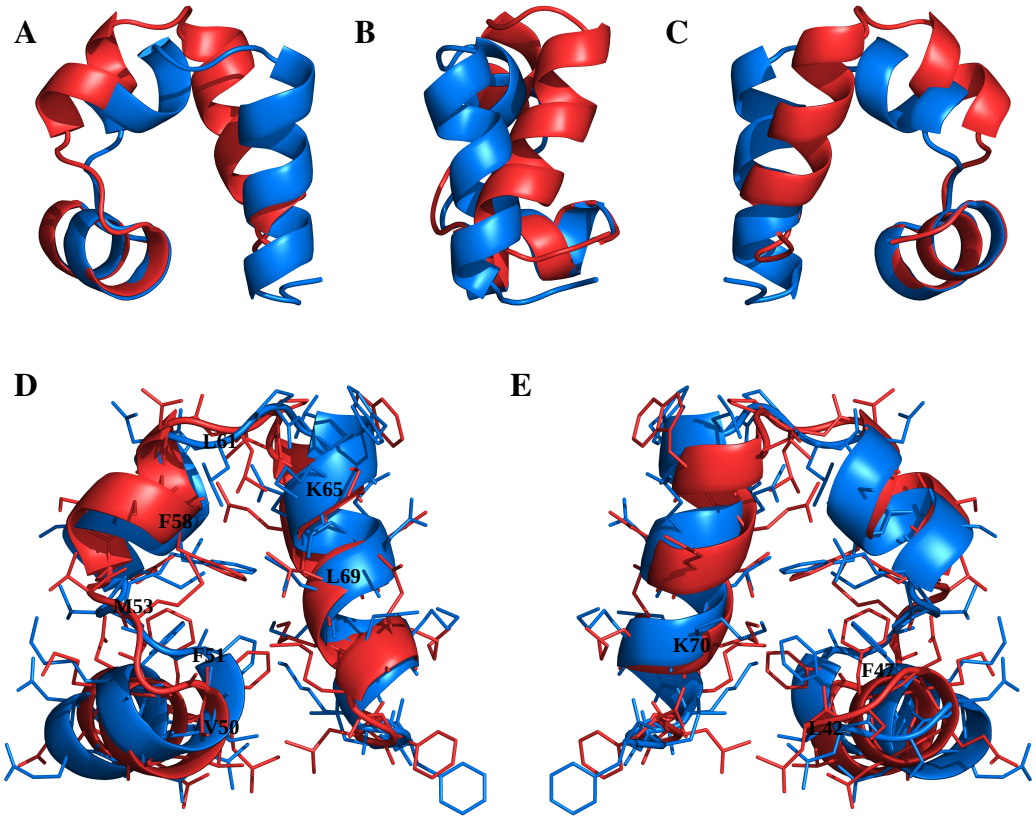

Figure 3.12.: **Superposition of the backbone heavy atoms of the final minimized average NMR structures of VHP35 at 0.1 MPa and 240 MPa (Tab. 3.6):** (A) shows the superposition of α1 (residues 44-51) and (D) for all backbone residues at 0.1 MPa (*blue*) and at 240 MPa (*red*) with an RMSD of 2.16 *Å* for the latter. (B) and (C) show the rotation by 90° and (E) shows the rotation by 180° about the y-axis. Side chains are shown as sticks without hydrogens, and hydrophobic core residues are labeled.

The main-chain RMSD between the final minimized average NMR structure at 0.1 MPa and 240 MPa is 2.16 *Å*. The superposition shows the pressure-induced different position and orientation of α1 or *vise versa* of α2 and α3 of VHP35 (Fig. 3.12). At 240 MPa, the distance between the amide protons of D44 (α1) and L63 (α3) shortens from 21.2 *Å* to 16.4 *Å*, shifting the N-terminal helix toward the C-terminal helix. This is consistent with the unique inter-residual NOEs found at each pressure, which occur mainly within α1 and the succeeding turn (Tab. A.4). Essentially, the pressure change leads to structural changes within the backbone of VHP35, but the orientation of most of the side chains remains the same (Fig. A.16). Among the hydrophobic core residues, only residues F47, M53, L61, and K65 show a significant pressure-induced change in the side chains by about 90°. In particular, the aromatic ring of F47, one of the three highly conserved and structure-stabilizing phenylalanines [64,133], changes from a perpendicular position

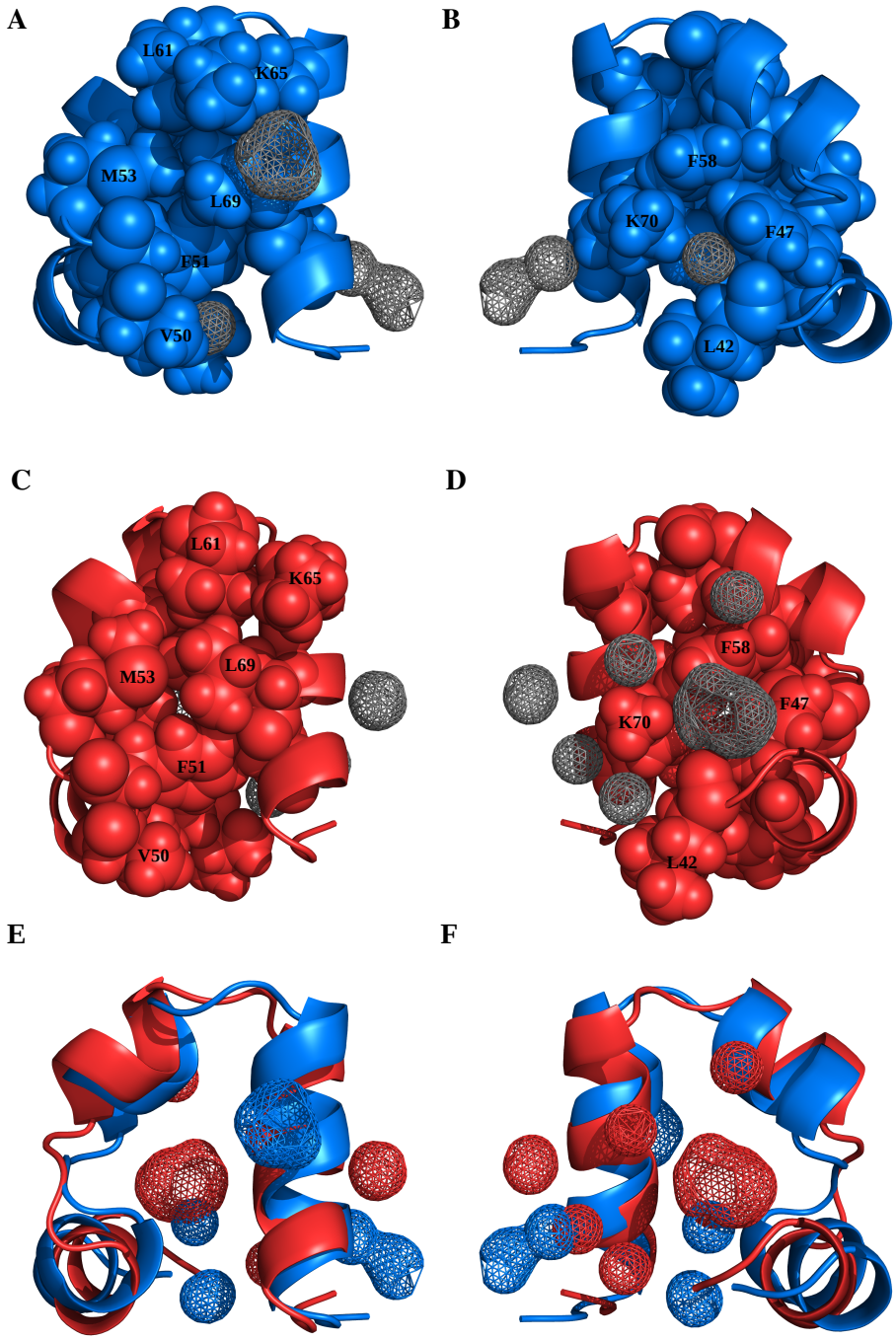

Figure 3.13.: **Solvent-accessible voids of the final minimized average NMR structure of VHP35 at 0.1 MPa and 240 MPa:** (A) and (C) show the voids (*gray*) for a solvent radius of 1.4 *Å* and a threshold of 3 radii at 0.1 MPa (*blue*) and at 240 MPa (*red*). (E) shows the superposition of the backbone structures and the voids at each pressure. (B), (D) and (F) show the rotation by 180° about the y-axis. Side chains of the hydrophobic core residues are shown as spheres and with labels.

against F58 to an energetically more favorable 45° position against F51 and F58 [134]. These pressure-induced structural changes also lead to changes in the volume and the cavity landscape. The theoretically calculated molecular surface volume (see Fig. 2.6) of VHP35 increases from 4519 $Å^3$, with a void volume of 870 $Å^3$, at 0.1 MPa to a more stable one of 4610 $Å^3$, with a larger void volume of 965 $Å^3$, at 240 MPa, according to Le Chatelier's principle (Tab. 3.8). This is accompanied by a redistribution of the water-accessible voids and a decrease of the solvent-accessible surface area from 2944 $Å^2$ at ambient pressure down to 2882 $Å^2$ at 240 MPa (Fig. 3.13).
Specifically, at 0.1 MPa, VHP35 exhibits a larger cavity between K65 and L69 with a size of ≈ 4 water molecules. In addition, there are two smaller cavities, one between L42, F47 and K70 and another between V50, F51 and L48, each with a volume of ≈ 1 water molecule. Another cavity is located in the vicinity of the KKEK motif (≈ 2 to 3 water molecules), which is enclosed by the positively charged K70 and K71 (Fig. A.17) and does not affect the hydrophobic core. Pressure-induced shift of $\alpha 1$ and the reorientation of F47 lead to the closure or redistribution of these cavities. Figure 3.13 (D) now shows a larger, solvent-accessible cavity with a size of ≈ 6 water molecules between L42, F47, F58 and K70 at 240 MPa. Near this cavity are three others, one above F58, one next to it between F58 and K70 and another below it, between L42 and K70, each with a volume of ≈ 1 to 1.5 water molecules. The latter is part of the cavities which, as at 0.1 MPa, are found in the periphery of the C-terminal helix at the KKEK motif. However, the pressure-induced reorientation of the helix at this position leads to a redistribution to two or, respectively, three additional cavities with a volume of about 1 to 1.5 water molecules each.
The pressure-induced conformational changes result in an increased molecular surface volume and void volume. Comparison of the distribution of the voids of the minimized average structures shows a higher number and a larger overall volume of the solvent-accessible voids at 240 MPa. However, at ambient pressure, the voids show a deeper penetration of water molecules into the hydrophobic core, corresponding to its larger solvent-accessible surface area. Nevertheless, there are no voids with a minimum water radius within the hydrophobic core of the structures.

3.3.2. NMR structures of VHP35_L69A

The 10 final or *control* conformers with lowest-energy of the variant VHP35_L69A at 0.1 MPa and 240 MPa fold into the three α-helical segments as in the wild type. The ensembles describe in atomic detail the changed conformation of the hydrophobic core residues with the mutation site L69A (Fig. A.21, A.22, A.23, A.24). The calculated ensembles show similar structural calculation statistics with respective overall main-chain RMSDs of ≈ 0.4 $Å$ (Tab. 3.7). The RMSD of the backbone heavy atoms between the final and the *control* minimized average NMR structure is 0.69 $Å$ at 0.1 MPa and 0.71 $Å$ at 240 MPa (Fig. 3.14). The RMSD between the respective *control* structures is 0.99 $Å$. As in the wild type, the respective *control* structures for each pressure reflect the same pressure-dependent orientation of the three α-helical segments and the hydrophobic core residues as the final structures. This also shows that all individual distance constraints

cause rearrangements due to smaller changes of the many cross-peak intensities. At 0.1 MPa, the structural differences are homogeneously distributed across the structures. And st 240 MPa, they are mainly found within the N-terminal helix (α1) and the C-terminal helix (α3). Nonetheless, the uniquely assigned NOEs of the final ensembles at 0.1 MPa or at 240 MPa are structurally consistent with the calculations and none of them violates distance restraints (Tab. A.8).

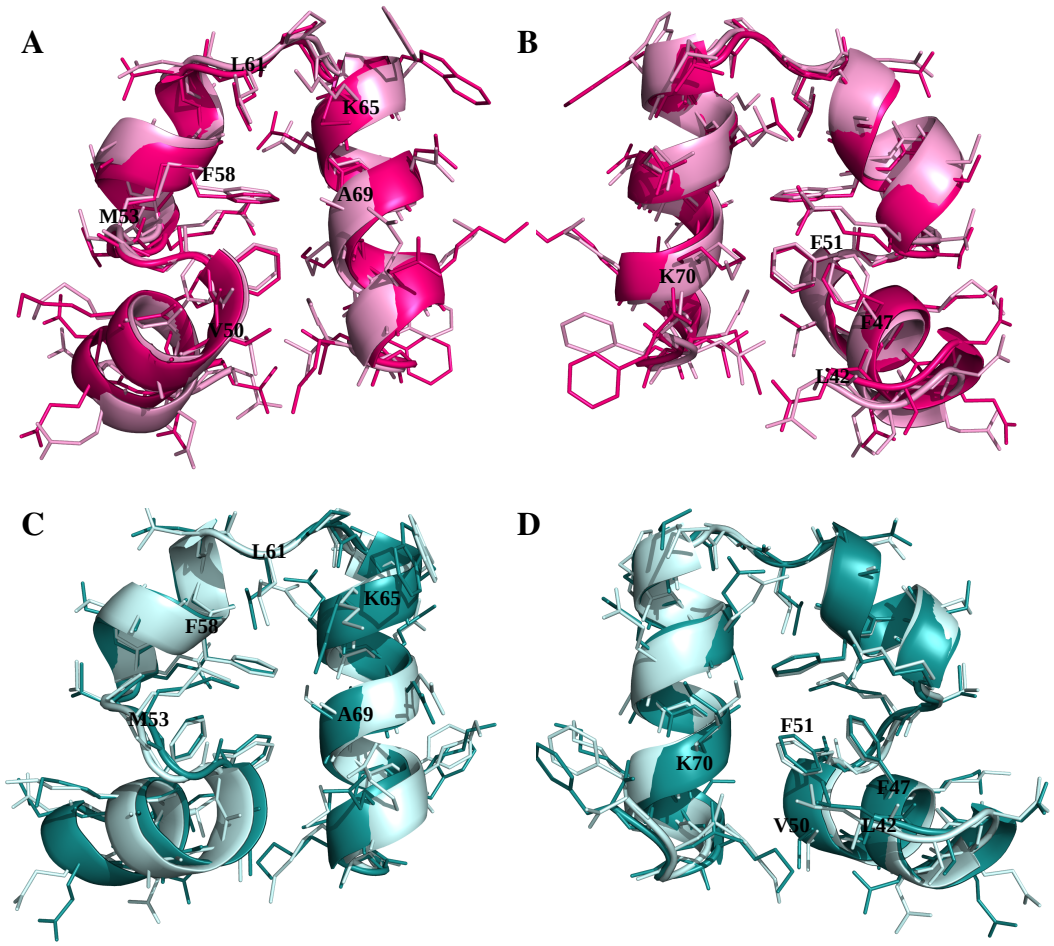

Figure 3.14.: **Superposition of the backbone heavy atoms of the final and the *control* minimized average NMR structures of VHP35_L69A at 0.1 MPa and 240 MPa (Tab. 3.6):** (A) shows VHP35_L69A at 0.1 MPa (*pink*) and the corresponding *control* structure (*light pink*) with an RMSD of 0.69 *Å*. (C) shows the structure of VHP35_L69A at 240 MPa (*green*) and the corresponding *control* structure (*light green*) with an RMSD of 0.71 *Å*. (B) and (D) show the rotation by 180° about the y-axis. Side chains are shown as sticks without hydrogens, and hydrophobic core residues are labeled.

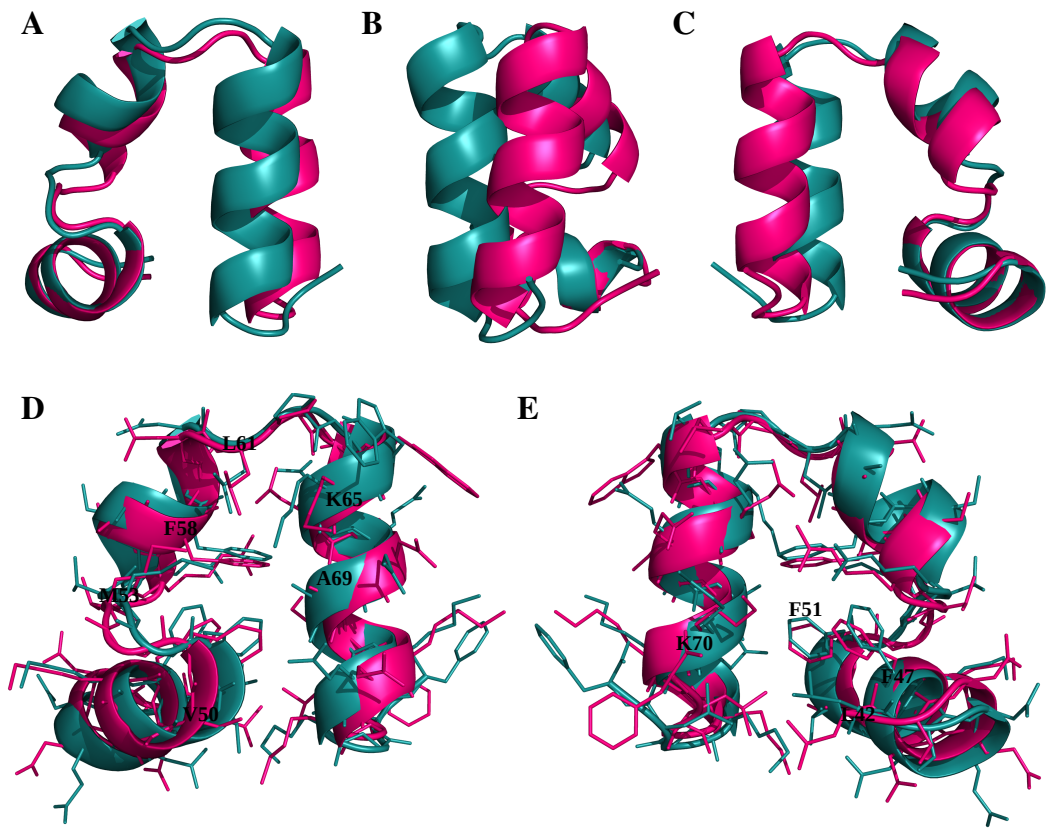

Figure 3.15.: **Superposition of the backbone heavy atoms of the final minimized average NMR structures of VHP35_L69A at 0.1 MPa and 240 MPa (Tab. 3.7):** (A) shows the superposition of α1 (residues 44-51) and (D) for all backbone residues of VHP35_L69A at 0.1 MPa (*pink*) and at 240 MPa (*green*) with an RMSD of 1.3 $\AA$ for the latter. (B) and (C) show the rotation by 90° and (E) shows the rotation by 180° about the y-axis. Side chains are shown as sticks without hydrogens, and hydrophobic core residues are labeled.

The main-chain RMSD between the final minimized average NMR structure at 0.1 MPa and 240 MPa is 1.3 $\AA$. The superposition shows the pressure-induced different position and orientation of the three α-helices of VHP35_L69A (Fig. 3.15). In particular, the reorientation of α1 compared to α3, with the pressure-induced changes mainly affect α3. At 240 MPa, this leads to an increase in the distance between the amide protons of D44 (α1) and L63 (α3) increases from 21.7 $\AA$ to 23.1 $\AA$, moving the N-terminal helix away from the upper C-terminal helix. This is consistent with the unique inter-residual NOEs found at each pressure being homogeneously distributed throughout the sequence at 0.1 MPa and occurring mainly in α1 and α3 at 240 MPa (Tab. A.8). As in the wild type, the change in pressure mainly lead to structural changes within the backbone of VHP35_L69A, and the orientation of most of the side chains remains the same except

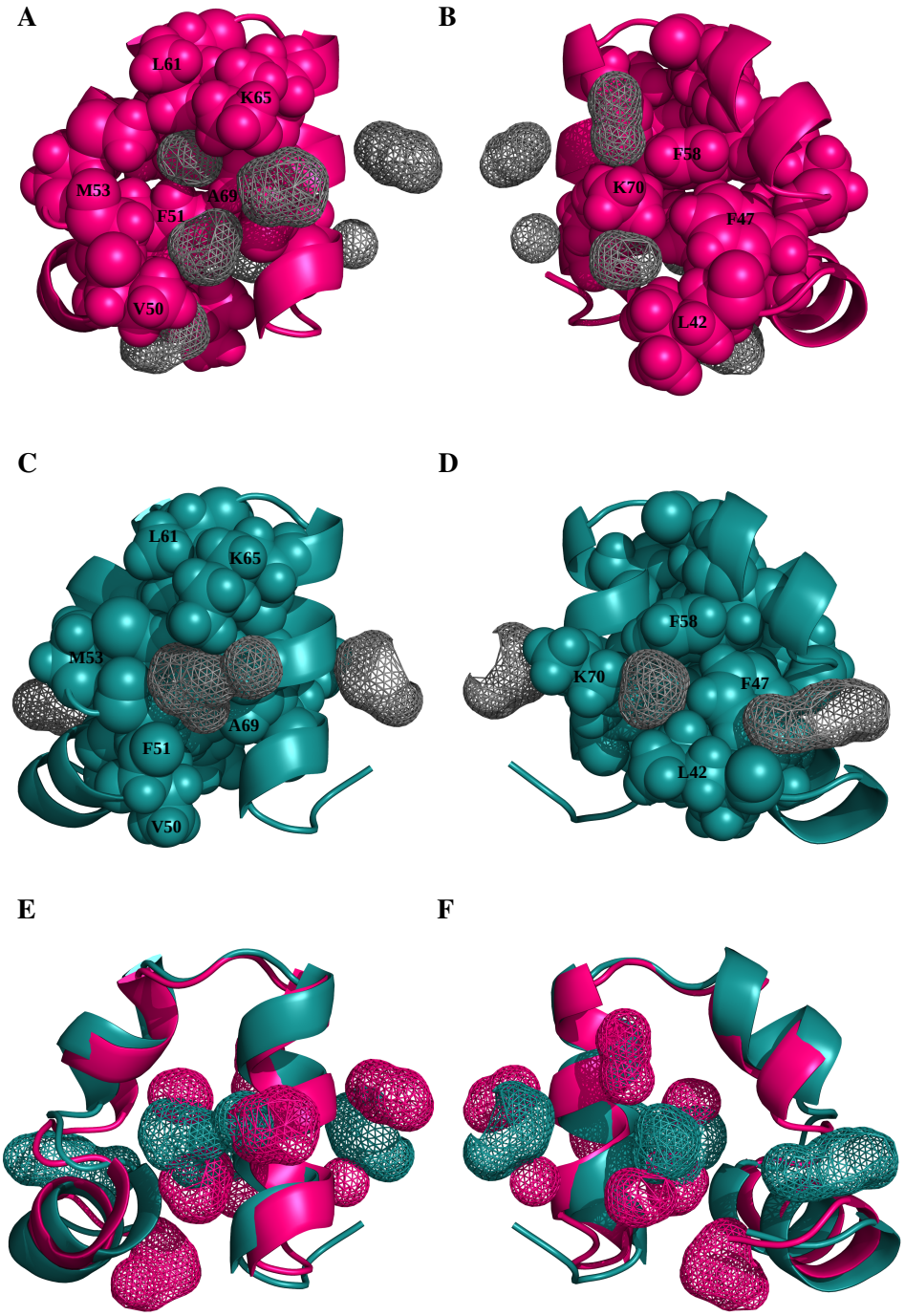

Figure 3.16.: **Solvent-accessible voids of the final minimized average NMR structures of VHP35_L69A at 0.1 MPa and 240 MPa:** (A) and (C) show the voids (*gray*) for a solvent radius of 1.4 *Å* and a threshold of 3 radii at 0.1 MPa (*pink*) and at 240 MPa (*green*). (E) shows the superposition of the backbone structures and the voids at each pressure. (B), (D) and (F) show the rotation by 180° about the y-axis. Side chains of the hydrophobic core residues are shown as spheres and with labels.

for some surface residues. Among the hydrophobic core residues, only K70 shows a significant pressure-induced rotation in the side chain by about 90° (Fig. A.25). Even the structurally stabilizing phenylalanines F47, F51 and F58 maintain their relative orientation to each other.
These pressure-induced conformational changes result in a small increase in the theoretically calculated molecular surface volume (see Fig. 2.6) of VHP35_L69A from 4489 $Å^3$, with a void volume of 886 $Å^3$, at 0.1 MPa to one of 4499 $Å^3$, with a void volume of 917 $Å^3$, at 240 MPa (Tab. 3.8). This is accompanied by a redistribution of the water-accessible voids and a small decrease of the solvent-accessible surface area from 2973 $Å^2$ at ambient pressure up to 2952 $Å^2$ at 240 MPa (Fig. 3.16).
At 0.1 MPa, the variant shows multiple cavities with different numbers of water molecule radii. The mutation site creates a void within the hydrophobic core between F51, M53, F58, L61, K65 and A69 with a volume of ≈ 1 to 2 water molecules. Below this is a water-accessible void with a size of ≈ 3 to 4 water molecules enclosed by V50, F51 and A69. In addition, below K65, is another larger cavity, also created by L69A, with a volume of ≈ 5 o 6 water molecules. With a volume of ≈ 7 to 8 water molecules, the largest cavity of the mutant is embedded between L42, V50 and F51. On the opposite side of VHP35_L69A are two other cavities, each with a volume of about 3 water molecules. One is an elongated one next to F58 and above K70 and the other is a more compact one between L42 and K70. Furthermore, there are two cavities in the periphery of the C-terminal helix at the KKEK motif, each with a volume of ≈ 1 and ≈ 3 to 4 water molecules, respectively (Fig. A.26). The pressure of 240 MPa closes the cavity on the mutation site L69A and leads to a shift from F51 (α1) toward A69 (α3). This creates a large, branched, more superficial cavity with a volume of ≈ 7 to 8 water molecules at this position (F51, M53, K65, A69). On the other hand, this creates a deeper void between L42, F47, F58 and K70 with a volume of ≈ 6 to 7 water molecules. The pressure-induced shift of α1 opens a longer cavity (L42, near F47) between this helix and α2 with a volume of about 5 to 6 water molecules. The peripheral cavities at 0.1 MPa on the C-terminal helix also merge under pressure to form a larger cavity with a volume of ≈ 7 to 8 water molecules.
Comparison of the cavity landscapes of the minimized average structures shows a shift from several smaller voids at 0.1 MPa to four larger solvent-accessible voids at 240 MPa. In particular, the deep, small cavity within the hydrophobic core, which is enclosed by the residues F51, M53, F58, L61, K65 and A69, is replaced by a bulkier one (L42, F47, F58 and K70) on the other side. However, the pressure-induced conformational changes hardly lead to a change in the molecular surface volume and void volume. Furthermore, the solvent-accessible surface area remains relatively the same as well as the overall volume of the voids.

3.3.3. Comparison of the structures of VHP35 and VHP35_L69A

Comparison of the wild type and the variant provides information on how the unfolding under pressure is affected by the change in void volume due to the mutation. Superposition of the final minimized average NMR structures of VHP35 and VHP35_L69A at 0.1

MPa shows basically similar position and orientation of the three α-helices with a main-chain RMSD of 1.14 $\AA$ (Fig. 3.17). The L69A mainly leads to a different orientation of α1, but with an unchanged distance of the amide proton of F51 to L69 or A69 of 10.7 $\AA$. The orientation, even of the hydrophobic core residues, of the side chains remains the same except for a few surface residues, and the L69A variation essentially leads only to conformational changes within the backbone. The only exception is the 90° rotation in the side chain of W64.

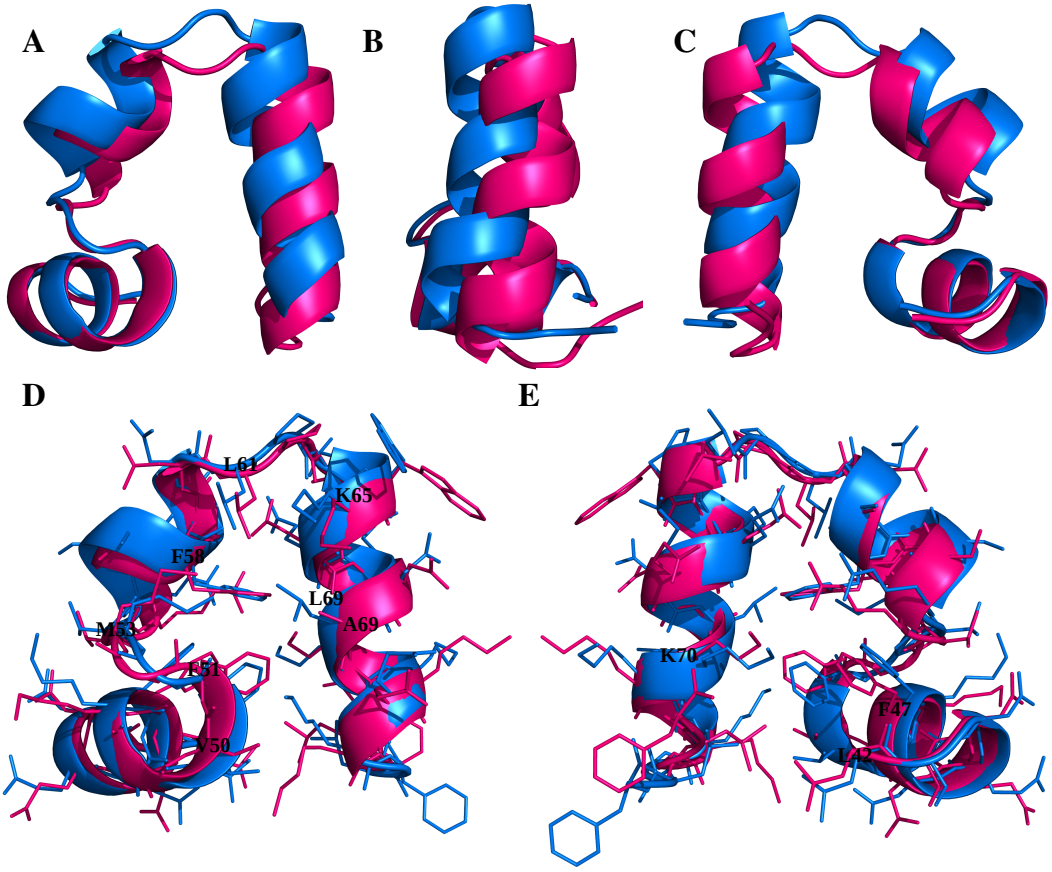

Figure 3.17.: **Superposition of the backbone heavy atoms of the final minimized average NMR structures of VHP35 and VHP35_L69A at 0.1 MPa (Tab. 3.6), 3.7):** (A) shows the superposition of α1 (residues 44-51) and (D) for all backbone residues of VHP35 (*blue*) and VHP35_L69A (*pink*) at 0.1 MPa with an RMSD of 1.14 $\AA$ for the latter. (B) and (C) show the rotation by 90° and (E) shows the rotation by 180° about the y-axis. Side chains are shown as sticks without hydrogens, and hydrophobic core residues are labeled.

As described above (Sec. 3.3.1, 3.3.2), the theoretically calculated molecular surface volume (see Fig. 2.6) at 0.1 MPa of the wild type is 4519 $\AA^3$ and of VHP35_L69A is 4482 $\AA^3$ (Tab. 3.8). Despite a lower molecular surface volume, the variant shows a larger

void volume of 886 $Å^3$ in contrast to 870 $Å^3$ for the wild type. This corresponds to a relative void volume of ≈ 19.75 % for VHP35_L69A *versus* ≈ 19.25 % for VHP35. This difference is also reflected in a slightly larger solvent-accessible surface area of the variant (VHP35_L69A: 2973 $Å^2$; VHP35: 2944 $Å^2$), which also has more water-accessible cavities with a larger overall void volume (Fig. 3.18). VHP35 and VHP35_L69A show some similar topologies of cavities, such as those between the residues L42, V50, and F51 or the peripheral cavity at the C-terminal helix near K70. And a cavity can also be seen near L69 and A69, respectively, in both structures. Here, that of the wild type is more superficial, in contrast to the steric gap caused by L69A, which enables the solvent to penetrate deeper into the hydrophobic core. In general, it can be stated that the mutation, at ambient pressure, leads to an increase in void volume with a larger solvent-accessible surface area.

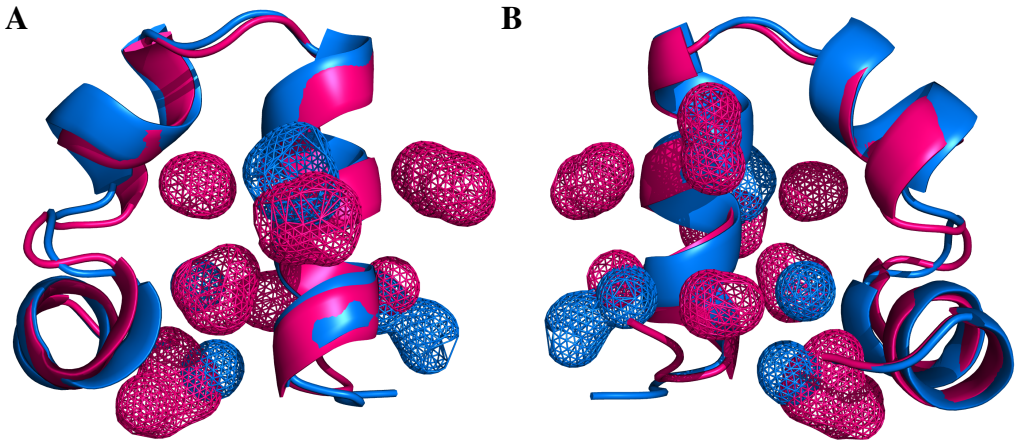

Figure 3.18.: **Superposition of the final minimized average NMR structures of VHP35 and VHP35_L69A at 0.1 MPa with the solvent-accessible voids:** (A) shows the voids in the corresponding colors for a solvent radius of 1.4 $Å$ and a threshold of 3 radii of VHP35 (*blue*) and VHP35_L69A (*pink*) at 0.1 MPa. (B) shows the rotation by 180° about the y-axis.

At high pressure, the three α-helices of the two proteins evolve into quite different orientations (Fig. 3.19). Superposition of the final minimized average NMR structures of VHP35 and VHP35_L69A at 240 MPa shows a main-chain RMSD of 2.64 $Å$. Compared to the wild type, the backbone of VHP35_L69A exhibits structural differences between the N-terminal helix and the middle helix, resulting in a significantly different conformation of the C-terminal helix. This is best illustrated by aligning only the helix α1 of the variant and the wild type (Fig. 3.19). In the case of VHP35_L69A, the increased pressure closes the steric gap created by the mutation by shifting the C-terminal end of α1 toward the C-terminal end of α3. This is also reflected in the different distances between the amide protons of F51 (α1) and L69 or A69 (α3) with 11.7 $Å$ for VHP35 and 9.7 $Å$ for VHP35_L69A. In contrast, the N-terminal end of α1 of VHP35 changes its position toward the N-terminal end of α3 under high pressure, which is then reflected

in the smaller distance between D44 and L63 of 16.4 $\AA$ for VHP35 *versus* 23.1 $\AA$ for VHP35_L69A. Despite the distinctly different conformation of the backbone of the two proteins, only minor structural changes are found in the side chains in comparison. The variant shows a rotation of the side chain of F47 $\approx$ 45°, V50 $\approx$ 180°, M53 $\approx$ 45°, L61 by $\approx$ 45°. The different position of F47 in VHP35_L69A leads to a less energetically stable planar orientation to F51. Compared to the wild type, where F47 is in a more energetically favorable perpendicular position to F51.

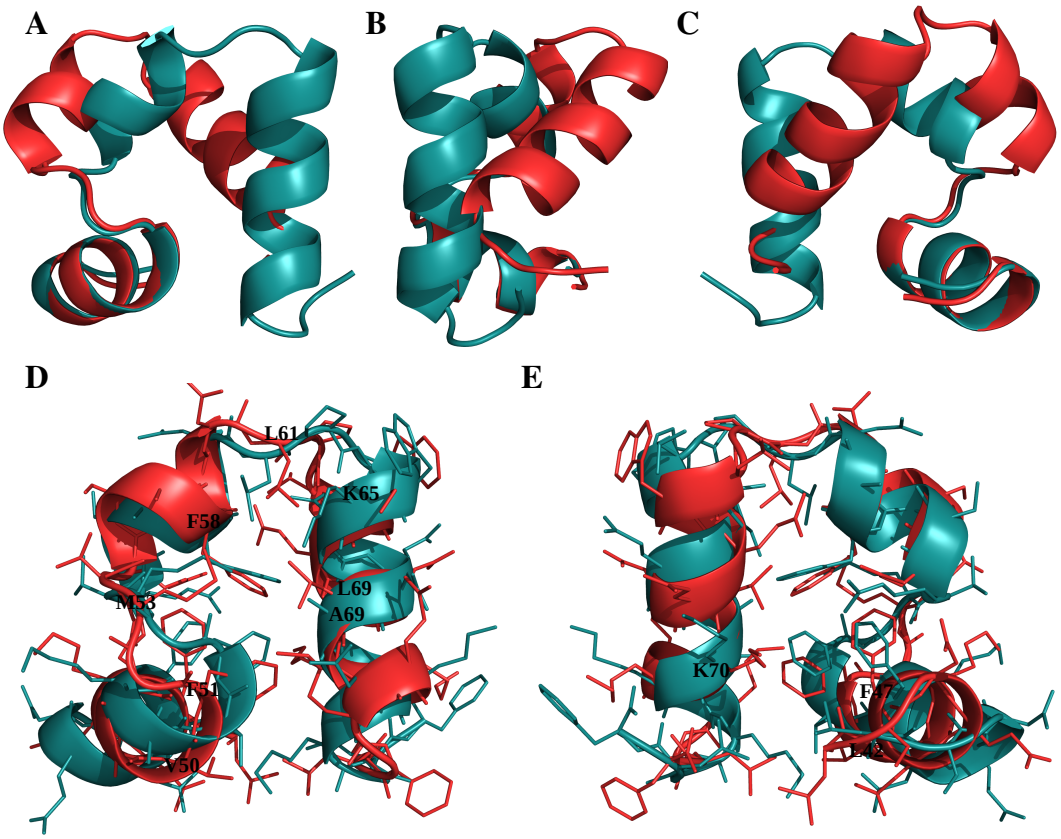

Figure 3.19.: **Superposition of the backbone heavy atoms of the final minimized average NMR structures of VHP35 and VHP35_L69A at 240 MPa (Tab. 3.6), 3.7):** (A) shows the superposition of α1 (residues 44-51) and (D) for all backbone residues of VHP35 (*red*) and VHP35_L69A VHP35 (*green*) at 240 MPa with an RMSD of 2.64 $\AA$ for the latter. (B) and (C) show the rotation by 90° and (E) shows the rotation by 180° about the y-axis. Side chains are shown as sticks without hydrogens, and hydrophobic core residues are labeled.

The pressure-induced volume changes result in a theoretically calculated molecular surface volume of the wild type of 4610 $\AA^3$, with a void volume of 965 $\AA^3$, and of VHP35_L69A of 4499 $\AA^3$, with a void volume of 917 $\AA^3$ (Tab. 3.8). In contrast to

the ambient pressure, VHP35 now shows with ≈ 20.93 % a larger relative void volume than that of VHP35_L69A with ≈ 20.38 %. Despite the larger volume, the wild type with 2882 $Å^2$ still shows a smaller solvent-accessible surface area than the mutant with 2952 $Å^2$. This is also reflected in the cavity landscape, where the wild type has more cavities, but with a smaller overall volume than the variant (Fig. 3.20). Both proteins show cavities around the residues L42, F47, F58, and K70 of approximately the same size and peripherally at the C-terminal helix near K70. Here, the peripheral cavity of VHP35_L69A is about is about twice the size of the two smaller of VHP35. In addition, VHP35 has three other smaller superficial cavities, each with a volume of ≈ 1 water molecule, around the bulky ones enclosed by L42, F47, F58 and K70. In contrast, the variant exhibits two large cavities with a volume of about 7 water molecules each, one at the position close to the mutation site (F51, M53, K65, A69) and the other between the two helices α1 and α2. In the final comparison, the mutant shows larger solvent accessibility at high pressure despite the smaller molecular surface volume but with a similar relative void volume.

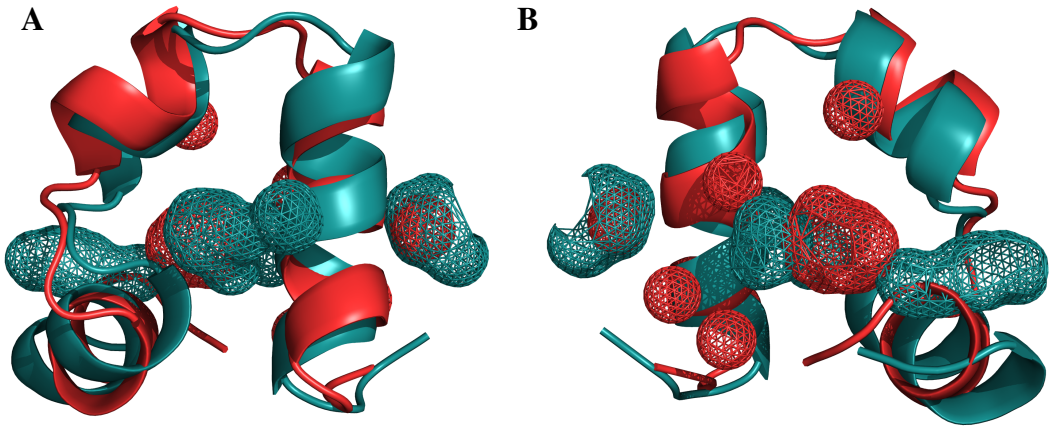

Figure 3.20.: **Superposition of the final minimized average NMR structures of VHP35 and VHP35_L69A at 240 MPa with the solvent-accessible voids:** (A) shows the voids in the corresponding colors for a solvent radius of 1.4 $Å$ and a threshold of 3 radii of VHP35 (*red*) and VHP35_L69A (*green*) at 240 MPa. (B) shows the rotation by 180° about the y-axis.

3.4. Pressure dependence of NMR backbone resonances

The effect of high pressure up to 240 MPa on the protein backbone was investigated by ^{1}H,^{15}N-HSQC experiments in 10 mM K_2HPO_4/KH_2PO_4 buffer (pH 7.0), 30 or 60 μM DSS-d_6 and 10 % D2O at 278 K. Since VHP35 or VHP35_L69A does not contain any histidine residues, the pressure-dependent pK_a change of the phosphate buffer [135] has no effect on the protonation state of the protein [1, 135]. The resulting pressure-

dependent changes in the chemical shifts of the amide protons and bound nitrogen nuclei provide structural and thermodynamic insights (Sec. 2.4.3). NMR resonance signals assignment of the backbone of VHP35 and of VHP35_L69A was achieved as described above in Section 2.2. The entire backbone assignment of the ^{1}H,^{15}N-HSQC spectra and the ^{1}H, ^{15}N chemical shifts at 278 K of VHP35 and VHP35_L69A can be seen in Figure A.9, A.18 and in the Tables A.1 - A.3, A.5 - A.7. The local pressure effects of the backbone were obtained determined by a series of ^{1}H,^{15}N-HSQC spectra measured in steps of 20 MPa from 0.1 MPa to 240 MPa.

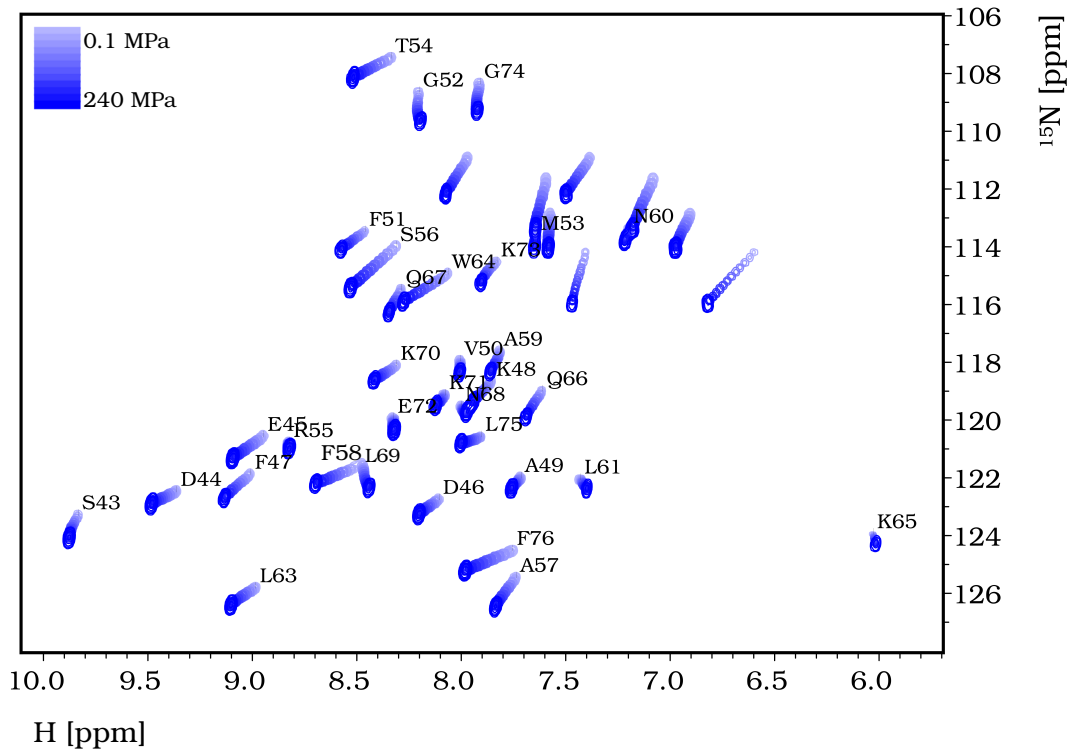

Figure 3.21.: **Superposition of ^{1}H,^{15}N-*f*HSQC spectra of VHP35 between 0.1 and 240 MPa:** Spectra recorded with increasing pressure in steps of 20 MPa at 278 K and pH 7.0 (K_2HPO_4/KH_2PO_4). Residue assignments are given at the respective resonances at 0.1 MPa.

Superposition of these spectra shows for most resonances a shift of the well-dispersed cross-peaks toward the low field with increasing pressure for both proteins, VHP35 and VHP35_L69A (Fig. 3.21, 3.22). This observation is considered to correlate with the pressure-dependent shortening of the hydrogen bonds [52, 57, 136]. A shorter distance corresponds to a stronger polarization of the hydrogen bond and thus leads to a weakening of the magnetic shielding, resulting in a low-field shift of these protons. This mechanism also applies to the corresponding nitrogen nuclei, but with a weaker low-field shift [137–139]. The magnitude of the shift depends on the type of the hydrogen bond, whether it is an intramolecular or extramolecular to enclosed water molecules or

to water molecules at the surface. Where the latter exhibit larger pressure-induced shifts than the others. This is true, for example, for amide protons at the N- and C-termini or in the loop regions of the protein [136].

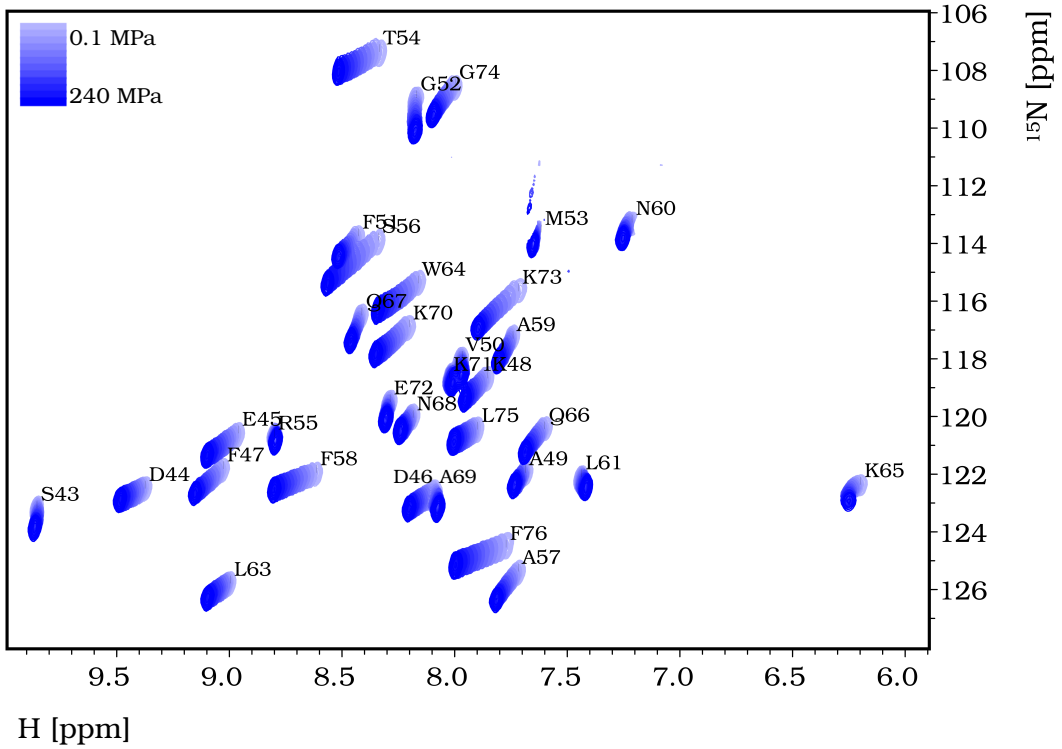

Figure 3.22.: **Superposition of ^{1}H,^{15}N-*f*HSQC spectra of VHP35_L69A between 0.1 and 240 MPa:** Spectra recorded with increasing pressure in steps of 20 MPa at 278 K and pH 7.0 (K_2HPO_4/KH_2PO_4). Residue assignments are given at the respective resonances at 0.1 MPa.

The cross-peaks in Figures 3.21 and 3.22 show linear and nonlinear pressure dependences for each chemical shift of ^{1}H and ^{15}N. These are not only the result of specific effects, such as conformational changes in the protein, but are also caused by the intrinsic pressure dependence of the protons or nitrogens of each amino acids. This nonspecific effect is caused by the pressure-dependent direct interaction between the solvent molecules and the solvent-exposed residues [140]. Separation and analysis of the nonspecific from the specific effects of the ^{1}H,^{15}N resonances is achieved by parameterizing the shifts to linear and nonlinear factors and by subtracting the residue-specific pressure-dependent factors derived from unstructured model tetrapeptides. The linear (b_1) and quadratic (b_2) coefficients of all backbone amides were obtained by fitting using a second-order Taylor expansion (Eq. 2.63, Fig. A.27, A.28, A.30, A.31). The derived pressure-dependent coefficients of the ^{1}H,^{15}N resonances of VHP35 and VHP35_L69A were corrected residue-specifically by a data set of pressure coefficients determined for the amide groups of the 20 canonical amino acids X in the model random coil Ac-Gly-Gly-X-Ala-

NH_2 [141]. The corrected coefficients of the ^1H and ^{15}N chemical shifts generally imply compressions within the folded ensemble (elastic effects) in the case of the linear factors and structural changes (conformational effects) in the case of the nonlinear factors. In particular, the linear coefficients are assumed to correlate with the changes in the distance of the corresponding hydrogen bond in the molecule (intra- or intermolecular) and the local variations of the dihedral angles [52, 53, 58, 136, 142]. Whereas the linear part of the nitrogen shift is more dependent on the latter [143]. The quadratic coefficients are related to structural fluctuations, such as the population shift to low-lying excited states [55, 60, 139]. In addition, it has been shown that residues near water-excluded cavities exhibit larger nonlinear deviations from the average values [50, 58, 144].

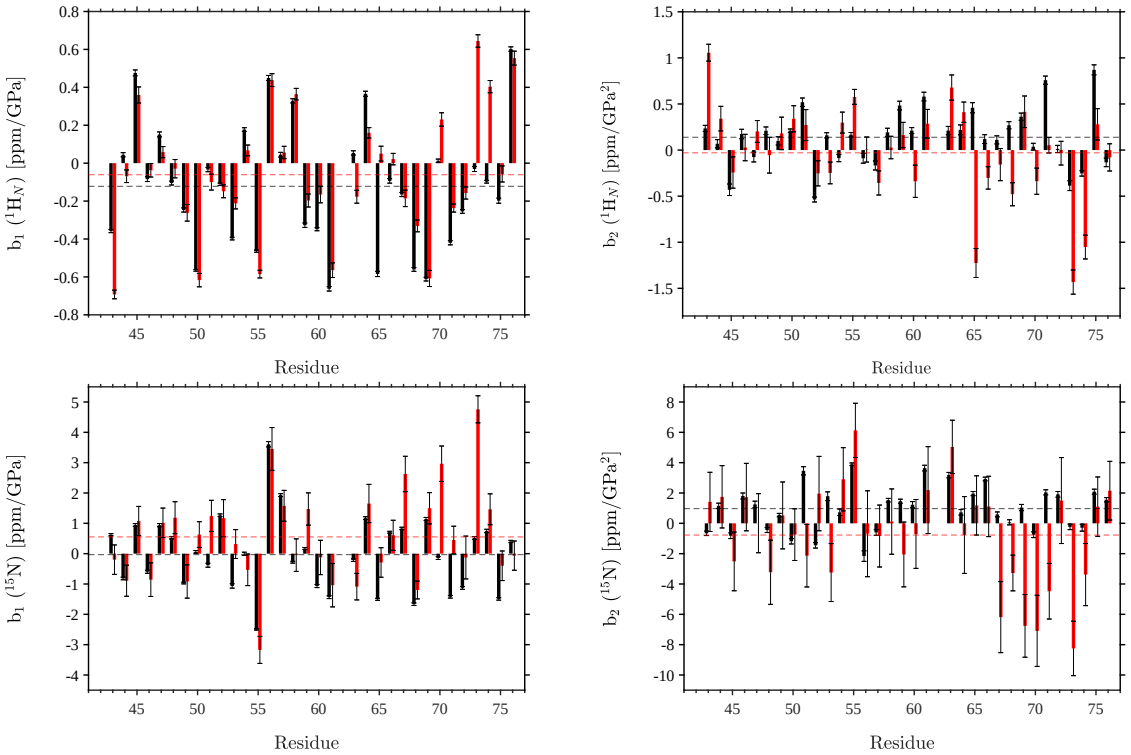

Figure 3.23.: **Pressure coefficients of the backbone of VHP35 (*black*) and VHP35_L69A (*red*) (Tab. A.9, A.10, A.11, A.12):** Residue-specific linear (b_1) and quadratic (b_2) pressure coefficients and the corresponding mean (*dashed* line) of the amide protons (^1H_N) and nitrogens (^{15}N) determined by equation 2.63.

Figure 3.23 shows the determined corrected linear and quadratic pressure coefficients for VHP35 and of VHP35_L69A. The corresponding single plots and a complete list of the derived pressure coefficients for each proteins can be found in Figures A.29, A.32 and in Tables A.9, A.10, A.11,A.12. The derived coefficients show a heterogeneous distribution, and considering the gyromagnetic ratio, those of the amide protons are larger than those of the nitrogens for most residues. In addition, VHP35_L69A generally shows larger pressure coefficients than the wild type, indicating that the system is more affected by

pressures up to 240 MPa.
To obtain more detailed insights into the derived coefficients for each protein, the most affected residues of the protein within the derived set were identified for all residues of the corresponding coefficient according to the following condition: $|x_\mathrm{i}| > (|\mu| + |\sigma|)$, where x is the value of the coefficient of the respective residue i and μ and σ are the mean and standard deviation of the corresponding set for all residues of the coefficient (Tab. A.9, A.10, A.11,A.12).
Given this condition for the linear coefficients of the amide protons, this applies to residues E45, V50, R55, L61, K65, N68, L69, and F76 of VHP35 and to residues S43, V50, R55, S56, L61, L69, K73, G74, and F76 of VHP35_L69A. And in the case of the linear coefficients of the nitrogens, this corresponds to residues R55, S56, A57, L61, K65, N68, K71, and L75 of VHP35 and to residues R55, S56, Q67, K70, and K73 of VHP35_L69A. Thus, for both proteins, the largest b_1 values for both amide protons and nitrogen atoms are found mainly within helix $\alpha 2$ and especially helix $\alpha 3$, with residues R55, S56 and L61 being the most abundant. In comparison and considering the signs, the overall linear coefficients of the amide protons and the nitrogens of both proteins show a similar distribution. As described above, for the hydrogen bonds, positive b_1 values can be interpreted as a decrease in distance of these within the molecule, and conversely, negative ones. This property is less pronounced for the nitrogens. With respect to the sign, the two proteins differ in b_1 ($^1\mathrm{H}_N$) in 7 residues (D44, L63, K65, Q66, K70, K73, G74) and in b_1 (^{15}N) in 5 residues (S43, F51, A57, K70, F76).
Combined with the distribution of the largest b_1 values of each protein, the differences between the linear coefficients of the amide protons of VHP35 and VHP35_L69A indicate different distance changes within the hydrogen bonding network in the C-terminal helix of the respective proteins. This is not apparent for the differences of the b_1 (^{15}N) values between the proteins. In general, the distribution of the linear coefficients in both cases does not show a clear pattern with respect to the secondary structure.
The pressure-induced nonlinear coefficients are considered to correlate with structural fluctuations caused by the redistribution of the internal cavities within the protein. At the atomic level, the nonlinear shifts around water-enclosed cavities exhibit larger deviations from the average values [58]. In this regard, the analysis of the derived set of nonlinear coefficients of the amide proton under the condition given above shows this for residues F51, G52, A59, L61, K65, K71, and L75 of VHP35 and for residues S43, R55, L63, K65, K73, and G74 of VHP35_L69A. And in the case of the nonlinear coefficients of nitrogens, this is shown for residues F51, R55, L61, L63, and Q66 of VHP35 and for residues R55, L63, Q67, A69, K70, K71, and K73 of VHP35_L69A. Residues F51 and L61 in VHP35, both residues of the hydrophobic core, show larger deviations for both nuclei. In the variant, this is apparent for residues R55 and L63.
As with the linear coefficients, there is an clustering of deviations from the average within helix $\alpha 2$ and mainly in helix $\alpha 3$ for both nuclei in both proteins. However, there is no direct pattern with respect to the solvent-accessible cavities for either proteins (Fig. 3.24, 3.25). Overall, the nonlinear backbone coefficients of VHP35 show that mainly residues in the region of the turns and at the edges of the helices are affected. Moreover, in the case of VHP35_L69A, residues near the mutation site show larger deviations from

the mean, especially those of the nitrogens. In comparison, the nonlinear coefficients of the proteins for both nuclei, considering the signs, show less similarities than the linear ones. Thus, the nonlinear coefficients of the amide protons differ in 12 residues (F47, K48, M53, T54, S56, N60, K65, Q66, Q67, N68, K70, E72) and those of the nitrogens in 11 residues (S43, F51, G52, M53, A59, N60, W64, Q67, N68, L/A69, K71). Together with the largest b_2 deviations from the mean of each protein, the differences between the nonlinear coefficients of both nuclei of VHP35 and VHP35_L69A indicate that the helix $\alpha 2$ and $\alpha 3$, in particular, are structurally affected by pressure.

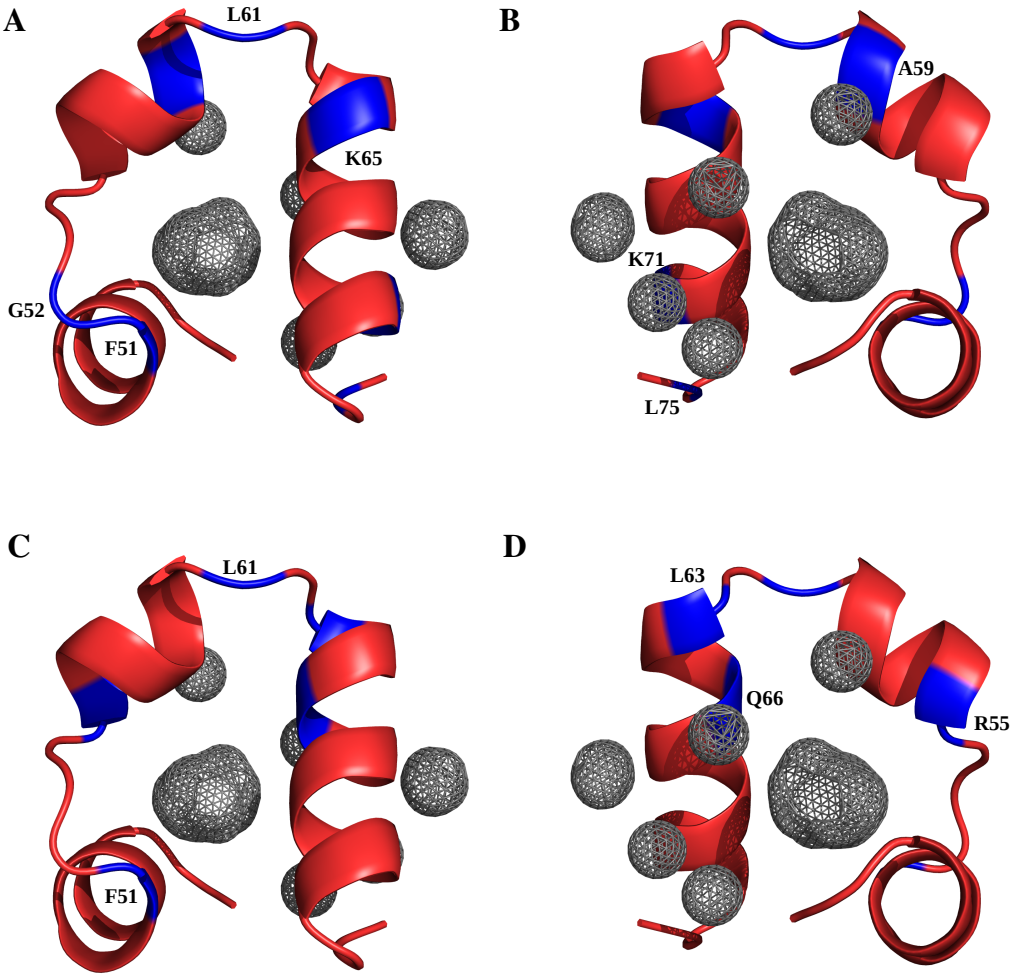

Figure 3.24.: **Structural visualization of the nonlinear backbone coefficients of the final minimized average NMR structure of VHP35 at 240 MPa:** (A) shows the residues (*blue*) with values of b_2 (^1H_N) and (C) of b_2 (N^{15}) according to the condition: $|b_2| > (|\mu| + |\sigma|)$ (Tab. A.9, A.10). (B) and (D) show the rotation by 180° about the y-axis. Structure is shown with corresponding cavity distribution (*gray*) (Fig. 3.13).

In summary, the deviations in the pressure coefficients of both proteins indicate pressure-induced local structural changes within $\alpha 2$ and $\alpha 3$, with residues R55 and L61 in VHP35 and residues R55 and K73 in VHP35_L69A showing larger deviations from the mean for both nuclei. Although interpretation of the coefficients with respect to the sign is complex and the magnitude of the signals was not considered in detail, the differences in the coefficients between the proteins nevertheless underpin structural changes within the two helices with relative to each other. Furthermore, the differences indicate a different pressure-induced local structural fluctuation.

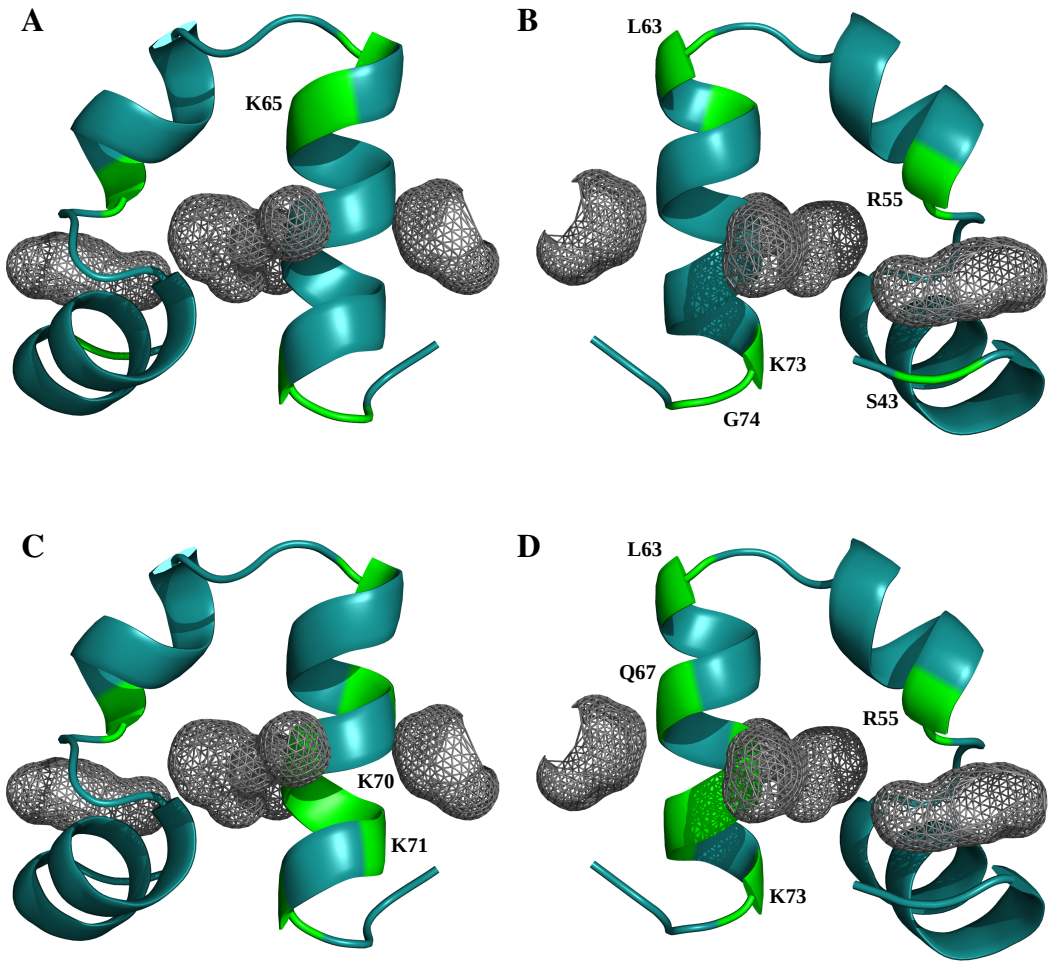

Figure 3.25.: **Structural visualization of the nonlinear backbone coefficients of the final minimized average NMR structure of VHP35_L69A at 240 MPa:** (A) shows the residues (*neon green*) with values of b_2 (^1H_N) and (C) of b_2 (N^{15}) according to the condition: $|b_2| > (|\mu|+|\sigma|)$ (Tab. A.11, A.12). (B) and (D) show the rotation by 180° about the y-axis. Structure is shown with corresponding cavity distribution (*gray*) (Fig. 3.16).

The ratio of the coefficients (Eq. 2.64) is related to the ratio of the differences in the compressibility factor and in the partial molar volume [59]. The interpretation of the ratio is ambiguous but can still be understood or used in terms of local volume changes [145]. The derived ratios show a heterogeneous distribution for both nuclei, with the ratios of the nitrogens being predominantly negative. Since the ratios for each residue (Fig. 3.26) are not based on a full pressure-induced transition, which also is reflected in the errors, the deviation from the mean was analyzed under the following condition: $(|(b_2/b_1)_i| - |\delta_i|) > (|\mu| + |\sigma|)$. Where (b_2/b_1) is the ratio of the coefficients and δ is the corresponding error of the respective residue i, and μ and σ are the mean and standard deviation of the corresponding set for all residues of the ratio (Tab. A.9, A.10, A.11,A.12).
Given this condition for the ratio of the pressure coefficients of the amide protons, this applies to residues F51, K73, and L75 of VHP35 and to residue K65 of VHP35_L69A. In the case of the nitrogens, this applies only to residues V50, F51, and L63 of VHP35. Looking at the deviations for both nuclei found in VHP35, they indicate local volume changes within helix $\alpha 1$ and $\alpha 3$. This can be assumed particularly for residue F51 of VHP35, which is part of the hydrophobic core. In the case of VHP35_L69A, the condition holds only for the ratio of the amide proton K65, which is a weak indication for a local volume change. However, the residue is a part the hydrophobic core and is located near the artificial gap created by the L69A mutation (Fig. 3.16).

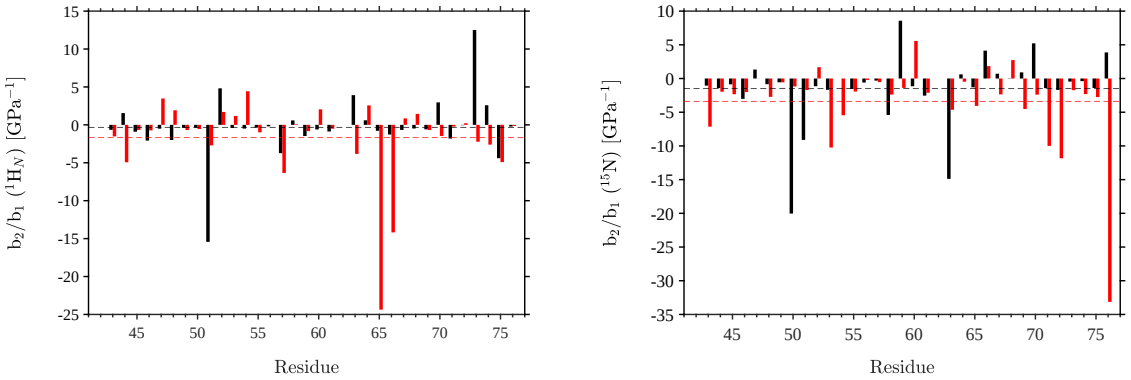

Figure 3.26.: **Ratio of the pressure coefficients of VHP35 (*black*) and VHP35_L69A (*red*):** Residue-specific ratio of the quadratic (b_2) and the linear (b_1) pressure coefficients and the corresponding mean (*dashed* line) of the amide protons (^1H_N) and the nitrogens (^{15}N) determined by equation 2.64. Residue T54 of VHP35, not shown, is defined as an outlier (Tab. A.10).

3.5. Effect of pressure on backbone dynamics

The pressure-dependent conformational motions of the backbone in the picosecond to nanosecond time scale were quantified by determining the longitudinal (R_1) and transverse (R_2) ^{15}N relaxation rates and the ^{15}N-^1H heteronuclear NOE ratio values (hNOE).

Here, R_1 is sensitive to the dynamics on the picosecond to nanosecond time scale and R_2 on the picosecond up to millisecond time scale. The corresponding ratio (R_2/R_1) is used to estimate the global tumbling or overall correlation time τ_m. The *h*NOE provides information about the motion of individual N-H bond vectors, moving faster than the overall tumbling of the molecule, resulting in a reduced *h*NOE intensity compared to the observed average. The assignment and measurement of the NMR resonance signals, the longitudinal (R_1) and transverse (R_2) ^{15}N relaxation rates and the ^{15}N-^{1}H heteronuclear NOE ratio values (*h*NOE) of the backbone of VHP35 and of VHP35_L69A at 278 K, $B_0 = 14{,}1$ T (600 MHz) and at 0.1 MPa and 240 MPa, respectively, were determined as described above in Section 2.2.

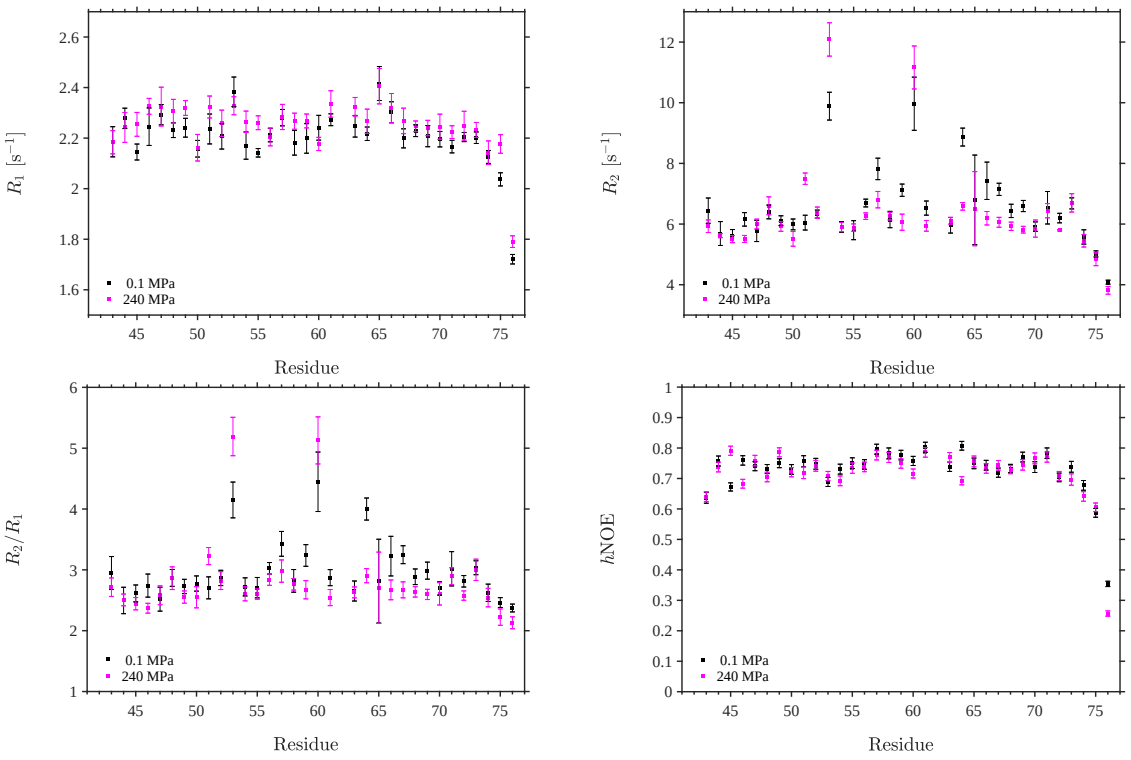

Figure 3.27.: **Relaxation parameters of the backbone of VHP35 at 0.1 MPa (*black*) and 240 MPa (*purple*) (Tab. A.13, A.14):** Longitudinal (R_1) and transverse (R_2) ^{15}N relaxation rates, the ratio (R_2/R_1), and the ^{15}N-^{1}H heteronuclear NOE ratio values (*h*NOE) at 278 K and $B_0 = 14{,}1$ T.

At ambient pressure, VHP35 shows residue-specific relaxation parameters similar to those previously reported for VHP36 at 279 K and $B_0 = 11{,}74$ T (500 MHz) [146]. In general, all residues show similar values for the respective relaxation parameters (Fig. 3.27). Only within the C-terminal region (G74 to F76) lower values occur and especially residues M53 and N60 show a significant deviation from the mean ($> 2\sigma$) for R_2 (Tab. A.13, A.14). The pressure change up to 240 MPa essentially follows the pattern at 0.1 MPa and therefore does not show significantly increased or decreased flexibility of any

region in the VHP35 backbone. This is also reflected in the pressure-dependent change in the mean from 2.21 s^{-1} to 2.25 s^{-1} for R_1, from 6.53 s^{-1} to 6.33 s^{-1} for R_2, and from 0.73 to 0.71 for hNOE. The relaxation rates R_1 and R_2 are relatively insensitive to the internal motion and depend mainly on the overall molecular tumbling [147]. This is described by the overall rotational correlation time τ_m, which can be used to determine the rotational diffusion of the molecule and, moreover, the axially symmetric diffusion tensors. A useful first estimate of τ_m is obtained via the 10 % trimmed weighted average of the R_2/R_1 ratio (Eq. A.1). At ambient pressure, this yields an estimated value of $\tau_m = 3.91$ ns for VHP35 (Tab. A.17), which agrees with previously determined values of $\tau_m = 4.36$ ns for VHP36 at 279 K and $B_0 = 11{,}74$ T (500 MHz) [148]. At 240 MPa, τ_m decreases slightly to 3.74 ns.

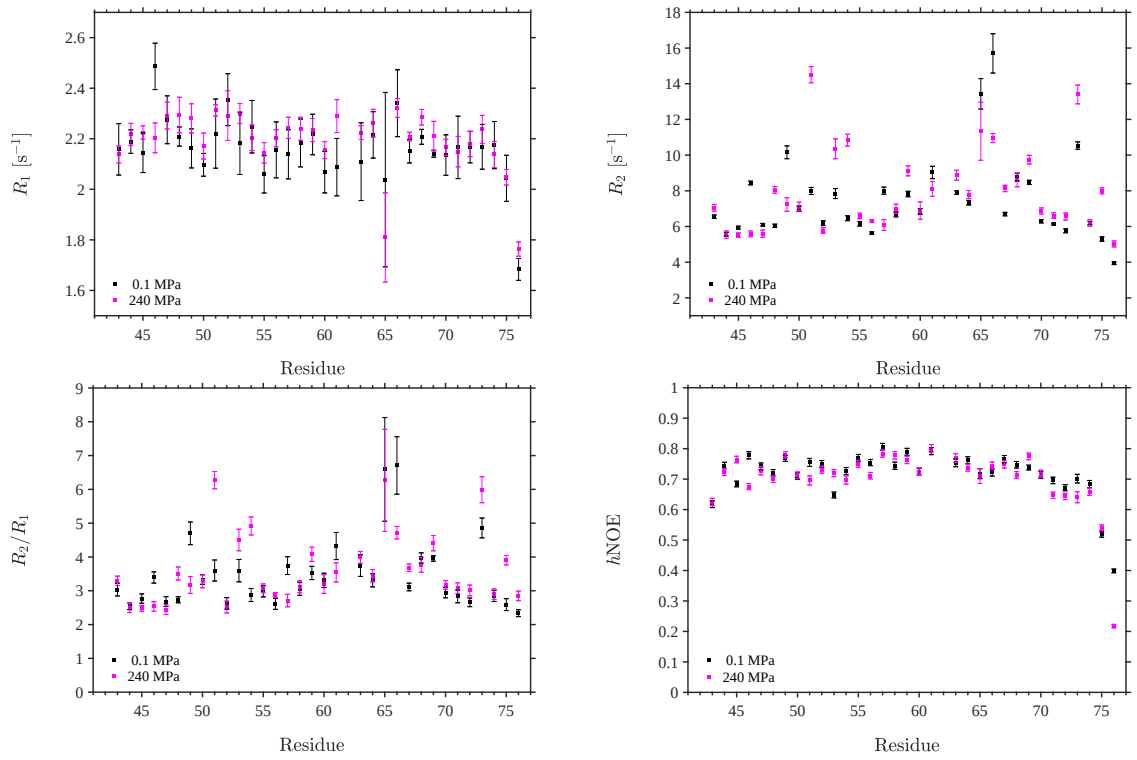

Figure 3.28.: **Relaxation parameters of the backbone of VHP35_L69A at 0.1 MPa (*black*) and 240 MPa (*purple*) (Tab. A.15, A.16):** Longitudinal (R_1) and transverse (R_2) ^{15}N relaxation rates, the ratio (R_2/R_1), and the ^{15}N-^{1}H heteronuclear NOE ratio values (hNOE) at 278 K and $B_0 = 14{,}1$ T.

Compared to the wild type, VHP35_L69A shows a broader range of values for the respective relaxation parameters, but also with lower ones within the C-terminal region (L75 to F76), indicating more pronounced motions along the sequence at both pressures (Fig. 3.28). This is also reflected in the number of residues showing a larger deviation from the mean ($> 2\sigma$), such as the R_1 rate of D46 and the R_2 rate of K65 and Q66 at ambient pressure (Tab. A.15, A.16). The pressure change up to 240 MPa leads to

a redistribution of the residue-specific relaxation rates, but in the same time ranges as at ambient pressure. This gives a different set of residues with a significant deviation from the mean, such as the R_1 rate of K65 and the R_2 rate of F51 and K73. But also to a small pressure-dependent variance in the mean from 2.16 s^{-1} to 2.19 s^{-1} for the R_1 and from 7.48 s^{-1} to 7.92 s^{-1} for the R_2 relaxation rate and from 0.72 to 0.7 for the *h*NOE. According to the equation A.1, the estimated value of the overall correlation time $\tau_m = 4.46$ ns at ambient pressure and $\tau_m = 4.63$ ns at 240 MPa for VHP35_L69A (Tab. A.17).
Comparing the mean values of the longitudinal relaxation rates and the heteronuclear NOE values of VHP35 and VHP35_L69A shows for both proteins similar values with equivalent values in the magnitude of the change with increasing pressure. In the case of the mean of the longitudinal relaxation rate, VHP35 shows a value of 6.53 s^{-1} and VHP35_L69A a value of 7.48 s^{-1} at 0.1 MPa. At 240 MPa, the mean of R_2 of VHP35 decreases to 6.33 s^{-1} whereby the mean of VHP35_L69A increases to 7.92 s^{-1}. This also applies to the overall correlation time at 0.1 MPa, with $\tau_m = 3.74$ ns for VHP35 and $\tau_m = 4.46$ ns for VHP35_L69A at 0.1 MPa and with an decrease of ≈ 0.2 ns at 240 MPa for the wild type and *vice versa* for the variant.

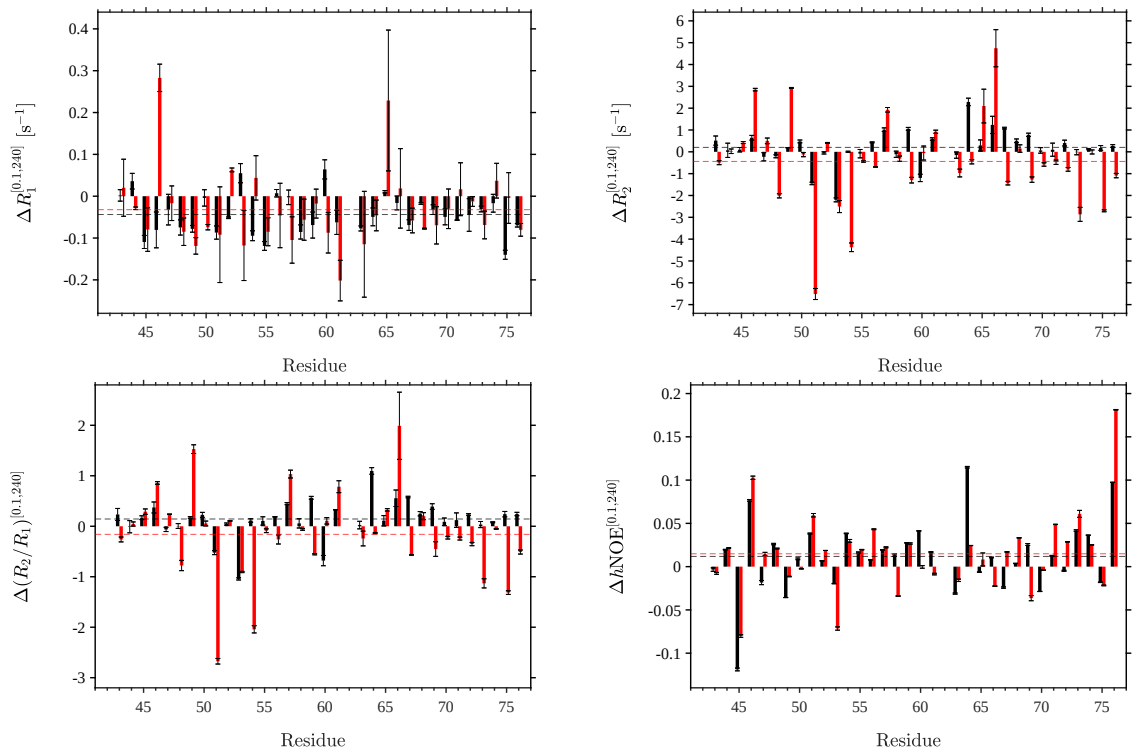

Figure 3.29.: **Pressure-dependent difference of relaxation parameters of the backbone of VHP35 (*black*) and VHP35_L69A (*red*) (Tab. A.13, A.14, A.15, A.16):** Difference (Δ) of longitudinal (R_1) or transverse (R_2) ^{15}N relaxation rates, the ratio (R_2/R_1) and the ^{15}N-^{1}H heteronuclear NOE ratio values (*h*NOE) at 0.1 MPa and 240 MPa, and the corresponding mean (*dashed* line).

To gain a more detailed insight into the pressure dependence of the relaxation parameters of the individual residues of each protein, the difference (Δ) between ambient and high pressure was calculated (Fig. 3.29). The derived difference sets were analyzed according to the following condition: $|x_\mathrm{i}| > (|\mu| + |\sigma|)$. Here x is the value of the respective difference of the relaxation parameter for the respective residue i and μ and σ are the mean and standard deviation of the corresponding set for all residues of the coefficient (Tab. A.13, A.14, A.15, A.16).
This condition holds for the pressure-dependent variations of the R_1 relaxation rates for residues E45, T54, R55, and L75 of VHP35 and for the residues D46, L61, and K65 of VHP35_L69A. And in the case of the R_2 relaxation rates, this corresponds to residues F51, M53, A57, A59, N60, W64, Q66, and Q67 of VHP35 and to residues D46, A49, F51, T54, Q66, K73, and L75 of VHP35_L69A. Together, both relaxation rates map motions in the picosecond to millisecond time scale. Consistent with this time scale and the applied pressure, larger pressure-dependent variations of motions found within the turn between the first and the second helix, the helix $\alpha 2$ and the helix $\alpha 3$ for VHP35 (Fig. 3.30). In contrast, larger deviations are found mainly for residues within the helix $\alpha 1$ and helix $\alpha 3$ for VHP35_L69A (Fig. 3.31). The heteronuclear NOE is sensitive to changes in internal motions at the level of an individual N-H bond vector. Analysis of the derived set of differences of the hNOE values under the condition given above shows larger deviations from the mean for residues E45, D46, W64, and F76 of VHP35 and E45, D46, M53, and F76 of VHP35_L69A. This pattern is identical for both proteins except for a single residue (Fig. 3.30, 3.31). In general, neither protein shows a specific dynamic pattern with respect to secondary structure. And with respect to the hydrophobic core, only the R_2 rates of F51 and M53 of VHP35 and the R_2 rate of F51 and the hNOE value of M53 of VHP35_L69A show larger deviation from the mean.

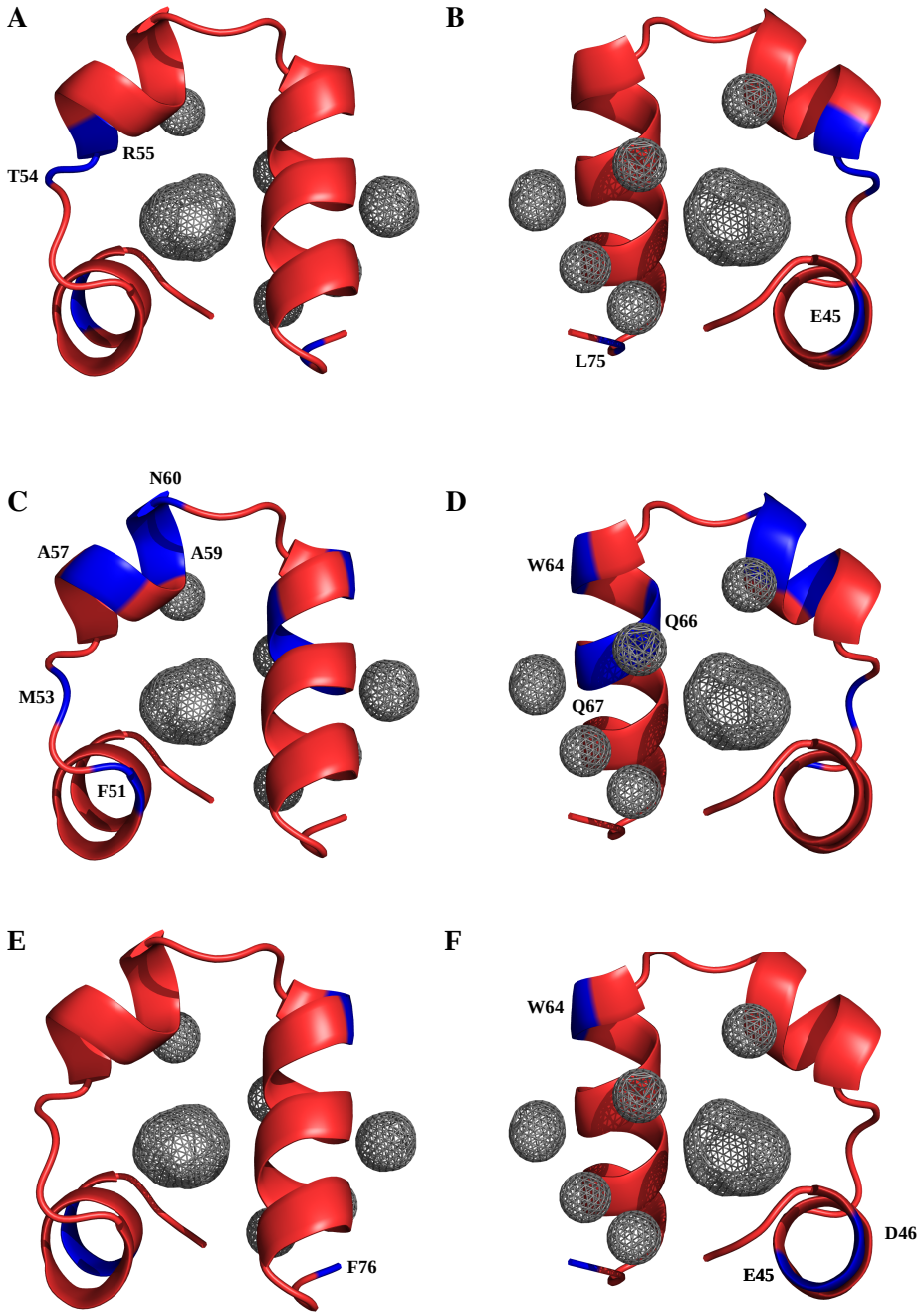

Figure 3.30.: **Structural visualization of the pressure-dependent difference of the relaxation parameters of the backbone of VHP35:** (A) shows the residues with the pressure-dependent difference (Δ) of R_1 and (C) of R_2 relaxation rates and (E) of the hNOE values according to the condition: $|x_\mathrm{i}| > (|\mu| + |\sigma|)$ (Tab. A.13, A.14). (B), (D) and (F) show the rotation by 180° about the y-axis. Structure is shown with the corresponding cavity distribution (*gray*) (Fig. 3.13).

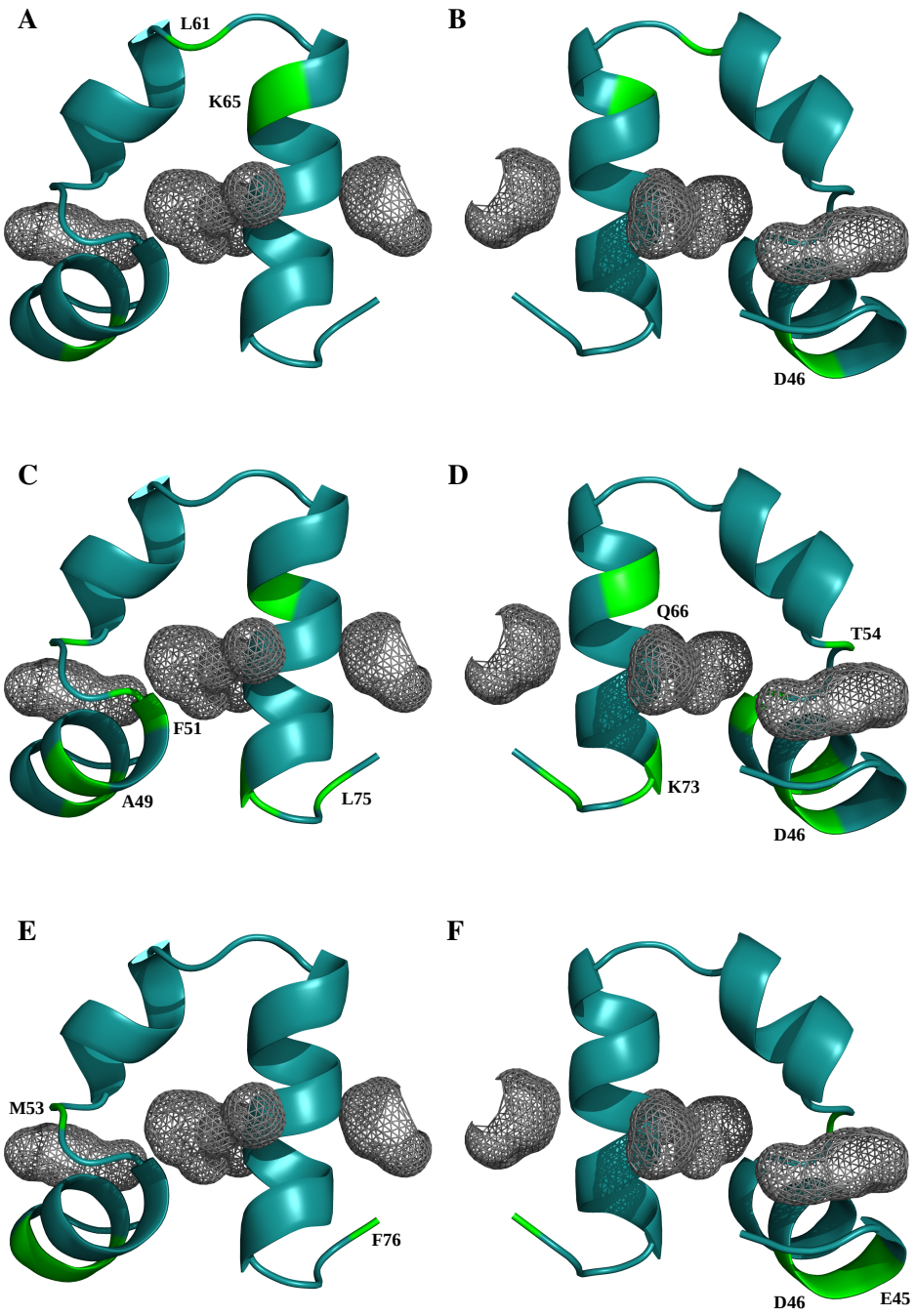

Figure 3.31.: **Structural visualization of the pressure-dependent difference of the relaxation parameters of the backbone of VHP35_L69A:** (A) shows the residues with the pressure-dependent difference (Δ) of the R_1 and (C) of the R_2 relaxation rates and (E) of the hNOE values according to the condition: $|x_i| > (|\mu| + |\sigma|)$ (Tab. A.15, A.16). (B), (D) and (F) show the rotation by 180° about the y-axis. Structure is shown with the corresponding cavity distribution (*gray*) (Fig. 3.16).

4. Discussion

The model protein VHP35 and the variant VHP35_L69A were characterized by extensive biophysical analysis under changing physical conditions using solution NMR.

4.1. Pressure stabilized conformer of VHP35

The obtained biophysical characteristics of the wild type at ambient pressure are consistent with those previously observed. Minor structural differences between the determined folded VHP35 NMR structure (Fig. 3.10) and previously published ones correspond to different physical conditions and methods [62, 65, 77, 132]. The local dynamics on a picosecond to nanosecond time scale and the corresponding overall rotational correlation time also consistent with literature values [146, 148]. With a $\Delta G^{\circ}_{\mathrm{u}}$ of 7.47 kJ/mol at 298 K and a transition temperature T_{m} of 340.6 K (Tab. 3.1), the determined thermodynamic stability is slightly reduced compared to the literature [61, 72–76].
Thermodynamic stability within the temperature–pressure phase space was derived by assuming a two-state model of an unfolded and a folded population that differ in their 1D ^{1}H NMR spectra under all experimental conditions. A comparison of the temperature transitions with increasing pressure shows a slight shift to higher transition temperatures, especially in the last step to 240 MPa, indicating stabilization of the system. This is also accompanied by a slight increase in $\Delta G^{\circ}_{\mathrm{u}}(T_{\max})$. However, the other thermodynamic parameters of the pressure-dependent temperature transitions remain fairly constant and show only small pressure-induced changes up to 240 MPa (Tab. 3.1, Fig. A.1). Thus, the pressure profile of $\Delta G^{\circ}_{\mathrm{u}}(p)$ at constant temperatures yields only imprecise ΔV and small $\Delta\hat{\beta}$ (Tab. 3.3, Fig. 3.8). On this basis, the pressure-induced increased stability of VHP35 results in a hyperbolic phase boundary (Eq. 2.50) in the pressure-temperature phase space (Fig. 3.9). The condition for this shape is $\Delta\hat{\alpha}^2 < \Delta c_{\mathrm{p}} \cdot \Delta\hat{\beta}/T_0$ and is defined by the small positive value of $\Delta\hat{\beta}$ (Tab. 3.5). In contrast, as the pressure increases from $\Delta V > 0$, the system shifts toward the section of $\Delta V < 0$ (see Fig. 2.9), corresponding to a smaller volume of VHP35 at 240 MPa. Since local unfolding of helix $\alpha 3$ [1] was not observed by the NMR data here presented, it can be assumed that the negative ΔV in combination with the increased stability is mainly the result of a smaller hydration shell of VHP35 at 240 MPa.
This conclusion from the pressure-dependent thermodynamics of VHP35 is underpinned by the comprehensive structural analysis at 278 K. Supported by control structure calculations, the pressure up to 240 MPa induces a different position of $\alpha 1$ *versus* of $\alpha 2$ and $\alpha 3$ or *vise versa* in VHP35 (Fig. 3.12). Specifically, the distance between the amide protons of D44 and L63 shortens, corresponding to the shift of the N-terminal helix toward

the upper C-terminal helix. The pressure-dependent conformational changes correspond mainly to a shift in the trajectory of the backbone of VHP35, and the orientation of most of the side chains, even the hydrophobic core residues, remains the same (Fig. A.16). Among the hydrophobic core residues, only F47, M53, L61, and K65 show a significant pressure-induced change in the side chains of about 90°. Which, especially in the case of the aromatic ring of F47, corresponds to an energetically more favorable position of 45° compared to F51 and F58 [134] (Fig. A.16).
In this context, the nonlinear pressure-dependent deviations from the mean of the ^{1}H and ^{15}N chemical shifts of the individual residues reveal mainly local structural fluctuations [55, 60, 139] at the edges of the helices and in the second turn within the protein backbone (Fig. 3.24, Tab. A.9, A.10). Residues around water-excluded cavities exhibit larger nonlinear deviations [58, 144]. Since this was observed in particular in the case of residues F51 and L61 for both nuclei, it can be assumed that they were involved in the rearrangement or reduction of internal water-inaccessible cavities (Fig. 3.13). Analysis of the linear pressure-dependent deviations of the ^{1}H and ^{15}N shifts, which correlate with the stability of hydrogen-bonds [52, 53, 57, 58, 136, 142], shows this for residues R55, L61, K65, and N68 (Tab. A.9, A.10). The observed distribution of the larger linear coefficients reveals local changes in distance within the hydrogen bond network in the second α2 helix, the succeeding turn, and the C-terminal helix α3 of VHP35.
Despite these pressure-induced structural changes, the local dynamics generally remain the same on a picosecond to nanosecond time scale (Fig. 3.27, Tab. A.13, A.14). This is also reflected in the small variances in the mean of the observed dynamic parameters, and only some residues at 0.1 MPa show a significant deviation from the mean in the R_2 rate like M53 and N60. However, an extensive analysis of the pressure-dependent differences in the dynamic parameters shows definite deviations from the corresponding mean of the R_1 or R_2 rates for residues within the turn between the first and the second helix, the helix α2, and the helix α3 (Fig. 3.30, A.33). The derived set shows a heterogenous distribution of residues that are unambiguously structurally affected by pressure, such as F51, R55, and those that are intermediate or adjacent. According to this methodology, larger variations in residue-specific internal motions were identified by differences in the pressure-dependent heteronuclear NOE values for the residues E45, D46, W64, and F76. Furthermore, the 10 % trimmed weighted average value of the R_2/R_1 ratio (Eq. A.1) provides a useful initial estimate of the overall rotational correlation time τ_m corresponding to the rotational diffusion of a molecule. The within the errors calculated decrease of τ_m from 3.91 ns at 0.1 MPa to 3.74 ns at 240 MPa (Tab. A.17) is consistent with the pressure-induced smaller volume at 278 K.
These structural and dynamical changes are also the result of the redistribution of the water-accessible voids of VHP35 (Fig. 3.13). The cavity landscape at 0.1 MPa is mainly characterized by a larger cavity with a size of $\approx$ 4 water molecules between L69, the positively charged K65, and the negatively charged E72, and by two smaller cavities, one between L42, F47 and K70 and another between V50, F51 and L48, each with a volume of $\approx$ 1 water molecule. There is a peripheral cavity embedded in the mainly positively charged KKEK motif located in the C-terminal helix α3 (Fig. A.17). The pressure-induced structural changes lead to the sealing of the three main solvent-

accessible cavities at ambient pressure, and a cavity with a size of ≈ 6 water molecules emerges between L42, F47, F58 and the negatively charged D44 and the positively charged R55 and K70 at 240 MPa. Near this cavity there are three others, above at F58, next to it between F58 and K70, and below between L42 and K70, each with a volume of ≈ 1 to 1.5 water molecules. The peripheral void at 0.1 MPa embedded in the KKEK motif is redistributed into two voids. Despite the observed higher number and larger overall volume of the solvent-accessible cavities at 240 MPa compared to 0.1 MPa, the solvent-accessible surface area decreases slightly with increasing pressure from 2944 $\AA^2$ to 2882 $\AA^2$. Moreover, and according to the Le Chatelier's principle, the pressure-dependent conformational changes result in a slight stabilizing increase in the theoretically calculated molecular surface volume together with an increase in the void volume from 870 $\AA^3$ at 0.1 MPa to 965 $\AA^3$ at 240 MPa (Tab. 3.8). Since the theoretical molecular surface volume corresponds to the volume of VHP35 without the hydration shell, it can be concluded that it is decreasing.
In summary, native VHP35 exhibits increased stability at 240 MPa with reduced volume. This results from a hyperbolic phase boundary defined by a slightly higher volume of the native state at ambient pressure compared to the unfolded state and by a higher compressibility of the native state compared to the unfolded state. The combination of increased molecular surface volume and void volume and decreased solvent-accessible surface corresponds to pressure induced increased conformational stability with a decreased hydration shell of unfolded VHP35 [149–151]. The pressure-induce structural changes occur mainly within the backbone, resulting in different positions of R55 and the hydrophobic core residues F47, F51, L61, and K65.

4.2. Entropy driven destabilization of VHP35_L69A

Compared to the wild type, the alanine mutation of VHP35 at the hydrophobic core residue leucine 69 within helix $\alpha 3$ leads to decreased thermodynamic stability at 0.1 MPa (Tab. 3.1, 3.2). The pressure-dependent decrease in transition temperatures indicates the destabilization of VHP35_L69A up to 240 MPa. This is also accompanied by a decrease, especially in the last step up to 240 MPa, of $\Delta G^\circ_\mathrm{u}(T_\mathrm{max})$, $\Delta H^\circ_\mathrm{u}(T_\mathrm{m})$ and $\Delta S^\circ_\mathrm{u}(T_\mathrm{m})$. In contrast, the heat capacity Δc_p generally remains the same over the observed pressure range, indicating a mainly pressure-induced destabilization of the system. The corresponding pressure profiles of $\Delta G^\circ_\mathrm{u}(p)$ at constant temperatures show that the pressure-induced destabilization is driven only by small negative $\Delta\hat{\beta}$ between the folded and unfolded states (Tab. 3.4). This results in a very small negative value of $\Delta\hat{\beta}$ between the two states caused by the leucine-alanine substitution, which satisfies the condition $\Delta\hat{\alpha}^2 > \Delta c_\mathrm{p} \cdot \Delta\hat{\beta}/T_0$ for the elliptic shape in the pressure-temperature phase space. Thus, the resulting elliptic phase boundary (Eq. 2.50) in the pressure-temperature phase space shows that the unfolding of VHP35_L69A is mainly determined by the change in entropy (Fig. 3.9, Tab. 3.5). Since $\Delta S = 0$ corresponds to p_max, the phase diagram shows that the system shifts from $\Delta S < 0$ to the section of $\Delta S > 0$ with increasing temperature (see Fig. 2.9), corresponding to an increase in entropy. At 278 K, the

increased pressure results to a decrease in stability in combination with a decrease in entropy of VHP35_L69A.
At this temperature and supported by control structure calculations, pressure results in a shift of the N-terminal helix $\alpha 1$ away from the upper C-terminal helix $\alpha 3$. In detail, the distance between D44 and L63 increases (Fig. 3.15). As in the wild type, the pressure-dependent conformational changes occur mainly within the backbone of VHP35_L69A, and the orientation of most of the side chains, even of the hydrophobic core residues, remains the same (Fig. A.25). Only the hydrophobic core residue K70 shows a significant pressure-induced rotation in the side chain of about 90°.
The nonlinear pressure-dependent deviations from the mean of the ^{1}H and ^{15}N chemical shifts of the individual residues show mainly local structural fluctuations within the helix $\alpha 3$ (Fig. 3.25, Tab. A.11, A.12). In particular, this corresponds to the positively charged lysins around the mutation and the residue L63 as well as the positively charged R55 and K73. The deviations of the linear pressure-dependent ^{1}H and ^{15}N shifts reflect local changes in the stability of the hydrogen bonds, mainly found within the helix $\alpha 2$ and $\alpha 3$. This was observed for both nuclei for the residues R55, S56 and K73.
With respect to the local dynamics on a picosecond to nanosecond time scale, VHP35_L69A shows pronounced pressure-dependent variations of the dynamic parameters, but with respect to the mean values, the dynamics remain little changed (Fig. 3.28, Tab. A.15, A.16). Therefore, only some residues show a significant deviation from the mean like the R_1 rate of D46 and the R_2 rate of K65 and Q66 at ambient pressure and the R_1 rate of K65 and the R_2 rate of F51 and K73 at 240 MPa. In this context, the analysis of the pressure-dependent differences of the dynamic parameters shows significant deviations for the R_1 and R_2 rates for residues within the helix $\alpha 1$ and helix $\alpha 3$ (Fig. 3.31, A.34). With the exception of K73, this corresponds to residues that are structurally unaffected in terms of larger nonlinear deviations of the ^{1}H and ^{15}N shifts. Regarding larger variations in residue-specific internal motions, residues E45, D46, M53, and F76 were identified in the differences in the pressure-dependent heteronuclear NOE values. The overall rotational correlation time (Eq. A.1) shows a slight pressure-dependent increase within the errors from 4.46 ns at 0.1 MPa to 4.63 ns at 240 MPa, consistent with the pressure-induced larger volume at 278 K (Tab. A.17).
Compared to the wild type, the artificial cavity generated by the L69A mutation also results in an increase in water-accessible surface area (Tab. 3.8). At ambient pressure, the artificial cavity buries a volume of $\approx$ 1 to 2 water molecules enclosed within the hydrophobic core by F51, M53, F58, L61, K65, and A69 (Fig. 3.16). Nearby are two cavities, the first below and enclosed by V50, F51, and A69, $\approx$ 4 water molecules, and the second between K65 and E72 with a volume of $\approx$ 6 water molecules (Fig. A.26). The largest cavity with a volume of $\approx$ 8 water molecules is located between L42, D46, V50, F51, and K73. Several smaller cavities occur at the C-terminal helix, one adjacent to F58, R55 and above K70, another between L42 and K70, and two peripheral ones next to K71. The pressure of up to 240 MPa closes the cavity on the L69A mutation site, resulting in a smaller number of water-accessible cavities but with a larger overall volume. The cavity at this position replaced by a branched, superficial one with a volume of $\approx$ 8 water molecules embedded between F51, M53, K65, A69, and E72. The

closure opens a cavity on the opposite side surrounded by the residues L42, F47, F58, and K70. The pressure-induced shift of the N-terminal helix α1 creates a void between itself and helix α2, enclosed by F47 and the positively charged K48, and R55 and the negatively charged D44. The peripheral cavities at the C-terminal helix merge under pressure to form a larger one between the K70 and K71. Nevertheless, the pressure-induced conformational changes lead to only a small decrease in the solvent-accessible surface area of about 1 % (Tab. 3.8). Moreover, the theoretically calculated molecular surface volume increases slightly together with the void volume, also about 1 % [152], which is in agreement with the pressure-induced volume increase obtained at 278 K (Tab. 3.4).
In summary, the elliptic phase boundary in the pressure-temperature phase space reveals that the unfolding of VHP35_L69A is mainly determined by an increase in entropy and a decreased in the volume of the entire system within the experimentally accessible temperature and pressure range. At the molecular level, this is accompanied by a slight increase in the molecular surface volume and the void volume of the folded state. The pressure-induce structural changes occur mainly within the backbone, resulting in different positions, especially within the KKEK motif and R55, L63, and K73. This is accompanied by an increased variation in flexibility within helix α1, particularly in D46, and helix α3.

4.3. Differences in pressure-dependent stability of VHP35 and VHP35_L69A

Compared with the wild type, the artificial void generated by the non-polar alanine mutation at the hydrophobic core residue leucine 69 in VHP35_L69A does not result in a significant change in the secondary structure and generally shows a similar topology of the three α-helices (Fig. 3.17). The sterically increased solvent-accessible surface area within the hydrophobic core leads to a reorganization of water molecules near the exposed hydrophobic side chains (Fig. 3.18, 3.16). The resulting reduced thermodynamic stability of the variant at 0.1 MPa (Tab. 3.1, 3.2), manifests in a reduced heat capacity difference between folded and unfolded protein because of the hydrophobic effect [153]. Since the mutation hardly affects the charge distribution of the protein, the ratio of thermal parameters remains relatively the same in the comparison of the two proteins [154]. Despite a slightly larger molecular surface volume of VHP35, substitution of the alanine residue results in a slightly larger relative void volume of $\approx$ 19.75 % for VHP35_L69A *versus* $\approx$ 19.25 % for VHP35 (Tab. 3.8). Therefore, the larger overall correlation time τ_{m} of 4.46 ns at ambient pressure of VHP35_L69A compare to the 3.91 ns of VHP35 might be explained by a larger hydration shell (Tab. A.17). This is consistent with the larger solvent-accessible surface area and a greater number and a larger overall volume of solvent-accessible voids (Fig. 3.18). Looking at the mean values of the two variants in comparison, except for the mean value of the R_2 rates, the local backbone dynamics remain the same on a time scale from picoseconds to nanoseconds at 0.1 MPa.

Within the temperature-pressure phase space of 278 to 368 K and 0.1 to 240 MPa, VHP35 shows a hyperbolic and VHP35_L69A an elliptic phase boundary (Fig. 3.9). In the observed pressure range, the wild type is stabilized and the variant is destabilized, essentially leading to the different shapes of the boundaries. Since Δc_p upon protein unfolding is always positive [155] and experimentally verified here for both VHP variants, the phase boundaries are defined by the sign of $\Delta\hat{\beta}$ (Tab. 3.5). The higher compressibility of the native state of VHP35 compared to the unfolded state gets lost by the L69A substitution, so that the entropic gain becomes dominant upon unfolding of VHP35_L69A.

At the molecular level, the respective pressure-dependent thermodynamic stabilities of the proteins are also reflected in conformational rearrangements at 278 K (Fig. 3.6, 3.19). At 240 MPa, pressure leads to different positions of the N-terminus of helix α1 *versus* the upper helix α3, resulting in a distance increase for VHP35 and a distance decrease for VHP35_L69A between residues D44 and L63. Comparison of the pressure-dependent conformers shows for both proteins that the structural changes occur mainly within the backbone but in different regions (Fig. 3.12, 3.15. One of the few exceptions that is also relevant in terms of stability is the pressure-induced change in the side chain of F47 in VHP35, which changes from a perpendicular position toward F58 to an energetically more favorable 45° position toward F51 and F58 [134]. Whereby the less favorable planar orientation of F47 toward F51 of VHP35_L69A is preserved. Combined with the nonlinear pressure-dependent deviations from the mean of the ^{1}H and ^{15}N shifts, structural changes occur at the edges of the helices, in the second turn, and especially at residues F51 and L61 in VHP35 (Fig. 3.24, Tab. A.9, A.10). In the case of VHP35_L69A, the local structural rearrangements occur within the helix α3 and the residue L63 and the positively charged R55 and K73 (Fig. 3.25, Tab. A.11, A.12). Since these residues are considered to exhibit larger deviations around water-excluded cavities [58, 144], it can be assumed that that those found here were also involved in the rearrangement or change of internal water-inaccessible cavities.

Local distance changes within the hydrogen bond network, reflected by the linear pressure-dependent coefficients of the ^{1}H and ^{15}N shifts, are found for both proteins mainly within helix α2 and especially helix α3. This essentially applies, also with respect to the sign, to the residues R55, L61, K65, and N68 of VHP35 and to residues R55, S56, and K73 of VHP35_L69A.

On a picosecond to nanosecond time scale and considering the mean, the R_1 rates decrease by the same order of magnitude for both proteins. With respect to the change of the mean values of the R_2 rates, the flexibility of VHP35 decreases and that of VHP35_L69A increases. In particular, the pressure-dependent variations of motions for VHP35 are localized within the turn between the first and the second helix, the helix α2, and the helix α3, and for VHP35_L69A within the helix α1 and helix α3 (Fig. 3.30), 3.31). Interestingly, the mean values of the heteronuclear NOE remain almost unchanged, but a more detailed analysis reveals a similar pattern of residues with larger deviations (E45, D46, F76), with exception of W64 of VHP35 and M53 of VHP35_L69A.

Taken together, these pressure-dependent structural and dynamic changes result in a more stable, larger molecular surface volume and void volume of VHP35 and, conversely, to a less stable reduced ones of VHP35_L69A (Tab. 3.8) [156]. Despite the increased volume, the wild type shows a smaller solvent-accessible surface area than the variant at 240 MPa. This is also reflected in the cavity landscape, where the wild type has more cavities, but with a smaller overall cavity volume than the variant (Fig. 3.20, 3.13, 3.16). In addition, the cavities of VHP35_L69A are more deeply embedded into the structure. Combined with a larger overall correlation time τ_{m} of VHP35_L69A, this implies a larger hydration shell than the wild type.
In this context, pressure generally leads to a redistribution of populations in proteins between the folded and unfolded states toward conformations with a smaller overall volume (Le Chatelier principle) due to the elimination of solvent-excluded voids by imperfect protein packing [24–28, 31–33]. This is accompanied by a weakening of hydrophobic interactions caused by the solvent water by increasing the solvent density on exposed surfaces in the unfolded state, and electrostriction of polar and charged groups [34–36]. In this process, hydrogen bonds are strengthened under pressure, while hydrophobic interactions are weakened by the penetration of water molecules into the inner cavities of the protein core [37–41]. At the pressures used here, up to 240 MPa, the equilibrium of a spherical monomeric system, such as VHP35 and the variant, can only be reversibly shifted to less populated, higher energy substates [1, 47–49]. However, in contrast to previous observations [157–159], opposing pressure-related structural and thermodynamic effects are evident for the two variants. In this regard, the pressure-dependent destabilization of VHP35_L69A at 278 K observed here reflects the generally observed pressure-destabilizing effects such as the volume decrease, increased solvation of hydrophobic groups caused by the alanine substitution, reduction of cavities inaccessible to water, and electrostriction of polar and charged groups. This results in the generally observed [22, 23, 128, 160, 161] elliptical phase boundary within the temperature-pressure phase space. In contrast, the hyperbolic phase boundary of VHP35, defined by a positive value of $\Delta\hat{\beta}$, is the result of opposing pressure effects that stabilize the system in contrast to those observed previously [50]. The pressure-stabilized conformer at 278 K is mainly characterized by a combination of a reduced hydration shell [149–151], a lager void volume, decreased solvent-accessible surface area and stabilizing side chain configuration within the three phenylalanins, but is less affected by electrostriction effects [162].

4.4. Conclusions and outlook

The hyperbolic phase boundary of VHP35 in the temperature-pressure phase space of 278 to 368 K and 0.1 to 240 MPa is the result of the pressure-induce stabilizing volumetric rearrangements including a smaller hydration shell leading to a higher compressibility within the native state compared to the unfolded state. The latter difference in compressibility disappears by the L69A substitution resulting in an elliptic phase boundary and entropic pressure-induced destabilization. At the molecular level, the pressure-dependent conformers at 278 K show distinct conformational differences relative to each

other within the backbone, especially in the C-terminal helix. In the case of VHP35, this corresponds to heterogeneously distributed structural and dynamic changes mainly within the helix $\alpha 2$ to helix $\alpha 3$ and in particular R55 and the hydrophobic core residues F47, F51, L61, K65. In contrast, the structural changes of VHP35_L69A occur mainly within the C-terminal helix $\alpha 3$, especially within the KKEK motif and R55, L63, and K73, accompanied by increased variation in flexibility within the helix $\alpha 1$, especially in D46, and helix $\alpha 3$. In particular, R55 plays an important role in pressure-dependent stability for both systems.
Further insight into the pressure-dependent structural changes could be gained by analyzing the corresponding chemical shifts of the side chains. Together with a more precise calculation of the cavity landscape with radii smaller than water molecules, a more accurate picture with respect to the nonlinear coefficients could be obtained. The thermodynamic parameters determined here, especially with respect to the pressure-dependent change in volume, could be verified by other methods such as CD spectroscopy, FRET or TTET. In this context, a more accurate determination of the hydrodynamic radius through measurements of the diffusion coefficient using NMR DOSY experiment would further elucidate the conclusions regarding the hydration shell.

References

[1] Neumaier, S. & Kiefhaber, T. Redefining the dry molten globule state of proteins. *Journal of Molecular Biology* **426**, 2520–2528 (2014).

[2] Fersht, A. R. *Structure and mechanism in protein science. A guide to enzyme catalysis and protein folding* (1999).

[3] Privalov, P. L. & Gill, S. J. Stability of Protein Structure and Hydrophobic Interaction. *Advances in Protein Chemistry* **39**, 191–234 (1988).

[4] Anfinsen, C. B., Haber, E., Sela, M. & White, F. H. The kinetics of formation of native ribonuclease during oxidation of the reduced polypeptide chain. *Proceedings of the National Academy of Sciences of the United States of America* **47**, 1309–1314 (1961).

[5] Anfinsen, C. B. Principles that govern protein folding. *Science* **181**, 223–230 (1973).

[6] Dill, K. A. & Chan, H. S. From levinthal to pathways to funnels. *Nature Structural Biology* **4**, 10–19 (1997).

[7] Dill, K. A., Ozkan, S. B., Shell, M. S. & Weikl, T. R. The protein folding problem. *Annual Review of Biophysics* **37**, 289–316 (2008).

[8] Senior, A. W. *et al.* Improved protein structure prediction using potentials from deep learning. *Nature* **577**, 706–710 (2020).

[9] Jumper, J. *Critical Assessment of Techniques for Protein Structure Prediction* (2020).

[10] Frauenfelder, H., Parak, F. & Young, R. D. Conformational substates in proteins. *Annual review of biophysics and biophysical chemistry* **17**, 451–479 (1988).

[11] Baxter, N. J., Hosszu, L. L., Waltho, J. P. & Williamson, M. P. Characterisation of low free-energy excited states of folded proteins. *Journal of Molecular Biology* **284**, 1625–1639 (1998).

[12] Korzhnev, D. M., Religa, T. L., Banachewicz, W., Fersht, A. R. & Kay, L. E. A transient and low-populated protein-folding intermediate at atomic resolution. *Science* **329**, 1312–1316 (2010).

[13] Nielsen, G., Jonker, H. R., Vajpai, N., Grzesiek, S. & Schwalbe, H. Kinase in motion: Insights into the dynamic nature of p38α by high-pressure NMR spectroscopic studies. *ChemBioChem* **14**, 1799–1806 (2013).

[14] Wüthrich, K. Protein structure determination in solution by NMR spectroscopy. *Journal of Biological Chemistry* **265**, 22059–22062 (1990).

[15] Winter, R. & Noll, F. *Methoden der Biophysikalischen Chemie* (1998).

[16] Jensen, M. R., Salmon, L., Nodet, G. & Blackledge, M. Defining conformational ensembles of intrinsically disordered and partially folded proteins directly from chemical shifts. *Journal of the American Chemical Society* **132**, 1270–1272 (2010).

[17] Kitahara, R. *et al.* High pressure NMR reveals active-site hinge motion of folate-bound Escherichia coli dihydrofolate reductase. *Biochemistry* **39**, 12789–12795 (2000).

[18] Boehr, D. D., McElheny, D., Dyson, H. J. & Wright, P. E. The dynamic energy landscape of dihydrofolate reductase catalysis. *Science* **313**, 1638–1642 (2006).

[19] Munte, C. E., Beck Erlach, M., Kremer, W., Koehler, J. & Kalbitzer, H. R. Distinct conformational states of the alzheimer β-amyloid peptide can be detected by high-pressure NMR spectroscopy. *Angewandte Chemie - International Edition* **52**, 8943–8947 (2013).

[20] Onuchic, J. N., Luthey-Schulten, Z. & Wolynes, P. G. Theory of Protein Folding: The Energy Landscape Perspective. *Annual Review of Physical Chemistry* **48**, 545–600 (1997).

[21] Dobson, C. M., Šali, A. & Karplus, M. Protein folding: A perspective from theory and experiment. *Angewandte Chemie - International Edition* **37**, 868–893 (1998).

[22] Hawley, S. A. Reversible Pressure-Temperature Denaturation of Chymotrypsinogen. *Biochemistry* **10**, 2436–2442 (1971).

[23] Lesch, H., Hecht, C. & Friedrich, J. Protein phase diagrams: The physics behind their elliptic shape. *Journal of Chemical Physics* **121**, 12671–12675 (2004).

[24] Chalikian, T. V. & Breslauer, K. J. On volume changes accompanying conformational transitions of biopolymers. *Biopolymers* **39**, 619–626 (1996).

[25] Kitahara, R., Yamada, H., Akasaka, K. & Wright, P. E. High pressure NMR reveals that apomyoglobin is an equilibrium mixture from the native to the unfolded. *Journal of Molecular Biology* **320**, 311–319 (2002).

[26] Akasaka, K. High pressure NMR study of proteins - Seeking roots for function, evolution, disease and food applications. *High Pressure Research* **30**, 453–457 (2010).

[27] Meersman, F. *et al.* High-pressure biochemistry and biophysics. *Reviews in Mineralogy and Geochemistry* **75**, 607–648 (2013).

[28] Silva, J. L. *et al.* High-pressure chemical biology and biotechnology. *Chemical Reviews* **114**, 7239–7267 (2014).

[29] Akasaka, K., Tezuka, T. & Yamada, H. Pressure-induced changes in the folded structure of lysozyme. *Journal of Molecular Biology* **271**, 671–678 (1997).

[30] Lopes, D., Grudzielanek, S., Vogtt, K. & Winter, R. Towards an understanding of the temperature/ pressure configurational and free-energy landscape of biomolecules. *Journal of Non-Equilibrium Thermodynamics* **32**, 41–97 (2007).

[31] Weber, G. & Drickamer, H. G. The effect of high pressure upon proteins and other biomolecules. *Quarterly Reviews of Biophysics* **16**, 89–112 (1983).

[32] Voloshin, V. P. *et al.* Volumetric properties of hydrated peptides: Voronoi-delaunay analysis of molecular simulation runs. *Journal of Physical Chemistry B* **115**, 14217–14228 (2011).

[33] Roche, J. & Royer, C. A. Lessons from pressure denaturation of proteins. *Journal of the Royal Society Interface* **15** (2018).

[34] Boonyaratanakornkit, B. B., Park, C. B. & Clark, D. S. Pressure effects on intra- and intermolecular interactions within proteins. *Biochimica et Biophysica Acta - Protein Structure and Molecular Enzymology* **1595**, 235–249 (2002).

[35] Rouget, J. B. *et al.* Size and sequence and the volume change of protein folding. *Journal of the American Chemical Society* **133**, 6020–6027 (2011).

[36] Luong, T. Q., Kapoor, S. & Winter, R. Pressure - A Gateway to Fundamental Insights into Protein Solvation, Dynamics, and Function. *ChemPhysChem* **16**, 3555–3571 (2015).

[37] Frye, K. J. & Royer, C. A. Probing the contribution of internal cavities to the volume change of protein unfolding under pressure. *Protein Science* **7**, 2217–2222 (1998).

[38] Inoue, K. *et al.* Pressure-induced local unfolding of the Ras binding domain of RalGDS. *Nature Structural Biology* **7**, 547–550 (2000).

[39] Eriksen, T. A., Wright, D. M., Purslow, P. P. & Duance, V. C. Filling a cavity dramatically increases pressure stability of the c-Myb R2 subdomain. *Proteins: Structure, Function and Genetics* **45**, 96–101 (2001).

[40] Ando, N. *et al.* Structural and thermodynamic characterization of T4 lysozyme mutants and the contribution of internal cavities to pressure denaturation. *Biochemistry* **47**, 11097–11109 (2008).

[41] Roche, J. *et al.* Cavities determine the pressure unfolding of proteins. *Proceedings of the National Academy of Sciences of the United States of America* **109**, 6945–6950 (2012).

[42] Urbauer, J. L., Ehrhardt, M. R., Bieber, R. J., Flynn, P. F. & Wand, A. J. High-resolution triple-resonance NMR spectroscopy of a novel calmodulin·peptide complex at kilobar pressures. *Journal of the American Chemical Society* **118**, 11329–11330 (1996).

[43] Yamada, H. *et al.* Pressure-resisting cell for high-pressure, high-resolution nuclear magnetic resonance measurements at very high magnetic fields. *Review of Scientific Instruments* **72**, 1463–1471 (2001).

[44] Arnold, M. R., Kalbitzer, H. R. & Kremer, W. High-sensitivity sapphire cells for high pressure NMR spectroscopy on proteins. *Journal of Magnetic Resonance* **161**, 127–131 (2003).

[45] Peterson, R. W. & Wand, A. J. Self-contained high-pressure cell, apparatus, and procedure for the preparation of encapsulated proteins dissolved in low viscosity fluids for nuclear magnetic resonance spectroscopy. *Review of Scientific Instruments* **76** (2005).

[46] Beck Erlach, M. *et al.* Ceramic cells for high pressure NMR spectroscopy of proteins. *Journal of Magnetic Resonance* **204**, 196–199 (2010).

[47] Kitahara, R. & Akasaka, K. Close identity of a pressure-stabilized intermediate with a kinetic intermediate in protein folding. *Proceedings of the National Academy of Sciences of the United States of America* **100**, 3167–3172 (2003).

[48] Li, H. & Akasaka, K. Conformational fluctuations of proteins revealed by variable pressure NMR. *Biochimica et Biophysica Acta - Proteins and Proteomics* **1764**, 331–345 (2006).

[49] Akasaka, K. Probing conformational fluctuation of proteins by pressure perturbation. *Chemical Reviews* **106**, 1814–1835 (2006).

[50] Klamt, A., Nagarathinam, K., Tanabe, M., Kumar, A. & Balbach, J. Hyperbolic Pressure-Temperature Phase Diagram of the Zinc-Finger Protein apoKti11 Detected by NMR Spectroscopy. *Journal of Physical Chemistry B* **123**, 792–801 (2019).

[51] Szyperski, T., Mills, J. L., Perl, D. & Balbach, J. Combined NMR-observation of cold denaturation in supercooled water and heat denaturation enables accurate measurement of ΔCp of protein unfolding. *European Biophysics Journal* **35**, 363–366 (2006).

[52] Wagner, G., Pardi, A. & Wüthrich, K. Hydrogen Bond Length and 1H NMR Chemical Shifts in Proteins. *Journal of the American Chemical Society* **105**, 5948–5949 (1983).

[53] Asakura, T., Taoka, K., Demura, M. & Williamson, M. P. The relationship between amide proton chemical shifts and secondary structure in proteins. *Journal of Biomolecular NMR* **6**, 227–236 (1995).

[54] Eliezer, D., Yao, J., Jane Dyson, H. & Wright, P. E. Structural and dynamic characterization of partially folded states of apomyoglobin and implications for protein folding. *Nature Structural Biology* **5**, 148–155 (1998).

[55] Akasaka, K. & Li, H. Low-Lying Excited States of Proteins Revealed from Nonlinear Pressure Shifts in 1H and 15N NMR. *Biochemistry* **40**, 8665–8671 (2001).

[56] Kalbitzer, H. R., Spoerner, M., Ganser, P., Hozsa, C. & Kremer, W. Fundamental link between folding states and functional states of proteins. *Journal of the American Chemical Society* **131**, 16714–16719 (2009).

[57] Nisius, L. & Grzesiek, S. Key stabilizing elements of protein structure identified through pressure and temperature perturbation of its hydrogen bond network. *Nature Chemistry* **4**, 711–717 (2012).

[58] Kitahara, R., Hata, K., Li, H., Williamson, M. P. & Akasaka, K. Pressure-induced chemical shifts as probes for conformational fluctuations in proteins. *Progress in Nuclear Magnetic Resonance Spectroscopy* **71**, 35–58 (2013).

[59] Beck Erlach, M. *et al.* Relationship between nonlinear pressure-induced chemical shift changes and thermodynamic parameters. *Journal of Physical Chemistry B* **118**, 5681–5690 (2014).

[60] La Penna, G., Mori, Y., Kitahara, R., Akasaka, K. & Okamoto, Y. Modeling 15N NMR chemical shift changes in protein backbone with pressure. *Journal of Chemical Physics* **145** (2016).

[61] McKnight, C. J., Doering, D. S., Matsudaira, P. T. & Kim, P. S. A thermostable 35-residue subdomain within villin headpiece. *Journal of Molecular Biology* **260**, 126–134 (1996).

[62] McKnight, C. J., Matsudaira, P. T. & Kim, P. S. NMR structure of the 35-residue villin headpiece subdomain. *Nature Structural Biology* **4**, 180–184 (1997).

[63] Vardar, D., Buckley, D. A., Frank, B. S. & McKnight, C. J. NMR structure of an F-actin-binding 'headpiece' motif from villin. *Journal of Molecular Biology* **294**, 1299–1310 (1999).

[64] Frank, B. S., Vardar, D., Buckley, D. A. & McKnight, C. J. The role of aromatic residues in the hydrophobic core of the villin headpiece subdomain. *Protein Science* **11**, 680–687 (2009).

[65] Chiu, T. K. *et al.* High-resolution x-ray crystal structures of the villin headpiece subdomain, an ultrafast folding protein. *Proceedings of the National Academy of Sciences of the United States of America* **102**, 7517–7522 (2005).

[66] Bretscher, A. & Weber, K. Villin: The major microfilament-associated protein of the intestinal microvillus. *Proceedings of the National Academy of Sciences of the United States of America* **76**, 2321–2325 (1979).

[67] Glenney, J. R. & Weber, K. Calcium control of microfilaments: uncoupling of the F-actin-severing and -bundling activity of villin by limited proteolysis in vitro. *Proceedings of the National Academy of Sciences of the United States of America* **78**, 2810–2814 (1981).

[68] Friederich, E., Vancompernolle, K., Louvard, D. & Vandekerckhove, J. Villin function in the organization of the actin cytoskeleton. Correlation of in vivo effects to its biochemical activities in vitro. *Journal of Biological Chemistry* **274**, 26751–26760 (1999).

[69] Bazari, W. L. *et al.* Villin sequence and peptide map identify six homologous domains. *Proceedings of the National Academy of Sciences of the United States of America* **85**, 4986–4990 (1988).

[70] Friederich, E. *et al.* An actin-binding site containing a conserved motif of charged amino acid residues is essential for the morphogenic effect of villin. *Cell* **70**, 81–92 (1992).

[71] Meng, J. *et al.* High-resolution crystal structures of villin headpiece and mutants with reduced F-actin binding activity. *Biochemistry* **44**, 11963–11973 (2005).

[72] Wang, M. *et al.* Dynamic NMR line-shape analysis demonstrates that the villin headpiece subdomain folds on the microsecond time scale. *Journal of the American Chemical Society* **125**, 6032–6033 (2003).

[73] Tang, Y., Grey, M. J., McKnight, C. J., Palmer, A. G. & Raleigh, D. P. Multistate folding of the villin headpiece domain. *Journal of Molecular Biology* **355**, 1066–1077 (2006).

[74] Bi, Y. *et al.* Rational design, structural and thermodynamic characterization of a hyperstable variant of the villin headpiece helical subdomain. *Biochemistry* **46**, 7497–7505 (2007).

[75] Reiner, A., Henklein, P. & Kiefhaber, T. An unlocking/relocking barrier in conformational fluctuations of villin headpiece subdomain. *Proceedings of the National Academy of Sciences of the United States of America* **107**, 4955–4960 (2010).

[76] Hosseini, A. S., Pace, C. J., Esposito, A. A. & Gao, J. Non-additive stabilization by halogenated amino acids reveals protein plasticity on a sub-angstrom scale. *Protein Science* **26**, 2051–2058 (2017).

[77] Vugmeyster, L. & McKnight, C. J. Slow motions in chicken villin headpiece subdomain probed by cross-correlated NMR relaxation of amide NH bonds in successive residues. *Biophysical Journal* **95**, 5941–5950 (2008).

[78] Cornilescu, G. *et al.* Solution structure of a small protein containing a fluorinated side chain in the core. *Protein Science* **16**, 14–19 (2006).

[79] Xiao, S., Bi, Y., Shan, B. & Raleigh, D. P. Analysis of core packing in a cooperatively folded miniature protein: The ultrafast folding villin headpiece helical subdomain. *Biochemistry* **48**, 4607–4616 (2009).

[80] Bunagan, M. R., Gao, J., Kelly, J. W. & Gai, F. Probing the folding transition state structure of the villin headpiece subdomain via side chain and backbone mutagenesis. *Journal of the American Chemical Society* **131**, 7470–7476 (2009).

[81] Vugmeyster, L. *et al.* Slow motions in the hydrophobic core of chicken villin headpiece subdomain and their contributions to configurational entropy and heat capacity from solid-state deuteron NMR measurements. *Biochemistry* **50**, 10637–10646 (2011).

[82] Nagarajan, S., Xiao, S., Raleigh, D. P. & Brian Dyer, R. Heterogeneity in the Folding of Villin Headpiece Subdomain HP36. *Journal of Physical Chemistry B* **122**, 11640–11648 (2018).

[83] Kubelka, J., Eaton, W. A. & Hofrichter, J. Experimental tests of villin subdomain folding simulations. *Journal of Molecular Biology* **329**, 625–630 (2003).

[84] Buscaglia, M., Kubelka, J., Eaton, W. A. & Hofrichter, J. Determination of ultrafast protein folding rates from loop formation dynamics. *Journal of Molecular Biology* **347**, 657–664 (2005).

[85] Brewer, S. H. *et al.* Effect of modulating unfolded state structure on the folding kinetics of the villin headpiece subdomain. *Proceedings of the National Academy of Sciences of the United States of America* **102**, 16662–16667 (2005).

[86] Kubelka, J., Chiu, T. K., Davies, D. R., Eaton, W. A. & Hofrichter, J. Sub-microsecond Protein Folding. *Journal of Molecular Biology* **359**, 546–553 (2006).

[87] Lei, H., Wu, C., Liu, H. & Duan, Y. Folding free-energy landscape of villin headpiece subdomain from molecular dynamics simulations. *Proceedings of the National Academy of Sciences of the United States of America* **104**, 4925–4930 (2007).

[88] Žoldák, G., Stigler, J., Pelz, B., Li, H. & Rief, M. Ultrafast folding kinetics and cooperativity of villin headpiece in single molecule autocorrelation force spectroscopy. *Proceedings of the National Academy of Sciences of the United States of America* **110**, 18156–61 (2013).

[89] Harpole, K. W. *et al.* The unusual internal motion of the villin headpiece subdomain. *Protein Science* **25**, 423–432 (2016).

[90] Piana, S., Lindorff-Larsen, K. & Shaw, D. E. Protein folding kinetics and thermodynamics from atomistic simulation. *Proceedings of the National Academy of Sciences of the United States of America* **109**, 17845–17850 (2012).

[91] Banushkina, P. V. & Krivov, S. V. High-resolution free-energy landscape analysis of α-helical protein folding: HP35 and its double mutant. *Journal of Chemical Theory and Computation* **9**, 5257–5266 (2013).

[92] Mori, T. & Saito, S. Molecular mechanism behind the fast folding/unfolding transitions of villin headpiece subdomain: Hierarchy and heterogeneity. *Journal of Physical Chemistry B* **120**, 11683–11691 (2016).

[93] Kubelka, J., Henry, E. R., Cellmer, T., Hofrichter, J. & Eaton, W. A. Chemical, physical, and theoretical kinetics of an ultrafast folding protein. *Proceedings of the National Academy of Sciences of the United States of America* **105**, 18655–18662 (2008).

[94] Henry, E. R., Best, R. B. & Eaton, W. A. Comparing a simple theoretical model for protein folding with all-atom molecular dynamics simulations. *Proceedings of the National Academy of Sciences of the United States of America* **110**, 17880–17885 (2013).

[95] Wang, E., Tao, P., Wang, J. & Xiao, Y. A novel folding pathway of the villin headpiece subdomain HP35. *Physical Chemistry Chemical Physics* **21**, 18219–18226 (2019).

[96] Klamt, A. *NMR - Spektroskopische Stabilitäts - und Strukturuntersuchungen an Proteinen unter Hochdruck*. Ph.D. thesis (2015).

[97] Mori, S., Abeygunawardana, C., Johnson, M. O. & van Zul, P. C. M. Improved sensitivity of HSQC spectra of exchanging protons at short interscan delays using a new fast HSQC (fHSQC) detection scheme that avoids water saturation. *Journal os Magnetic Ressonance* **108**, 94–98 (1995).

[98] Ikura, M., Kay, L. E. & Bax, A. A Novel Approach for Sequential Assignment of 1H, 13C, and 15N Spectra of Larger Proteins: Heteronuclear Triple-Resonance Three-Dimensional NMR Spectroscopy. Application to Calmodulin. *Biochemistry* **29**, 4659–4667 (1990).

[99] Salzmann, M., Wider, G., Pervushin, K., Senn, H. & Wüthrich, K. TROSY-type triple-resonance experiments for sequential NMR assignments of large proteins. *Journal of the American Chemical Society* **121**, 844–848 (1999).

[100] Grzesiek, S. & Bax, A. Improved 3D triple-resonance NMR techniques applied to a 31 kDa protein. *Journal of Magnetic Resonance (1969)* **96**, 432–440 (1992).

[101] Davis, A. L., Keeler, J., Laue, E. D. & Moskau, D. Experiments for recording pure-absorption heteronuclear correlation spectra using pulsed field gradients. *Journal of Magnetic Resonance (1969)* **98**, 207–216 (1992).

[102] Vuister, G. W. & Bax, A. Resolution Enhancement and Spectral Editing of Uniformly 13C- Enriched Proteins by Homonuclear Broadband 13C Decoupling. *Journal of Magnetic Resonance* **98**, 428–435 (1992).

[103] Bax, A., Clore, G. M. & Gronenborn, A. M. 1H1H correlation via isotropic mixing of 13C magnetization, a new three-dimensional approach for assigning 1H and 13C spectra of 13C-enriched proteins. *Journal of Magnetic Resonance (1969)* **88**, 425–431 (1990).

[104] Dayie, K. T. & Wagner, G. Relaxation-rate measurements for 15N-1H groups with pulsed-feld gradients and preservation of coherence pathways. *Journal of Magnetic Resonance* **111**, 121–126 (1994).

[105] Loria, J. P., Rance, M. & Palmer, A. G. A relaxation-compensated Carr-Purcell-Meiboom-Gill sequence for characterizing chemical exchange by NMR spectroscopy. *Journal of the American Chemical Society* **121**, 2331–2332 (1999).

[106] Keller, R. *Optimizing the process of nuclear magnetic resonance spectrum analysis and computer aided resonance assignment*. Ph.D. thesis (2004). URL `http://cara.nmr.ch/`.

[107] Ahlner, A., Carlsson, M., Jonsson, B. H. & Lundström, P. PINT: A software for integration of peak volumes and extraction of relaxation rates. *Journal of Biomolecular NMR* **56**, 191–202 (2013).

[108] Cavanagh, J. *Protein NMR Spectroscopy: Principles and Practice* (Academic Press, 2006), 2 edn.

[109] Piotto, M., Saudek, V. & Sklenář, V. Gradient-tailored excitation for single-quantum NMR spectroscopy of aqueous solutions. *Journal of Biomolecular NMR* **2**, 661–665 (1992).

[110] Marion, D., Ikura, M., Tschudin, R. & Bax, A. Rapid recording of 2D NMR spectra without phase cycling. Application to the study of hydrogen exchange in proteins. *Journal of Magnetic Resonance (1969)* **85**, 393–399 (1989).

[111] Sattler, M., Schleucher, J. & Griesinger, C. Heteronuclear multidimensional NMR experiments for the structure determination of proteins in solution employing pulsed field gradients. *Progress in Nuclear Magnetic Resonance Spectroscopy* **34**, 93–158 (1999).

[112] Ulrich, E. L. *et al.* BioMagResBank. *Nucleic Acids Research* **36**, 402–408 (2008).

[113] Kempf, J. G. & Loria, J. P. Protein dynamics from solution NMR: Theory and applications. *Cell Biochemistry and Biophysics* **37**, 187–211 (2002).

[114] Zeeb, M. & Balbach, J. Protein folding studied by real-time NMR spectroscopy. *Methods* **34**, 65–74 (2004).

[115] Abragam, A. *The Principles of Nuclear Magnetism* (1989).

[116] Hiyama, Y., Niu, C. H., Silverton, J. V., Bavoso, A. & Torchia, D. A. Determination of 15N Chemical Shift Tensor via 15N-2H Dipolar Coupling in Boc-glycylglycyl[15N]glycine Benzyl Ester. *Journal of the American Chemical Society* **110**, 2378–2383 (1988).

[117] Weininger, U., Diehl, C. & Akke, M. 13C relaxation experiments for aromatic side chains employing longitudinal-and transverse-relaxationoptimized NMR spectroscopy. *Journal of Biomolecular NMR* **53**, 181–190 (2012).

[118] Macura, S. & Ernst, R. R. Elucidation of cross relaxation in liquids by two-dimensional N.M.R. spectroscopy. *Molecular Physics* 95–117 (1980).

[119] Jeener, J., Meier, B. H., Bachmann, P. & Ernst, R. R. Investigation of exchange processes by two-dimensional NMR spectroscopy. *The Journal of Chemical Physics* **71**, 4546–4553 (1979).

[120] Kalk, A. & Berendsen, H. J. Proton magnetic relaxation and spin diffusion in proteins. *Journal of Magnetic Resonance (1969)* **24**, 343–366 (1976).

[121] Rieping, W., Bardiaux, B., Bernard, A., Malliavin, T. E. & Nilges, M. ARIA2: Automated NOE assignment and data integration in NMR structure calculation. *Bioinformatics* **23**, 381–382 (2007).

[122] Brünger, A. T. *et al.* Crystallography and NMR system: A new software suite for macromolecular structure determination. *Acta Crystallographica Section D: Biological Crystallography* **54**, 905–921 (1998).

[123] Shen, Y., Delaglio, F., Cornilescu, G. & Bax, A. TALOS+: A hybrid method for predicting protein backbone torsion angles from NMR chemical shifts. *Journal of Biomolecular NMR* **44**, 213–223 (2009).

[124] Laskowski, R. A., Rullmann, J. A. C., MacArthur, M. W., Kaptein, R. & Thornton, J. M. AQUA and PROCHECK-NMR: Programs for checking the quality of protein structures solved by NMR. *Journal of Biomolecular NMR* **8**, 477–486 (1996).

[125] Chen, C. R. & Makhatadze, G. I. ProteinVolume: Calculating molecular van der Waals and void volumes in proteins. *BMC Bioinformatics* **16**, 1–6 (2015).

[126] Ramachandran, G. N., Ramakrishnan, C. & Sasisekharan, V. Stereochemistry of polypeptide chain configurations. *Journal of Molecular Biology* **7**, 95–99 (1963).

[127] Wishart, D. S., Sykes, B. D. & Richards, F. M. The Chemical Shift Index : A Fast and Simple Method for the Assignment of Protein Secondary Structure Through NMR Spectroscopy. *Biochemistry* **31**, 1647–1651 (1992).

[128] Smeller, L. Pressure-temperature phase diagrams of biomolecules. *Biochimica et Biophysica Acta - Protein Structure and Molecular Enzymology* **1595**, 11–29 (2002).

[129] Balny, C., Masson, P. & Heremans, K. High pressure effects on biological macromolecules: From structural changes to alteration of cellular processes. *Biochimica et Biophysica Acta - Protein Structure and Molecular Enzymology* **1595**, 3–10 (2002).

[130] Baskaran, K., Brunner, K., Munte, C. E. & Kalbitzer, H. R. Mapping of protein structural ensembles by chemical shifts. *Journal of Biomolecular NMR* **48**, 71–83 (2010).

[131] Akasaka, K. Highly fluctuating protein structures revealed by variable-pressure nuclear magnetic resonance. *Biochemistry* **42**, 10875–10885 (2003).

[132] Wickstrom, L., Bi, Y., Hornak, V., Raleigh, D. P. & Simmerling, C. Reconciling the solution and X-ray structures of the villin headpiece helical subdomain: Molecular dynamics simulations and double mutant cycles reveal a stabilizing cation-π interaction. *Biochemistry* **46**, 3624–3634 (2007).

[133] Vermeulen, W. *et al.* Solution structures of the C-terminal headpiece subdomains of human villin and advillin, evaluation of headpiece F-actin-binding requirements. *Protein science : a publication of the Protein Society* **13**, 1276–1287 (2004).

[134] Hunter, C. A., Singh, J. & Thornton, J. M. Π-Π Interactions: the Geometry and Energetics of Phenylalanine-Phenylalanine Interactions in Proteins. *Journal of Molecular Biology* **218**, 837–846 (1991).

[135] Neuman, R. C., Kauzmann, W. & Zipp, A. Pressure dependence of weak acid lonization in aqueous buffers. *Journal of Physical Chemistry* **77**, 2687–2691 (1973).

[136] Li, H., Yamada, H. & Akasaka, K. Effect of pressure on individual hydrogen bonds in proteins. Basic pancreatic trypsin inhibitor. *Biochemistry* **37**, 1167–1173 (1998).

[137] Asakawa, N. *et al. Structural Studies of Hydrogen-bonded Peptides and Polypeptides by Solid-state NMR*, vol. 35 (1998).

[138] Kalbitzer, H. R. *et al.* 15N and 1H NMR study of histidine containing protein (hpr) from staphylococcus carnosus at high pressure. *Protein Science* **9**, 693–703 (2000).

[139] Xu, X. P. & Case, D. A. Probing multiple effects on 15N, 13Cα, 13Cβ, and 13C' chemical shifts in peptides using density functional theory. *Biopolymers* **65**, 408–423 (2002).

[140] Arnold, M. R., Kremer, W., Lüdemann, H. D. & Kalbitzer, H. R. 1H-NMR parameters of common amino acid residues measured in aqueous solutions of the linear tetrapeptides Gly-Gly-X-Ala at pressures between 0.1 and 200 MPa. *Biophysical Chemistry* **96**, 129–140 (2002).

[141] Koehler, J. *et al.* Pressure Dependence of 15N Chemical Shifts in Model Peptides Ac-Gly-Gly-X-Ala-NH2. *Materials* **5**, 1774–1786 (2012).

[142] Marchi, M. & Akasaka, K. Simulation of hydrated BPTI at high pressure: Changes in hydrogen bonding and its relation with NMR experiments. *Journal of Physical Chemistry B* **105**, 711–714 (2001).

[143] Akasaka, K. *et al.* Pressure response of protein backbone structure. Pressure-induced amide 15N chemical shifts in BPTI. *Protein science : a publication of the Protein Society* **8**, 1946–1953 (1999).

[144] Narayanan, S. P. *et al.* Structural transitions in full-length human prion protein detected by xenon as probe and spin labeling of the N-terminal domain. *Scientific Reports* **6**, 1–17 (2016).

[145] Erlach, M. B. *et al.* Pressure dependence of backbone chemical shifts in the model peptides Ac-Gly-Gly-Xxx-Ala-NH2. *Journal of Biomolecular NMR* **65**, 65–77 (2016).

[146] Vugmeyster, L., Trott, O., James McKnight, C., Raleigh, D. P. & Palmer, A. G. Temperature-dependent dynamics of the villin headpiece helical subdomain, an unusually small thermostable protein. *Journal of Molecular Biology* **320**, 841–854 (2002).

[147] Kay, L. E., Torchia, D. A. & Bax, A. Backbone Dynamics of Proteins As Studied by 15N Inverse Detected Heteronuclear NMR Spectroscopy: Application to Staphylococcal Nuclease. *Biochemistry* **28**, 8972–8979 (1989).

[148] Vugmeyster, L. & Ostrovsky, D. Temperature dependence of fast carbonyl backbone dynamics in chicken villin headpiece subdomain. *Journal of Biomolecular NMR* **50**, 119–127 (2011).

[149] Smolin, N. & Winter, R. Effect of temperature, pressure, and cosolvents on structural and dynamic properties of the hydration shell of SNase: A molecular dynamics computer simulation study. *Journal of Physical Chemistry B* **112**, 997–1006 (2008).

[150] Pattni, V. & Heyden, M. Pressure Effects on Protein Hydration Water Thermodynamics. *Journal of Physical Chemistry B* **123**, 6014–6022 (2019).

[151] Chalikian, T. V. Does the release of hydration water come with a Gibbs energy contribution? *Journal of Chemical Thermodynamics* **158**, 106409 (2021).

[152] Yamada, H., Nagae, T. & Watanabe, N. High-pressure protein crystallography of hen egg-white lysozyme. *Acta Crystallographica Section D: Biological Crystallography* **71**, 742–753 (2015).

[153] Buchner, J. & Kiefhaber, T. *Protein Folding Handbook*, vol. 1 (Wiley-VCH: Weinheim, 2008).

[154] Lazaridis, T. & Karplus, M. Thermodynamics of protein folding: A microscopic view. *Biophysical Chemistry* **100**, 367–395 (2003).

[155] Privalov, P. L. Stability of proteins: Small Globular Proteins. *Advances in Protein Chemistry* **33**, 167–241 (1979).

[156] Kurpiewska, K. *et al.* Structural investigation of ribonuclease A conformational preferences using high pressure protein crystallography. *Chemical Physics* **468**, 53–62 (2016).

[157] Collins, M. D., Hummer, G., Quillin, M. L., Matthews, B. W. & Gruner, S. M. Cooperative water filling of a nonpolar protein cavity observed by high-pressure crystallography and simulation. *Proceedings of the National Academy of Sciences of the United States of America* **102**, 16668–16671 (2005).

[158] Collins, M. D., Quillin, M. L., Hummer, G., Matthews, B. W. & Gruner, S. M. Structural Rigidity of a Large Cavity-containing Protein Revealed by High-pressure Crystallography. *Journal of Molecular Biology* **367**, 752–763 (2007).

[159] Xue, M. *et al.* How internal cavities destabilize a protein. *Proceedings of the National Academy of Sciences of the United States of America* **116**, 21031–21036 (2019).

[160] Panick, G. *et al.* Exploring the temperature-pressure phase diagram of staphylococcal nuclease. *Biochemistry* **38**, 4157–4164 (1999).

[161] Maeno, A., Matsuo, H. & Akasaka, K. The pressure-temperature phase diagram of hen lysozyme at low pH. *Biophysics* **5**, 1–9 (2009).

[162] Dreydoppel, M. *et al.* Equilibrium and Kinetic Unfolding of GB1: Stabilization of the Native State by Pressure. *Journal of Physical Chemistry B* **122**, 8846–8852 (2018).

List of Tables

List of Figures

A. Appendix

A.1. Thermodynamic parameters as a function of pressure

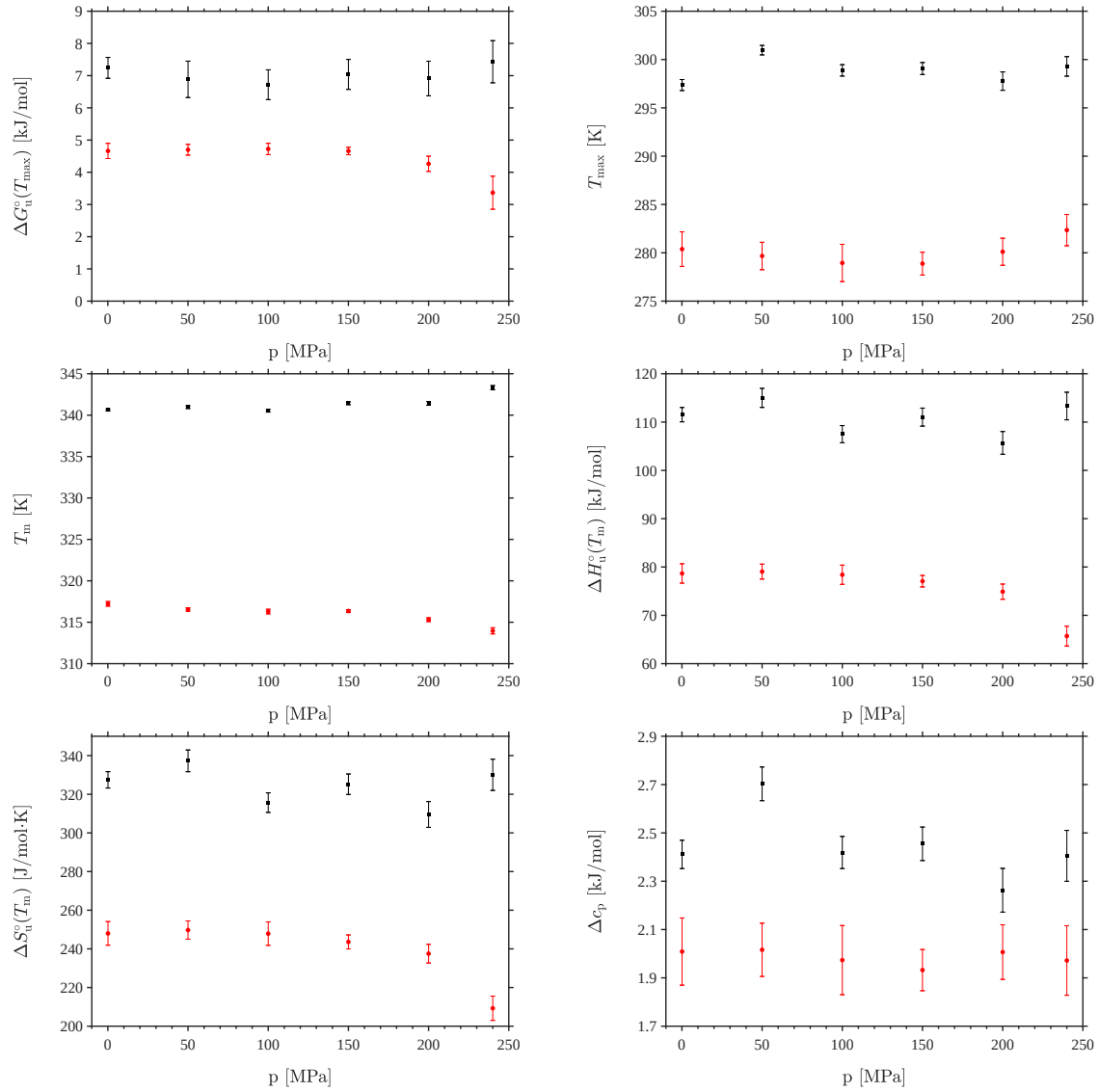

Figure A.1.: **Thermodynamic parameters of VHP35 (*black* squares) and VHP35_L69A (*red* circles) as a function of pressure (Tab. 3.1, 3.2):** Error bars are partially within the symbol size.

A.2. 1D ^{1}H NMR spectra

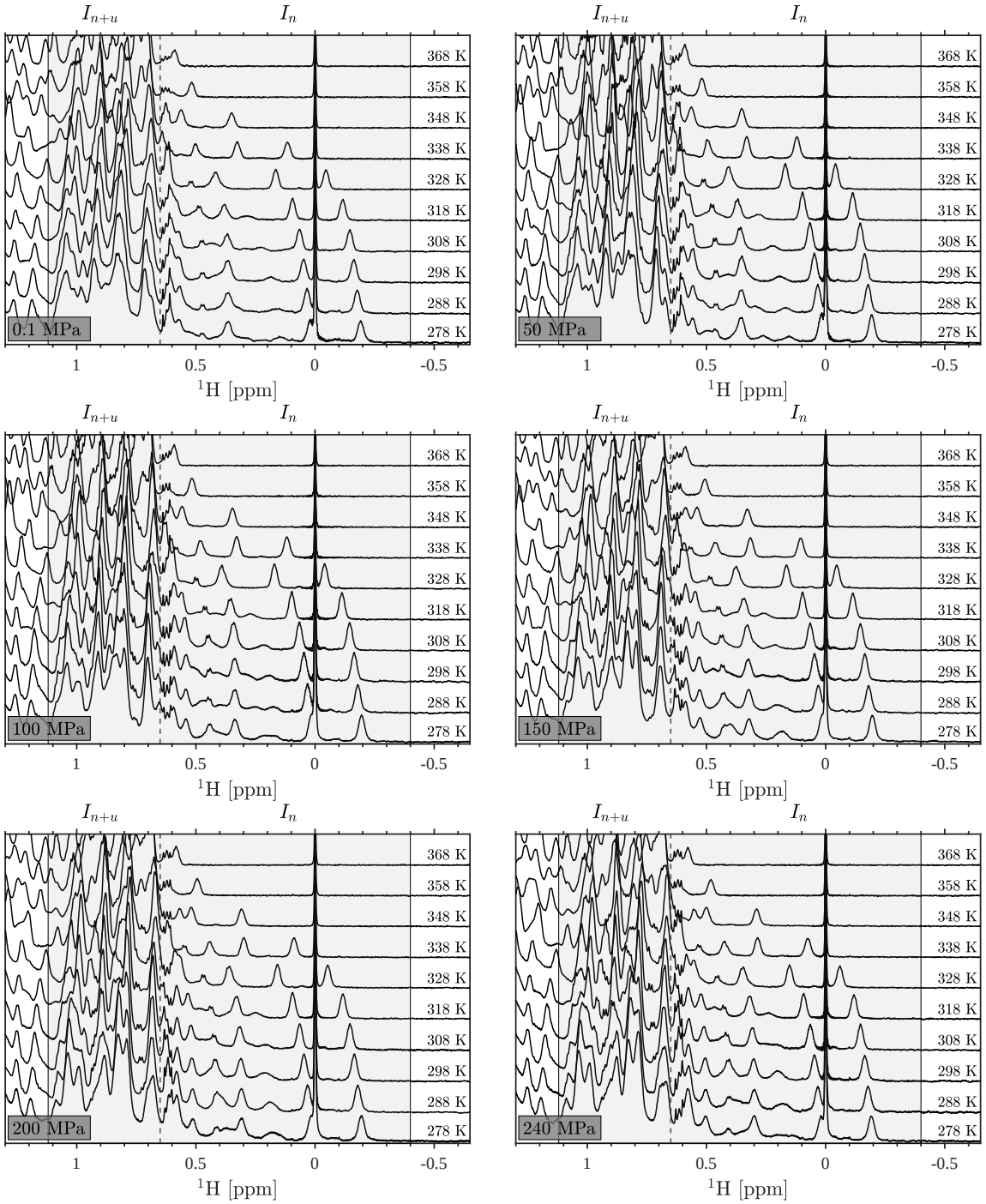

Figure A.2.: **High-field region of the 1D ^{1}H NMR spectra of VHP35 at different temperatures and pressures:** The *grey* area (-0.4 to 1.105 ppm) shows the intervals of $I_{\mathrm{n+u}}$ and the solely native region I_{n} (Eq. 2.35), subdivided by the *dashed* line (at 0.65 ppm). The native region contains the proton resonances of L61(Hδ_1) and V50(Hγ_2). Spectra are referenced to DSS-d_6 set at 0 ppm.

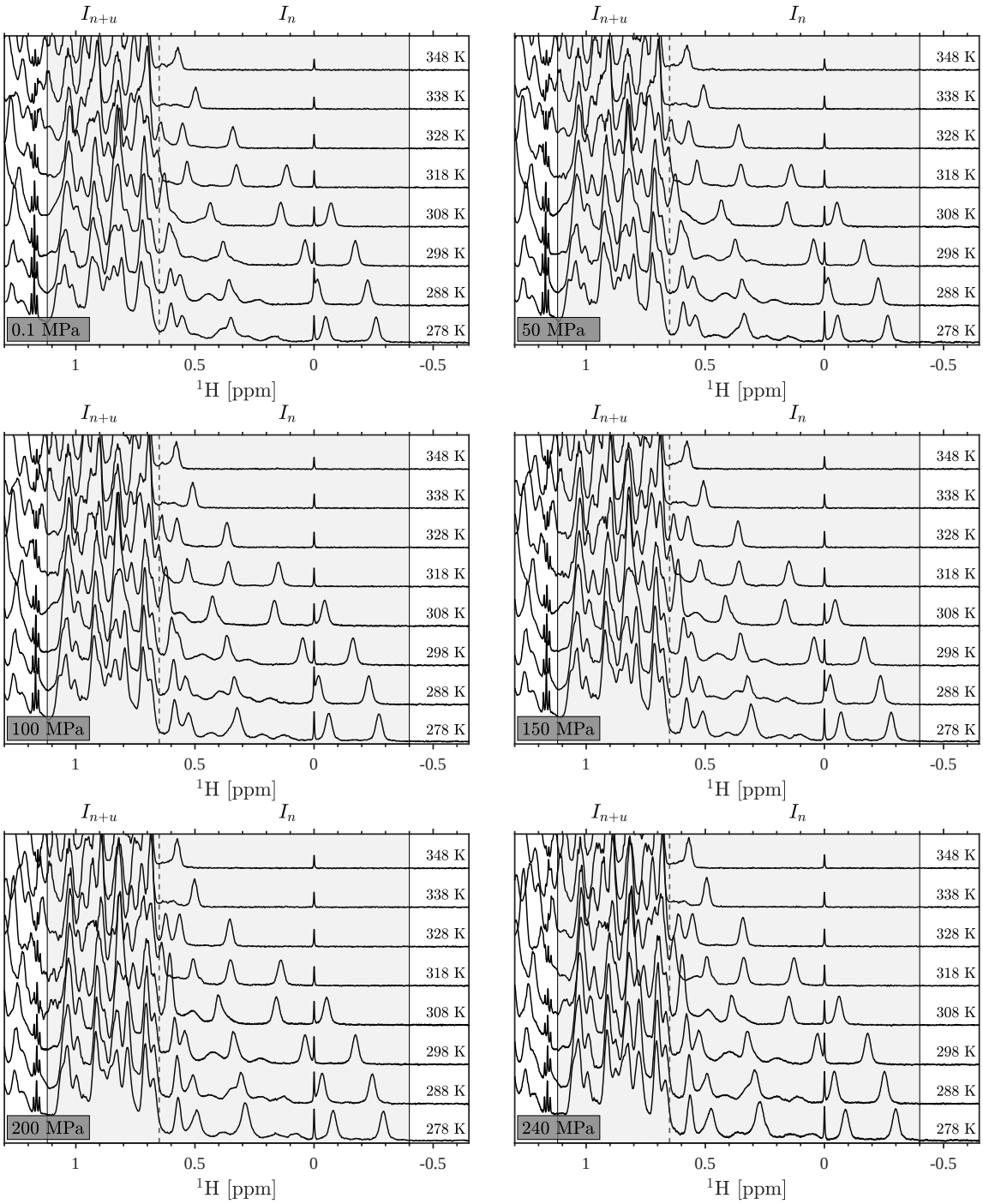

Figure A.3.: **High-field region of the 1D ^{1}H NMR spectra of VHP35_L69A at different temperatures and pressures:** The *grey* area (-0.4 to 1.12 ppm) shows the intervals of $I_{\mathrm{n+u}}$ and the solely native region I_{n} (Eq. 2.35), subdivided by the *dashed* line (at 0.65 ppm). The native region contains the proton resonances of L61(Hδ_1) and V50(Hγ_2). Spectra are referenced to DSS-d_6 set at 0 ppm.

A.3. ΔG°_u, ΔH°_u and ΔS°_u as a function of temperature

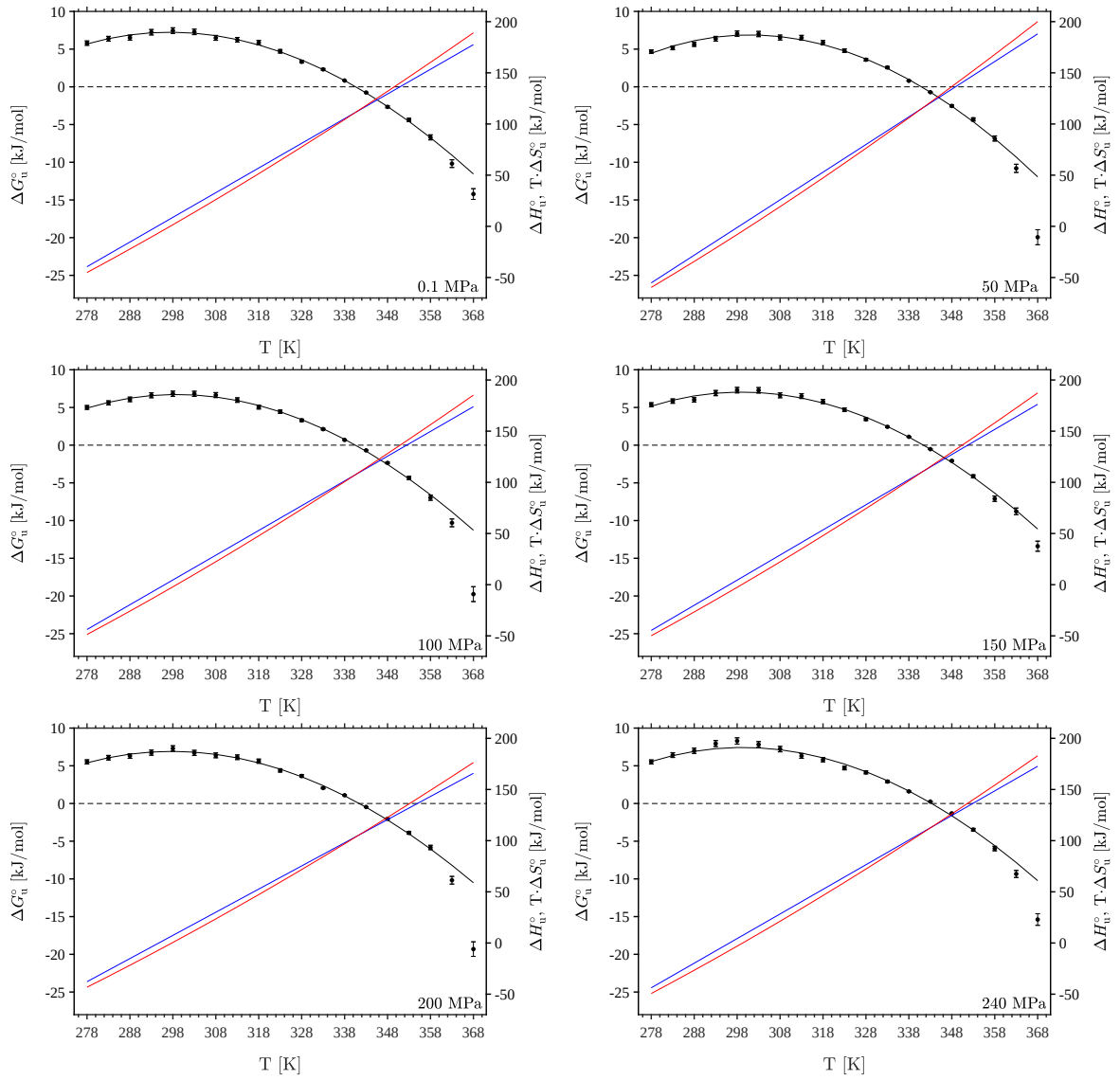

Figure A.4.: **The Gibbs free energy (ΔG°_u), enthalpy (ΔH°_u) and entropy (ΔS°_u) of VHP35 as a function of temperature at different pressures:** The change of ΔG°_u is determined by the equation 2.37 and the error was assumed to be 5 %. The fits of ΔG°_u (*black*), ΔH°_u (*blue*) and ΔS°_u (*red*) are given by equation 2.40 and 2.39.

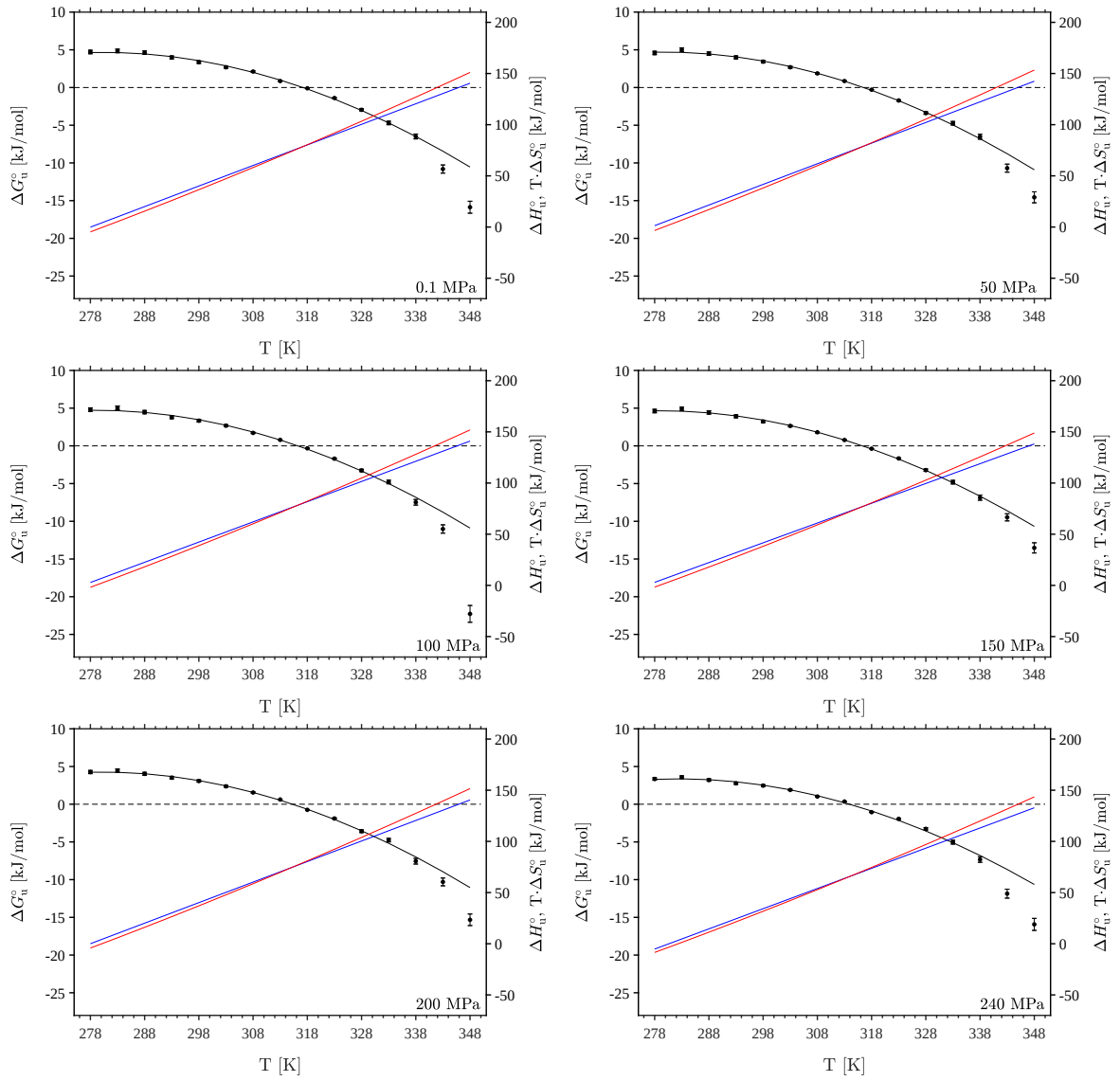

Figure A.5.: **The Gibbs free energy ($\Delta G^\circ_\mathrm{u}$), enthalpy ($\Delta H^\circ_\mathrm{u}$) and entropy ($\Delta S^\circ_\mathrm{u}$) of VHP35_L69A as a function of temperature at different pressures:** The change of $\Delta G^\circ_\mathrm{u}$ is determined by the equation 2.37 and the error was assumed to be 5 %. The fits of $\Delta G^\circ_\mathrm{u}$ (*black*), $\Delta H^\circ_\mathrm{u}$ (*blue*) and $\Delta S^\circ_\mathrm{u}$ (*red*) are given by equation 2.40 and 2.39.

A.4. $\Delta G_{\mathrm{u}}^{\circ}$ as a function of pressure

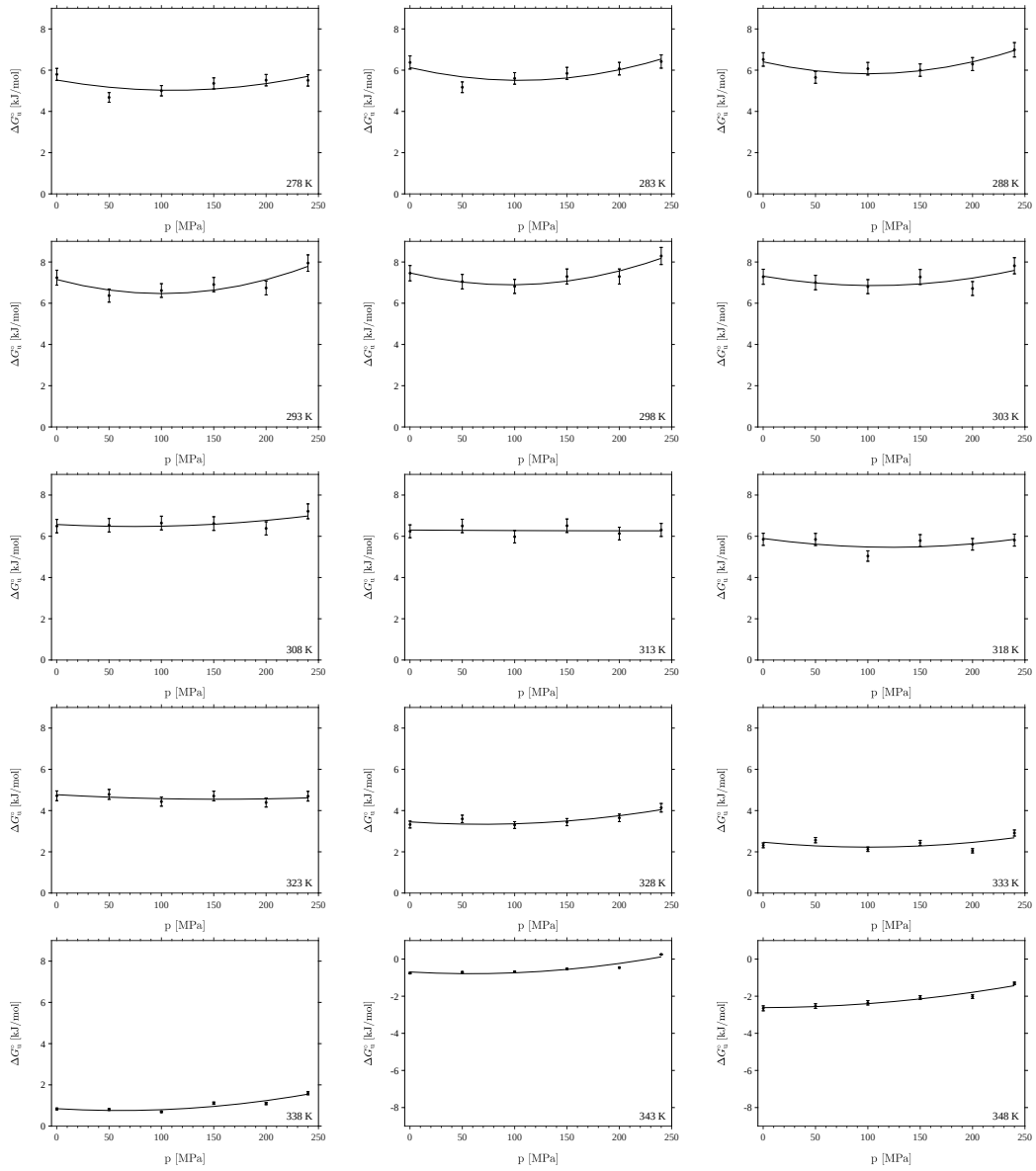

Figure A.6a: **The Gibbs free energy ($\Delta G_{\mathrm{u}}^{\circ}$) of VHP35 as a function of pressure at different temperatures:** The change in $\Delta G_{\mathrm{u}}^{\circ}$ is determined by the equation 2.37 and the error was assumed to be 5 %. The fits of $\Delta G_{\mathrm{u}}^{\circ}$ (*solid* line) are given by equation 2.45.

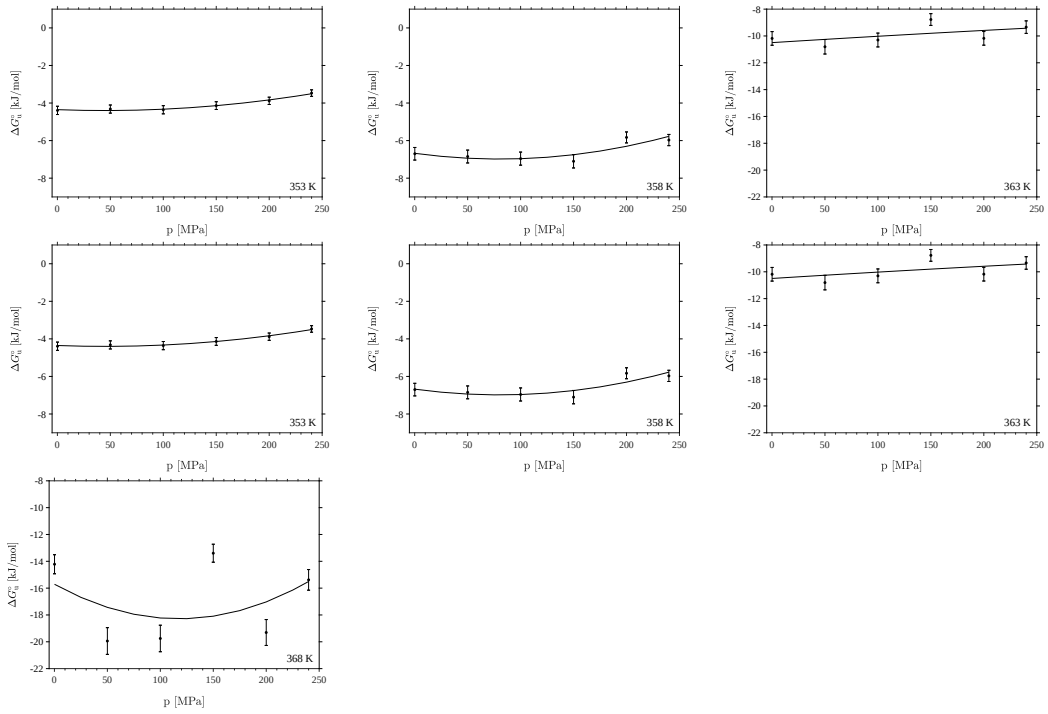

Figure A.6b: **The Gibbs free energy ($\Delta G^\circ_\mathbf{u}$) of VHP35 as a function of pressure at different temperatures:** The change in $\Delta G^\circ_\mathrm{u}$ is determined by the equation 2.37 and the error was assumed to be 5 %. The fits of $\Delta G^\circ_\mathrm{u}$ (*solid* line) are given by equation 2.45.

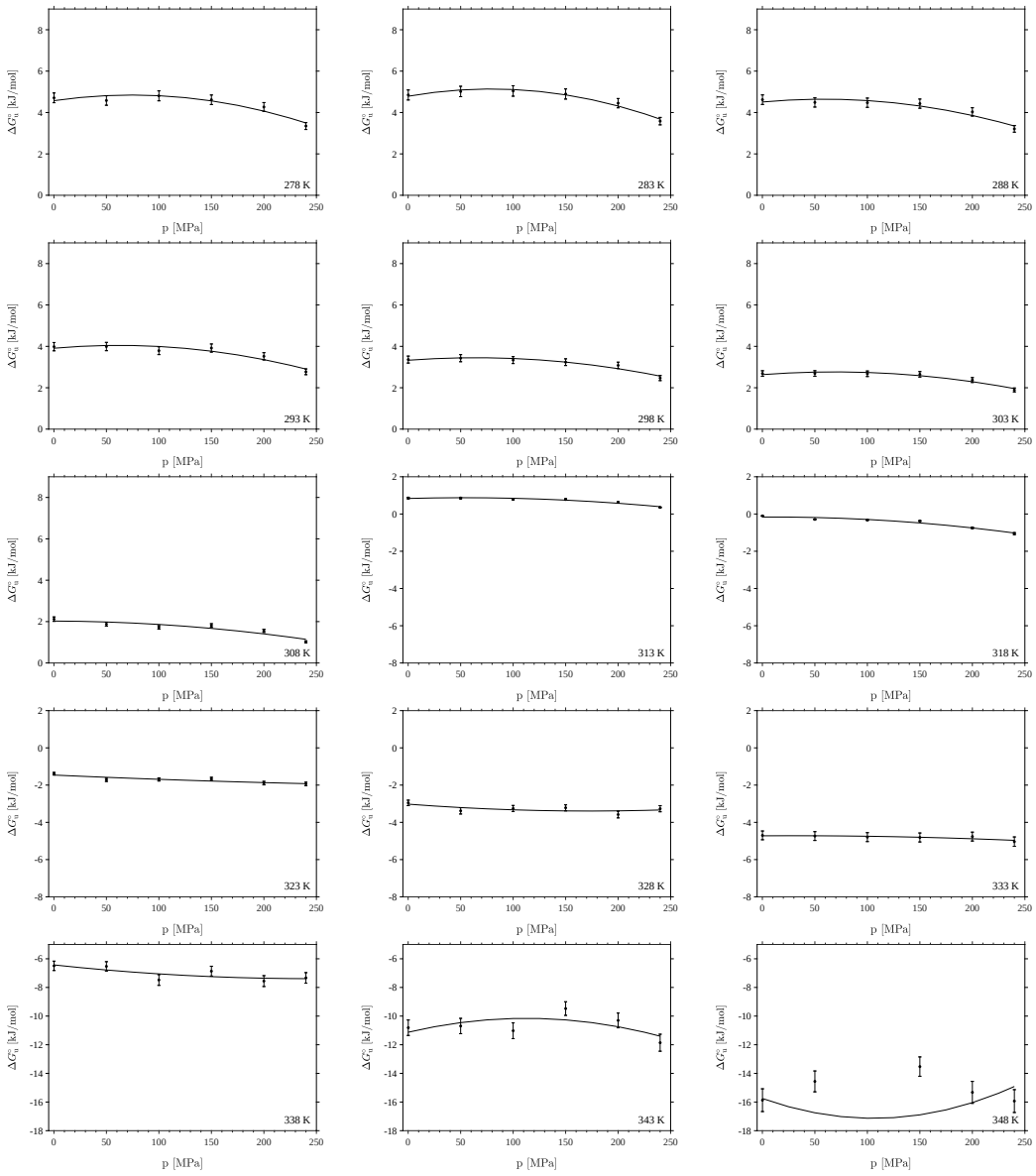

Figure A.7.: **The Gibbs free energy ($\Delta G_{\mathrm{u}}^\circ$) of VHP35_L69A as a function of pressure at different temperatures:** The change in $\Delta G_{\mathrm{u}}^\circ$ is determined by the equation 2.37 and the error was assumed to be 5 %. The fits of $\Delta G_{\mathrm{u}}^\circ$ (*solid* line) are given by equation 2.45.

A.5. Thermodynamic parameters as a function of temperature

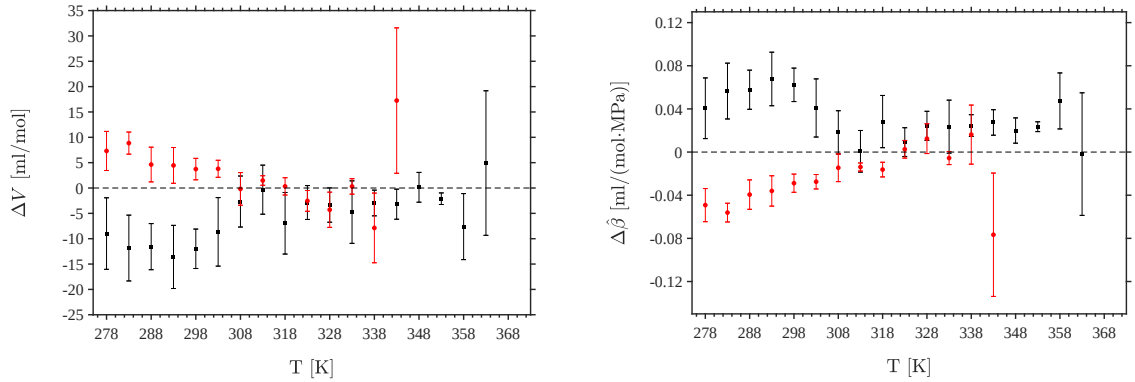

Figure A.8.: **Thermodynamic parameters ΔV and $\Delta\hat{\beta}$ of VHP35 (*black* squares) and VHP35_L69A (*red* circles) as a function of temperature (Tab. 3.3 and 3.4):** Values of VHP35 at 368 K and of VHP35_L69A at 348 K are not shown.

A.6. HSQC spectra and chemical shift assignments of VHP35

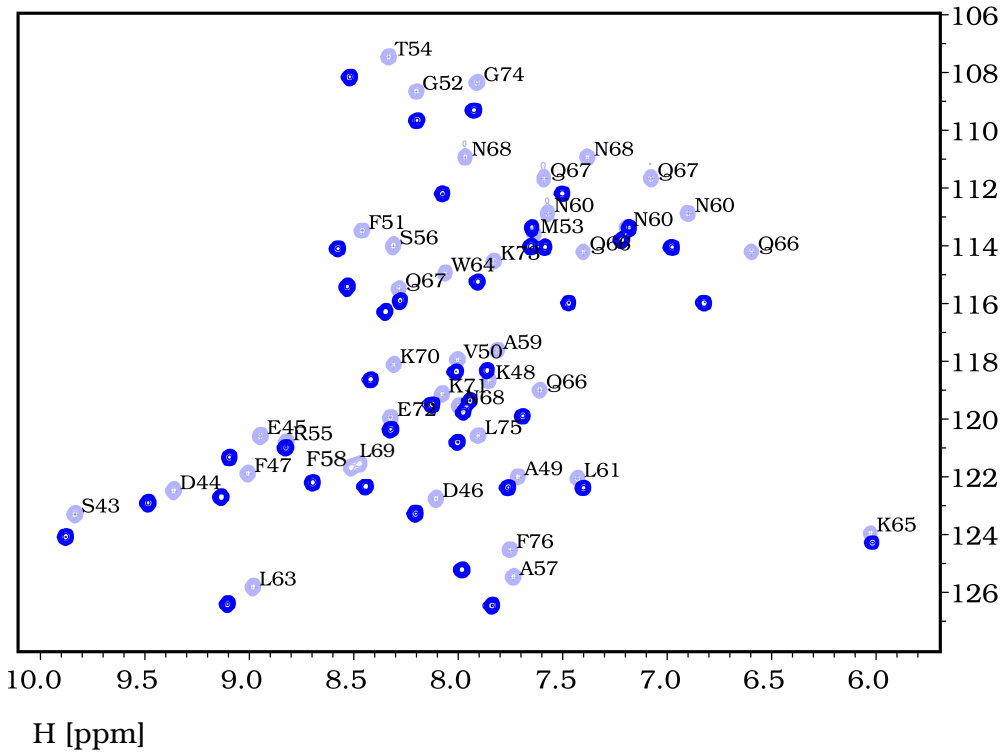

Figure A.9.: **^{1}H,^{15}N-*f*HSQC of VHP35:** Spectra recorded at 0.1 MPa (*light blue*) and 240 MPa (*blue*), 278 K, pH 7.0 (K_2HPO_4/KH_2PO_4), and protein concentration of 1.3 mM. The residue labels of the resonances correspond to 0.1 MPa (Tab. A.1, A.2, A.3).

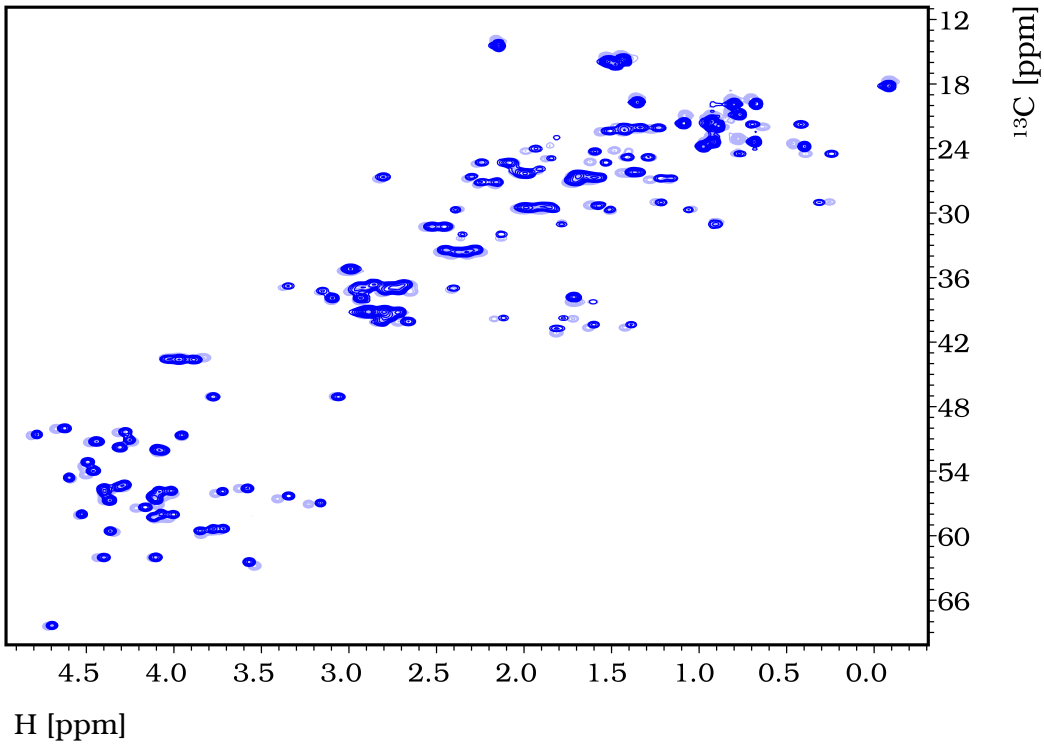

Figure A.10.: **^{1}H,^{13}C-*ct*HSQC of the aliphatic region of VHP35:** Spectra recorded at 0.1 MPa (*light blue*) and 240 MPa (*blue*), 278 K, pH 7.0 (K_2HPO_4/KH_2PO_4), and protein concentration of 1.3 mM. For clarity, the resonances have not been labeled (Tab. A.1, A.2, A.3).

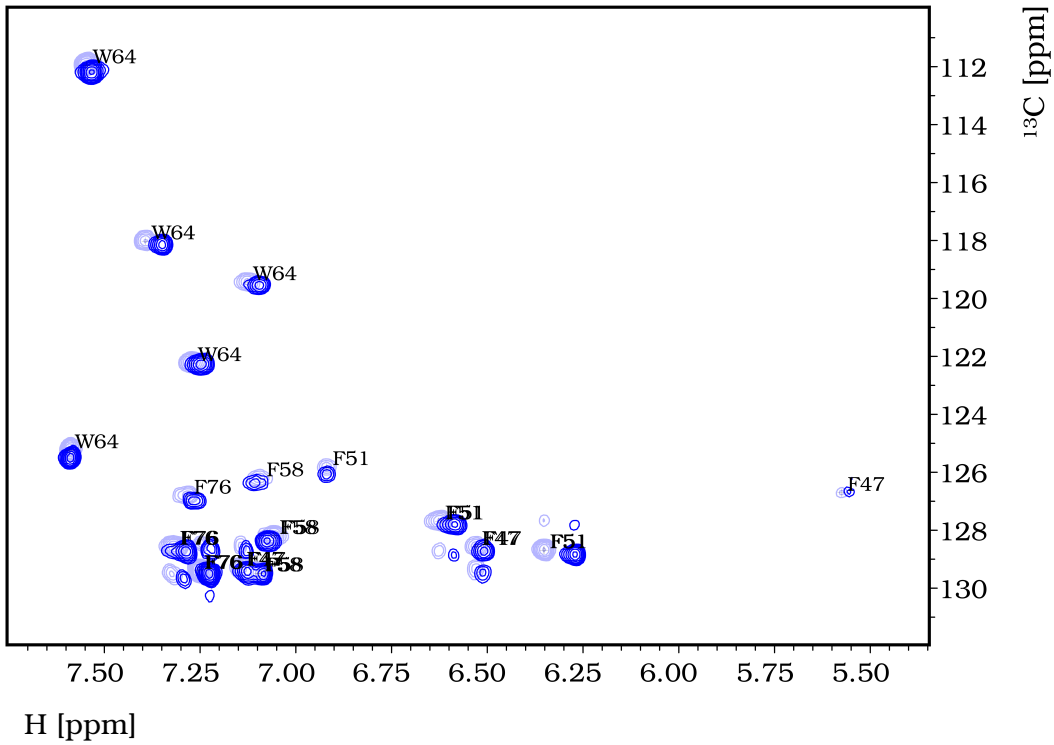

Figure A.11.: **^{1}H,^{13}C-*ct*HSQC of the aromatic region of VHP35:** Spectra recorded at 0.1 MPa (*light blue*) and 240 MPa (*blue*), 278 K, pH 7.0 (K_2HPO_4/KH_2PO_4), and protein concentration of 1.3 mM. The residue labels of the resonances correspond to 0.1 MPa (Tab. A.1, A.2, A.3).

Table A.1.: **Chemical shift (CS) assignments of VHP35 from L42 to R55 at 0.1 MPa and 240 MPa.**

AA	Atom	CS 0.1 MPa [ppm]	CS 240 MPa [ppm]	AA	Atom	CS 0.1 MPa [ppm]	CS 240 MPa [ppm]	AA	Atom	CS 0.1 MPa [ppm]	CS 240 MPa [ppm]	AA	Atom	CS 0.1 MPa [ppm]	CS 240 MPa [ppm]
L42	CA	51.268	51.121	E45	HN	8.946	9.093	K48	HD3	1.624	1.58	F51	HD2	6.351	6.268
L42	CB	41.163	40.747	D46	CA	54.271	53.989	K48	HE2	2.913	2.891	F51	HE1	6.627	6.589
L42	CD1	22.924	23.352	D46	CB	37.331	37.363	K48	HE3	2.904	2.887	F51	HE2	6.621	6.582
L42	CD2	22.992	23.411	D46	HA	4.499	4.465	K48	HG2	1.356	1.337	F51	HZ	6.92	6.918
L42	CG	23.743	23.519	D46	HB2	2.803	2.786	K48	HG3	1.27	1.235	F51	N	113.487	114.118
L42	HA	4.236	4.25	D46	HB3	2.65	2.724	K48	N	118.685	119.381	F51	HN	8.459	8.574
L42	HB2	1.822	1.821	D46	N	122.77	123.287	K48	HN	7.852	7.943	G52	CA	43.481	43.613
L42	HB3	1.808	1.807	D46	HN	8.106	8.202	A49	CA	52.133	51.984	G52	HA1	4.016	4.024
L42	HD1	0.935	0.921	F47	CA	59.871	59.585	A49	CB	15.564	15.884	G52	HA2	3.835	3.881
L42	HD2	0.925	0.914	F47	CB	36.938	36.779	A49	HA	4.084	4.085	G52	N	108.665	109.672
L42	HG	1.853	1.819	F47	CD1	129.292	129.43	A49	HB	1.534	1.516	G52	HN	8.202	8.195
S43	CA	54.682	54.556	F47	CD2	129.293	129.427	A49	N	122.014	122.384	M53	CA	50.717	50.577
S43	CB	62.058	62.044	F47	CE1	128.577	128.727	A49	HN	7.713	7.76	M53	CB	32.354	32.002
S43	HA	4.589	4.593	F47	CE2	128.577	128.727	V50	CA	62.775	62.459	M53	CE	14.045	14.39
S43	HB2	4.434	4.402	F47	CZ	126.71	126.685	V50	CB	29.82	29.681	M53	CG	26.819	26.673
S43	HB3	4.118	4.104	F47	HA	3.849	3.854	V50	CG1	19.543	19.852	M53	HA	4.816	4.784
S43	N	123.304	124.089	F47	HB2	3.377	3.349	V50	CG2	17.8	18.203	M53	HB2	2.36	2.355
S43	HN	9.834	9.877	F47	HB3	2.966	2.929	V50	HA	3.544	3.569	M53	HB3	2.131	2.127
D44	CA	55.637	55.482	F47	HD1	7.146	7.13	V50	HB	1.508	1.515	M53	HE	2.162	2.144
D44	CB	36.912	36.924	F47	HD2	7.14	7.124	V50	HG1	0.818	0.803	M53	HG2	2.825	2.8
D44	HA	4.359	4.313	F47	HE1	6.531	6.512	V50	HG2	-0.086	-0.087	M53	HG3	2.317	2.298
D44	HB2	2.744	2.759	F47	HE2	6.525	6.505	V50	N	117.965	118.375	M53	N	113.629	114.038
D44	HB3	2.667	2.723	F47	HZ	5.576	5.555	V50	HN	8.003	8.007	M53	HN	7.637	7.651
D44	N	122.495	122.918	F47	N	121.902	122.714	F51	CA	57.409	57.4	T54	CA	58.095	57.959
D44	HN	9.362	9.483	F47	HN	9.007	9.131	F51	CB	37.114	36.922	T54	CB	68.408	68.332
E45	CA	56.823	56.426	K48	CA	55.775	55.55	F51	CD1	128.687	128.859	T54	CG2	19.316	19.712
E45	CB	26.377	26.303	K48	CB	29.554	29.375	F51	CD2	128.687	128.859	T54	HA	4.542	4.529
E45	CG	33.835	33.637	K48	CD	26.882	26.673	F51	CE1	127.695	127.809	T54	HB	4.72	4.695
E45	HA	4.106	4.104	K48	CE	39.203	39.175	F51	CE2	127.695	127.809	T54	HG2	1.367	1.35
E45	HB2	2.014	1.998	K48	CG	22.177	22.033	F51	CZ	125.819	126.073	T54	N	107.48	108.171
E45	HB3	2.003	1.988	K48	HA	4.383	4.392	F51	HA	4.216	4.161	T54	HN	8.332	8.517
E45	HG2	2.412	2.378	K48	HB2	1.918	1.884	F51	HB2	2.941	2.918	R55	CA	57.072	56.991
E45	HG3	2.323	2.328	K48	HB3	1.904	1.856	F51	HB3	2.412	2.405	R55	CB	26.954	26.777
E45	N	120.59	121.34	K48	HD2	1.63	1.609	F51	HD1	6.353	6.274	R55	CD	40.078	40.063

Table A.2.: **Chemical shift (CS) assignments of VHP35 from R55 to Q66 at 0.1 MPa and 240 MPa.**

AA	Atom	CS 0.1 MPa [ppm]	CS 240 MPa [ppm]	AA	Atom	CS 0.1 MPa [ppm]	CS 240 MPa [ppm]	AA	Atom	CS 0.1 MPa [ppm]	CS 240 MPa [ppm]	AA	Atom	CS 0.1 MPa [ppm]	CS 240 MPa [ppm]
R55	CG	24.494	24.49	F58	HB3	2.996	2.96	L61	HG	1.841	1.809	W64	HA	4.396	4.403
R55	CZ	156.261	155.885	F58	HD1	7.099	7.086	L61	N	122.069	122.407	W64	HB2	3.486	3.475
R55	HA	3.23	3.163	F58	HD2	7.094	7.082	L61	HN	7.429	7.399	W64	HB3	3.214	3.203
R55	HB2	1.28	1.216	F58	HE1	7.059	7.078	P62	CA	59.67	59.589	W64	HD1	7.592	7.588
R55	HB3	1.172	1.159	F58	HE2	7.053	7.072	P62	CB	29.676	29.682	W64	HE1	10.604	10.57
R55	HD2	2.833	2.812	F58	HZ	7.093	7.105	P62	CD	47.037	47.046	W64	HE3	7.392	7.349
R55	HD3	2.718	2.66	F58	N	121.674	122.208	P62	CG	25.315	25.312	W64	HH2	7.271	7.246
R55	HE	7.106	7.116	F58	HN	8.512	8.694	P62	HA	4.345	4.364	W64	HZ2	7.546	7.533
R55	HG2	0.79	0.766	A59	CA	50.767	50.713	P62	HB2	1.039	1.058	W64	HZ3	7.127	7.095
R55	HG3	0.392	0.244	A59	CB	15.477	15.747	P62	HB3	2.372	2.393	W64	N	114.958	115.915
R55	N	120.802	121.01	A59	HA	3.957	3.957	P62	HD2	3.786	3.779	W64	NE1	130.525	131.036
R55	HN	8.822	8.824	A59	HB	1.446	1.427	P62	HD3	3.073	3.06	W64	HN	8.063	8.277
S56	CA	58.245	57.957	A59	N	117.639	118.336	P62	HG2	2.077	2.088	K65	CA	55.632	55.627
S56	CB	59.468	59.321	A59	HN	7.813	7.86	P62	HG3	1.624	1.529	K65	CB	29	28.998
S56	HA	4.07	4.072	N60	CA	50.044	50.028	L63	CA	56.049	55.905	K65	CD	26.272	26.196
S56	HB2	3.779	3.775	N60	CB	36.66	36.648	L63	CB	38.287	37.872	K65	CE	39.245	39.239
S56	HB3	3.742	3.717	N60	HA	4.672	4.62	L63	CD1	21.629	21.897	K65	CG	21.972	21.756
S56	N	114.019	115.441	N60	HB2	2.864	2.857	L63	CD2	21.09	21.488	K65	HA	3.626	3.576
S56	HN	8.311	8.529	N60	HB3	2.665	2.691	L63	CG	24.356	24.217	K65	HB2	1.243	1.217
A57	CA	52.219	52.057	N60	HD21	7.571	7.583	L63	HA	3.76	3.717	K65	HB3	0.254	0.308
A57	CB	15.899	16.158	N60	HD22	6.898	6.975	L63	HB2	1.718	1.719	K65	HD2	1.432	1.363
A57	HA	4.086	4.08	N60	N	113.38	113.815	L63	HB3	1.713	1.711	K65	HD3	1.395	1.361
A57	HB	1.483	1.477	N60	ND2	112.892	114.058	L63	HD1	0.899	0.892	K65	HE2	2.733	2.724
A57	N	125.473	126.47	N60	HN	7.192	7.216	L63	HD2	0.936	0.93	K65	HE3	2.726	2.719
A57	HN	7.736	7.836	L61	CA	50.437	50.308	L63	HG	1.6	1.592	K65	HG2	0.858	0.692
F58	CA	58.488	58.291	L61	CB	38.279	38.287	L63	N	125.829	126.425	K65	HG3	0.638	0.421
F58	CB	37.345	37.196	L61	CD1	23.541	23.806	L63	HN	8.983	9.102	K65	N	123.959	124.299
F58	CD1	129.488	129.522	L61	CD2	19.439	19.848	W64	CA	55.976	55.77	K65	HN	6.028	6.017
F58	CD2	129.487	129.522	L61	CG	23.167	22.987	W64	CB	24.085	24.081	Q66	CA	56.591	56.313
F58	CE1	128.197	128.381	L61	HA	4.314	4.275	W64	CD1	125.234	125.519	Q66	CB	26.117	25.861
F58	CE2	128.197	128.381	L61	HB2	1.598	1.604	W64	CE3	118.026	118.168	Q66	CG	30.862	31.045
F58	CZ	126.204	126.389	L61	HB3	0.787	0.778	W64	CH2	122.229	122.3	Q66	HA	3.404	3.347
F58	HA	4.109	4.116	L61	HD1	0.461	0.397	W64	CZ2	111.952	112.215	Q66	HB2	1.931	1.912
F58	HB2	3.17	3.149	L61	HD2	0.708	0.676	W64	CZ3	119.438	119.561	Q66	HB3	1.917	1.905

Table A.3.: **Chemical shift (CS) assignments of VHP35 from Q66 to F76 at 0.1 MPa and 240 MPa.**

AA	Atom	CS 0.1 MPa [ppm]	CS 240 MPa [ppm]	AA	Atom	CS 0.1 MPa [ppm]	CS 240 MPa [ppm]	AA	Atom	CS 0.1 MPa [ppm]	CS 240 MPa [ppm]	AA	Atom	CS 0.1 MPa [ppm]	CS 240 MPa [ppm]
Q66	HE21	7.401	7.47	L69	CG	24.95	24.899	K71	HD3	1.708	1.685	G74	HA1	3.976	3.97
Q66	HE22	6.596	6.821	L69	HA	4.282	4.294	K71	HE2	2.915	2.89	G74	HA2	3.837	3.884
Q66	HG2	1.783	1.782	L69	HB2	2.172	2.114	K71	HE3	2.903	2.889	G74	N	108.365	109.32
Q66	HG3	0.886	0.905	L69	HB3	1.72	1.771	K71	HG2	1.559	1.51	G74	HN	7.91	7.923
Q66	N	119.006	119.908	L69	HD1	0.97	0.975	K71	HG3	1.442	1.426	L75	CA	51.326	51.259
Q66	NE2	114.227	116.001	L69	HD2	1.078	1.083	K71	N	119.145	119.517	L75	CB	40.671	40.334
Q66	HN	7.61	7.69	L69	HG	1.878	1.846	K71	HN	8.077	8.122	L75	CD1	23.138	23.398
Q67	CA	56.098	55.779	L69	N	121.554	122.347	E72	CA	56.318	55.902	L75	CD2	20.539	20.804
Q67	CB	25.455	25.312	L69	HN	8.472	8.441	E72	CB	27.363	27.087	L75	CG	24.225	23.858
Q67	CG	31.316	31.315	K70	CA	58.366	58.084	E72	CG	33.647	33.436	L75	HA	4.477	4.441
Q67	HA	4.014	4.02	K70	CB	29.642	29.459	E72	HA	4.053	4.085	L75	HB2	1.636	1.604
Q67	HB2	2.27	2.241	K70	CD	27.024	26.965	E72	HB2	2.261	2.253	L75	HB3	1.424	1.389
Q67	HB3	2.08	2.086	K70	CE	39.247	39.237	E72	HB3	2.169	2.162	L75	HD1	0.774	0.676
Q67	HE21	7.591	7.645	K70	CG	24.229	24.081	E72	HG2	2.475	2.444	L75	HD2	0.822	0.765
Q67	HE22	7.076	7.18	K70	HA	4.058	4.002	E72	HG3	2.26	2.306	L75	HG	1.483	1.439
Q67	HG2	2.558	2.521	K70	HB2	2.018	1.986	E72	N	119.962	120.372	L75	N	120.589	120.823
Q67	HG3	2.45	2.457	K70	HB3	1.909	1.858	E72	HN	8.324	8.321	L75	HN	7.904	8.001
Q67	N	115.502	116.301	K70	HD2	1.727	1.71	K73	CA	51.747	51.806	F76	CA	56.666	56.721
Q67	NE2	111.686	113.384	K70	HD3	1.714	1.696	K73	CB	29.272	29.272	F76	CB	38.084	37.876
Q67	HN	8.285	8.346	K70	HE2	2.825	2.801	K73	CD	24.835	24.766	F76	CD1	129.404	129.515
N68	CA	53.586	53.17	K70	HE3	2.815	2.797	K73	CE	39.649	39.766	F76	CD2	129.404	129.515
N68	CB	35.418	35.144	K70	HG2	1.99	1.935	K73	CG	22.006	22.072	F76	CE1	128.568	128.738
N68	HA	4.51	4.491	K70	HG3	1.4	1.388	K73	HA	4.306	4.313	F76	CE2	128.568	128.737
N68	HB2	3.01	2.993	K70	N	118.128	118.643	K73	HB2	1.622	1.571	F76	CZ	126.802	126.991
N68	HB3	2.998	2.988	K70	HN	8.309	8.417	K73	HB3	1.611	1.565	F76	HA	4.396	4.365
N68	HD21	7.966	8.074	K71	CA	56.999	56.501	K73	HD2	1.421	1.413	F76	HB2	3.1	3.093
N68	HD22	7.381	7.5	K71	CB	29.612	29.543	K73	HD3	1.284	1.287	F76	HB3	2.94	2.928
N68	N	119.552	119.775	K71	CD	26.748	26.543	K73	HE2	2.816	2.791	F76	HD1	7.256	7.231
N68	ND2	110.947	112.208	K71	CE	39.298	39.238	K73	HE3	2.808	2.787	F76	HD2	7.251	7.222
N68	HN	7.999	7.974	K71	CG	22.449	22.303	K73	HG2	1.474	1.431	F76	HE1	7.319	7.289
L69	CA	55.499	55.357	K71	HA	4.103	4.11	K73	HG3	1.455	1.422	F76	HE2	7.314	7.281
L69	CB	39.802	39.786	K71	HB2	2.025	1.994	K73	N	114.55	115.257	F76	HZ	7.282	7.265
L69	CD1	23.537	23.807	K71	HB3	2.007	1.978	K73	HN	7.829	7.905	F76	N	124.538	125.231
L69	CD2	20.945	21.622	K71	HD2	1.72	1.693	G74	CA	43.481	43.613	F76	HN	7.753	7.981

A.7. Unique inter-residual NOEs of VHP35

Table A.4.: **Unique inter-residual NOEs of VHP35 at 0.1 MPa and 240 MPa.**

0.1 MPa					240 MPa				
AA	**Atom**		**AA**	**Atom**	**AA**	**Atom**		**AA**	**Atom**
S43	HB3	:	D44	HB3	S43	HA	:	D46	HB3
K48	HG2	:	M53	H	D44	H	:	E45	H
K48	HG2	:	T54	H	D44	HB3	:	S43	HB2
A49	HA	:	F58	H	D46	HB2	:	L42	HD1
W64	H	:	L63	H	D46	H	:	E45	HG2
K73	HE3	:	F51	HE1	D46	H	:	L42	HD1
L75	H	:	F76	H	V50	HA	:	F51	H
					F51	HZ	:	L42	HD1
					F51	HB3	:	M53	HB3
					M53	H	:	F51	H
					T54	HA	:	R55	HA
					R55	HA	:	F47	HE1
					S56	HA	:	A57	H
					A57	H	:	M53	HG3
					F58	HZ	:	L42	HD1
					A59	H	:	L61	H
					P62	HB3	:	L63	H
					K71	HA	:	K73	HG3

A.8. 10 lowest-energy conformers of VHP35

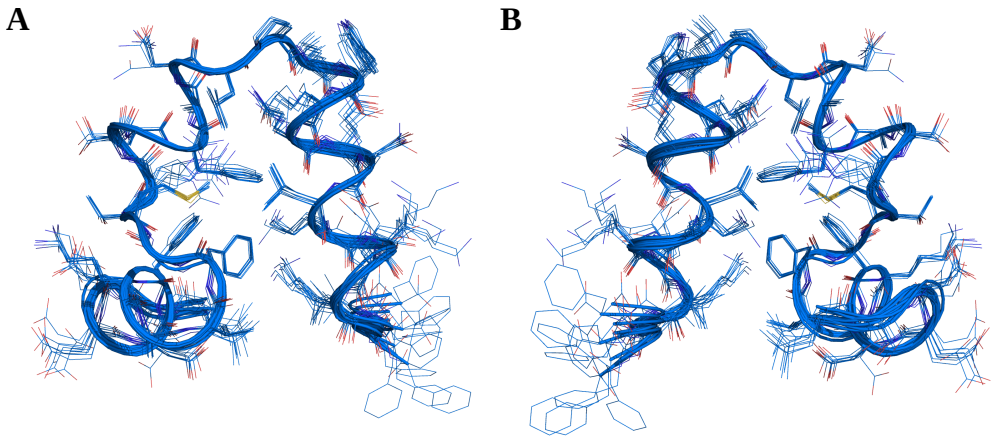

Figure A.12.: **Superposition of the backbone heavy atoms of the 10 lowest-energy final conformers of VHP35 at 0.1 MPa:** (A) shows the 10 lowest-energy structures of the final calculations with an RMSD of 0.61 *Å*. (B) shows the rotation by 180° about the y-axis. Side chains are shown as sticks without hydrogens.

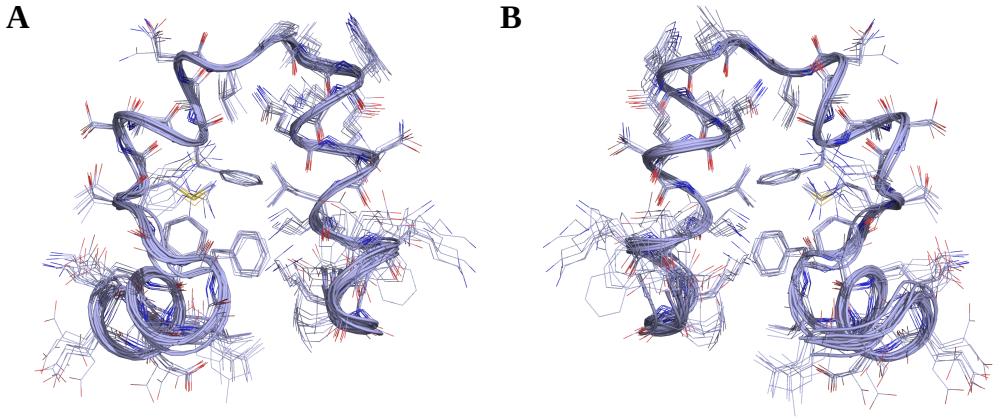

Figure A.13.: **Superposition of the backbone heavy atoms of the 10 lowest-energy *control* conformers of VHP35 at 0.1 MPa:** (A) shows the 10 lowest-energy structures of the *control* calculations with an RMSD of 0.59 *Å*. (B) shows the rotation by 180° about the y-axis. Side chains are shown as sticks without hydrogens. Side chains are shown as sticks without hydrogens.

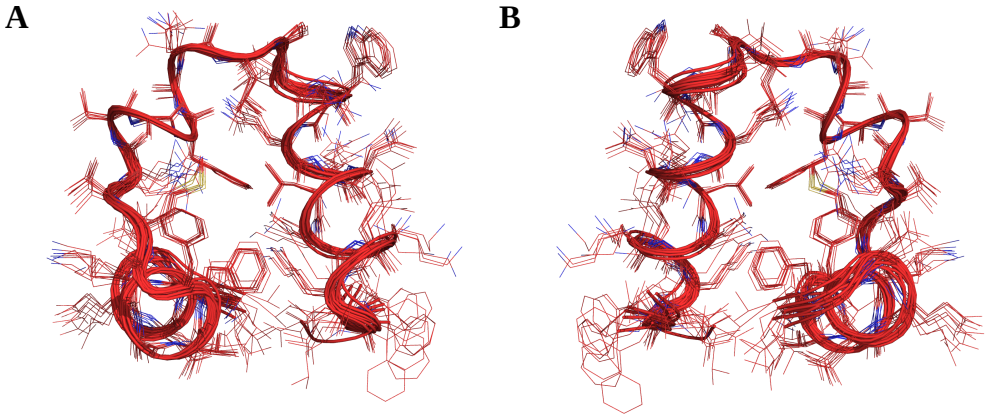

Figure A.14.: **Superposition of the backbone heavy atoms of the 10 lowest-energy final conformers of VHP35 at 240 MPa:** (A) shows the 10 lowest-energy structures of the final calculations with an RMSD of 0.58 Å. (B) shows the rotation by 180° about the y-axis. Side chains are shown as sticks without hydrogens.

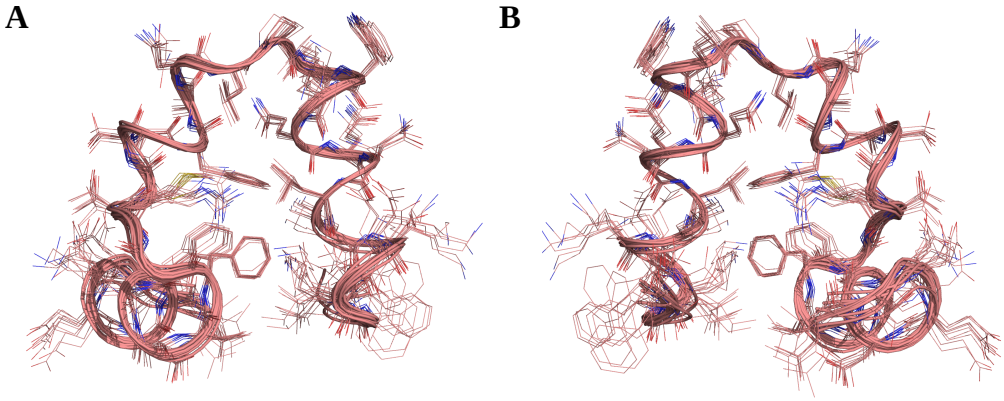

Figure A.15.: **Superposition of the backbone heavy atoms of the 10 lowest-energy *control* conformers of VHP35 at 240 MPa:** (A) shows the 10 lowest-energy structures of the *control* calculations with an RMSD of 0.56 Å. (B) shows the rotation by 180° about the y-axis. Side chains shown as sticks without hydrogens.

A.9. Local superposition of VHP35

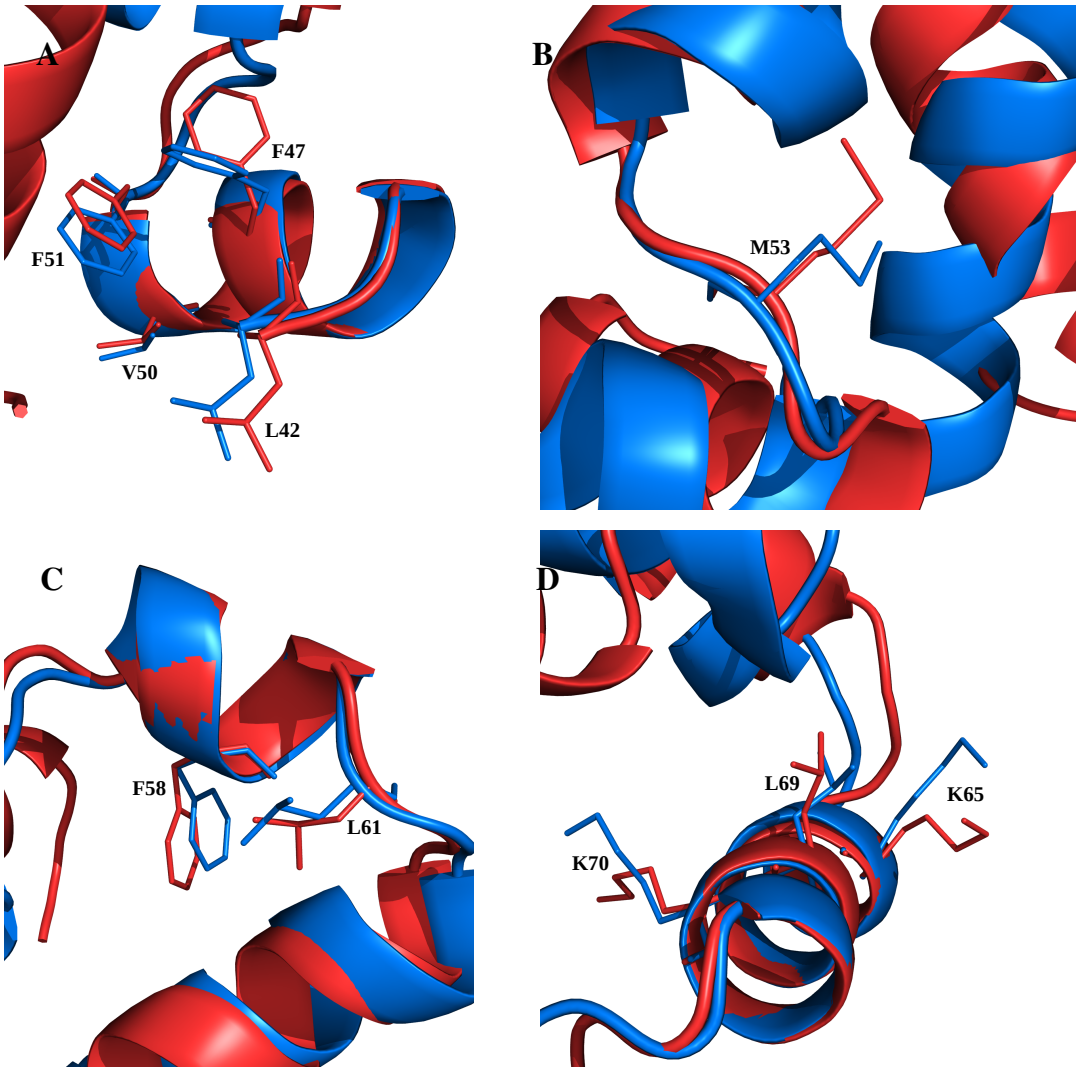

Figure A.16.: **Local superposition of the final minimized average NMR structures of VHP35 at 0.1 MPa and 240 MPa with the hydrophobic core residues:** Backbone alignment of (A) the N-terminal helix $\alpha 1$, (B) the first turn, (C) the second helix $\alpha 2$ and turn 2, and (D) the C-terminal helix $\alpha 3$ of VHP35 at 0.1 MPa (*blue*) and at 240 MPa (*red*). Side chains of the hydrophobic core are shown as sticks without hydrogens and with labels.

A.10. Charged side chains of VHP35

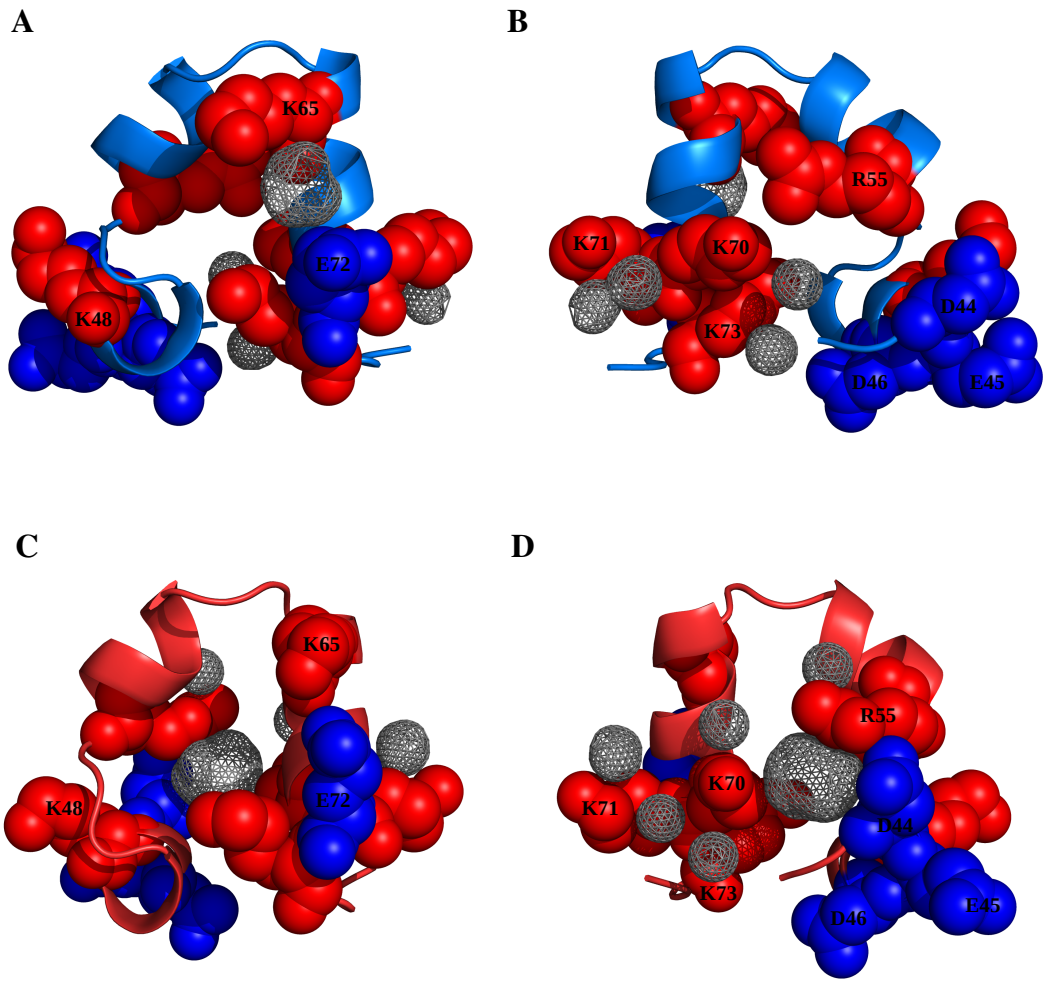

Figure A.17.: **Charged side chains of the final minimized average NMR structures of VHP35 at 0.1 MPa and 240 MPa:** (A) shows the positively (*blue*) and negatively (*red*) charged residues of VHP35 at 0.1 MPa and (C) at 240 MPa. The side chains are shown as spheres without hydrogens and with labels. (B) and (D) show the rotation by 180° about the y-axis. Structures are shown with the corresponding cavity distribution (*gray*) (Fig. 3.13).

A.11. HSQC spectra and chemical shift assignments of VHP35_L69A

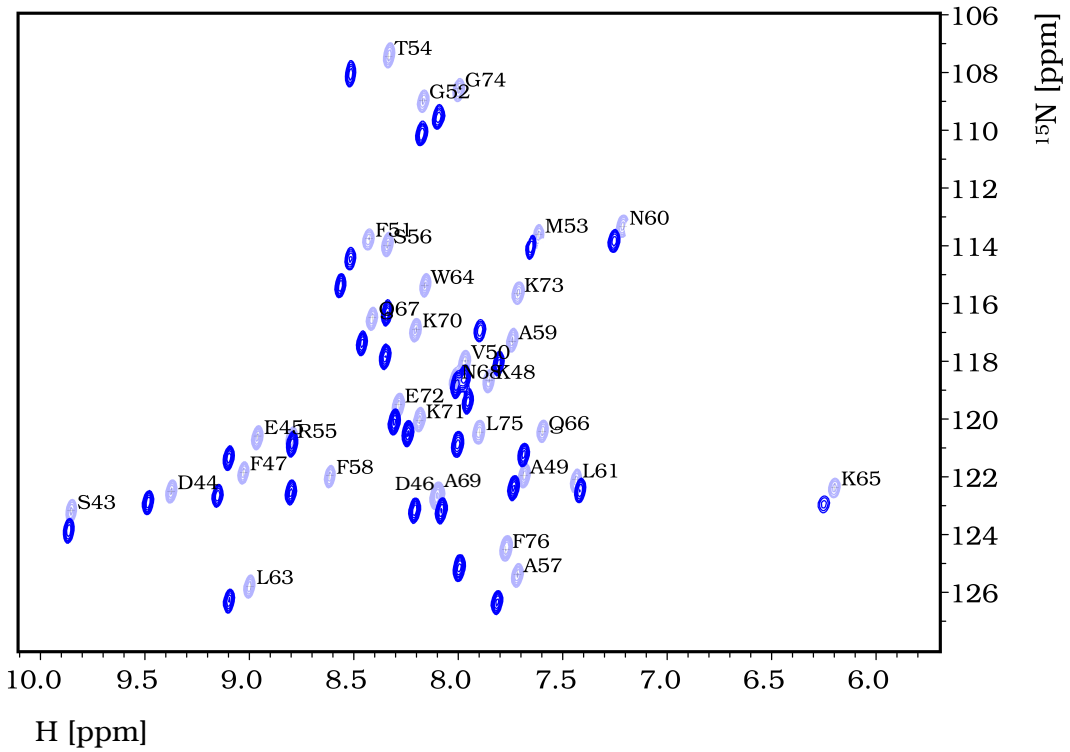

Figure A.18.: **^{1}H,^{15}N-*f*HSQC of VHP35_L69A:** Spectra recorded at 0.1 MPa (*light blue*) and 240 MPa (*blue*), 278 K, pH 7.0 (K_2HPO_4/KH_2PO_4), and protein concentration of 1.3 mM. The residue labels of the resonances correspond to 0.1 MPa (Tab. A.5, A.6, A.7).

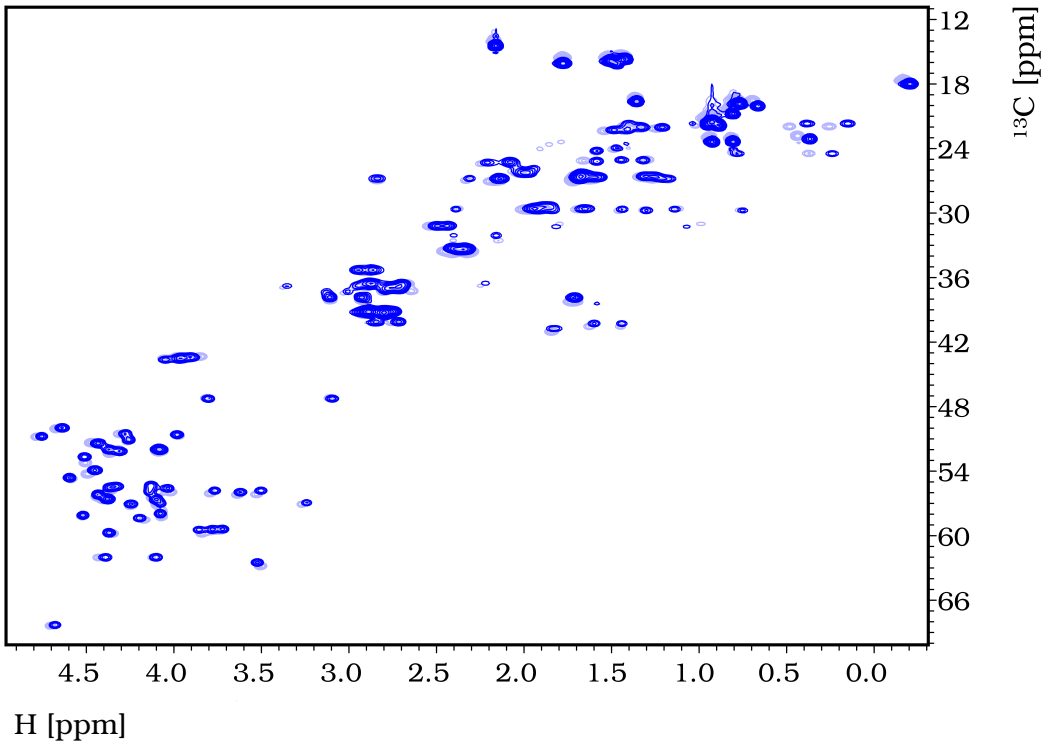

Figure A.19.: **^{1}H,^{13}C-*ct*HSQC of the aliphatic region of VHP35_L69A:** Spectra recorded at 0.1 MPa (*light blue*) and 240 MPa (*blue*), 278 K, pH 7.0 (K_2HPO_4/KH_2PO_4), and protein concentration of 1.3 mM. For clarity, the resonances have not been labeled (Tab. A.5, A.6, A.7).

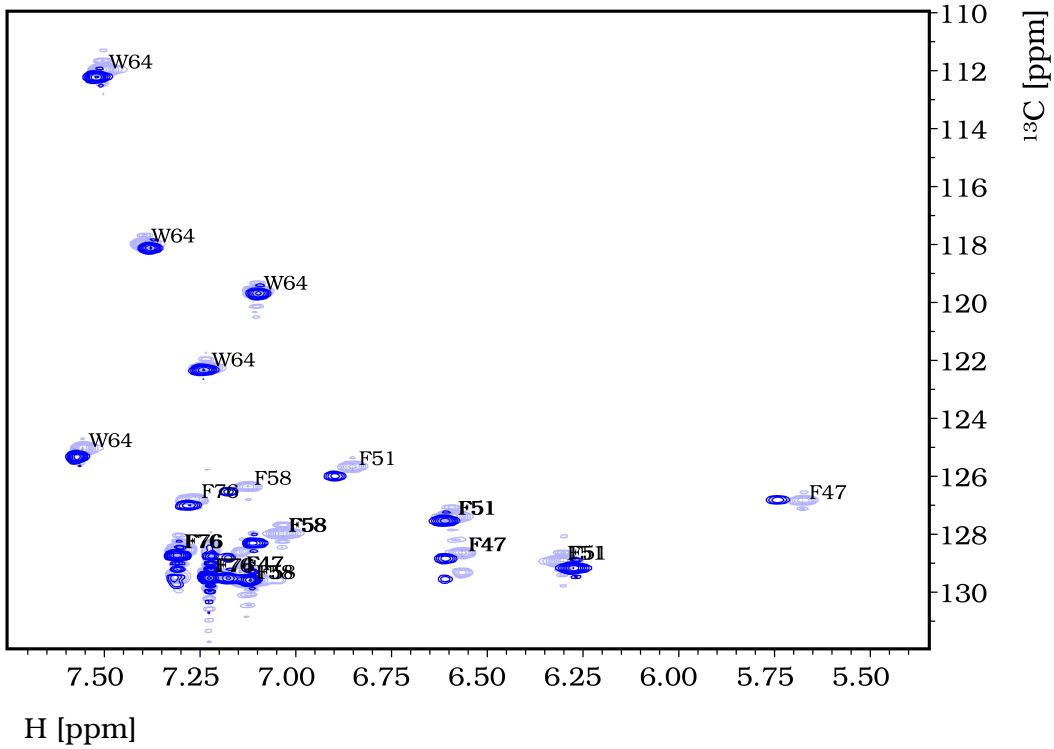

Figure A.20.: **^{1}H,^{13}C-*ct*HSQC of the aromatic region of VHP35_L69A:** Spectra recorded at 0.1 MPa (*light blue*) and 240 MPa (*blue*), 278 K, pH 7.0 (K_2HPO_4/KH_2PO_4), and protein concentration of 1.3 mM. The residue labels of the resonances correspond to 0.1 MPa (Tab. A.5, A.6, A.7).

Table A.5.: **Chemical shift (CS) assignments of VHP35_L69A from L42 to R55 at 0.1 MPa and 240 MPa.**

AA	Atom	CS 0.1 MPa [ppm]	CS 240 MPa [ppm]	AA	Atom	CS 0.1 MPa [ppm]	CS 240 MPa [ppm]	AA	Atom	CS 0.1 MPa [ppm]	CS 240 MPa [ppm]	AA	Atom	CS 0.1 MPa [ppm]	CS 240 MPa [ppm]
L42	CA	51.165	51.027	E45	HN	8.961	9.095	K48	HD3	1.617	1.592	F51	HD2	6.308	6.273
L42	CB	41.056	40.775	D46	CA	54.302	53.891	K48	HE2	2.902	2.893	F51	HE1	6.593	6.613
L42	CD1	22.956	23.342	D46	CB	37.229	37.174	K48	HE3	2.895	2.887	F51	HE2	6.59	6.607
L42	CD2	22.956	23.426	D46	HA	4.486	4.451	K48	HG2	1.337	1.333	F51	HZ	6.852	6.898
L42	CG	23.575	23.328	D46	HB2	2.796	2.776	K48	HG3	1.241	1.208	F51	N	113.75	114.425
L42	HA	4.267	4.264	D46	HB3	2.645	2.719	K48	N	118.673	119.348	F51	HN	8.427	8.517
L42	HB2	1.849	1.832	D46	N	122.769	123.174	K48	HN	7.852	7.951	G52	CA	43.51	43.643
L42	HB3	1.839	1.82	D46	HN	8.106	8.206	A49	CA	52.118	51.978	G52	HA1	4.059	4.047
L42	HD1	0.936	0.95	F47	CA	59.774	59.488	A49	CB	15.51	15.909	G52	HA2	3.955	3.967
L42	HD2	0.942	0.927	F47	CB	36.953	36.812	A49	HA	4.08	4.089	G52	N	108.965	110.177
L42	HG	1.857	1.755	F47	CD1	129.307	129.518	A49	HB	1.522	1.511	G52	HN	8.169	8.175
S43	CA	54.713	54.575	F47	CD2	129.307	129.518	A49	N	121.954	122.368	M53	CA	50.756	50.748
S43	CB	61.98	61.963	F47	CE1	128.657	128.858	A49	HN	7.686	7.738	M53	CB	32.581	32.048
S43	HA	4.589	4.593	F47	CE2	128.657	128.858	V50	CA	62.774	62.491	M53	CE	13.981	14.415
S43	HB2	4.432	4.391	F47	CZ	126.843	126.812	V50	CB	29.729	29.703	M53	CG	26.982	26.828
S43	HB3	4.121	4.107	F47	HA	3.845	3.859	V50	CG1	19.472	19.871	M53	HA	4.781	4.76
S43	N	123.183	123.86	F47	HB2	3.378	3.358	V50	CG2	17.693	17.96	M53	HB2	2.409	2.401
S43	HN	9.854	9.867	F47	HB3	2.971	2.953	V50	HA	3.503	3.522	M53	HB3	2.146	2.158
D44	CA	55.672	55.411	F47	HD1	7.147	7.179	V50	HB	1.458	1.441	M53	HE	2.167	2.159
D44	CB	36.816	36.948	F47	HD2	7.145	7.174	V50	HG1	0.789	0.771	M53	HG2	2.832	2.837
D44	HA	4.362	4.36	F47	HE1	6.566	6.612	V50	HG2	-0.177	-0.202	M53	HG3	2.332	2.313
D44	HB2	2.753	2.765	F47	HE2	6.564	6.605	V50	N	117.986	118.533	M53	N	113.614	114.019
D44	HB3	2.685	2.72	F47	HZ	5.666	5.73	V50	HN	7.967	7.972	M53	HN	7.616	7.653
D44	N	122.495	122.903	F47	N	121.839	122.629	F51	CA	57.186	57.034	T54	CA	58.137	58.124
D44	HN	9.374	9.485	F47	HN	9.028	9.15	F51	CB	36.814	36.539	T54	CB	68.376	68.342
E45	CA	57.037	56.62	K48	CA	55.832	55.601	F51	CD1	128.943	129.184	T54	CG2	19.332	19.606
E45	CB	26.302	26.294	K48	CB	29.578	29.437	F51	CD2	128.945	129.184	T54	HA	4.519	4.515
E45	CG	33.678	33.523	K48	CD	26.848	26.698	F51	CE1	127.397	127.545	T54	HB	4.703	4.684
E45	HA	4.095	4.101	K48	CE	39.145	39.139	F51	CE2	127.397	127.545	T54	HG2	1.366	1.356
E45	HB2	2.015	1.998	K48	CG	22.124	22.056	F51	CZ	125.681	126.001	T54	N	107.454	108.118
E45	HB3	1.988	1.988	K48	HA	4.368	4.375	F51	HA	4.25	4.248	T54	HN	8.333	8.518
E45	HG2	2.427	2.384	K48	HB2	1.906	1.895	F51	HB2	2.879	2.879	R55	CA	57.037	56.902
E45	HG3	2.317	2.342	K48	HB3	1.898	1.854	F51	HB3	2.254	2.222	R55	CB	26.974	26.825
E45	N	120.587	121.268	K48	HD2	1.624	1.615	F51	HD1	6.301	6.276	R55	CD	40.097	40.092

Table A.6.: **Chemical shift (CS) assignments of VHP35_L69A from R55 to Q66 at 0.1 MPa and 240 MPa.**

AA	Atom	CS 0.1 MPa [ppm]	CS 240 MPa [ppm]	AA	Atom	CS 0.1 MPa [ppm]	CS 240 MPa [ppm]	AA	Atom	CS 0.1 MPa [ppm]	CS 240 MPa [ppm]	AA	Atom	CS 0.1 MPa [ppm]	CS 240 MPa [ppm]
R55	CG	24.389	24.517	F58	HB3	3.035	3.007	L61	HG	1.787	1.767	W64	HA	4.439	4.436
R55	CZ	156.261	156.261	F58	HD1	7.121	7.121	L61	N	122.091	122.493	W64	HB2	3.487	3.484
R55	HA	3.268	3.247	F58	HD2	7.115	7.117	L61	HN	7.437	7.419	W64	HB3	3.208	3.204
R55	HB2	1.272	1.229	F58	HE1	7.036	7.119	P62	CA	59.77	59.76	W64	HD1	7.556	7.57
R55	HB3	1.178	1.176	F58	HE2	7.033	7.111	P62	CB	29.581	29.629	W64	HE1	10.591	10.553
R55	HD2	2.848	2.846	F58	HZ	7.125	7.173	P62	CD	47.2	47.2	W64	HE3	7.393	7.379
R55	HD3	2.754	2.72	F58	N	121.964	122.496	P62	CG	25.08	25.202	W64	HH2	7.235	7.241
R55	HE	7.106	7.106	F58	HN	8.615	8.799	P62	HA	4.346	4.373	W64	HZ2	7.504	7.521
R55	HG2	0.805	0.786	A59	CA	50.748	50.61	P62	HB2	1.117	1.142	W64	HZ3	7.099	7.098
R55	HG3	0.369	0.24	A59	CB	15.373	15.65	P62	HB3	2.379	2.393	W64	N	115.385	116.337
R55	N	120.717	120.853	A59	HA	3.97	3.983	P62	HD2	3.815	3.798	W64	NE1	130.321	130.839
R55	HN	8.801	8.798	A59	HB	1.429	1.426	P62	HD3	3.113	3.095	W64	HN	8.16	8.339
S56	CA	58.262	57.986	A59	N	117.305	118.116	P62	HG2	2.083	2.08	K65	CA	56.214	55.939
S56	CB	59.496	59.366	A59	HN	7.741	7.808	P62	HG3	1.662	1.582	K65	CB	29.718	29.716
S56	HA	4.064	4.076	N60	CA	50.069	49.93	L63	CA	56.079	55.801	K65	CD	26.694	26.57
S56	HB2	3.769	3.78	N60	CB	36.679	36.495	L63	CB	38.189	37.902	K65	CE	39.349	39.3
S56	HB3	3.737	3.719	N60	HA	4.673	4.639	L63	CD1	21.656	21.794	K65	CG	21.933	21.654
S56	N	113.985	115.382	N60	HB2	2.875	2.872	L63	CD2	20.975	21.512	K65	HA	3.641	3.624
S56	HN	8.341	8.565	N60	HB3	2.676	2.703	L63	CG	24.253	24.241	K65	HB2	1.318	1.3
A57	CA	52.256	52.1	N60	HD21	7.585	7.598	L63	HA	3.798	3.765	K65	HB3	0.773	0.755
A57	CB	15.789	16.095	N60	HD22	6.914	6.99	L63	HB2	1.728	1.72	K65	HD2	1.323	1.309
A57	HA	4.079	4.074	N60	N	113.335	113.877	L63	HB3	1.716	1.711	K65	HD3	1.297	1.257
A57	HB	1.475	1.474	N60	ND2	113.065	114.151	L63	HD1	0.898	0.894	K65	HE2	2.811	2.809
A57	N	125.373	126.325	N60	HN	7.211	7.255	L63	HD2	0.93	0.927	K65	HE3	2.8	2.791
A57	HN	7.717	7.816	L61	CA	50.489	50.497	L63	HG	1.585	1.583	K65	HG2	0.477	0.381
F58	CA	58.54	58.395	L61	CB	38.326	38.451	L63	N	125.782	126.286	K65	HG3	0.258	0.148
F58	CB	37.435	37.347	L61	CD1	22.878	23.153	L63	HN	8.997	9.095	K65	N	122.362	122.903
F58	CD1	129.61	129.594	L61	CD2	19.603	20.017	W64	CA	56.241	56.209	K65	HN	6.197	6.249
F58	CD2	129.61	129.593	L61	CG	23.427	23.185	W64	CB	23.981	24.109	Q66	CA	56.205	55.8
F58	CE1	127.987	128.309	L61	HA	4.314	4.279	W64	CD1	125.06	125.348	Q66	CB	26.165	25.858
F58	CE2	127.987	128.308	L61	HB2	1.584	1.583	W64	CE3	118	118.138	Q66	CG	30.965	31.221
F58	CZ	126.359	126.548	L61	HB3	0.851	0.849	W64	CH2	122.274	122.356	Q66	HA	3.533	3.501
F58	HA	4.173	4.199	L61	HD1	0.431	0.366	W64	CZ2	111.992	112.248	Q66	HB2	2.065	2.028
F58	HB2	3.128	3.127	L61	HD2	0.696	0.662	W64	CZ3	119.629	119.707	Q66	HB3	1.962	1.958

Table A.7.: **Chemical shift (CS) assignments of VHP35_L69A from Q66 to F76 at 0.1 MPa and 240 MPa.**

AA	Atom	CS 0.1 MPa [ppm]	CS 240 MPa [ppm]	AA	Atom	CS 0.1 MPa [ppm]	CS 240 MPa [ppm]	AA	Atom	CS 0.1 MPa [ppm]	CS 240 MPa [ppm]	AA	Atom	CS 0.1 MPa [ppm]	CS 240 MPa [ppm]
Q66	HE21	7.452	7.505	A69	N	122.636	123.178	E72	CA	55.946	55.39	L75	CD2	20.323	20.797
Q66	HE22	6.626	6.857	A69	HN	8.099	8.081	E72	CB	27.003	26.841	L75	CG	24.082	23.97
Q66	HG2	1.799	1.816	K70	CA	57.803	56.967	E72	CG	33.554	33.393	L75	HA	4.47	4.435
Q66	HG3	0.992	1.068	K70	CB	29.714	29.702	E72	HA	4.095	4.136	L75	HB2	1.629	1.599
Q66	N	120.446	121.169	K70	CD	27.014	26.835	E72	HB2	2.185	2.148	L75	HB3	1.444	1.441
Q66	NE2	114.565	116.202	K70	CE	39.273	39.265	E72	HB3	2.145	2.14	L75	HD1	0.819	0.802
Q66	HN	7.599	7.684	K70	CG	23.979	23.695	E72	HG2	2.441	2.39	L75	HD2	0.821	0.804
Q67	CA	55.941	55.645	K70	HA	4.073	4.102	E72	HG3	2.317	2.343	L75	HG	1.489	1.469
Q67	CB	25.457	25.336	K70	HB2	1.989	1.94	E72	N	119.495	120.162	L75	N	120.45	120.851
Q67	CG	31.218	31.213	K70	HB3	1.909	1.846	E72	HN	8.287	8.308	L75	HN	7.898	8.003
Q67	HA	4.018	4.031	K70	HD2	1.709	1.677	K73	CA	51.991	52.116	F76	CA	56.611	56.616
Q67	HB2	2.24	2.207	K70	HD3	1.618	1.598	K73	CB	29.706	29.572	F76	CB	38.049	37.826
Q67	HB3	2.066	2.081	K70	HE2	2.816	2.813	K73	CD	25.069	25.064	F76	CD1	129.376	129.511
Q67	HE21	7.624	7.668	K70	HE3	2.803	2.801	K73	CE	39.388	39.381	F76	CD2	129.376	129.51
Q67	HE22	7.078	7.17	K70	HG2	1.912	1.8	K73	CG	21.907	21.659	F76	CE1	128.548	128.744
Q67	HG2	2.537	2.5	K70	HG3	1.399	1.411	K73	HA	4.314	4.31	F76	CE2	128.548	128.744
Q67	HG3	2.427	2.44	K70	N	116.891	117.844	K73	HB2	1.687	1.66	F76	CZ	126.817	127.011
Q67	N	116.488	117.298	K70	HN	8.202	8.347	K73	HB3	1.671	1.646	F76	HA	4.407	4.374
Q67	NE2	111.833	113.47	K71	CA	56.486	55.913	K73	HD2	1.445	1.442	F76	HB2	3.113	3.111
Q67	HN	8.411	8.457	K71	CB	29.602	29.57	K73	HD3	1.3	1.317	F76	HB3	2.926	2.923
N68	CA	53.211	52.659	K71	CD	26.717	26.591	K73	HE2	2.901	2.89	F76	HD1	7.228	7.228
N68	CB	35.32	35.309	K71	CE	39.272	39.207	K73	HE3	2.802	2.799	F76	HD2	7.222	7.224
N68	HA	4.502	4.513	K71	CG	22.338	22.285	K73	HG2	1.429	1.396	F76	HE1	7.309	7.313
N68	HB2	2.918	2.942	K71	HA	4.126	4.14	K73	HG3	1.022	1.036	F76	HE2	7.304	7.306
N68	HB3	2.911	2.862	K71	HB2	1.992	1.953	K73	N	115.663	116.887	F76	HZ	7.263	7.276
N68	HD21	8.015	8.083	K71	HB3	1.983	1.935	K73	HN	7.715	7.894	F76	N	124.53	125.11
N68	HD22	7.374	7.474	K71	HD2	1.712	1.683	G74	CA	43.376	43.482	F76	HN	7.772	7.996
N68	N	118.669	118.802	K71	HD3	1.701	1.668	G74	HA1	3.97	3.965	-	-	-	-
N68	ND2	111.563	112.785	K71	HE2	2.904	2.899	G74	HA2	3.847	3.913	-	-	-	-
N68	HN	8.014	8.005	K71	HE3	2.895	2.888	G74	N	108.554	109.504	-	-	-	-
A69	CA	52.257	51.977	K71	HG2	1.538	1.488	G74	HN	7.998	8.09	-	-	-	-
A69	CB	15.513	16.05	K71	HG3	1.43	1.41	L75	CA	51.31	51.428	-	-	-	-
A69	HA	4.361	4.373	K71	N	120.039	120.443	L75	CB	40.512	40.237	-	-	-	-
A69	HB	1.773	1.773	K71	HN	8.185	8.238	L75	CD1	23.023	23.422	-	-	-	-

A.12. Unique inter-residual NOEs of VHP35_L69A

Table A.8.: **Unique inter-residual NOEs of VHP35_L69A at 0.1 MPa and 240 MPa.**

0.1 MPa					240 MPa				
AA	**Atom**		**AA**	**Atom**	**AA**	**Atom**		**AA**	**Atom**
42 L42	HG	:	F47	HB2	D46	HB3	:	A49	HA
43 S43	HB3	:	E45	HB2	F47	HE2	:	M53	HG2
47 F47	HD1	:	R55	HB3	F47	HE2	:	T54	HA
47 F47	HE2	:	R55	HD3	A49	HB	:	V50	HA
47 F47	HE2	:	R55	HD2	F51	HE1	:	V50	HB
47 F47	HD1	:	R55	HA	F51	HD1	:	V50	H
47 F47	HD2	:	F58	HB3	F51	HZ	:	K70	HG2
47 F47	HD2	:	F58	HB2	M53	HE	:	L61	HD1
50 V50	HG1	:	F47	HA	S56	HA	:	F47	HE2
51 F51	HD1	:	F47	HB3	F58	HD2	:	R55	HA
51 F51	HD1	:	V50	HG1	F58	HA	:	L61	HD2
51 F51	HB3	:	M53	HG2	F58	HE1	:	K65	HA
51 F51	HE1	:	K73	HG3	F58	HZ	:	K70	HG3
53 M53	HB2	:	E45	HG3	P62	HD3	:	L61	H
55 R55	HB2	:	F58	HD2	P62	HA	:	L63	HG
55 R55	HG2	:	F58	HE2	P62	HG3	:	K65	HG3
57 A57	HA	:	R55	HD3	P62	HB2	:	K65	HG3
57 A57	HB	:	S56	HA	L63	H	:	P62	HG3
58 F58	HD1	:	F51	HD1	L63	HG	:	Q67	HB3
58 F58	HE2	:	R55	HG3	K65	HB3	:	P62	HB3
58 F58	HB3	:	A57	HB	K65	H	:	P62	HB3
58 F58	HE2	:	K70	HE2	K65	H	:	W64	HB2
59 A59	H	:	L61	HA	Q67	HG3	:	L63	HG
63 L63	HD1	:	Q66	HE22	A69	H	:	Q67	HB2
63 L63	HD2	:	Q66	HE22	A69	HB	:	E72	HB3
66 Q66	H	:	W64	HA	E72	HB3	:	L69	HB
67 Q67	HB3	:	Q66	H	K73	HG3	:	V50	HG1
68 N68	HB3	:	L69	HB					
70 K70	HG3	:	L69	HB					
71 K71	H	:	K73	HB2					
73 K73	HG2	:	V50	HG2					
73 K73	HD2	:	V50	HG2					
73 K73	HB2	:	K70	HE3					
73 K73	HE2	:	L75	HB2					

A.13. 10 lowest-energy conformers of VHP35_L69A

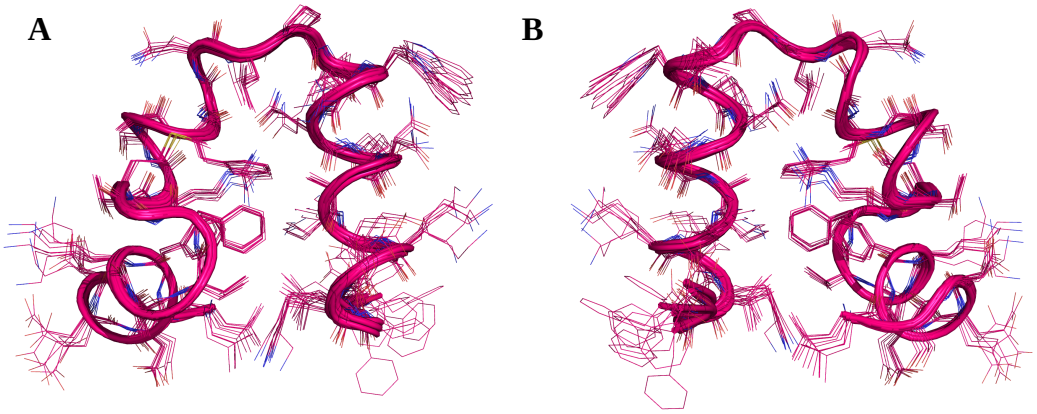

Figure A.21.: **Superposition of the backbone heavy atoms of the 10 lowest-energy final conformers of VHP35_L69A at 0.1 MPa:** (A) shows the 10 lowest-energy structures of the final calculations with an RMSD of 0.32 Å. (B) shows the rotation by 180° about the y-axis. Side chains are shown as sticks without hydrogens.

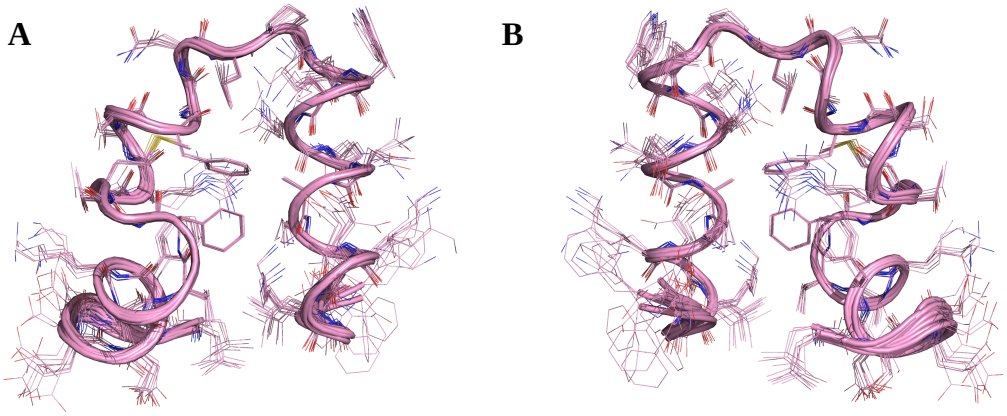

Figure A.22.: **Superposition of the backbone heavy atoms of the 10 lowest-energy *control* conformers of VHP35_L69A at 0.1 MPa:** (A) shows the 10 lowest-energy structures of the *control* calculations with an RMSD of 0.33 Å. (B) shows the rotation by 180° about the y-axis. Side chains are shown as sticks without hydrogens.

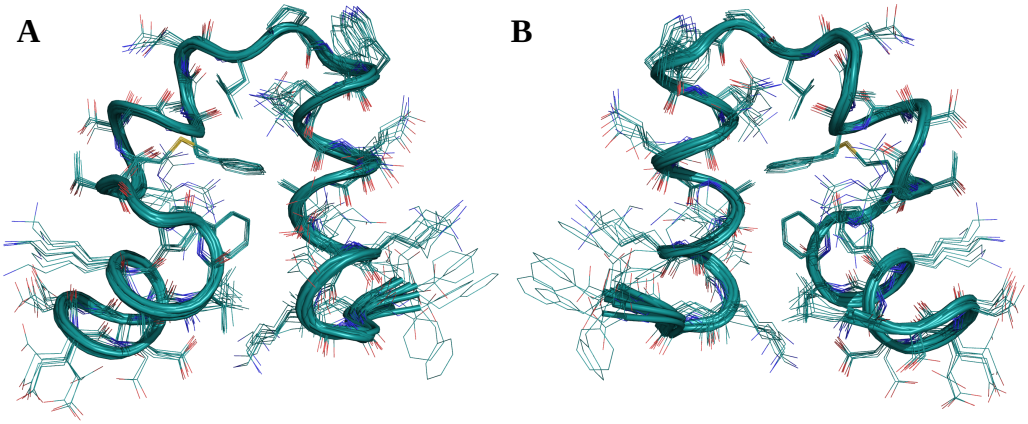

Figure A.23.: **Superposition of the backbone heavy atoms of the 10 lowest-energy final conformers of VHP35_L69A at 240 MPa:** (A) shows the 10 lowest-energy structures of the final calculations with an 0.44 RMSD of *Å*. (B) shows the rotation by 180° about the y-axis. Side chains are shown as sticks without hydrogens.

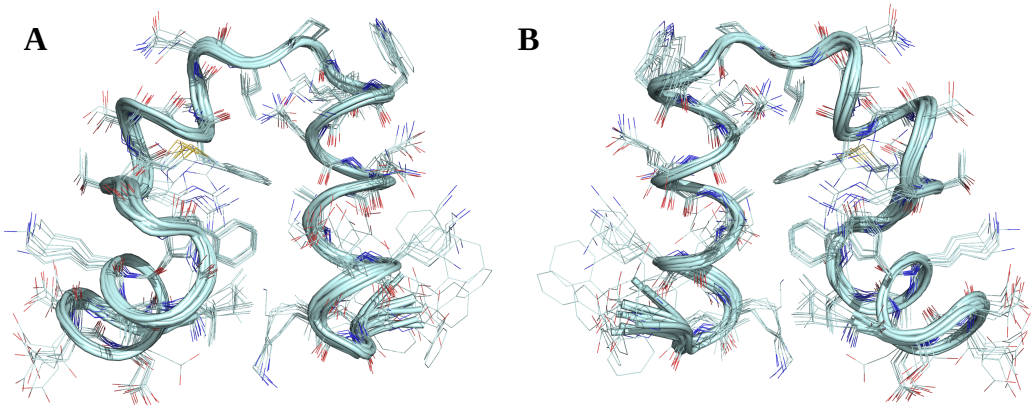

Figure A.24.: **Superposition of the backbone heavy atoms of the 10 lowest-energy *control* conformers of VHP35_L69A at 240 MPa:** (A) shows the 10 lowest-energy structures of the *control* calculations with an RMSD of 0.43 *Å*. (B) shows the rotation by 180° about the y-axis. Side chains are shown as sticks without hydrogens.

A.14. Local superposition of VHP35_L69A

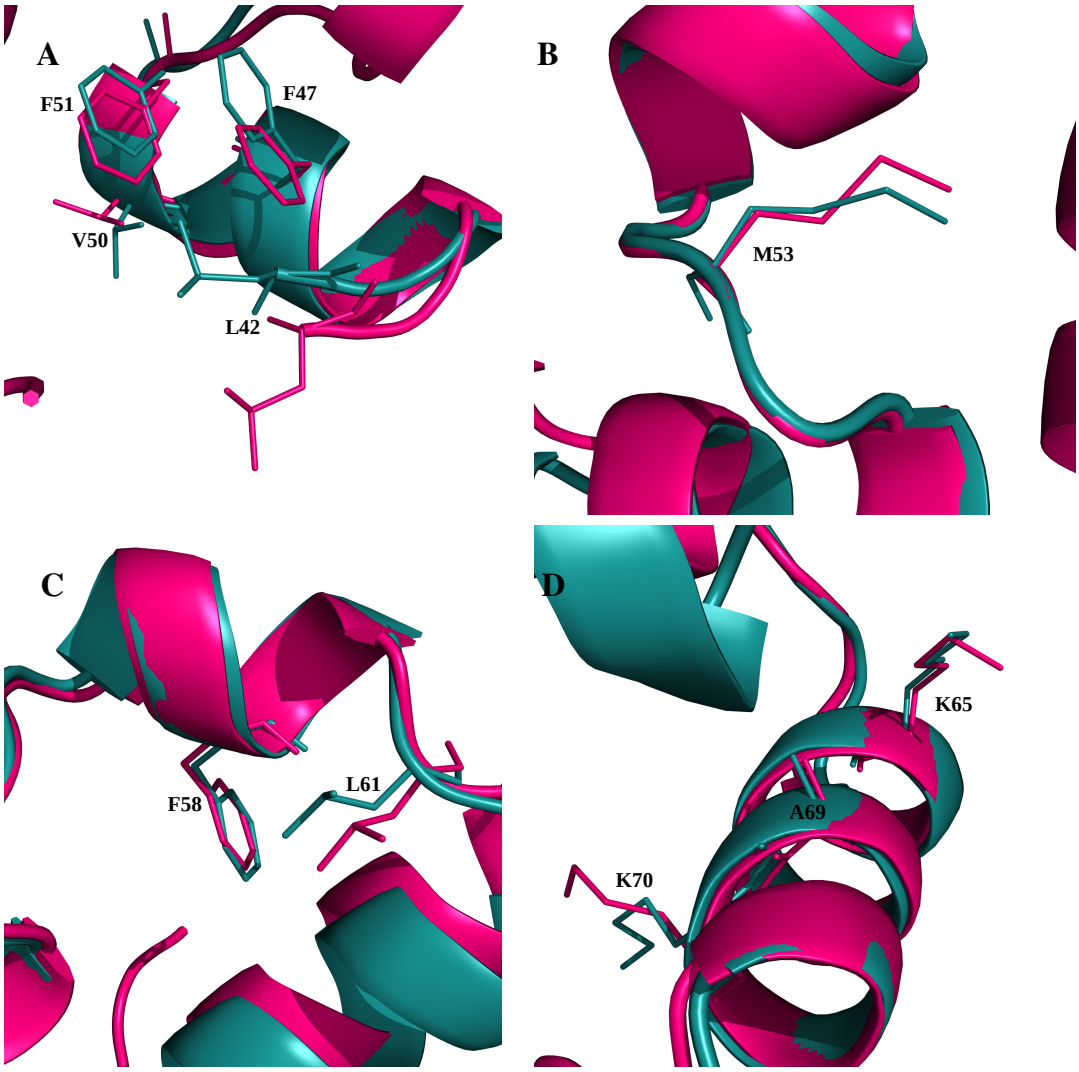

Figure A.25.: **Local superposition of the final minimized average NMR structures of VHP35_L69A at 0.1 MPa and 240 MPa with the hydrophobic core residues:** Backbone alignment of (A) the N-terminal helix α1, (B) the first turn, (C) the second helix α2 and turn 2, and (D) the C-terminal helix α3 of VHP35_L69A at 0.1 MPa (*purple*) and at 240 MPa (*green*). Side chains of the hydrophobic core are shown as sticks without hydrogens and with labels.

A.15. Charged side chains of VHP35_L69A

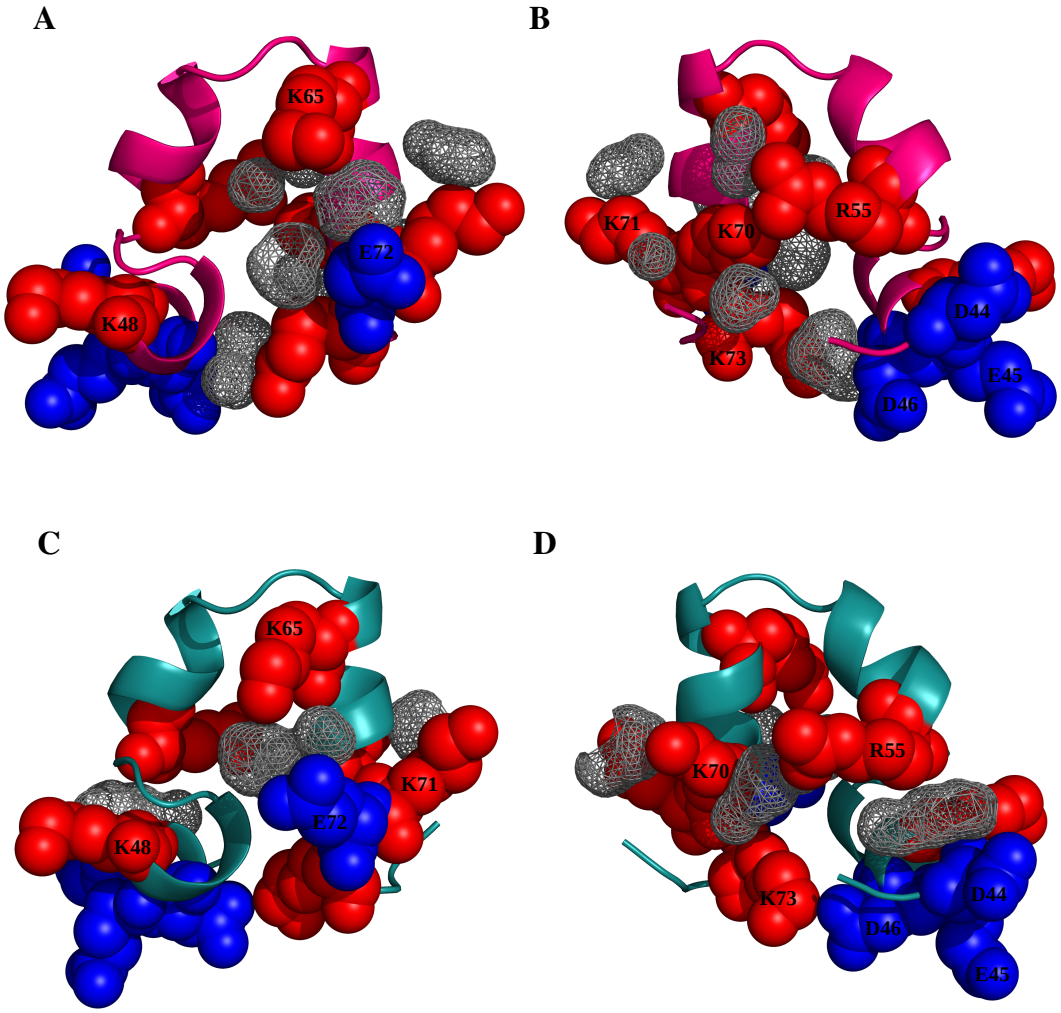

Figure A.26.: **Charged side chains of the final minimized average NMR structures of VHP35_L69A at 0.1 MPa and 240 MPa:** (A) shows the positively (*blue*) and negatively (*red*) charged residues of VHP35_L69A at 0.1 MPa and (C) at 240 MPa. The side chains are shown as spheres without hydrogens and with labels. (B) and (D) show the rotation by 180° about the y-axis. Structures are shown with the corresponding cavity distribution (*gray*) (Fig. 3.16).

A.16. Pressure dependence of the ^{1}H and ^{15}N chemical shifts of VHP35

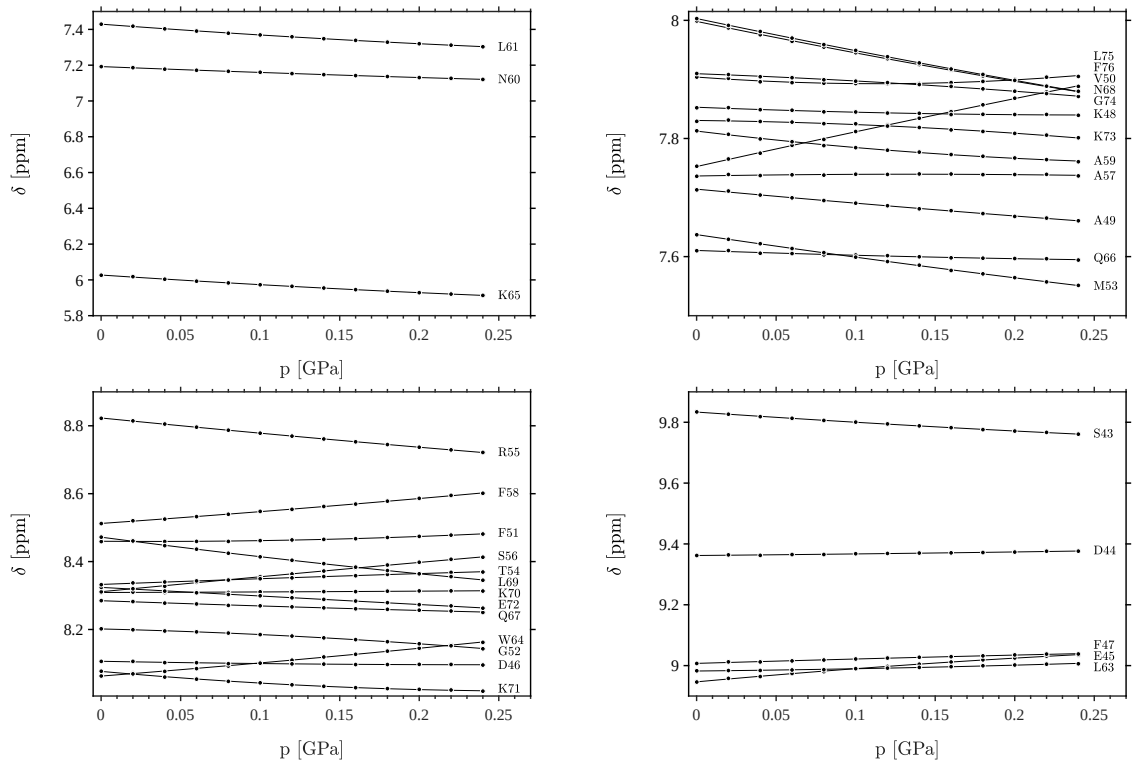

Figure A.27.: **Pressure dependence of the chemical shifts of the amide protons of VHP35 (Fig. 3.21):** Chemical shifts (δ) as a function of pressure (p) from ambient pressure up to 0.24 GPa in steps of 0.02 GPa at 278 K and at pH 7.0. Second-order polynomial fit (*solid* line) determined by the equation 2.63

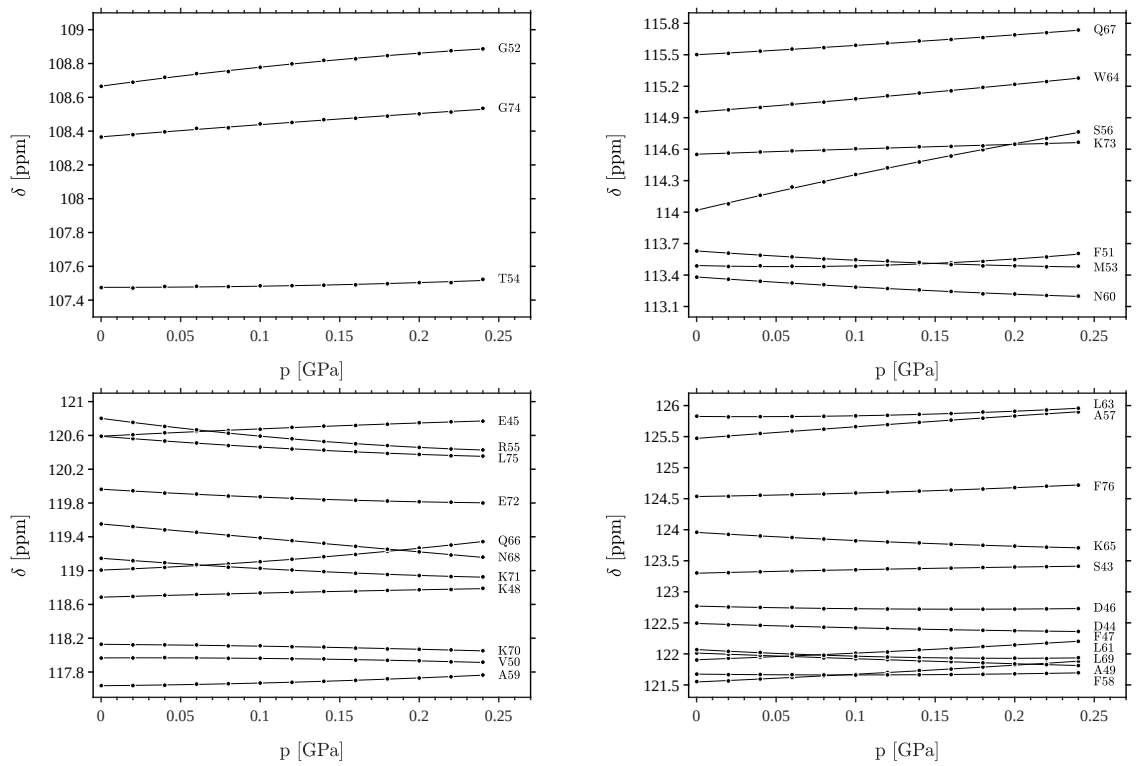

Figure A.28.: **Pressure dependence of the chemical shifts of the backbone nitrogens of VHP35 (Fig. 3.21):** Chemical shifts (δ) as function of pressure (p) from ambient pressure up to 0.24 GPa in steps of 0.02 GPa at 278 K and at pH 7.0. Second-order polynomial fit (*solid* line) determined by the equation 2.63

A.17. Pressure coefficients of the ^{1}H and ^{15}N chemical shifts of VHP35

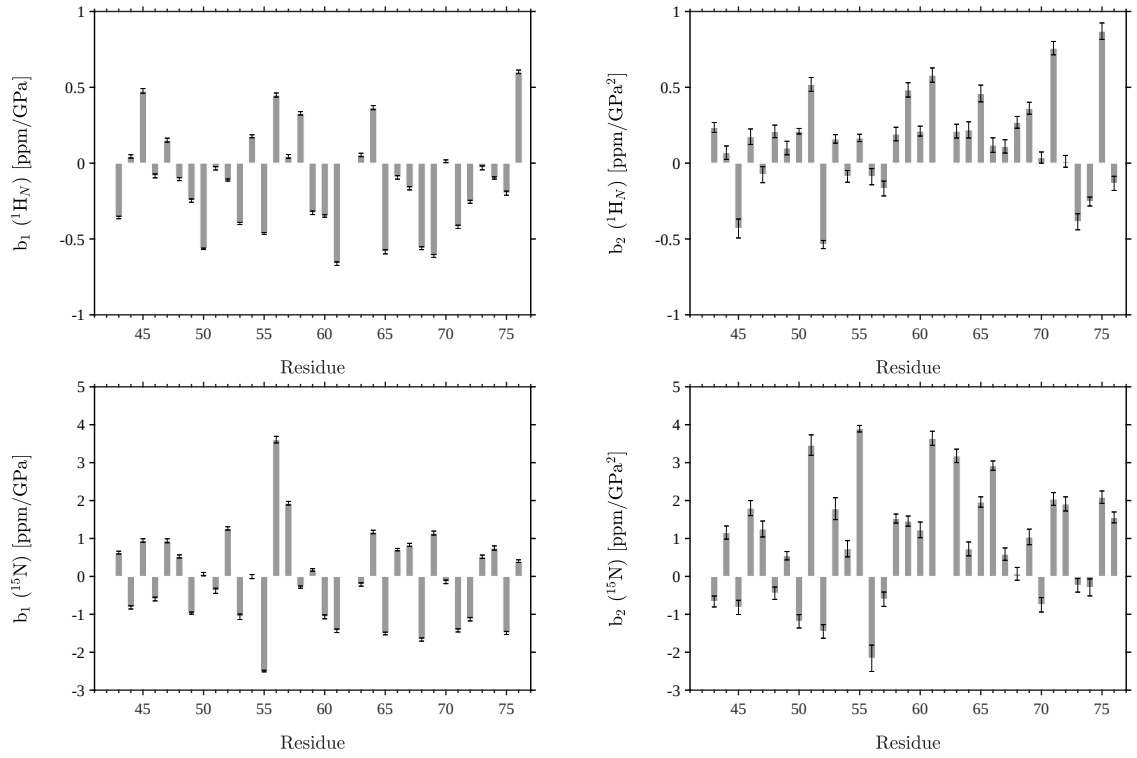

Figure A.29.: **Pressure coefficients of the protein backbone of VHP35:** Residue-specific linear (b_1) and quadratic (b_2) pressure coefficients of the amide protons ($^{1}H_N$) and nitrogens (^{15}N) determined by the equation 2.63.

Table A.9.: **Pressure coefficients and the ratio (b_2/b_1) of the amide protons ($^1\mathbf{H}_N$) of VHP35 with the corresponding mean (μ) and standard deviation (σ). Values (x) in bold: $|x| > (|\mu| + |\sigma|)$.**

AA	b_0 [ppm]	b_1 [ppm/GPa]	b_2 [ppm/GPa^2]	b_2/b_1 [GPa^{-1}]
L42	-	-	-	-
S43	9.83 ±0.000	-0.36 ±0.008	0.24 ±0.033	-0.66 ±0.076
D44	9.36 ±0.001	0.04 ±0.011	0.07 ±0.044	1.55 ±1.382
E45	8.95 ±0.001	**0.48** ±0.016	-0.43 ±0.062	-0.91 ±0.101
D46	8.11 ±0.001	-0.08 ±0.013	0.17 ±0.051	-2.07 ±0.294
F47	9.01 ±0.001	0.15 ±0.013	-0.08 ±0.053	-0.50 ±0.306
K48	7.85 ±0.001	-0.10 ±0.010	0.21 ±0.041	-2.00 ±0.197
A49	7.71 ±0.001	-0.25 ±0.011	0.10 ±0.045	-0.40 ±0.162
V50	8.00 ±0.000	**-0.57** ±0.005	0.21 ±0.018	-0.37 ±0.029
F51	8.46 ±0.001	-0.03 ±0.011	**0.52** ±0.046	**-15.43** ±3.867
G52	8.20 ±0.000	-0.11 ±0.007	**-0.54** ±0.027	**4.82** ±0.530
M53	7.64 ±0.000	-0.40 ±0.007	0.16 ±0.028	-0.40 ±0.064
T54	8.33 ±0.000	0.18 ±0.010	-0.09 ±0.039	-0.49 ±0.192
R55	8.82 ±0.000	**-0.46** ±0.006	0.17 ±0.024	-0.36 ±0.047
S56	8.31 ±0.001	0.45 ±0.013	-0.09 ±0.053	-0.20 ±0.113
A57	7.74 ±0.001	0.04 ±0.012	-0.17 ±0.049	-3.73 ±0.077
F58	8.51 ±0.001	0.33 ±0.011	0.19 ±0.045	0.58 ±0.155
A59	7.81 ±0.001	-0.33 ±0.012	**0.48** ±0.047	-1.48 ±0.091
N60	7.19 ±0.000	-0.35 ±0.008	0.21 ±0.033	-0.61 ±0.080
L61	7.43 ±0.001	**-0.66** ±0.012	**0.58** ± 0.047	-0.88 ±0.055
P62	-	-	-	-
L63	8.98 ±0.001	0.05 ±0.011	0.21 ±0.045	3.92 ±1.653
W64	8.06 ±0.001	0.37 ±0.013	0.22 ±0.054	0.60 ±0.168
K65	6.03 ±0.001	**-0.58** ±0.014	**0.46** ± 0.055	-0.79 ±0.076
Q66	7.61 ±0.001	-0.09 ±0.012	0.12 ±0.048	-1.27 ±0.349
Q67	8.28 ±0.001	-0.17 ±0.011	0.11 ±0.044	-0.67 ±0.221
N68	8.00 ±0.000	**-0.56** ±0.010	0.27 ±0.039	-0.48 ±0.061
L69	8.47 ±0.001	**-0.61** ±0.010	0.36 ±0.039	-0.59 ±0.055
K70	8.31 ±0.000	0.01 ±0.009	0.04 ±0.037	2.96 ±5.167
K71	8.08 ±0.001	-0.42 ±0.011	**0.76** ±0.044	-1.81 ±0.058
E72	8.32 ±0.000	-0.25 ±0.010	0.01 ±0.039	-0.05 ±0.151
K73	7.83 ±0.001	-0.03 ±0.013	-0.39 ±0.053	**12.52** ±7.064
G74	7.91 ±0.000	-0.10 ±0.007	-0.25 ±0.029	2.59 ±0.494
L75	7.90 ±0.001	-0.20 ±0.014	**0.87** ±0.054	**-4.40** ±0.026
F76	7.75 ±0.001	**0.60** ±0.012	-0.13 ±0.047	-0.22 ±0.073
$\mu \pm \sigma$	8.15 ±0.679	-0.12 ±0.333	0.14 ±0.314	-0.34 ±3.960

Table A.10.: **Pressure coefficients and the ratio (b_2/b_1) of the nitrogens of VHP35 with the corresponding mean (μ) and standard deviation (σ) (values in brackets defined as outliers). Values (x) in bold: $|x| > (|\mu| + |\sigma|)$.**

AA	b_0 [ppm]	b_1 [ppm/GPa]	b_2 [ppm/GPa^2]	b_2/b_1 [GPa^{-1}]
L42	-	-	-	-
S43	123.30 ±0.002	0.63 ±0.036	-0.66 ±0.144	-1.05 ±0.170
D44	122.49 ±0.002	-0.82 ±0.043	1.16 ±0.173	-1.41 ±0.137
E45	120.59 ±0.002	0.95 ±0.047	-0.82 ±0.187	-0.86 ±0.155
D46	122.77 ±0.003	-0.60 ±0.049	1.80 ±0.198	-3.02 ±0.082
F47	121.91 ±0.003	0.94 ±0.052	1.25 ±0.210	1.33 ±0.297
K48	118.69 ±0.002	0.53 ±0.040	-0.44 ±0.163	-0.84 ±0.244
A49	122.01 ±0.001	-0.97 ±0.027	0.54 ±0.110	-0.56 ±0.098
V50	117.97 ±0.002	0.06 ±0.044	-1.18 ±0.177	**-20.03** ±11.909
F51	113.49 ±0.003	-0.38 ±0.067	**3.46** ±0.270	**-9.11** ±0.900
G52	108.67 ±0.002	1.27 ±0.044	-1.45 ±0.178	-1.15 ±0.101
M53	113.63 ±0.004	-1.06 ±0.072	1.79 ±0.289	-1.68 ±0.158
T54	107.48 ±0.003	-0.01 ±0.053	0.73 ±0.214	(-128.97 ±1178.743)
R55	120.80 ±0.001	**-2.50** ±0.021	**3.90** ±0.086	-1.56 ±0.021
S56	114.02 ±0.004	**3.61** ±0.087	-2.16 ±0.348	-0.60 ±0.082
A57	125.47 ±0.002	**1.93** ±0.047	-0.60 ±0.189	-0.31 ±0.090
F58	121.67 ±0.002	-0.28 ±0.030	1.53 ±0.119	-5.41 ±0.146
A59	117.64 ±0.002	0.17 ±0.033	1.46 ±0.134	**8.57** ±2.470
N60	113.38 ±0.003	-1.07 ±0.051	1.23 ±0.206	-1.15 ±0.138
L61	122.07 ±0.002	**-1.43** ±0.046	**3.64** ±0.187	-2.54 ±0.048
P62	-	-	-	-
L63	125.82 ±0.002	-0.21 ±0.044	**3.18** ±0.177	**-14.89** ±2.240
W64	114.95 ±0.002	1.17 ±0.046	0.72 ±0.183	0.62 ±0.181
K65	123.96 ±0.002	**-1.51** ±0.034	1.96 ±0.137	-1.30 ±0.062
Q66	119.01 ±0.002	0.71 ±0.031	**2.92** ±0.123	4.14 ±0.353
Q67	115.50 ±0.002	0.83 ±0.041	0.59 ±0.163	0.71 ±0.230
N68	119.55 ±0.002	**-1.67** ±0.042	0.07 ±0.169	-0.04 ±0.100
L69	121.55 ±0.003	1.14 ±0.051	1.04 ±0.205	0.91 ±0.220
K70	118.13 ±0.002	-0.14 ±0.048	-0.75 ±0.191	5.22 ±3.058
K71	119.15 ±0.002	**-1.42** ±0.042	2.04 ±0.168	-1.43 ±0.076
E72	119.96 ±0.002	-1.13 ±0.046	1.91 ±0.186	-1.69 ±0.095
K73	114.55 ±0.002	0.52 ±0.045	-0.24 ±0.179	-0.46 ±0.306
G74	108.37 ±0.003	0.75 ±0.056	-0.29 ±0.223	-0.39 ±0.270
L75	120.59 ±0.002	**-1.49** ±0.041	2.09 ±0.163	-1.40 ±0.071
F76	124.53 ±0.002	0.40 ±0.036	1.56 ±0.143	3.87 ±0.699
$\mu \pm \sigma$	118.60 ±4.853	-0.03 ±1.238	0.97 ±1.533	-1.48 ±5.20

A.18. Pressure dependence of the ^{1}H and ^{15}N chemical shifts of VHP35_L69A

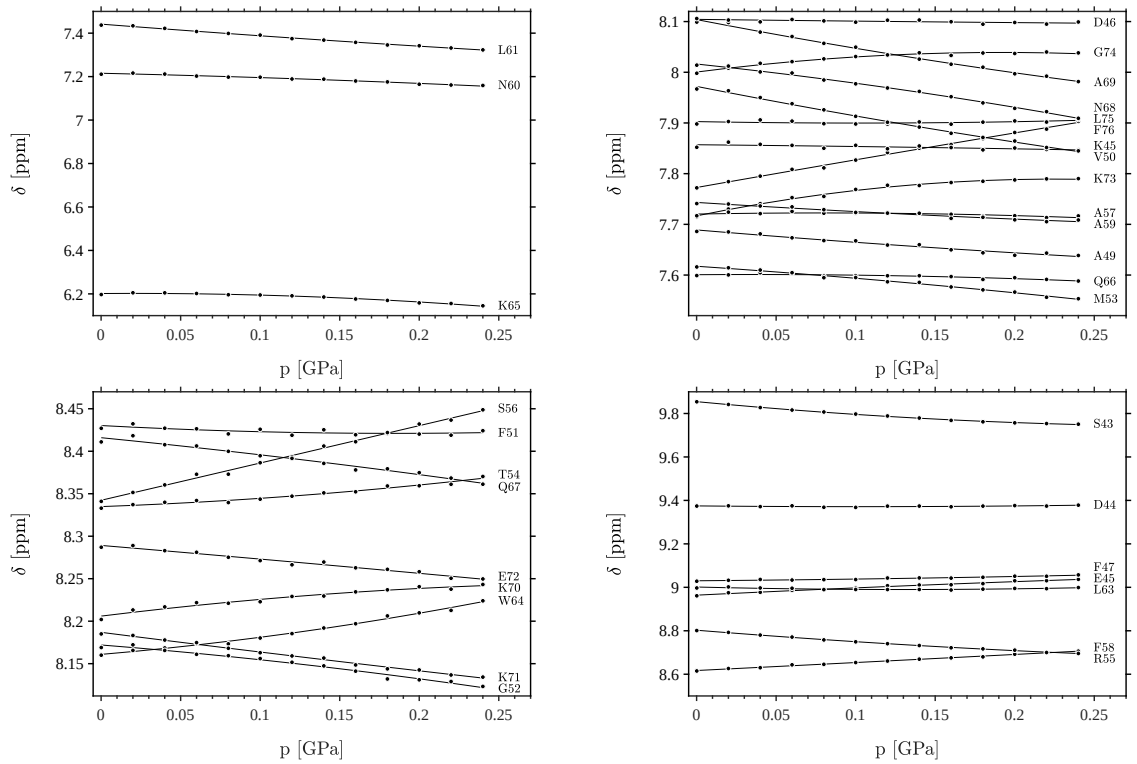

Figure A.30.: **Pressure dependence of the chemical shifts of the amide protons of VHP35_L69A (Fig. 3.22):** Chemical shifts (δ) as function of pressure (p) from ambient pressure up to 0.24 GPa in steps of 0.02 GPa at 278 K and at pH 7.0. Second-order polynomial fit (*solid* line) determined by the equation 2.63

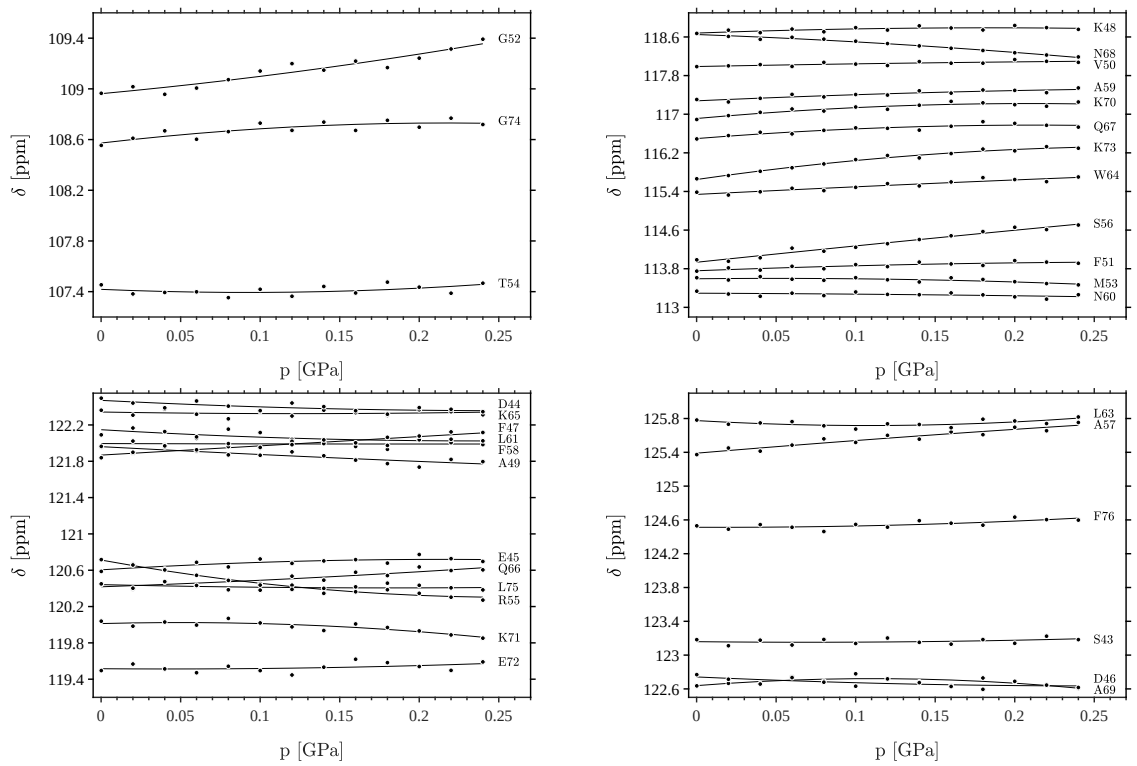

Figure A.31.: **Pressure dependence of the chemical shifts of the backbone nitrogens of VHP35_L69A (Fig. 3.22):** Chemical shifts (δ) as function of pressure (p) from ambient pressure up to 0.24 GPa in steps of 0.02 GPa at 278 K and at pH 7.0. Second-order polynomial fit (*solid* line) determined by the equation 2.63

A.19. Pressure coefficients of the ^{1}H and ^{15}N chemical shifts of VHP35_L69A

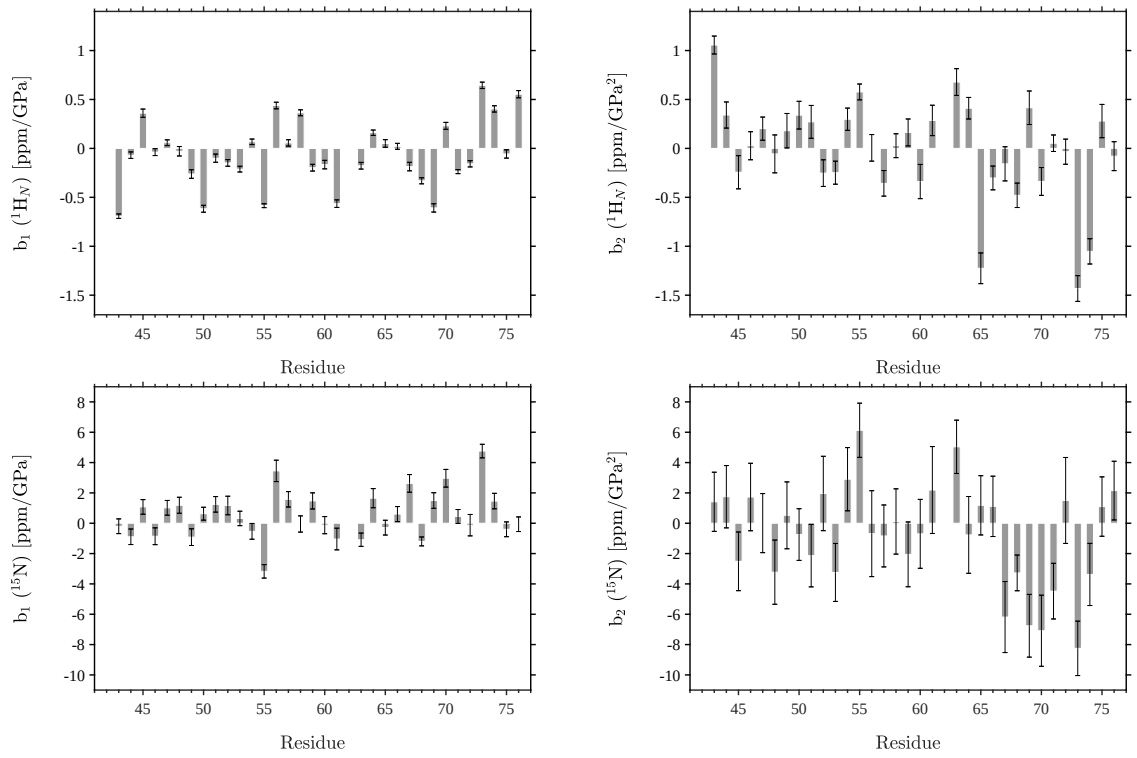

Figure A.32.: **Pressure coefficients of the protein backbone of VHP35_L69A:** Residue-specific linear (b_1) and quadratic (b_2) pressure coefficients of the amide protons ($^{1}H_N$) and nitrogens (^{15}N) determined by the equation 2.63.

Table A.11.: **Pressure coefficients and the ratio (b_2/b_1) of the amide protons ($^{1}H_N$) of VHP35_L69A with the corresponding mean (μ) and standard deviation (σ). Values (x) in bold: $|x| > (|\mu| + |\sigma|)$.**

AA	b_0 [ppm]	b_1 [ppm/GPa]	b_2 [ppm/GPa^2]	b_2/b_1 [GPa^{-1}]
L42	-	-	-	-
S43	9.85 ±0.001	**-0.69** ±0.023	**1.06** ±0.091	-1.53 ±0.082
D44	9.37 ±0.002	-0.07 ±0.033	0.34 ±0.133	-4.94 ±0.443
E45	8.96 ±0.002	0.36 ±0.042	-0.24 ±0.170	-0.68 ±0.392
D46	8.10 ±0.002	-0.04 ±0.036	0.03 ±0.143	-0.73 ±3.131
F47	9.03 ±0.002	0.06 ±0.029	0.20 ±0.118	3.47 ±3.799
K48	7.86 ±0.002	-0.03 ±0.048	-0.06 ±0.194	1.92 ±9.804
A49	7.69 ±0.002	-0.26 ±0.044	0.18 ±0.176	-0.69 ±0.557
V50	7.97 ±0.002	**-0.62** ±0.035	0.34 ±0.142	-0.55 ±0.198
F51	8.43 ±0.002	-0.10 ±0.042	0.27 ±0.168	-2.71 ±0.545
G52	8.17 ±0.002	-0.15 ±0.034	-0.25 ±0.136	1.70 ±1.305
M53	7.62 ±0.002	-0.21 ±0.029	-0.25 ±0.118	1.17 ±0.716
T54	8.33 ±0.001	0.07 ±0.028	0.30 ±0.114	4.43 ±3.550
R55	8.80 ±0.001	**-0.59** ±0.020	**0.58** ±0.081	-0.99 ±0.104
S56	8.34 ±0.002	**0.44** ±0.034	0.01 ±0.136	0.01 ±0.311
A57	7.72 ±0.002	0.06 ±0.033	-0.36 ±0.131	-6.34 ±1.346
F58	8.62 ±0.002	0.36 ±0.030	0.03 ±0.122	0.08 ±0.341
A59	7.74 ±0.002	-0.20 ±0.034	0.16 ±0.137	-0.83 ±0.554
N60	7.22 ±0.002	-0.17 ±0.044	-0.34 ±0.175	2.05 ±1.593
L61	7.44 ±0.002	**-0.56** ±0.039	0.29 ±0.155	-0.51 ±0.240
P62	-	-	-	-
L63	9.00 ±0.002	-0.18 ±0.034	**0.68** ±0.137	-3.83 ±0.036
W64	8.16 ±0.001	0.16 ±0.027	0.41 ±0.110	2.57 ±1.127
K65	6.20 ±0.002	0.05 ±0.039	**-1.23** ±0.157	**-24.37** ±15.819
Q66	7.60 ±0.002	0.02 ±0.030	-0.30 ±0.121	**-14.18** ±14.428
Q67	8.42 ±0.002	-0.19 ±0.043	-0.16 ±0.174	0.85 ±1.138
N68	8.02 ±0.002	-0.33 ±0.031	-0.48 ±0.125	1.45 ±0.513
L69	8.10 ±0.002	**-0.61** ±0.043	0.42 ±0.171	-0.68 ±0.234
K70	8.21 ±0.002	0.23 ±0.035	-0.34 ±0.142	-1.47 ±0.392
K71	8.19 ±0.001	-0.24 ±0.021	0.05 ±0.084	-0.22 ±0.336
E72	8.29 ±0.002	-0.16 ±0.032	-0.03 ±0.128	0.21 ±0.859
K73	7.72 ±0.002	**0.64** ±0.033	**-1.43** ±0.131	-2.22 ±0.091
G74	8.00 ±0.002	**0.40** ±0.032	**-1.05** ±0.129	-2.61 ±0.112
L75	7.90 ±0.002	-0.06 ±0.042	0.28 ±0.170	-4.91 ±0.665
F76	7.77 ±0.002	**0.55** ±0.037	-0.08 ±0.148	-0.14 ±0.257
$\mu \pm \sigma$	8.15 ±0.669	-0.06 ±0.339	-0.03 ±0.513	-1.67 ±5.265

Table A.12.: **Pressure coefficients and the ratio (b_2/b_1) of the nitrogens (^{15}N) of VHP35_L69A with the corresponding mean (μ) and standard deviation (σ). Values (x) in bold: $|x| > (|\mu| + |\sigma|)$.**

AA	b_0 [ppm]	b_1 [ppm/GPa]	b_2 [ppm/GPa^2]	b_2/b_1 [GPa^{-1}]
L42	-	-	-	-
S43	123.16 ±0.025	-0.20 ±0.486	1.41 ±1.951	-7.15 ±7.687
D44	122.47 ±0.026	-0.89 ±0.512	1.75 ±2.054	-1.96 ±1.178
E45	120.60 ±0.025	1.08 ±0.482	-2.51 ±1.935	-2.33 ±0.753
D46	122.74 ±0.029	-0.86 ±0.554	1.73 ±2.224	-2.02 ±1.291
F47	121.87 ±0.025	1.02 ±0.485	0.01 ±1.948	0.01 ±1.920
K48	118.68 ±0.027	1.19 ±0.527	-3.23 ±2.116	-2.72 ±0.575
A49	121.96 ±0.028	-0.92 ±0.549	0.52 ±2.205	-0.57 ±2.063
V50	117.99 ±0.022	0.63 ±0.424	-0.75 ±1.704	-1.18 ±1.909
F51	113.76 ±0.027	1.25 ±0.513	-2.13 ±2.061	-1.71 ±0.948
G52	108.96 ±0.032	1.17 ±0.610	1.96 ±2.451	1.68 ±2.968
M53	113.59 ±0.025	0.32 ±0.476	-3.24 ±1.911	**-10.24** ±9.346
T54	107.42 ±0.027	-0.53 ±0.519	2.90 ±2.085	-5.44 ±1.390
R55	120.71 ±0.023	**-3.17** ±0.445	**6.13** ±1.787	-1.93 ±0.292
S56	113.93 ±0.036	**3.45** ±0.705	-0.69 ±2.832	-0.20 ±0.780
A57	125.39 ±0.026	1.58 ±0.509	-0.84 ±2.042	-0.53 ±1.123
F58	122.00 ±0.028	-0.05 ±0.536	0.12 ±2.153	-2.38 ±18.016
A59	117.28 ±0.027	1.47 ±0.532	-2.05 ±2.136	-1.39 ±0.947
N60	113.29 ±0.029	-0.13 ±0.566	-0.70 ±2.271	5.57 ±43.210
L61	122.15 ±0.037	-1.04 ±0.714	2.19 ±2.866	-2.10 ±1.311
P62	-	-	-	-
L63	125.78 ±0.023	-1.09 ±0.438	**5.04** ±1.757	-4.63 ±0.249
W64	115.34 ±0.033	1.65 ±0.631	-0.77 ±2.533	-0.47 ±1.354
K65	122.34 ±0.025	-0.29 ±0.487	1.18 ±1.954	-4.07 ±0.085
Q66	120.42 ±0.026	0.61 ±0.495	1.11 ±1.989	1.84 ±4.788
Q67	116.50 ±0.030	**2.63** ±0.583	**-6.18** ±2.342	-2.35 ±0.369
N68	118.65 ±0.015	-1.20 ±0.293	-3.27 ±1.176	2.73 ±1.649
L69	122.64 ±0.027	1.50 ±0.515	-6.76 ±2.068	-4.52 ±0.172
K70	116.91 ±0.030	**2.96** ±0.584	**-7.09** ±2.344	-2.39 ±0.320
K71	120.01 ±0.024	0.45 ±0.457	**-4.48** ±1.834	**-10.00** ±6.100
E72	119.52 ±0.036	-0.13 ±0.706	1.50 ±2.834	**-11.83** ±43.427
K73	115.65 ±0.023	**4.76** ±0.447	**-8.25** ±1.793	-1.73 ±0.214
G74	108.57 ±0.026	1.46 ±0.510	-3.38 ±2.049	-2.31 ±0.595
L75	120.44 ±0.025	-0.40 ±0.488	1.10 ±1.958	-2.75 ±1.540
F76	124.51 ±0.025	-0.06 ±0.482	2.15 ±1.934	**-33.13** ±215.933
$\mu \pm \sigma$	118.64 ±4.762	0.55 ±1.544	-0.77 ±3.366	-3.40 ±6.407

A.20. Relaxation rates of VHP35

Table A.13.: R_1 **and** R_2 **relaxation rates of VHP35 at 0.1 MPa and 240 MPa and the corresponding difference (**Δ**) with the mean (**μ**) and standard deviation (**σ**). Values (x) in bold:** $|x| > (|\mu| + |\sigma|)$**.**

AA	R_1 [s^{-1}]		$\Delta R_1^{[0.1,240]}$ [s^{-1}]	R_2 [s^{-1}]		$\Delta R_2^{[0.1,240]}$ [s^{-1}]
	0.1 MPa	240 MPa		0.1 MPa	240 MPa	
L42	-	-	-	-	-	-
S43	2.19 ±0.06	2.18 ±0.05	0.00 ±0.01	6.44 ±0.42	5.93 ±0.21	0.51 ±0.21
D44	2.28 ±0.04	2.24 ±0.06	0.04 ±0.02	5.69 ±0.39	5.62 ±0.07	0.07 ±0.33
E45	2.15 ±0.03	2.25 ±0.05	**-0.11** ±0.02	5.60 ±0.21	5.51 ±0.11	0.10 ±0.10
D46	2.25 ±0.07	2.33 ±0.03	-0.08 ±0.04	6.15 ±0.22	5.51 ±0.11	0.64 ±0.11
F47	2.29 ±0.04	2.32 ±0.08	-0.03 ±0.04	5.77 ±0.35	6.00 ±0.16	-0.23 ±0.19
K48	2.23 ±0.03	2.31 ±0.05	-0.07 ±0.02	6.40 ±0.23	6.60 ±0.29	-0.20 ±0.07
A49	2.24 ±0.04	2.32 ±0.03	-0.08 ±0.01	6.11 ±0.16	5.92 ±0.16	0.19 ±0.00
V50	2.16 ±0.03	2.16 ±0.05	0.00 ±0.02	5.99 ±0.18	5.51 ±0.24	0.48 ±0.06
F51	2.24 ±0.06	2.32 ±0.04	-0.09 ±0.02	6.05 ±0.24	7.50 ±0.19	**-1.45** ±0.06
G52	2.21 ±0.05	2.26 ±0.05	-0.05 ±0.00	6.33 ±0.13	6.38 ±0.18	-0.05 ±0.05
M53	2.38 ±0.06	2.33 ±0.04	0.06 ±0.02	9.89 ±0.46	12.09 ±0.55	**-2.20** ±0.09
T54	2.17 ±0.05	2.26 ±0.04	**-0.09** ±0.01	5.90 ±0.18	5.90 ±0.15	0.00 ±0.03
R55	2.14 ±0.02	2.26 ±0.03	**-0.12** ±0.01	5.80 ±0.31	5.88 ±0.12	-0.08 ±0.19
S56	2.21 ±0.03	2.20 ±0.04	0.01 ±0.01	6.69 ±0.13	6.26 ±0.11	0.43 ±0.02
A57	2.28 ±0.03	2.28 ±0.05	0.00 ±0.02	7.82 ±0.35	6.80 ±0.27	**1.01** ±0.08
F58	2.18 ±0.05	2.27 ±0.03	-0.09 ±0.02	6.15 ±0.27	6.26 ±0.13	-0.11 ±0.14
A59	2.20 ±0.06	2.27 ±0.03	-0.07 ±0.03	7.12 ±0.20	6.06 ±0.27	**1.05** ±0.06
N60	2.24 ±0.05	2.18 ±0.03	0.06 ±0.02	9.97 ±0.88	11.16 ±0.71	**-1.20** ±0.17
L61	2.27 ±0.02	2.34 ±0.05	-0.06 ±0.03	6.53 ±0.23	5.94 ±0.18	0.59 ±0.06
P62	-	-	-	-	-	-
L63	2.25 ±0.04	2.32 ±0.04	-0.08 ±0.01	5.96 ±0.26	6.11 ±0.11	-0.15 ±0.14
W64	2.22 ±0.03	2.27 ±0.05	-0.05 ±0.02	8.87 ±0.30	6.58 ±0.12	**2.29** ±0.17
K65	2.42 ±0.07	2.41 ±0.07	0.01 ±0.00	6.80 ±1.48	6.51 ±1.22	0.29 ±0.25
Q66	2.30 ±0.04	2.32 ±0.06	-0.02 ±0.02	7.43 ±0.62	6.19 ±0.22	**1.23** ±0.39
Q67	2.20 ±0.04	2.27 ±0.05	-0.07 ±0.01	7.15 ±0.20	6.06 ±0.16	**1.09** ±0.04
N68	2.23 ±0.02	2.25 ±0.02	-0.02 ±0.00	6.43 ±0.22	5.93 ±0.14	0.51 ±0.08
L69	2.21 ±0.04	2.24 ±0.03	-0.03 ±0.01	6.60 ±0.18	5.82 ±0.11	0.78 ±0.07
K70	2.20 ±0.03	2.25 ±0.05	-0.05 ±0.02	5.92 ±0.16	5.85 ±0.28	0.06 ±0.13
K71	2.17 ±0.02	2.22 ±0.03	-0.06 ±0.00	6.54 ±0.54	6.44 ±0.24	0.10 ±0.30
E72	2.20 ±0.02	2.25 ±0.06	-0.04 ±0.04	6.20 ±0.16	5.80 ±0.02	0.40 ±0.13
K73	2.20 ±0.02	2.23 ±0.03	-0.03 ±0.01	6.68 ±0.18	6.70 ±0.30	-0.02 ±0.12
G74	2.13 ±0.03	2.14 ±0.05	-0.02 ±0.02	5.57 ±0.24	5.45 ±0.21	0.12 ±0.03
L75	2.04 ±0.03	2.18 ±0.04	**-0.14** ±0.01	5.02 ±0.10	4.84 ±0.21	0.18 ±0.11
F76	1.72 ±0.02	1.79 ±0.02	-0.07 ±0.00	4.08 ±0.07	3.81 ±0.13	0.27 ±0.06
$\mu \pm \sigma$	2.21 ±0.11	2.25 ±0.10	-0.04 ±0.05	6.53 ±1.20	6.33 ±1.50	0.20 ±0.79

Table A.14.: **Ratio of the R_2 and R_1 relaxation rates (Tab. A.13) and the heteronuclear NOE ratio values of VHP35 at 0.1 MPa and 240 MPa and the corresponding difference (Δ) with the mean (μ) and standard deviation (σ). Values (x) in bold: $|x| > (|\mu| + |\sigma|)$.**

AA	R_2/R_1		$\Delta R_2/R_1^{[0.1,240]}$	*het*NOE		Δ *het*NOE$^{[0.1,240]}$
	0.1 MPa	240 MPa		0.1 MPa	240 MPa	
L42	-	-	-	-	-	-
S43	2.95 ±0.27	2.71 ±0.15	0.23 ±0.12	0.64 ±0.02	0.64 ±0.02	0.00 ±0.00
D44	2.50 ±0.22	2.51 ±0.10	-0.01 ±0.12	0.76 ±0.02	0.74 ±0.02	0.02 ±0.00
E45	2.61 ±0.14	2.44 ±0.10	0.17 ±0.04	0.67 ±0.01	0.79 ±0.02	**-0.12** ±0.00
D46	2.74 ±0.19	2.37 ±0.08	0.37 ±0.11	0.76 ±0.02	0.68 ±0.01	**0.08** ±0.00
F47	2.52 ±0.20	2.58 ±0.16	-0.06 ±0.04	0.74 ±0.01	0.76 ±0.02	-0.02 ±0.00
K48	2.87 ±0.14	2.86 ±0.19	0.00 ±0.05	0.73 ±0.01	0.70 ±0.02	0.03 ±0.00
A49	2.73 ±0.12	2.55 ±0.10	0.17 ±0.02	0.75 ±0.01	0.79 ±0.01	-0.04 ±0.00
V50	2.78 ±0.12	2.55 ±0.17	0.23 ±0.05	0.73 ±0.02	0.72 ±0.01	0.01 ±0.00
F51	2.70 ±0.18	3.23 ±0.14	**-0.52** ±0.04	0.76 ±0.02	0.72 ±0.02	0.04 ±0.00
G52	2.87 ±0.13	2.82 ±0.15	0.04 ±0.02	0.75 ±0.02	0.74 ±0.02	0.01 ±0.00
M53	4.15 ±0.29	5.19 ±0.32	**-1.04** ±0.02	0.69 ±0.01	0.71 ±0.02	-0.02 ±0.00
T54	2.72 ±0.15	2.61 ±0.12	0.11 ±0.03	0.73 ±0.02	0.69 ±0.02	0.04 ±0.00
R55	2.71 ±0.17	2.60 ±0.09	0.10 ±0.08	0.75 ±0.02	0.73 ±0.02	0.02 ±0.00
S56	3.03 ±0.09	2.84 ±0.09	0.19 ±0.00	0.75 ±0.02	0.74 ±0.02	0.01 ±0.00
A57	3.43 ±0.20	2.98 ±0.18	**0.45** ±0.02	0.80 ±0.02	0.78 ±0.02	0.02 ±0.00
F58	2.82 ±0.19	2.76 ±0.09	0.06 ±0.09	0.78 ±0.02	0.77 ±0.02	0.01 ±0.00
A59	3.24 ±0.18	2.67 ±0.15	0.56 ±0.03	0.78 ±0.02	0.75 ±0.02	0.03 ±0.00
N60	4.45 ±0.49	5.13 ±0.39	**-0.68** ±0.10	0.76 ±0.01	0.72 ±0.01	0.04 ±0.00
L61	2.87 ±0.13	2.54 ±0.13	0.33 ±0.00	0.80 ±0.02	0.79 ±0.02	0.02 ±0.00
P62	-	-	-	-	-	-
L63	2.65 ±0.16	2.63 ±0.09	0.02 ±0.07	0.74 ±0.02	0.77 ±0.02	-0.03 ±0.00
W64	4.00 ±0.18	2.90 ±0.12	**1.10** ±0.07	0.81 ±0.01	0.69 ±0.01	**0.11** ±0.00
K65	2.81 ±0.69	2.71 ±0.59	0.11 ±0.10	0.75 ±0.02	0.76 ±0.02	-0.01 ±0.00
Q66	3.23 ±0.33	2.67 ±0.16	**0.55** ±0.16	0.74 ±0.02	0.73 ±0.02	0.01 ±0.00
Q67	3.25 ±0.15	2.67 ±0.13	**0.58** ±0.02	0.72 ±0.02	0.74 ±0.02	-0.02 ±0.00
N68	2.89 ±0.13	2.64 ±0.09	0.25 ±0.04	0.73 ±0.01	0.73 ±0.01	0.00 ±0.00
L69	2.99 ±0.14	2.60 ±0.08	0.39 ±0.06	0.77 ±0.02	0.74 ±0.02	0.03 ±0.00
K70	2.69 ±0.11	2.61 ±0.18	0.09 ±0.07	0.74 ±0.02	0.77 ±0.02	-0.03 ±0.00
K71	3.02 ±0.28	2.90 ±0.14	0.12 ±0.14	0.78 ±0.02	0.77 ±0.02	0.01 ±0.00
E72	2.81 ±0.09	2.58 ±0.08	0.23 ±0.02	0.70 ±0.01	0.71 ±0.01	0.00 ±0.00
K73	3.03 ±0.11	3.00 ±0.18	0.03 ±0.06	0.74 ±0.02	0.70 ±0.02	0.04 ±0.00
G74	2.62 ±0.14	2.54 ±0.15	0.08 ±0.01	0.68 ±0.02	0.64 ±0.02	0.04 ±0.00
L75	2.46 ±0.08	2.22 ±0.13	0.24 ±0.05	0.59 ±0.01	0.61 ±0.01	-0.02 ±0.00
F76	2.37 ±0.06	2.13 ±0.10	0.24 ±0.03	0.35 ±0.01	0.26 ±0.01	**0.10** ±0.00
$\mu \pm \sigma$	2.95 ±0.47	2.81 ±0.64	0.14 ±0.37	0.73 ±0.08	0.71 ±0.09	0.01 ±0.04

A.21. Pressure-dependent difference of the dynamic parameters of VHP35

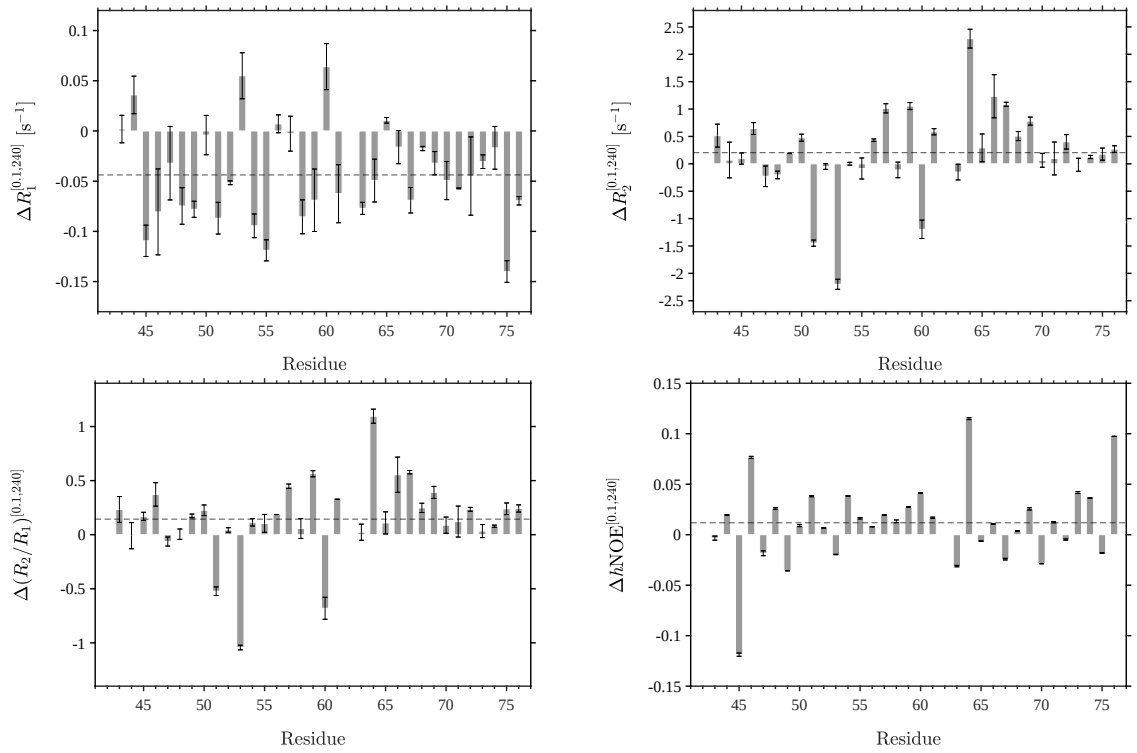

Figure A.33.: **Pressure-dependent difference of the dynamic parameters of the backbone amide protons of VHP35 (Tab. A.13, A.14):** Difference (Δ) of longitudinal (R_1) or transverse (R_2) relaxation rates, the ratio (R_2/R_1) and heteronuclear NOE ratio values at 0.1 MPa and 240 MPa, respectively, and the corresponding mean (*dashed* line).

A.22. Relaxation rates of VHP35_L69A

Table A.15.: R_1 **and** R_2 **relaxation rates of VHP35_L69A at 0.1 MPa and 240 MPa and the corresponding difference (**Δ**) with the mean (**μ**) and standard deviation (**σ**). Values (x) in bold:** $|x| > (|\mu| + |\sigma|)$**.**

AA	R_1 [s^{-1}]		$\Delta R_1^{[0.1,240]}$ [s^{-1}]	R_2 [s^{-1}]		$\Delta R_2^{[0.1,240]}$ [s^{-1}]
	0.1 MPa	240 MPa		0.1 MPa	240 MPa	
L42	-	-	-	-	-	-
S43	2.16 ±0.10	2.14 ±0.03	0.02 ±0.07	6.55 ±0.10	7.05 ±0.19	-0.50 ±0.09
D44	2.19 ±0.05	2.22 ±0.04	-0.03 ±0.00	5.57 ±0.11	5.54 ±0.21	0.03 ±0.10
E45	2.14 ±0.08	2.22 ±0.03	-0.08 ±0.05	5.94 ±0.08	5.52 ±0.12	0.42 ±0.05
D46	2.49 ±0.09	2.20 ±0.06	**0.28** ±0.03	8.44 ±0.10	5.59 ±0.16	**2.85** ±0.06
F47	2.28 ±0.09	2.29 ±0.05	-0.02 ±0.04	6.10 ±0.07	5.60 ±0.20	0.50 ±0.13
K48	2.21 ±0.04	2.29 ±0.07	-0.08 ±0.03	6.04 ±0.09	8.05 ±0.19	-2.02 ±0.10
A49	2.16 ±0.08	2.28 ±0.06	-0.12 ±0.02	10.16 ±0.36	7.23 ±0.38	**2.93** ±0.02
V50	2.10 ±0.04	2.17 ±0.05	-0.07 ±0.01	6.99 ±0.15	7.12 ±0.24	-0.13 ±0.10
F51	2.22 ±0.14	2.31 ±0.02	-0.09 ±0.11	7.99 ±0.20	14.51 ±0.45	**-6.51** ±0.25
G52	2.35 ±0.10	2.29 ±0.10	0.06 ±0.00	6.18 ±0.13	5.77 ±0.15	0.41 ±0.02
M53	2.18 ±0.12	2.30 ±0.04	-0.12 ±0.08	7.85 ±0.28	10.35 ±0.56	-2.51 ±0.28
T54	2.25 ±0.10	2.20 ±0.05	0.04 ±0.05	6.46 ±0.14	10.84 ±0.33	**-4.37** ±0.20
R55	2.06 ±0.07	2.14 ±0.04	-0.09 ±0.03	6.15 ±0.12	6.59 ±0.15	-0.44 ±0.03
S56	2.16 ±0.11	2.20 ±0.03	-0.05 ±0.08	5.63 ±0.06	6.33 ±0.06	-0.70 ±0.00
A57	2.14 ±0.10	2.24 ±0.04	-0.10 ±0.06	8.01 ±0.20	6.08 ±0.30	1.93 ±0.10
F58	2.18 ±0.09	2.24 ±0.05	-0.06 ±0.05	6.68 ±0.14	6.99 ±0.26	-0.31 ±0.12
A59	2.22 ±0.08	2.23 ±0.05	-0.02 ±0.03	7.82 ±0.15	9.12 ±0.28	-1.30 ±0.13
N60	2.07 ±0.08	2.16 ±0.03	-0.09 ±0.05	6.84 ±0.17	6.89 ±0.49	-0.06 ±0.32
L61	2.09 ±0.11	2.29 ±0.06	**-0.20** ±0.05	9.03 ±0.35	8.11 ±0.42	0.92 ±0.07
P62	-	-	-	-	-	-
L63	2.11 ±0.15	2.22 ±0.03	-0.11 ±0.13	7.90 ±0.10	8.87 ±0.28	-0.97 ±0.18
W64	2.22 ±0.09	2.26 ±0.06	-0.05 ±0.04	7.33 ±0.13	7.79 ±0.22	-0.46 ±0.10
K65	2.04 ±0.34	1.81 ±0.18	**0.23** ±0.17	13.43 ±0.85	11.34 ±1.63	2.10 ±0.77
Q66	2.34 ±0.13	2.32 ±0.04	0.02 ±0.10	15.70 ±1.10	10.95 ±0.25	**4.75** ±0.85
Q67	2.15 ±0.05	2.21 ±0.02	-0.06 ±0.03	6.69 ±0.10	8.13 ±0.18	-1.44 ±0.08
N68	2.21 ±0.03	2.29 ±0.03	-0.08 ±0.00	8.76 ±0.22	8.61 ±0.39	0.15 ±0.17
L69	2.14 ±0.01	2.21 ±0.06	-0.07 ±0.04	8.47 ±0.12	9.74 ±0.24	-1.27 ±0.12
K70	2.14 ±0.08	2.17 ±0.03	-0.03 ±0.05	6.29 ±0.09	6.87 ±0.17	-0.58 ±0.08
K71	2.17 ±0.12	2.15 ±0.06	0.02 ±0.06	6.13 ±0.06	6.61 ±0.16	-0.48 ±0.10
E72	2.17 ±0.06	2.18 ±0.05	-0.01 ±0.01	5.76 ±0.11	6.56 ±0.20	-0.80 ±0.08
K73	2.17 ±0.09	2.24 ±0.06	-0.07 ±0.03	10.53 ±0.21	13.40 ±0.53	**-2.87** ±0.32
G74	2.17 ±0.09	2.14 ±0.05	0.04 ±0.04	6.19 ±0.09	6.20 ±0.19	-0.01 ±0.09
L75	2.04 ±0.09	2.05 ±0.03	0.00 ±0.06	5.29 ±0.12	8.00 ±0.17	**-2.70** ±0.04
F76	1.68 ±0.04	1.76 ±0.03	-0.08 ±0.02	3.93 ±0.07	5.02 ±0.17	-1.09 ±0.10
$\mu \pm \sigma$	2.16 ±0.13	2.20 ±0.12	-0.03 ±0.09	7.48 ±2.32	7.92 ±2.30	-0.44 ±2.09

Table A.16.: **Ratio of the R_2 and R_1 relaxation rates (Tab. A.15) and the heteronuclear NOE ratio values of VHP35_L69A at 0.1 MPa and 240 MPa and the corresponding difference (Δ) with the mean (μ) and standard deviation (σ). Values (x) in bold: $|x| > (|\mu| + |\sigma|)$.**

AA	R_2/R_1		$\Delta R_2/R_1^{[0.1,240]}$	*het*NOE		Δ *het*NOE$^{[0.1,240]}$
	0.1 MPa	240 MPa		0.1 MPa	240 MPa	
L42	-	-	-	-	-	-
S43	3.03 ±0.19	3.30 ±0.14	-0.26 ±0.05	0.62 ±0.011	0.63 ±0.01	-0.01 ±0.00107
D44	2.54 ±0.10	2.50 ±0.14	0.04 ±0.04	0.74 ±0.011	0.72 ±0.01	0.02 ±0.00047
E45	2.77 ±0.14	2.48 ±0.08	0.29 ±0.05	0.68 ±0.009	0.76 ±0.01	**-0.08** ±0.00154
D46	3.39 ±0.17	2.54 ±0.14	0.86 ±0.03	0.78 ±0.012	0.68 ±0.01	**0.10** ±0.00191
F47	2.68 ±0.14	2.44 ±0.15	0.24 ±0.00	0.74 ±0.011	0.73 ±0.01	0.01 ±0.00188
K48	2.73 ±0.09	3.51 ±0.19	-0.78 ±0.10	0.72 ±0.010	0.70 ±0.01	0.02 ±0.00052
A49	4.70 ±0.33	3.17 ±0.25	**1.53** ±0.09	0.77 ±0.010	0.78 ±0.01	-0.01 ±0.00025
V50	3.33 ±0.14	3.28 ±0.19	0.05 ±0.05	0.71 ±0.011	0.71 ±0.01	0.00 ±0.00003
F51	3.60 ±0.31	6.27 ±0.26	**-2.67** ±0.06	0.75 ±0.013	0.70 ±0.02	0.06 ±0.00198
G52	2.63 ±0.17	2.52 ±0.18	0.11 ±0.00	0.75 ±0.011	0.73 ±0.01	0.02 ±0.00002
M53	3.60 ±0.33	4.50 ±0.32	-0.91 ±0.01	0.65 ±0.010	0.72 ±0.01	**-0.07** ±0.00190
T54	2.88 ±0.19	4.92 ±0.27	**-2.04** ±0.07	0.73 ±0.012	0.70 ±0.01	0.03 ±0.00174
R55	2.99 ±0.17	3.07 ±0.13	-0.09 ±0.04	0.77 ±0.011	0.75 ±0.01	0.02 ±0.00026
S56	2.61 ±0.16	2.87 ±0.07	-0.26 ±0.09	0.75 ±0.010	0.71 ±0.01	0.04 ±0.00048
A57	3.74 ±0.26	2.71 ±0.19	1.03 ±0.08	0.81 ±0.011	0.78 ±0.01	0.02 ±0.00058
F58	3.06 ±0.20	3.12 ±0.18	-0.06 ±0.02	0.74 ±0.012	0.78 ±0.01	-0.03 ±0.00054
A59	3.53 ±0.20	4.08 ±0.21	-0.55 ±0.01	0.79 ±0.011	0.76 ±0.01	0.03 ±0.00082
N60	3.31 ±0.21	3.20 ±0.28	0.11 ±0.06	0.72 ±0.011	0.72 ±0.01	0.00 ±0.00153
L61	4.32 ±0.40	3.54 ±0.28	0.78 ±0.12	0.79 ±0.012	0.80 ±0.01	-0.01 ±0.00091
P62	-	-	-	-	-	-
L63	3.75 ±0.32	3.99 ±0.17	-0.24 ±0.15	0.75 ±0.013	0.77 ±0.01	-0.02 ±0.00139
W64	3.31 ±0.20	3.44 ±0.18	-0.13 ±0.01	0.76 ±0.011	0.74 ±0.01	0.02 ±0.00006
K65	6.59 ±1.53	6.27 ±1.51	0.33 ±0.02	0.72 ±0.016	0.71 ±0.02	0.01 ±0.00752
Q66	6.71 ±0.85	4.72 ±0.18	**1.99** ±0.67	0.72 ±0.012	0.74 ±0.01	-0.02 ±0.00017
Q67	3.11 ±0.11	3.68 ±0.11	-0.57 ±0.00	0.77 ±0.012	0.75 ±0.01	0.02 ±0.00004
N68	3.97 ±0.15	3.77 ±0.22	0.20 ±0.07	0.75 ±0.011	0.71 ±0.01	0.03 ±0.00014
L69	3.96 ±0.08	4.41 ±0.23	-0.45 ±0.14	0.74 ±0.008	0.77 ±0.01	-0.04 ±0.00302
K70	2.95 ±0.15	3.17 ±0.13	-0.23 ±0.03	0.71 ±0.011	0.72 ±0.01	0.00 ±0.00018
K71	2.83 ±0.19	3.08 ±0.16	-0.24 ±0.03	0.70 ±0.011	0.65 ±0.01	0.05 ±0.00021
E72	2.66 ±0.13	3.01 ±0.16	-0.35 ±0.03	0.67 ±0.010	0.64 ±0.01	0.03 ±0.00019
K73	4.86 ±0.29	5.99 ±0.38	**-1.13** ±0.09	0.70 ±0.014	0.64 ±0.02	0.06 ±0.00400
G74	2.85 ±0.17	2.90 ±0.16	-0.05 ±0.01	0.68 ±0.012	0.66 ±0.01	0.03 ±0.00013
L75	2.59 ±0.18	3.90 ±0.14	**-1.31** ±0.04	0.52 ±0.009	0.54 ±0.01	-0.02 ±0.00041
F76	2.34 ±0.10	2.85 ±0.14	-0.51 ±0.04	0.40 ±0.006	0.22 ±0.01	**0.18** ±0.00031
$\mu \pm \sigma$	3.45 ±1.03	3.61 ±1.05	-0.16 ±0.89	0.72 ±0.079	0.70 ±0.10	0.01 ±0.04698

A.23. Pressure-dependent difference of the dynamic parameters of VHP35_L69A

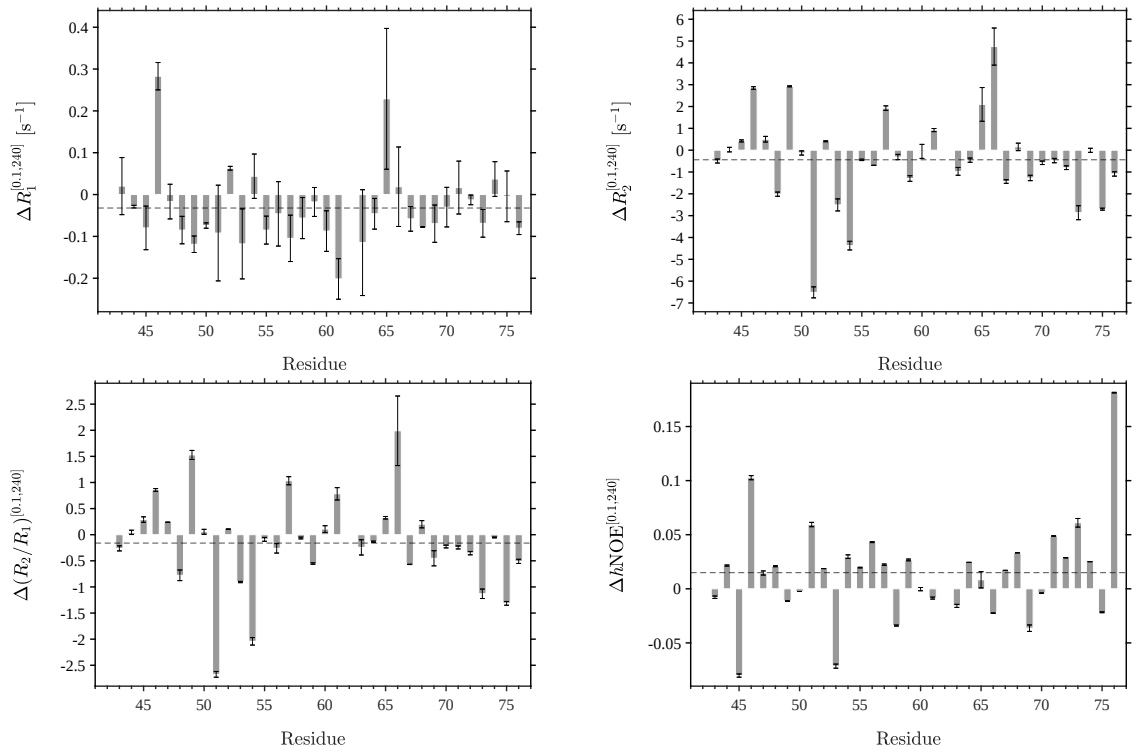

Figure A.34.: **Pressure-dependent difference of the dynamic parameters of the backbone amide protons of VHP35_L69A (Tab. A.15, A.16):** Difference (Δ) of longitudinal (R_1) or transverse (R_2) relaxation rates, the ratio (R_2/R_1) and heteronuclear NOE ratio values at 0.1 MPa and 240 MPa, respectively, and the corresponding mean (*dashed* line).

A.24. τ_m of VHP35 and VHP35_L69A

The overall rotational correlation time τ_m as a function of the ratio of longitudinal (R_1) and transverse (R_2) ^{15}N relaxation rates [147]:

$$\tau_m = \frac{1}{4\pi\nu_N}\sqrt{6\frac{R_2}{R_1} - 7}, \tag{A.1}$$

where ν_N is the ^{15}N resonance frequency in Hz.

Table A.17.: **Overall rotational correlation time τ_m of VHP35 and VHP35_L69A at 0.1 MPa and 240 MPa determined by equation A.1.**

	VHP35	VHP35_L69A
Pressure [MPa]	τ_m [ns]	τ_m [ns]
0.1	3.91 ±0.55	4.46 ±1.06
240	3.74 ±0.79	4.63 ±1.05

B. Pulse Sequences

Some of the pulse programs used were implemented and tested by different people within the research group. This can be recognized by the respective file extensions (first line): *.uw: Ulrich Weininger, *.mk: Michael Kovermann.

B.1. 1D ^{1}H spectra

Table B.1.: **1D ^{1}H: zgpr**

```
;zgpr
;avance-version (12/01/11)
;1D sequence with f1 presaturation

#include <Avance.incl>

d12=20u

acqt0=-p1*2/3.1416
```

```
1 ze
2 30m
d12 pl9:f1
d1 cw:f1 ph29
4u do:f1
d12 pl1:f1
p1 ph1
go=2 ph31
30m mc #0 to 2 F0(zd)
exit
```

```
ph1=0 2 2 0 1 3 3 1
ph29=0
ph31=0 2 2 0 1 3 3 1
```

Table B.2.: **1D ^{1}H: zgprwg.mk**

```
;zgprwg.mk
;p3919gp
;avance-version (02/05/31)
;1D sequence
;water suppression using 3-9-19
;pulse sequence with gradients
;
;M. Piotto, V. Saudek & V. Sklenar,
;J. Biomol. NMR 2, 661 - 666 (1992)
;V. Sklenar, M. Piotto, R. Leppik &
;V. Saudek, J. Magn. Reson.,
; Series A 102, 241 -245 (1993)
;
;$CLASS=HighRes
;$DIM=1D
;$TYPE=
;$SUBTYPE=
;$COMMENT=
;$COMMENT=
; tested on ubiquitin at 23/11/06

;$WNER=nmrsu
p16=1000u
p28=40u
d12=20u
d13=3u
d16=100u
d19=90u
```

```
#nclude <Avance.incl>
#nclude <Grad.incl>



1 ze
2 30m pl9:f1
d1 cw:f1
d13 do:f1
d12 pl1:f1
p1 ph1
50u UNBLKGRAD
p16:gp1
d16 pl18:f1
p28*0.231 ph3
d19*2
p28*0.692 ph3
d19*2
p28*1.462 ph3
d19*2
p28*1.462 ph4
d19*2
p28*0.692 ph4
d19*2
p28*0.231 ph4
46u
p16:gp1
d16
4u BLKGRAD
```

```
go=2 ph31
30m pl9:f1 mc # to 2 F0(zd)
exit



ph1=0 2
ph3=0 0 1 1 2 2 3 3
ph4=2 2 3 3 0 0 1 1
ph31=0 2 2 0

;pl1 : f1 channel - power level
; for pulse (default)
;pl18: f1 channel - power level
; for 3-9-19-pulse (watergate)
;p0 : f1 channel - 90 degree
; pulse at pl18
; use for fine adjustment
;p1 : f1 channel - 90 degree
; high power pulse
;p16: homospoil/gradient pulse
;p27: f1 channel - 90 degree
; pulse at pl18
;d1 : relaxation delay; 1-5 * T1
;d16: delay for homospoil/gradient
; recovery
;d19: delay for binomial water
; suppression
```

```
; d19 = (1/(2*d)), d = distance
; of next null (in Hz)
;NS: 8 * n, total number of scans:
; NS * TD0
;DS: 4
";use gradient ratio: gp 1"
"; 20"

;for z-only gradients:
;gpz1: 20%

;use gradient files:
;gpnam1: SINE.100



;$I: p3919gp,v 1.12 2005/11/10
; 12:17:00 ber Exp $
```

B.2. Backbone and side chain assignment

Table B.3.: ^{1}H,^{15}N-*f*HSQC: fhsqcN15.uw

```
;fhsqcN15.uw
;avance-version
;2D H-1/X correlation via double inept transfer
;phase sensitive using States-TPPI method
;with decoupling during acquisition
;S. Mori, C. Abeygunawardana,
;M. O'Neil-Johnson & P.C.M. van Zijl,
; J. Magn. Reson. B 108, 94-98 (1995)

; tested on ubiquitin at 22/11/06


;$OWNER=nmrsu

#include <Avance.incl>
#include <Grad.incl>
#include <Delay.incl>

in0=inf1/2


p2=p1*2
p4=p3*2
p22=p21*2
p16=1m
p28=40u
d11=30m
d12=20u
d16=100u
d19=90u
d26=2.5m


DELTA=d19-p22/2
DELTA1=d26-p16-d16-p28*3-d19*5+p22/2
DELTA2=d26-p16-d16-p28*3-d19*5+
p22/2-8u-p21-108u

TAU=d26-p16-d16-4u

CEN_HN2=(p22*2+6u-p2)/2
CEN_HC2=(p4*2+6u-p2)/2
d0=(in0-(p21*1.273+6u+4*p3))*0.5

;;"l3=(td1/2)"

1 ze
d11 pl16:f3
2 d1 do:f3
3m
3 d11
4 d12 pl1:f1
50u UNBLKGRAD
(p1 ph0)
4u
p16:gp1
d16
TAU pl3:f3
(CEN_HN2 p2 ph0) (p21 ph0 3u p22
ph1 3u p21 ph0):f3
TAU
4u
p16:gp1
d16 pl2:f2
(p1 ph1)
4u
p16:gp2
d16
(p21 ph4):f3
d0
(CEN_HC2 p2 ph6) (p3 ph0 3u p4
ph1 3u p3 ph0):f2
d0
(p21 ph5):f3
4u
p16:gp2
d16
(p1 ph2)
DELTA1
p16:gp3
d16 pl18:f1
p28*0.231 ph1
d19*2
p28*0.692 ph1
d19*2
p28*1.462 ph1
DELTA
(p22 ph0):f3
DELTA
p28*1.462 ph3
d19*2
p28*0.692 ph3
d19*2
p28*0.231 ph3
4u
p16:gp3
d16
4u BLKGRAD
DELTA2
(p21 ph0):f3
4u
100u pl16:f3
4u
go=2 ph31 cpd3:f3
d1 do:f3 mc #0 to 2 F1PH(ip4, id0)
exit
ph0=0
ph1=1
ph2=2
ph3=3
ph4=0 2
ph5=0 0 0 0 2 2 2 2
ph6=0 0 2 2
ph31=0 2 0 2 2 0 2 0

;pl1 : f1 channel - 1H PL for p1 (high pow)
;pl18: f1 channel - 1H PL for p28 (3-9-19)
;pl2 : f2 channel - 13C PL for p3 (high pow)
;pl3 : f3 channel - 15N PL for p21 (high pow)
;pl16: f3 channel - 15N PL for pcpd3 (decoup.)
;p1 : f1 channel - 90 deg high power pulse
;p3 : f2 channel - 90 deg high power pulse
;p21 : f3 channel - 90 deg high power pulse
;p28 : f1 channel - 90 deg pulse (3-9-19)
;p16 : gradient pulse
;d16 : delay for gradient recovery
;pcpd3: f3 channel - 90 deg dec. pulse at pl16
;cpdprg3: composite pulse dec. for ch.3 [garp]
;d26 : ca. 1/(2*J(N,HN)) [2.5m]
;d19: delay for binomial water suppression
; d19 = (1/(2*d)), d = distance of next null (in Hz)
; d19 = 90u for 600 MHz
;d1 : relaxation delay
;ND0 = 2
;NS = N*2
;DS >= 8
;phc0(F1) = 90 deg, phc1(F1) = -180 deg
;gradient ration : 50 : 80 : 30
;use sine.100
;d31:in0


;gpz1: 50%
;gpz2: 80%
;gpz3: 30%

;gpnam1: SINE.100
;gpnam2: SINE.100
;gpnam3: SINE.100
```

Table B.4.: ^{1}**H,**^{13}**C-*ct*HSQC: hsqc_C13ct.mk**

```
;hsqc_C13ct.mk
;Constant Time HSQC
;avance-version
;off-resonance carbonyl decoupling
;using shaped pulse
;N15 refocusing pulses on F3-channel
;phase sensitive using echo/antiecho method
;G.W. Vuister & A. Bax,
;J. Magn. Reson. 98, 428-435 (1992)
;using gradient coherence selection without
;Sensitivity enhancement

;Author: Kristian Schweimer, 28.12.1997
;gradients (p16=1.5ms)
;gpz1: 13.0%
;gpz2: 90.0%
;gpz3: = 80.0%
;gpz4: =-20.1%

;p14/sp5 = G3.256, 130ppm offresonant, 320us

;$OWNER=nmrsu
#include <Avance.incl>
#include <Grad.incl>
#include <Delay.incl>

in0=inf1/4

p2=p1*2
p4=p3*2
p16=1.5m
d0=3u

in6=in0

d4=1.7m
d7=13.3m
d6=(d7-p14)*0.5-3u
d8=(d7-p14)*0.5-3u-d0
d9=d8-p16-d16
d11=30m
d12=20u
d13=4u
d16=100u
d21=d4-(d13+p16+d16+4u)
CEN_HC2=(p3*4.5+6u-p2)/2
CEN_HC1=(p14-p2)/2
CEN_CN1=(p14-p22)/2

spoffs5=19620

;"l3=(td1/2)"
```

```
1 ze
d11 pl12:f2 pl3:f3
2 d1 do:f2
9m
3 d11*4
4 d11 pl2:f2
50u UNBLKGRAD
(p3 ph0):f2
4u
p16:gp1
2m
(p1 ph0)
d4
(CEN_HC2 p2 ph0) (p3 ph0 3u p3*2.5
ph1 3u p3 ph0):f2
d4
p1 ph0
d13
(p1 ph1)
4u
p16:gp2
d16
(p3 ph4):f2
d6 ;; d8=(d7-p14)*0.5
3u pl0:f2 ;; setting pl for c13
to 120dB, d0 = 20u
(CEN_HC1 p2 ph7) (p14:sp5 ph7):f2
(CEN_CN1 p22 ph0):f3
d6
3u pl2:f2
(p4 ph8):f2
d8
d0
3u pl0:f2
(CEN_HC1 p2 ph7) (p14:sp5 ph7):f2
(CEN_CN1 p22 ph0):f3
d9
d0
3u pl2:f2
p16:gp3
d16
(p1 ph0) (p3 ph5):f2
d4
(CEN_HC2 p2 ph0) (p3 ph0 3u p3*2.5
ph1 3u p3 ph0):f2
d21
d13
p16:gp4*EA
d16 pl12:f2
4u BLKGRAD
go=2 ph31 cpd2:f2
d1 do:f2 mc #0 to 2
F1EA(igrad EA, id0 & dd6 &
ip4*2 & ip31*2)
exit
```

```
ph0=0
ph1=1
ph2=2
ph3=3
ph4=0 2
ph5=0 0 2 2
ph6=1 1 3 3
ph7=0 0 2 2
ph8=0 0 0 0 2 2 2 2 1 1 1 1 3 3 3 3
ph31=0 2 2 0 0 2 2 0 2 0 0 2 2 0 0 2


;gpz1: 13.0%
;gpz2: 90.0%
;gpz3: 80.0%
;gpz4:-20.1%
```

Table B.5.: ^{1}**H,**^{13}**C-*ct*HSQC-TOCSY: hsqcA_ct_tocsy.uw**

```
;hsqcA_ct_tocsy.uw
;Constant Time HSQC-TOCSY
;avance-version
;N15 refocusing pulses on F3-channel
;phase sensitive using echo/antiecho method

;gradients (p16=1.0ms)
;gpz1 = 13.0%
;gpz2 = 90.0%
;gpz3 = 80.0%
;gpz4 =-20.1%



;$OWNER=nmrsu
#include <Avance.incl>
#include <Grad.incl>
#include <Delay.incl>

in0=inf1/4

p2=p1*2
p4=p3*2
p16=1.0m
d0=3u
p14=970u

in6=in0



d7=8.928m
d6=(d7-p22)*0.5
d8=(d7-p22)*0.5-d0
d9=d8-p16-d16
d11=30m
d13=4u
d16=100u
;"d21=d4-(d13+p16+d16+4u)"
d21=p16+d16+7u



p6=25u
FACTOR1=(d15/(p6*172.659))/2+0.5
l1=FACTOR1*2
d14=p6*1.599

spoff5=0



;"l3=(td1/2)"

1 ze
d11 pl12:f2 pl3:f3
2 d1 do:f2
9m
3 d11*4
4 d11 pl2:f2 pl1:f1
50u UNBLKGRAD
(p3 ph0):f2
4u
p16:gp1
2m
(p1 ph0)
d4 pl0:f2
(center (p2 ph0) (p14:sp5 ph0):f2 )
d4 pl2:f2
p1 ph0
d13
(p1 ph1)
4u
p16:gp2
d16
(p3 ph4):f2
d6
(center (p2 ph0) (p22 ph0):f3 )
d6
(p4 ph0):f2
d8
d0
(center (p2 ph0) (p22 ph0):f3 )
d9
d0
p16:gp3
d16
(center (p1 ph0) (p3 ph5):f2 )
d4
(center (p2 ph0) (p4 ph0):f2 )
d4
7 p6*2.000 ph23
d14
p6*1.556 ph23
p6*3.556 ph25
d14
p6*1.000 ph25
p6*3.000 ph23
d14
p6*0.222 ph23
p6*2.222 ph25
d14
p6*0.944 ph25
p6*0.333 ph23
p6*1.389 ph25
d14
p6*1.333 ph25
p6*3.333 ph23
d14
p6*0.833 ph23
p6*2.833 ph25
d14
p6*0.111 ph25
p6*2.111 ph23
d14
p6*2.000 ph23
p6*2.000 ph25
d14
p6*1.556 ph25
p6*3.556 ph23
d14
p6*1.000 ph23
p6*3.000 ph25
d14
p6*0.222 ph25
p6*2.222 ph23
d14
p6*0.944 ph23
p6*0.333 ph25
p6*1.389 ph23
d14
p6*1.333 ph23
p6*3.333 ph25
d14
p6*0.833 ph25
p6*2.833 ph23
d14
p6*0.111 ph23
p6*2.111 ph25
d14
p6*2.000 ph25
p6*2.000 ph23
d14
p6*1.556 ph23
p6*3.556 ph25
d14
p6*1.000 ph25
p6*3.000 ph23
d14
p6*0.222 ph25
p6*2.222 ph23
d14
p6*0.944 ph25
p6*0.333 ph23
p6*1.389 ph25
d14
p6*1.333 ph25
p6*3.333 ph23
d14
p6*0.833 ph23
p6*2.833 ph25
d14
p6*0.111 ph25
p6*2.111 ph23
d14
p6*2.000 ph23
lo to 7 times l1

d21
(p2 ph0)
3u
p16:gp4*EA
d16 pl12:f2 pl10:f1
4u BLKGRAD

go=2 ph31 cpd2:f2
d1 do:f2 mc #0 to 2
F1EA(igrad EA, id0 & dd6 &
ip4*2 & ip31*2)
exit

ph0=0
ph1=1
ph2=2
ph3=3
ph4=0 2
ph5=0 0 2 2
ph23=3
ph25=1
ph31=0 2 2 0


;d4: 1.60m (F,Y), 1.35m (all), 1.25m (H)
```

Table B.6.: ***tr*HNCACB: trhncacb.uw**

```
;trhncacb.uw
;TROSY-HNCACB
;avance-version

;$OWNER=nmrsu
#include <Avance.incl>
#include <Grad.incl>
#include <Delay.incl>

in0=inf1/2
in10=inf2/4

p2=p1*2
p4=p3*2
p22=p21*2
p16=1m
p28=40u

;GPZ=50-80-(-80)-(-30)-(-65)
;p14/sp3 G3.256
;p14/sp5 G3.256 131ppm offset

d3=12.4m
d11=30m
d16=100u
d17=200u
d19=90u

d0=10u
d10=4u
d23=(3.5m-p14)*0.5
d26=2.65m
d30=d3*0.5
d29=d30-d10
"d28=d29-p16-d16+p21*1.273
+DELTA1-p11-28u"
TAU=d26-p16-d16-4u
DELTA=d0*2-10u+3u+p22
DELTA1=4u
DELTA2=d26-p16-d17-4u
"DELTA3=0.5*(p16+d17
+8u-p28*4-0.77
d19*10-p22-DELTA1)"
"DELTA4=DELTA2-p28
*4.77-d19*10"
TAU1=p14

CEN_HN1=(p21-p1)/2
CEN_HN2=(p22-p2)/2
CEN_CN2=(p14-p22)/2
CEN_HC2=(p14-p2)/2

spoffs3=0
spoffs5=19770

"in30=in10" ;; nd0 = 4

aqseq 321
```

```
1 ze
d11
2 d11
d1 pl11:f1 pl2:f2 pl3:f3
50u UNBLKGRAD
(p11 ph3)
4u
20u pl1:f1
4u
(p1 ph0)
4u
p16:gp1
d16
TAU
(CEN_HN2 p2 ph1) (p22 ph0):f3
4u
TAU
p16:gp1
d16
(p1 ph3)
4u
p16:gp2*EA
d16
(p21 ph7):f3
d3
(p14:sp3 ph10):f2
3u
(p22 ph0):f3
3u
TAU1
d3 pl1:f1 pl2:f2
(p21 ph1):f3
4u
(p3 ph8):f2
4u
d23 pl0:f2
(p14:sp5 ph0):f2
4u
d23 pl2:f2
(p4 ph10):f2
4u
d23 pl0:f2
(p14:sp5 ph0):f2
4u
d23 pl2:f2
(p3 ph12):f2
4u
d0 pl0:f2
(p2 ph0):f1
3u
(p14:sp5 ph10):f2
3u
(p22 ph0):f3
d0
4u pl2:f2
(p4 ph10):f2
4u
DELTA pl0:f2
```

```
(p2 ph2):f1
3u
(p14:sp5 ph7):f2
10u
4u pl2:f2

(p3 ph11):f2
4u
d23 pl0:f2
(p14:sp5 ph10):f2
4u
d23 pl2:f2
(p4 ph0):f2
4u
d23 pl0:f2
(p14:sp5 ph0):f2
4u
d23 pl2:f2
(p3 ph13):f2
4u

(p21 ph6):f3
d30 pl0:f2
(p14:sp5 ph10):f2
d30
(p14:sp3 ph11):f2
3u
(p22 ph9):f3
3u
TAU1
d29
d10

(p14:sp5 ph12):f2
d10
d28
p16:gp3*EA
d16 pl11:f1
(p11 ph0):f1
4u
20u pl1:f1
4u
(p1 ph4)
4u
p16:gp4
d16
TAU
(CEN_HN2 p2 ph1) (p22 ph0):f3
4u
TAU
p16:gp4
d16
(p1 ph2)
DELTA1
(p21 ph1):f3
4u
p16:gp5
d17 pl18:f1
```

```
DELTA2
DELTA3
(p22 ph0):f3
DELTA3
p28*0.231 ph0
d19*2
p28*0.692 ph0
d19*2
p28*1.462 ph0
d19*2
p28*1.462 ph2
d19*2
p28*0.692 ph2
d19*2
p28*0.231 ph2
4u
DELTA4
p16:gp5
d17
(p21 ph5):f3
4u
p16:gp3*0.1013
d16
4u BLKGRAD
go=2 ph31
d11 mc #0 to 2
F1PH(rd10 & rd30 & ip11 & ip13, id0)
F2EA(igrad EA & ip4*2 & ip5*2, id10
& dd30 & ip6*2 & ip31*2)
exit


ph0=0
ph1=1
ph2=2
ph3=3
ph4=1
ph5=0
ph6=1 3
ph7=0
ph8=0 0 2 2
ph9=0 0 0 0 0 0 0 0
2 2 2 2 2 2 2 2
ph10=0
ph11=3 3 3 3 1 1 1 1
ph12=1 1 1 1 3 3 3 3
ph13=0
ph31=0 2 2 0


;gpz1: 50%
;gpz2: 80%
;gpz3: -80%
;gpz4: -30%
;gpz5: -65%
```

Table B.7.: **HNCO: hncogp3d**

```
;hncogp3d
;avance-version (15/02/27)
;HNCO
;3D sequence with
; inverse correlation for triple resonance
; using multiple inept transfer steps
;
; F1(H) -> F3(N) -> F2(C=O,t1) ->
; F3(N,t2) -> F1(H,t3)
;
;on/off resonance Ca and C=O pulses
; using shaped pulse
;phase sensitive (t1)
;phase sensitive using Echo/Antiecho
; gradient selection (t2)
;using constant time in t2
;(use parameterset HNCOGP3D)
;
;S. Grzesiek & A. Bax, J. Magn. Reson. 96,
; 432 - 440 (1992)
;J. Schleucher, M. Sattler & C. Griesinger,
; Angew. Chem. Int. Ed. 32, 1489-1491 (1993)
;L.E. Kay, G.Y. Xu & T. Yamazaki,
; J. Magn. Reson. A109, 129-133 (1994)
;
;$CLASS=HighRes
;$DIM=3D
;$TYPE=
;$SUBTYPE=
;$COMMENT=


prosol relations=<triple>



#include <Avance.incl>
#include <Grad.incl>
#include <Delay.incl>


p2=p1*2
p22=p21*2
d11=30m
d13=4u

d21=5.5m
d23=12m
d26=2.3m


d0=3u
d10=d23/2-p14/2
d29=d23/2-p14/2-p26-d21-4u
d30=d23/2-p14/2

in0=inf1/2
in10=inf2/4

in29=in10
in30=in10

td2=tdmax(td2,d30*2,in30)


DELTA=d0*2+larger(p14,p22)-p14
DELTA1=p16+d16+d13+4u
DELTA2=d23-d21-p26
DELTA3=d21-p16-d16-4u
spoff2=0
spoff3=0
spoff5=bf2*(cnst22/1000000)-o2
spoff8=0



aqseq 321



1 d11 ze
d11 pl16:f3
2 d11 do:f3
3 d1 pl1:f1
p1 ph1
d26 pl3:f3
(center (p2 ph1) (p22 ph1):f3 )
d26 UNBLKGRAD
(p1 ph2):f1

4u pl0:f1
(p11:sp1 ph1:r):f1
4u
p16:gp1
d16

(p21 ph3):f3
d21 pl19:f1
(p26 ph2):f1
DELTA2 cpds1:f1 ph1
(center (p14:sp3 ph1):f2 (p22 ph1):f3 )
d23
(p21 ph1):f3

d13 do:f1
(p26 ph7):f1
4u
p16:gp2
d16

(p13:sp2 ph4):f2
d0
(center (p14:sp5 ph1):f2 (p22 ph1):f3 )
d0
4u
(p14:sp3 ph1):f2
DELTA
(p14:sp5 ph1):f2
4u
(p13:sp8 ph1):f2

4u
p16:gp3
d16
(p26 ph2):f1
20u cpds1:f1 ph1

(p21 ph1):f3
d30
(p14:sp5 ph1):f2
d30
(center (p14:sp3 ph1):f2 (p22 ph8):f3 )
d10
(p14:sp5 ph1):f2
d29
4u do:f1
(p26 ph7):f1
4u
p16:gp4*EA
d16
DELTA3 pl1:f1

(center (p1 ph1) (p21 ph5):f3 )
d26
(center (p2 ph1) (p22 ph1):f3 )
d26
(center (p1 ph2) (p21 ph6):f3 )
d26
(center (p2 ph1) (p22 ph1):f3 )
d26
(p1 ph1)
DELTA1
(p2 ph1)
d13
p16:gp5
d16 pl16:f3
4u BLKGRAD
go=2 ph31 cpd3:f3
d11 do:f3 mc #0 to 2
F1PH(calph(ph4, +90), caldel(d0, +in0))
F2EA(calgrad(EA) & calph(ph6, +180),
caldel(d10, +in10) & caldel(d29, +in29)
& caldel(d30, -in30))
exit


ph1=0
ph2=1
ph3=0 0 0 0 0 0 0 0 2 2 2 2 2 2 2 2
ph4=0 2
ph5=0 0 2 2
ph6=3 3 1 1
ph7=3
ph8=0 0 0 0 2 2 2 2
ph31=0 2 2 0 0 2 2 0 2 0 0 2 2 0 0 2


;use gradient ratio:
; gp 1 : gp 2 : gp 3 : gp 4 : gp 5
; 60 : -40 : 10 : 80 : 8.1

;for z-only gradients:
;gpz1: 60%
;gpz2: -40%
;gpz3: 10%
;gpz4: 80%
;gpz5: 8.1%

;use gradient files:
;gpnam1: SMSQ10.100
;gpnam2: SMSQ10.100
;gpnam3: SMSQ10.100
;gpnam4: SMSQ10.100
;gpnam5: SMSQ10.100

;$Id: hncogp3d,v 1.18.2.1 2015/03/03
; 11:21:23 ber Exp $
```

Table B.8.: **HCCH-TOCSY: hcchtocsy.uw**

```
;hcchtocsy.uw
;hcchdigp3d.2
;avance-version (00/12/15)
;HCCH-TOCSY
;3D sequence with
; inverse correlation using multiple
; inept transfer and
; C-C DIPSI3 spinlock
;
; F1(H,t1) -> F2(C,t2) ->
; F2(C') -> F1(H',t3)
;
;off resonance C=O pulse using shaped pulse
;phase sensitive (t1)
;phase sensitive (t2)
;(use parameterset HCCHDIGP3D)
;
;(L.E. Kay, G.Y. Xu, A.U. Singer,
; D.R. Muhandiram & J. D. Forman-Kay
; J. Magn. Reson. B 101, 333 - 337 (1993))


;$OWNER=nmrsu
#include <Avance.incl>
#include <Grad.incl>
#include <Delay.incl>

in0=inf1/2
in10=inf2/2

p2=p1*2
p4=p3*2
d0=3u
d10=3u
d11=30m
d12=20u
d16=100u
"""d4=1.6m"" ;tau a"
"""d21=1.1m"" ;tau c"
"""d23=475u"" ;tau b"

l1=4


p9=20u
p28=1m

p16=500u
p19=2m
p29=300u
p30=5m
p31=4.4m


DELTA1=d4-p16-d16-4u
DELTA2=d4-p16-d16-4u+d0*2+p4
DELTA3=d23-p29-d16
DELTA4=p22+p2+d10*2+4u
DELTA5=d21-p16-d16-4u
DELTA6=d4-p16-d16-p3*2-7u+p1

TAU=(p3*2+3u)-p1

;"CEN_HC1=(p1-p3)/2"
;"CEN_HC2=(p2-p4)/2"
CEN_HC1=(p3-p1)/2
CEN_HC2=(p4-p2)/2

spoffs5=19770

aqseq 312
1 d11 ze
d11 pl12:f2
2 d11 do:f2
3 d1
50u UNBLKGRAD
d12 pl1:f1

(p1 ph3)
4u
p16:gp1
d16
DELTA1 pl2:f2
d0
(p4 ph1):f2
d0
(p2 ph1)
DELTA2 pl3:f3
p16:gp1
d16
4u
(p1 ph2)

p19:gp3
d16

(p3 ph4):f2
d10
(p22 ph1):f3
4u
p29:gp2
d16
DELTA3 pl0:f2
(p14:sp5 ph1):f2
4u
p29:gp2
d16
DELTA3 pl2:f2
p2 ph1
d10
(p4 ph1):f2
DELTA4
p29:gp2
d16
DELTA3 pl0:f2
(p14:sp5 ph1):f2
4u
p29:gp2
d16
DELTA3 pl2:f2
(p3 ph2):f2
4u
d12 pl15:f2
" ;begin DIPSI3"
9 (p9*2.722 ph7):f2
(p9*4.389 ph9):f2
(p9*2.778 ph7):f2
(p9*3.056 ph9):f2
(p9*0.333 ph7):f2
(p9*2.556 ph9):f2
(p9*4.000 ph7):f2
(p9*2.722 ph9):f2
(p9*4.111 ph7):f2
(p9*3.778 ph9):f2
(p9*3.889 ph7):f2
(p9*2.889 ph9):f2
(p9*3.000 ph7):f2
(p9*0.333 ph9):f2
(p9*2.500 ph7):f2
(p9*4.050 ph9):f2
(p9*2.830 ph7):f2
(p9*4.389 ph9):f2
(p9*2.722 ph9):f2
(p9*4.389 ph7):f2
(p9*2.778 ph9):f2
(p9*3.056 ph7):f2
(p9*0.333 ph9):f2
(p9*2.556 ph7):f2
(p9*4.000 ph9):f2
(p9*2.722 ph7):f2
(p9*4.111 ph9):f2
(p9*3.778 ph7):f2
(p9*3.889 ph9):f2
(p9*2.889 ph7):f2
(p9*3.000 ph9):f2
(p9*0.333 ph7):f2
(p9*2.500 ph9):f2
(p9*4.050 ph7):f2
(p9*2.830 ph9):f2
(p9*4.389 ph7):f2
(p9*2.722 ph7):f2
(p9*4.389 ph9):f2
(p9*2.778 ph7):f2
(p9*3.056 ph9):f2
(p9*0.333 ph7):f2
(p9*2.556 ph9):f2
(p9*4.000 ph7):f2
(p9*2.722 ph9):f2
(p9*4.111 ph7):f2
(p9*3.778 ph9):f2
(p9*3.889 ph7):f2
(p9*2.889 ph9):f2
(p9*3.000 ph7):f2
(p9*0.333 ph9):f2
(p9*2.500 ph7):f2
(p9*4.050 ph9):f2
(p9*2.830 ph7):f2
(p9*4.389 ph9):f2
lo to 9 times l1
" ;end DIPSI3"
d12
(p28 ph1)
(p28*2 ph2)
4u
p30:gp4
d16
(p1 ph1)
4u
p31:gp4
d16 pl2:f2

(p3 ph2):f2
4u
p16:gp1
d16
DELTA5
(p2 ph1) (CEN_HC2 p4 ph1):f2
; (CEN_HC2 p2 ph1) (p4 ph1):f2
4u
p16:gp1
d16
DELTA5
(p1 ph1) (CEN_HC1 p3 ph1):f2
; (CEN_HC1 p1 ph1) (p3 ph1):f2

4u
p16:gp1
d16
DELTA1
(p2 ph1) (CEN_HC2 p4 ph1):f2
; (CEN_HC2 p2 ph1) (p4 ph1):f2
4u
p16:gp1
d16
DELTA6
(TAU p1 ph1) (p3 ph1 3u p3 ph5):f2
4u pl12:f2
4u BLKGRAD
go=2 ph31 cpd2:f2
d11 do:f2 mc #0 to 2
F1PH(ip3, id0)
F2PH(rd0 & ip4, id10)
exit


ph1=0
ph2=1
ph3=0 2
ph4=0 0 2 2
ph5=0 0 0 0 2 2 2 2
ph7=1
ph9=3
ph31=0 2 2 0


;use gradient ratio: gp 1 : gp 2 : gp 3 : gp4
; 16 : 16 : -80 : -60
```

B.3. NOESY

Table B.9.: **NOESY-HSQC: noesyhsqcetf3gp3d**

```
;noesyhsqcetf3gp3d
;avance-version (12/01/11)
;NOESY-HSQC
;3D sequence with
; homonuclear correlation via
; dipolar coupling
; dipolar coupling may be due to
; noe or chemical exchange.
; H-1/X correlation via double inept transfer
;phase sensitive (t1)
;phase sensitive using Echo/Antiecho-TPPI
; gradient selection (t2)
;using trim pulses in inept transfer
;with decoupling during acquisition
;(use parameterset NOESYHSQCETF3GP3D)
;
;A.L. Davis, J. Keeler, E.D. Laue & D. Moskau,
; J. Magn. Reson. 98, 207-216 (1992)
;
;$CLASS=HighRes
;$DIM=3D
;$TYPE=
;$SUBTYPE=
;$COMMENT=


#include <Avance.incl>
#include <Grad.incl>
#include <Delay.incl>


p2=p1*2
p22=p21*2
d11=30m
d12=20u
d13=4u
d26=1s/(cnst4*4)


d0=3u
d10=3u

in0=inf1/2
in10=inf2/2


DELTA2=d26-p16-d13-4u

# ifdef LABEL_CN
DELTA=larger(p14,p22)+d0*2
DELTA1=p16+d16+larger(p2,p14)+d10*2
# else
DELTA=p22+d0*2
DELTA1=p16+d16+p2+d10*2
# endif /*LABEL_CN*/


aqseq 321
```

```
1 ze
d11 pl16:f3
2 d1 do:f3
3 d12 pl3:f3
(p1 ph7)
DELTA
(p2 ph8)
d0
# ifdef LABEL_CN
(center (p14:sp3 ph1):f2 (p22 ph1):f3 )
# else
(p22 ph1):f3
# endif /*LABEL_CN*/

d0
(p1 ph1):f1
d8
(p1 ph1):f1
d26
(center (p2 ph1) (p22 ph6):f3 )
d26 UNBLKGRAD
p28 ph1
d13
(p1 ph2) (p21 ph3):f3
d10

# ifdef LABEL_CN
(center (p2 ph5) (p14:sp3 ph1):f2 )
# else
(p2 ph5)
# endif /*LABEL_CN*/

d10
p16:gp1*EA
d16
(p22 ph4):f3
DELTA1
(ralign (p1 ph1) (p21 ph4):f3 )
d26
(center (p2 ph1) (p22 ph1):f3 )
d13
p16:gp2
DELTA2 pl16:f3
4u BLKGRAD
go=2 ph31 cpd3:f3
d1 do:f3 mc #0 to 2
F1PH(calph(ph7, +90) & calph(ph8, +90),
caldel(d0, +in0))
F2EA(calgrad(EA), caldel(d10, +in10) &
calph(ph3, +180) & calph(ph6, +180) &
calph(ph31, +180))
exit
```

```
ph1=0
ph2=1
ph3=0 2
ph4=0 0 0 0 0 0 0 0 2 2 2 2 2 2 2 2
ph5=0 0 2 2
ph6=0
ph7=0 0 0 0 2 2 2 2
ph8=1 1 1 1 3 3 3 3
ph31=0 2 0 2 2 0 2 0 2 0 2 0 0 2 0 2


;use gradient ratio: gp 1 : gp 2
; 80 : 20.1 for C-13
; 80 : 8.1 for N-15

;for z-only gradients:
;gpz1: 80%
;gpz2: 20.1% for C-13, 8.1% for N-15

;use gradient files:
;gpnam1: SMSQ10.100
;gpnam2: SMSQ10.100

;preprocessor-flags-start
;LABEL_CN: for C-13 and N-15 labeled samples
; start experiment with
; option -DLABEL_CN (eda: ZGOPTNS)
;preprocessor-flags-end


;for older datasets use AQORDER : 3 - 2 - 1


;$Id: noesyhsqcetf3gp3d,v 1.8 2012/01/31
; 17:49:27 ber Exp $
```

B.4. Protein dynamics

Table B.10.: ***h*NOE: hsqcnoef3gpsi**

```
;hsqcnoef3gpsi
;avance-version (12/01/11)
;2D H-1/X correlation via double
; inept transfer
; using sensitivity improvement
;for measuring H1-N15 NOEs
;phase sensitive using Echo/Antiecho-TPPI
; gradient selection
;with decoupling during acquisition
;using f3 - channel
;recording NONOE and NOE interleaved
;(use parameterset HSQCNOEF3GPSI)
;
;$CLASS=HighRes
;$DIM=2D
;$TYPE=
;$SUBTYPE=
;$COMMENT=


prosol relations=<triple>


#include <Avance.incl>
#include <Grad.incl>
#include <Delay.incl>



p2=p1*2
p22=p21*2
d11=30m
d12=20u
d24=1s/(cnst4*cnst11)
d25=1s/(cnst4*cnst12)
d26=1s/(cnst4*4)

p0=p1*4/3


d0=3u

in0=inf1/2

" "
DELTA2=p16+d16+8u
DELTA3=d25-p16-d16-4u

# ifdef LABEL_CN
DELTA1=d25-p16-d16-larger(p2,p8)-d0*2
# else
DELTA1=d25-p16-d16-p2-d0*2
# endif /*LABEL_CN*/


l0=1
l4=d1/(p0+5m)
```

```
spoff1=0
spoff13=bf2*((cnst21+cnst22)/2000000)-o2



1 ze
d11 pl16:f3
2 d11 do:f3
3 d12

if "l0 %2 == 1"
{
d1
50u UNBLKGRAD
4u pl0:f1
(p11:sp1 ph1:r):f1
4u
4u pl1:f1
}
else
{
4 (p0 ph1)
5m
lo to 4 times l4
4u
50u UNBLKGRAD
}

(p1 ph1)
p16:gp1
d16 pl3:f3

(p21 ph8):f3
4u
p16:gp2*-1*EA
d16
DELTA3
(p22 ph6):f3
d0

# ifdef LABEL_CN
(center (p2 ph9) (p8:sp13 ph1):f2 )
# else
(p2 ph9)
# endif /*LABEL_CN*/

d0
p16:gp2*EA
d16
DELTA1

(center (p1 ph1) (p21 ph4):f3 )
d24
(center (p2 ph1) (p22 ph1):f3 )
d24
(center (p1 ph2) (p21 ph5):f3 )
d26
(center (p2 ph1) (p22 ph1):f3 )
```

```
d26
(p1 ph1)
DELTA2
(p2 ph1)
4u
p16:gp3
d16 pl16:f3
4u BLKGRAD
go=2 ph31 cpd3:f3
d11 do:f3 mc #0 to 2
F1I(iu0, 2)
F1EA(calgrad(EA) & calph(ph5, +180),
caldel(d0, +in0) & calph(ph6, +180) &
calph(ph8, +180) & calph(ph31, +180))
exit


ph1=0
ph2=1
ph4=0 0 2 2
ph5=3 3 1 1
ph6=0
ph7=3
ph8=1 3
ph9=0 0 2 2
ph31=0 2 2 0


;use gradient ratio: gp 1 : gp 2 : gp 3
"; 50 : 80 : 16.2"
; for N-15

;for z-only gradients:
;gpz1: 50%
;gpz2: 80%
;gpz3: 16.2%

;use gradient files:
;gpnam1: SMSQ10.100
;gpnam2: SMSQ10.100
;gpnam3: SMSQ10.100


;preprocessor-flags-start
;LABEL_CN: for C-13 and N-15 labeled
;samples start experiment with
;option -DLABEL_CN (eda: ZGOPTNS)
;preprocessor-flags-end


;use AU-program split [2] to separate NOE
; and NONOE data into
; different datasets



;$ Id: hsqcnoef3gpsi,v 1.11 2012/01/31
; 17:49:26 ber Exp $
```

Table B.11.: R_1 **relaxation rate: r1N.uw**

```
;r1N.uw
; R1 15N Lopt - PEPHSQC detection
; Using channel 3 for 15N
; based on Lopt 13C aro relax experiments
"; 1) use vclist for different"
; blocks of T1 delays
"; 3) use interleaved acquisition"
; ns - T1 - hypercomplex - t1
; works for signals between 10.5 and
; 6.5 ppm @ 600 MHz


#include <Avance.incl>
#include <Delay.incl>
#include <Grad.incl>

define list<loopcounter> r1list = <$VCLIST>

aqseq 312

in10=inf2/2

;***** PULSES *****
p2=p1*2
p22=p21*2
p13=1150u
p14=1600u

;***** LOOPS *****
l4=(td2/2)
l5=(td1)


;***** DELAYS *****
d10=3u
d16=100u
d3=50m
d21=1/(4.0*cnst21)
DELTA1=d20-p28-d16-3u
DELTA2=d21-p23-d16-3u
DELTA3=d20-p13-3u

DELTA4=d3/2-p14/2

DELTA6=d21-p18-d16-6u-p2
DELTA7=d21-p18-d16-6u

spoff5=2500
spoff6=-1680
spoff7=-1680


ze
10u pl1:f1 pl3:f3
1 31m do:f3
11 5m
2 3m
3 10m
l3=r1list
12 3u


;***** INEPT *****
d1 pl1:f1 pl3:f3
(p21 ph4):f3
50u UNBLKGRAD
p20:gp20
d16
(p1 ph4):f1
3u
p28:gp28
d16
DELTA1
(center (p2 ph4):f1 (p22 ph4):f3 )
3u
DELTA1
p28:gp28
d16
(p1 ph1):f1
3u pl10:f1
(p13:sp7 ph2):f1
3u pl1:f1
(p21 ph7):f3
3u
p23:gp23
d16
DELTA2
(center (p2 ph4):f1 (p22 ph4):f3 )
3u
DELTA2
p23:gp23
d16
;***** T1 *****
(p21 ph1):f3
if "l3 == 0" goto 7
20 DELTA4 pl10:f1
(p14:sp5 ph4):f1
DELTA4 pl1:f1
lo to 20 times l3
7 (p21 ph5):f3
;***** t1 LABELING + inphase -> antiphase *****
d10
DELTA6
p18:gp18*EA
d16
(center (p2 ph4):f1 (p4 ph4):f2 )
d10
(p22 ph4):f3
6u
p18:gp18*EA*-1
d16
DELTA7
;***** PEP period *****
"(p1 ph4):f1 (p21 ph9):f3 "
3u pl10:f1
(p13:sp7 ph2):f1
DELTA3 pl1:f1
"(center (p2 ph4):f1 (p22 ph4):f3 ) "
DELTA3 pl10:f1
(p13:sp6 ph1):f1
3u pl1:f1
(p1 ph1):f1 (p21 ph8):f3
d20
(center (p2 ph4):f1 (p22 ph4):f3 )
d20
(p1 ph4):f1
3u pl10:f1
(p13:sp7 ph4):f1
3u pl1:f1
(p2 ph4):f1
3u
50u
p18:gp18*0.2026 ; decode gradient
d16 pl16:f3
3u BLKGRAD

; ***** ACQUISITION *****
go=1 ph0 cpd3:f3
30m do:f3 wr #0 if #0 zd
1m r1list.inc
lo to 11 times l5
1m ip9*2
1m igrad EA
1m r1list.res
lo to 2 times 2
1m id10
1m ip5*2
1m ip0*2
lo to 3 times l4
exit


ph0 = 0 2 0 2 2 0 2 0

ph1 = 1
ph2 = 2
ph3 = 3
ph4 = 0
ph5 = 1 3
ph7 = 0 0 0 0 2 2 2 2

ph8 = 1 1 3 3
;ph8 = 1
ph9 = 0
;ph9 = 0 0 2 2


;*** VARIABLES SET BY USER ***
";cnst21: JNH [93 Hz]"
;d1: recycle delay 1-5*T1
;d3 : loopdelay T1 = 50ms
;d16 : grad delay [100u]
;d20 : inept delay 1 [2.5m]
;d21 : 1/4JNH [2.69m]
;td1: 2* number of complex points
;p1: 1H 90 pulse length @ pl1
;p21: 15N 90 pulse length @ pl3
;p18: encoding gradient [1000u]
;p20: gradient purge for 15N [1000u]
;p23: gradient purge for P-element [300u]
;p28: gradient purge for 180 pulse [1000u]


;pl1: 1H full power
;pl10: 120 dB
;pl3: 15N full power



;l3: r1list, timeT1 = l3*50ms

;spnam5: reburp.1000
;spnam6: eburp2.1000
;spnam7: eburp2tr.1000

;gpz18 80%
;gpz20 20%
;gpz23 7.5%
;gpz26 7.5%
;gpz28 6.25%

;gpnam18: SINE.100
;gpnam20: SINE.100
;gpnam23: SINE.32
;gpnam26: SINE.32
;gpnam28: SINE.100
```

Table B.12.: R_2 **relaxation rate: r2N.uw**

```
;r2N.uw
; R2 15N Lopt - PEPHSQC detection
; Using channel 3 for 15N
; based on Lopt 13C aro relax experiments
"; 1) use vclist for different blocks"
; of T2 delays
"; 3) use interleaved acquisition"
; ns - T2 - hypercomplex - t1
; works for signals between 10.5 and
; 6.5 ppm @ 600 MHz


#include <Avance.incl>
#include <Delay.incl>
#include <Grad.incl>

define list<loopcounter> r2list = <$VCLIST>

aqseq 312

in10=inf2/2

;***** PULSES *****
p2=p1*2
p22=p21*2
p13=1150u
p14=1600u

;***** LOOPS *****
l4=(td2/2)
l5=(td1)


;***** DELAYS *****
d10=3u
d16=100u
d3=250u
d21=1/(4.0*cnst21)
DELTA1=d20-p28-d16-3u
DELTA2=d21-p23-d16-3u
DELTA3=d20-p13-3u

DELTA4=d3-p8/2

DELTA6=d21-p18-d16-6u-p2
DELTA7=d21-p18-d16-6u

spoff5=2500
spoff6=-1680
spoff7=-1680


ze
10u pl1:f1 pl3:f3
1 31m do:f3
11 5m
2 3m
3 10m
l3=r2list
12 3u

;***** INEPT *****
d1 pl1:f1 pl3:f3
(p21 ph4):f3
50u UNBLKGRAD
p20:gp20
d16
(p1 ph4):f1
3u
p28:gp28
d16
DELTA1
(center (p2 ph4):f1 (p22 ph4):f3 )
3u
DELTA1
p28:gp28
d16
(p1 ph1):f1
3u pl10:f1
(p13:sp7 ph2):f1
3u pl1:f1
(p21 ph7):f3
3u
p23:gp23
d16
DELTA2
(center (p2 ph4):f1 (p22 ph4):f3 )
3u
DELTA2
p23:gp23
d16
;***** gradient filter *****
(p21 ph1):f3
3u
p23:gp24
d16
(p21 ph5):f3
;***** T2 relaxation *****
if "l3 == 0" goto 7
20 DELTA4 pl10:f1 pl8:f3
(center (p14:sp5 ph4):f1 (p8 ph4 DELTA4
DELTA4 p8 ph4 DELTA4 DELTA4 p8 ph1 DELTA4
DELTA4 p8 ph3 DELTA4 DELTA4 p8 ph4 DELTA4
DELTA4 p8 ph4 DELTA4 DELTA4 p8 ph3 DELTA4
DELTA4 p8 ph1):f3)
DELTA4
DELTA4
(center (p14:sp5 ph2):f1 (p8 ph4 DELTA4
DELTA4 p8 ph4 DELTA4 DELTA4 p8 ph1 DELTA4
DELTA4 p8 ph3 DELTA4 DELTA4 p8 ph4 DELTA4
DELTA4 p8 ph4 DELTA4 DELTA4 p8 ph3 DELTA4
DELTA4 p8 ph1):f3)
DELTA4 pl1:f1 pl3:f3
lo to 20 times l3
;***** t1 LABELING + inphase -> antiphase *****
7 d10
DELTA6
p18:gp18*EA
d16
(center (p2 ph4):f1 (p4 ph4):f2 )
d10
(p22 ph4):f3
6u
p18:gp18*EA*-1
d16
DELTA7
;***** PEP period *****
"(p1 ph4):f1 (p21 ph9):f3 "
3u pl10:f1
(p13:sp7 ph2):f1
DELTA3 pl1:f1
"(center (p2 ph4):f1 (p22 ph4):f3 ) "
DELTA3 pl10:f1
(p13:sp6 ph1):f1
3u pl1:f1
(p1 ph1):f1 (p21 ph8):f3
d20
(center (p2 ph4):f1 (p22 ph4):f3 )
d20
(p1 ph4):f1
3u pl10:f1
(p13:sp7 ph4):f1
3u pl1:f1
(p2 ph4):f1
3u
50u
p18:gp18*0.2026 ; decode gradient
d16 pl16:f3
3u BLKGRAD

; ***** ACQUISITION *****
go=1 ph0 cpd3:f3
30m do:f3 wr #0 if #0 zd
1m r2list.inc
lo to 11 times l5
1m ip9*2
1m igrad EA
1m r2list.res
lo to 2 times 2
1m id10
1m ip5*2
1m ip0*2
lo to 3 times l4
exit

ph0 = 0 2 0 2 2 0 2 0


ph1 = 1
ph2 = 2
ph3 = 3
ph4 = 0
ph5 = 1 3
ph7 = 0 0 0 0 2 2 2 2

ph8 = 1 1 3 3
;ph8 = 1
ph9 = 0
;ph9 = 0 0 2 2


;*** VARIABLES SET BY USER ***
";cnst21: JNH [93 Hz]"
;d1: recycle delay 1-5*T1
;d3 : loopdelay T1 = 50ms
;d16 : grad delay [100u]
;d20 : inept delay 1 [2.5m]
;d21 : 1/4JNH [2.69m]
;td1: 2* number of complex points
;p1: 1H 90 pulse length @ pl1
;p21: 15N 90 pulse length @ pl3
;p8: 15N CPMG (180) pulse @ pl8 [110u]
;p18: encoding gradient [1000u]
;p20: gradient purge for 15N [1000u]
;p23: gradient purge for P-element [300u]
;p28: gradient purge for 180 pulse [1000u]


;pl1: 1H full power
;pl10: 120 dB
;pl3: 15N full power
;pl8: 15N CPMG power (calibrate)


;l3: r2list, timeT2 = l3*8ms

;spnam5: reburp.1000
;spnam6: eburp2.1000
;spnam7: eburp2tr.1000

;gpz18 80%
;gpz20 20%
;gpz23 7.5%
;gpz24 30%
;gpz28 6.25%

;gpnam18: SINE.100
;gpnam20: SINE.100
;gpnam23: SINE.32
;gpnam24: SINE.32
;gpnam28: SINE.100
```

Curriculum Vitae

Personal Information

Name	Paul Becker
Date of birth	04.09.1984
Birthplace	Schwerin

Education

2015 – 2022	Martin Luther University Halle-Wittenberg, Department of Physics, biophysics group, research associate and PhD student
2012 – 2015	University of Lübeck, Molecular Life Science (M.Sc.)
2009 – 2012	University of Lübeck, Molecular Life Science (B.Sc.)
2006 – 2009	Asklepios-Klinik St.-Georg Hamburg, Apprenticeship state-certified nurse
1995 – 2004	Gymnasium Gadebusch, Abitur

Publications

[1] Dreydoppel, M., Becker, P., Raum, H.N., Gröger, S., Balbach, J., & Weininger, U. Equilibrium and Kinetic Unfolding of GB1: Stabilization of the Native State by Pressure. *J. Phys. Chem. B* **122**, 8846-8852 (2018).

Acknowledgment

I would like to take this opportunity to express my sincere gratitude to all those who have contributed to the success of this work:

The present work was done in the department of biophysics under the supervision of Prof. Dr. Jochen Balbach at the Martin Luther University Halle-Wittenberg. I would like to thank him especially for giving me the interesting topic, his constant willingness to discuss it, many helpful advices and also the freedom in working on and carrying out projects and project ideas.

I would like to thank Prof. Dr. Thomas Kiefhaber for the cooperation, for the interesting discussions and for the preparation and provision of the protein samples, for the latter especially Uwe Fandrich.

I would like to thank all former and current members of the group for the good atmosphere, helpfulness and willingness to discuss: Matthias Altenstein, Dr. Monika Baumann, Natalie Breitkopf, Heike Böcker, Matthias Dreydoppel, Stefan Gröger, Dr. Tobias Gruber, Dr. Susanne Link, Rositta Mothes, Malte Neudorf, Heiner Raum, Prof. Dr. Detlef Reichert, Shubhra Sachan, Bruno Voigt, Kathrin Waldheim, Dr. Ulrich Weininger and Constanze Westphal. Special thanks to Stefan and Uli for their support with NMR spectroscopic questions, the implementation of pulse sequences and the training and support with ARIA, Matthias (Dreydoppel) for the support in MATLAB and Katrin for the instruction and support in the laboratory.

Furthermore, I would also like to thank Prof. Dr. Kay Saalwächter and his solid-state NMR group for the good atmosphere at Betty-Heimann-Straße.

I would like to thank the Deutsche Forschungsgemeinschaft (DFG) and the SFB TRR 102 (Polymere unter Zwangsbedigungen) for the financial support during my PhD thesis.

Last but not least I would like to thank my family especially Frank, Kerstin and Luise Becker, and also Christine Köchy for their support during this time. Furthermore, I would like to thank the many dear people from Halle, especially the J8, Berlin, Hamburg, Rostock and Vig.

Statutory Declaration

I hereby declare that this dissertation

"Biophysical characterization of the VHP35 protein by NMR spectroscopy"

is solely my original work. I have used only the sources and materials indicated and have not received any unauthorized assistance from others. All citations from other works as well as paraphrases or summaries of other works have been identified as such and properly indicated in the dissertation. This dissertation or any parts thereof has not been submitted to any domestic or foreign educational institution as part of an examination or degree program.

Halle (Saale), 18. May 2022 .....
(Paul Becker)